JSCSEN 80(5)595–729(2015)

ISSN 1820-7421(Online)

Journal of the Serbian Chemical Society

eVersion
Electronic

Volume 80 : : 2015 : : 85 Years of the Journal

1930 Glasnik Hemijskog Društva Kraljevine Jugoslavije
Journal of the Chemical Society of the Kingdom of Yugoslavia
1947 Glasnik hemijskog društva Beograd
Journal of the Chemical Society of Belgrade
1985 Journal of the Serbian Chemical Society

VOLUME 80

No 5

BELGRADE 2015

Available on line at

СХД 1897

www.shd.org.rs/JSCS/

Journal of the Serbian Chemical Society
eVersion electronic
JSCS-info@shd.org.rs • www.shd.org.rs/JSCS

J. Serb. Chem. Soc. Vol. 80, No. 5 (2015)

CONTENTS

Organic Chemistry

Biochemistry and Biotechnology

Inorganic Chemistry

Theoretical Chemistry

Physical Chemistry

Electrochemistry

Thermodynamics

Materials

Environmental

Published by the Serbian Chemical Society
Karnegijeva 4/III, P.O. Box 36, 11120 Belgrade, Serbia
Printed by the Faculty of Technology and Metallurgy
Karnegijeva 4, P.O. Box 35-03, 11120 Belgrade, Serbia

Journal of the Serbian Chemical Society
JSCS-info@shd.org.rs • www.shd.org.rs/JSCS

J. Serb. Chem. Soc. 80 (5) 595–604 (2015)
JSCS–4740

UDC 547.594+542.9+547.7:546.561'13+
+546.171:544.4
Original scientific paper

Double catalytic effect of $(PhNH_3)_2CuCl_4$ in a novel, highly efficient synthesis of 2-oxo- and thioxo-1,2,3,4-tetrahydropyrimidines

NENAD JANKOVIĆ*#, ZORICA BUGARČIĆ and SVETLANA MARKOVIĆ

University of Kragujevac, Faculty of Science, Department of Chemistry, Radoja Domanovića 12, 34 000 Kragujevac, Serbia

(Received 28 October 2014, revised 13 February, accepted 13 February 2015)

Abstract: An innovative route for the construction of 2-oxo- and thioxo-1,2,3,4-tetrahydropyrimidines was delineated through a multicomponent reaction under Biginelli conditions, starting from different aromatic aldehydes, β-keto esters and urea or thiourea. The proper choice of the copper complex $(PhNH_3)_2CuCl_4$, as a novel homogeneous catalyst, enabled a facile, efficient, and inexpensive reaction under mild experimental conditions. Moreover, the first application of this complex salts in organic synthesis ever is presented. The obtained products were of high purity, and could be easily isolated from the reaction mixture in good to excellent yields. Moreover, compared to the classical Biginelli reaction conditions, the present method has the advantages of higher yields and experimental and work-up simplicity. To illustrate the joint catalytic action of the Cu^{2+} and phenylammonium ions, two key steps of Biginelli reaction were examined using the M06 functional.

Keywords: aldehydes; multicomponent reactions; heterocycles; homogeneous catalysis; density functional calculations.

INTRODUCTION

The 2-oxo- and thioxo-1,2,3,4-tetrahydropyrimidines (3,4-dihydropyrimidine-2(1*H*)-thi(ones)) are a class of compounds that have attracted the enormous interest of the medicinal chemistry community in recent years. Dihydropyrimidinones are very attractive compounds because of the wide range of their biological activities, such as: antihypertensive,[1–4] anti-HIV,[5] antitumor,[6–10] antiepileptic,[11] antimalarial,[12] anti-inflammatory,[13] antitubercular,[14] antioxidative[15] and anti-HBV (hepatitis B virus).[16] In addition, they act as potassium channel blockers[17,18] and α_{1A} adrenergic receptor antagonists.[19] Therefore, the pre-

---

* Corresponding author. E-mail: nenad.jankovic@kg.ac.rs
# Serbian Chemical Society member.
doi: 10.2298/JSC141028011J

paration of this heterocyclic nucleus has gained great importance in organic synthesis. A simple method for the preparation of the dihydropyrimidinones was first reported by Biginelli in 1893 (Fig. 1).[20] His original reaction is the acid-supported cyclocondensation of an aldehyde, *β*-ketoester and urea. However, this method suffers from low product yields (20–50 %), strong acidic condition and difficult isolation of the products.

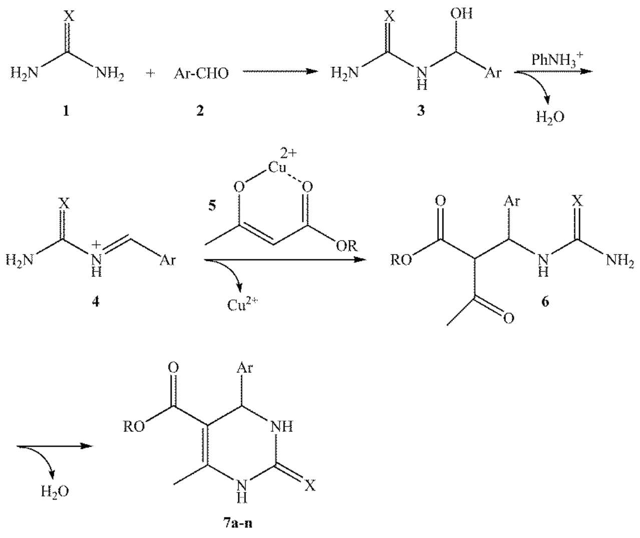

	Ar	R	X
7a	C_6H_4, 3-NO_2	Et-	O
7b	C_6H_5	Et-	O
7c	C_6H_3, 4-OH, 3-OCH_3	Et-	O
7d	$C_6H_5CH=CH$	Et-	O
7e	C_6H_5	Et-	S
7f	C_6H_3, 4-OH, 3-OCH_3	Et-	S
7g	2-Furyl	Et-	O
7h	C_6H_5	Me-	O
7i	C_6H_3, 4-OH, 3-OCH_3	Me-	O
7j	$C_6H_5CH=CH$	Me-	O
7k	C_6H_4, 3-NO_2	Me-	O
7l	2-Furyl	Me-	O
7m	C_6H_3, 4-OH, 3-OCH_3	Me-	S
7n	C_6H_5	Me-	S

Fig. 1. General outline of the Biginelli Reaction.

In the last decades, numerous improved procedures with new catalysts for Biginelli reaction have been reported[21,22]. Many Lewis acids, such as copper salts, proved to be very good catalysts for the preparation of dihydropyrimidinones. This field of investigation is still very vigorous. Namely, some copper-based catalysts, such as: $Cu(OTf)_2$,[23] copper methanesulfonate (CMS),[24] $CuCl_2$,[25] $Cu(NO_3)_2\cdot3H_2O$,[26] Cu sulfamate,[27] $Cu(NTf)_2$,[28] [[Gmim]Cl–Cu(II)],[29] Cu nanoparticles,[30] $Cu(acac)_2[bmim]BF_4$,[31] $CuCl_2\cdot2H_2O$,[32] $Cu(ClO_4)_2\cdot6H_2O$,[33] $Cu(BF_4)_2$,[34] poly(4-vinylpyridine-co-divinylbenzene)–Cu(II) complex,[35] and CuI[36] have recently been successfully employed. However, some inorganic and organic ammonium salts, such as ammonium carbonate,[37] alkylammonium salts,[38] and benzyltriethylammonium chloride,[39] were used as catalysts in the Biginelli reaction.

The catalytic behavior of Cu(II) and ammonium compounds in the Biginelli reaction motivated us to focus our attention on the application of a compound with Cu(II) and the phenylammonium ion in same molecule, that is bis(phenylammonium) tetrachloridocuprate(2–), $(PhNH_3)_2CuCl_4$. This complex salt was synthesized by modification of earlier described procedures[40] and successfully applied as a catalyst for the synthesis of dihydropyrimidinones. To elucidate the catalytic role of the complex, a mechanistic insight into the crucial reaction steps is provided.

It is generally accepted that the catalytic action of the Cu^{2+} conforms to the mechanism depicted in Fig. 1. The first phase of the reaction is a spontaneous proton transfer from urea (**1**) to the oxygen of an aromatic aldehyde (**2**), whereby N-substituted (thio)urea (**3**) is built. In the further course of the reaction, a Brønsted acid removes HO^- from **3**, thus yielding the imminium ion (**4**). In the next reaction step, a new C–C bond between the benzylidene carbon of **4** and the α-C atom of an active methylene compound (**5**) is formed. This phase of the Biginelli reaction is catalyzed by Cu^{2+}, and yields the condensation product (**6**). This intermediate undergoes intramolecular nucleophilic addition, followed by the formation of a new C–N bond and dehydration. In this way, the final product of the reaction, dihydropyrimidinone (**7**) is formed.

EXPERIMENTAL

General

The ^1H- and ^{13}C-NMR spectra were recorded in DMSO-d_6 on a Varian Gemini 200 MHz NMR spectrometer. The IR spectra were obtained with a Perkin-Elmer Model 137B and Nicolet 7000 FT spectrophotometers. Microanalyses for C, H and N were obtained on a Dornis & Kolbe instrument. Melting points (m.p.) were determined on a System Kofler type WME apparatus and are uncorrected. Thin layer chromatography (TLC) was performed on 0.25 mm Merck precoated silica gel plates (60F-254) using an ethyl acetate–methanol (8:2) mixture as the mobile phase and UV light for visualization. All aromatic aldehydes, β-keto-esters, urea and thiourea were used as supplied by Aldrich. Aniline (reagent grade) from Merck was distilled prior to use. Copies of the ^1H- and ^{13}C-NMR spectra of all compounds (**7a**–**n**, Figs. S-1–S-26), as well as analytical and spectral data are given in the Supplementary material to this paper.

Preparation of the catalyst $(PhNH_3)_2CuCl_4$

Hydrochloric acid (6 M, 20 mL) was taken in a 100-mL round-bottom flask and $CuSO_4\cdot 5H_2O$ (2.49 g, 10 mmol) was added slowly with stirring and constant cooling. To the resulting dark green solution, freshly distilled aniline (1.86 g, 0.02 mmol) was added very slowly. The precipitated yellow powder was filtered and washed with ethanol (5 mL, 95 %) and dichloromethane (5 mL). The copper complex powder was dried at 100 °C to constant weight.

General experimental procedures for the synthesis of 2-oxo- and thioxo-1,2,3,4-tetrahydro-pyrimidines

In a 50-mL round-bottom flask, urea or thiourea (15 mmol) was dissolved in ethanol (20 mL, 95 %). Then an aromatic aldehyde (10 mmol), β-keto ester (12 mmol) and catalyst (10 mol % with respect to aldehyde) were added. The solution was magnetically stirred at room temperature. The reaction was followed by TLC to verify its completion. The formed white solid was filtered, washed with small portions of cold ethanol and DCM, and then dried under vacuum to afford the desired product with a good purity grade.

Computational details

All calculations were performed with the Gaussian 09 program package[41] using the M06 functional. This hybrid meta functional was developed by Zhao and Truhlar as "a functional with good accuracy "across-the-board" for transition metals, main group thermochemistry, medium-range correlation energy, and barrier heights".[42] This method was recommended "for application in organometallic and inorganometallic chemistry and for noncovalent interactions".[43] The 6-311+G(d,p) basis set was applied for C, H, N, and O, whereas the Def2-TZVPD basis set[44] was used for Cu. These triple split valence basis sets add the polarization functions to all atoms and diffuse functions to heavy atoms. The structures of all investigated species in ethanol were optimized, and frequency calculations performed. The influence of the solvent (dielectric constant = 24.852) was taken into account by applying the CPCM solvation model (polarizable conductor calculation model).[45] An unrestricted scheme was applied for the open shell structures containing a Cu^{2+}. The obtained stationary points were verified to be equilibrium geometries (no imaginary frequencies), or transition states (one imaginary frequency) on the potential energy surface. The activation free energies were calculated at 298.15 K. Natural bond orbital (NBO) analysis[46-48] was realized for all calculated structures.

The ^{13}C-NMR chemical shifts for all carbon atoms of **7h** in DMSO relative to TMS were calculated using the gauge independent atomic orbital (GIAO) method, as implemented in Gaussian 09. For this purpose, the geometries of **7h** and TMS in DMSO were optimized using the M06/6-311+G(d,p) and CPCM models (dielectric constant of DMSO = 46.826). The nuclear magnetic shielding tensors were calculated for TMS and **7h**. The values for all carbon atoms in **7h** were subtracted from the value for the carbon in TMS (178.4833). Compound **7h** belongs to the C_1 point group and, thus, the *ortho* and *meta* carbons show two different chemical shifts. In this case, the corresponding mean values were taken to represent the chemical shifts of the *ortho* and *meta* carbons. As the so-obtained chemical shifts were systematically overestimated, their values were scaled by a factor of 0.94.

RESULTS AND DISCUSSION

In this paper, a simple but effective and convenient method for the synthesis of 2-oxo- and thioxo-1,2,3,4-tetrahydropyrimidines from urea or thiourea (**1**), some aromatic aldehydes (**2**) and *β*-keto ester (**5**) in the presence of copper complex $(PhNH_3)_2CuCl_4$ as a catalyst is reported. The results of the investigation are given in Tables I–III.

TABLE I. Optimization of the solvent for synthesis of the product **7h** at room temperature for 24 h (*ε* - dielectric constant, *DN* - donor number, *AN* - acceptor number, *HBD* - hydrogen bond donor, *HBA*- hydrogen bond acceptor)

Entry	Solvent	*ε*[49]	*DN*[50]	*AN*[50]	*HBD* / *α*[51]	HBA / *β*[52]	Catalyst, mol %	Yield[a], %
1	DCM	8.9	–	20.4	–	–	1	8
2	Toluene	2.4	–	–	–	–	1	11
3	MeOH	32.7	20.0	41.5	0.99	0.70	1	32
4	EtOH	24.6	19.0	37.1	0.85	0.77	1	41
5	THF	7.6	20.0	8.0	–	0.52	1	28
6	MeCN	36.6	14.1	18.9	0.29	–	1	24

[a]Isolated yields

For the purpose of the investigations, the reaction of benzaldehyde, methyl acetoacetate and urea was selected as a model reaction. The first task was to optimize the conditions of the Biginelli reaction. To investigate the effects of different solvents on the catalytic process, the reaction was performed in the presence of 1 mol % of the catalyst at room temperature, in solvents of different polarity. The results of optimization of the solvent for synthesis of **7h** are presented In Table I. Based on the isolated yields, the best results were achieved with ethanol as the solvent (Entry 4). In the Biginelli reaction, the solvent polarity plays a very important role. In light of this, the polar solvents (MeOH, EtOH, THF, MeCN) were found to be very suited for the reaction conditions. The solvent polarity had effects on the reaction yield, but it was not of crucial importance. For example, the solvents MeCN and MeOH, in spite of having higher values of ε (36.6 and 32.7) than EtOH (24.6) afforded 24 and 32 % of **7h**, respectively. Moreover, the donor number (*DN*) did not exert the main effect on the yield, because MeOH and THF have identical values (DN = 20.0), but the yields were different. The key for better yields in EtOH than in all other applied solvents is the value of hydrogen bond acceptor (*HBA*). The oxygen atom in EtOH is a very strong hydrogen bond acceptor. This solvent probably coordinates with the hydrogen atoms on the α-C atom of the active methylene compound, and thus promotes the generation of the carbanion. The best results were obtained by performing the reaction with 1:1.2:1.5 mol ratios of aldehyde, β-keto ester and urea or thiourea.

After the solvent had been optimized, the effects of different amounts (1, 5 and 10 mol %) of the catalyst on the yields were investigated (Table II). All used amounts of the catalyst gave different results, implying that the amount of the added catalyst is of significant importance for the reaction yields.

TABLE II. Optimization of the amount of catalyst for the synthesis of **7h** at room temperature in EtOH

Entry	Time, h	Catalyst, mol %	Yield[a], %
1	1	1	4
2	3	1	5
3	5	1	5
4	7	1	7
5	9	1	8
6	24	1	41
7	24	5	71
8	24	10	89

[a] Isolated yields

First, the reaction with 1 mol % catalyst was performed with increasing reaction time. The maximum yield of **7h** was obtained after 24 h with 1 mol % of the catalyst (see Entry 6). Then, two parallel reactions were performed with 5 and

10 mol % of the catalyst. The dose of 10 mol % catalyst gave a yield of 89 % after 24 h. However, the best yield of the product **7h** was achieved after 28 h (91 %). Equimolar amounts of the catalyst were also used, but no increases in the product yields were registered. The reaction conditions optimized in this way were further applied to a series of reactions of various aldehydes, *β*-keto esters and urea or thiourea. The results for the copper complex-promoted reactions are presented in Table III. All the obtained products were characterized by their m.p., and IR, ^{1}H- and ^{13}C-NMR spectra. Very good yields were achieved in all cases.

TABLE III. Yields for the Cu(II) complex-catalyzed syntheses of 2-oxo- and thioxo-1,2,3,4-tetrahydropyrimidines at room temperature

Product	Ar	R	X	Reaction time, h	Yield[a], %
7a	C_6H_4, 3-NO_2	CH_3CH_2–	O	19	96
7b	C_6H_5	CH_3CH_2–	O	24	90
7c	C_6H_3, 4-OH, 3-OCH_3	CH_3CH_2–	O	29	94
7d	$C_6H_5CH=CH$	CH_3CH_2–	O	28	93
7e	C_6H_5	CH_3CH_2–	S	19	95
7f	C_6H_3, 4-OH, 3-OCH_3	CH_3CH_2–	S	25	92
7g	2-Furyl	CH_3CH_2–	O	30	96
7h	C_6H_5	CH_3–	O	28	91
7i	C_6H_3, 4-OH, 3-OCH_3	CH_3–	O	27	88
7j	$C_6H_5CH=CH$	CH_3–	O	28	97
7k	C_6H_4, 3-NO_2	CH_3–	O	40	90
7l	2-Furyl	CH_3–	O	24	93
7m	C_6H_3, 4-OH, 3-OCH_3	CH_3–	S	27	82
7n	C_6H_5	CH_3–	S	34	95

[a] Isolated yields

It could be concluded, based on the presented results, that this improved procedure is very suitable for the preparation of 2-oxo- and thioxo-1,2,3,4-tetrahydropyrimidines and related systems. It is characterized with high yields and purity of the obtained products, the mildness of the reaction conditions and simplicity of the experimental process.

In spite of the fact that different copper and ammonium compounds as catalysts of Biginelli reaction were the subject of numerous investigations,[23–39] their catalytic role was not elucidated at the molecular level.

To gain insight into the synergic action of the Cu^{2+} and phenylammonium ions, two crucial steps of the model reaction were examined: the formation of the imminium ion and the new C–C bond (Fig. 2). The phenylammonium ion is involved in the formation of **4**. This reaction step occurs *via* the transition state TS1 (Fig. 2), which requires an activation energy of 64.2 kJ mol^{-1}. In TS1, the simultaneous cleavage of the C–O and N–H bonds, and the formation of O–H bonds occur, whereby the C–N bond becomes double. In this way, a water molecule is liberated, and the formed intermediate **4** further reacts with **5** yielding the reactant complex RC2. It could be supposed that the *α*-C atom will perform a nucleophilic attack at the benzylidene carbon. This assumption was supported with the NBO charges on these atoms (–0.497 and 0.308), and confirmed by revealing the transition state TS2. This transition state, in which a new C–C bond is being formed, requires an activation energy of 60.3 kJ mol^{-1}. In RC2, TS2 and PC2, copper is chelated with the oxygens of methyl acetoacetate. The NBO analysis of all three structures showed that the unpaired electron is delocalized over Cu and the proximate oxygens. Further liberation of the Cu^{2+} and intramolecular cyclization of intermediate **6** led to the formation of the final product **7**.

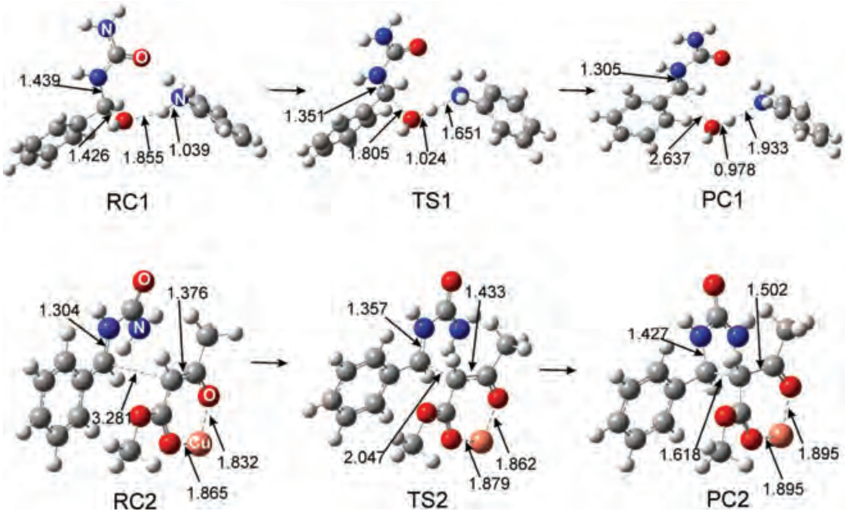

Fig. 2. Optimized geometries of the reactant complexes (RCs), transition states (TSs), and product complexes (PCs) for two crucial catalytic steps, with bond distances (Å) indicated.

To the best of our knowledge, the crystal structure of methyl 6-methyl-2-oxo-4-phenyl-1,2,3,4-tetrahydropyrimidine-5-carboxylate (**7h**), the product of the model reaction, is not available in the literature. For this reason, the ^{13}C-NMR spectrum of **7h** in DMSO was simulated. The calculated chemical shifts are given (in brackets) with the corresponding experimental values in the Supplementary material for **7h**, whereas a plot of the calculated *versus* the experimental chemical shifts is depicted in Fig. S-27 of the Supplementary material. The average absolute error is notably small (2.0 ppm), and the correlation coefficient is high (0.9990). The very good agreement between the experimental and simulated ^{13}C-NMR spectra confirmed the predicted arrangement of atoms in the carbon skeleton of **7h** (Fig. 3; the Cartesian coordinates for **7h** are provided in Table S-I of the Supplementary material). The carbonyl group of the ester moiety and double bond of the heterocycle adopt the *s-trans* position. The dihedral angle C5–C4–C1′–C2′ of 41.6° determines the mutual position of the two rings.

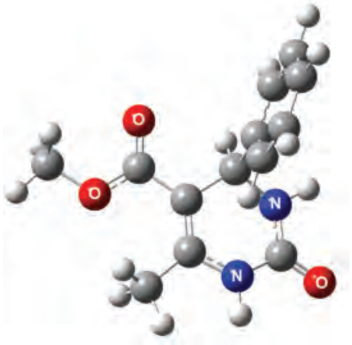

Fig. 3. Optimized structure of **7h** in ethanol.

CONCLUSIONS

Bis(phenylammonium) tetrachloridocuprate(2–), a non-hygroscopic, very stable, and easy to synthesize complex, proved to be an efficient and inexpensive catalyst for the Biginelli reaction. This is the first use of the said complex salt in organic synthesis. The catalytic behavior of the complex is realized through the synergic action of the Cu^{2+} and phenylammonium ions. As for the yields and purity of the reaction products, the procedure described herein achieves excellent results. Bearing in mind the other merits, such as the mildness of the reaction conditions and simplicity of the experimental work, this procedure could be considered very attractive for the one-pot conversion of different aromatic aldehydes, β-keto esters and urea or thiourea into 2-oxo- and thioxo-1,2,3,4-tetrahydropyrimidines.

SUPPLEMENTARY MATERIAL

Analytical and spectral data, copies of the ^{1}H- and ^{13}C-NMR spectra (Figs. S-1–S-26) of all compounds, a plot of the calculated *versus* experimental chemical shifts (Fig. S-27) and the Cartesian coordinates for **7h** (Table S-I) are available electronically from http:// //www.shd.org.rs/JSCS/, or from the corresponding author on request.

Acknowledgements. The authors are grateful to the Ministry Education, Science and Technological Development of the Republic of Serbia for financial support (Grants 172011 and 172016).

ИЗВОД

ДВОСТРУКИ КАТАЛИТИЧКИ ЕФЕКТ $(PhNH_3)_2CuCl_4$ У НОВОЈ, ВИСОКО ЕФИКАСНОЈ СИНТЕЗИ 2-ОКСО- И ТИОКСО-1,2,3,4-ТЕТРАХИДРОПИРИМИДИНА

НЕНАД ЈАНКОВИЋ, ЗОРИЦА БУГАРЧИЋ И СВЕТЛАНА МАРКОВИЋ

Универзитет у Крагујевцу, Природно-математички факултет, Институт за хемију,
Радоја Домановића 12, 34000 Крагујевац

Представљен је иновативни пут за синтезу 2-оксо- и тиоксо-1,2,3,4-тетрахидропиримидина преко мултикомпонентне Бигинелијеве реакције полазећи од различитих ароматичних алдехида, β-кето-естара и уреe или тиоурее. Избор $(PhNH_3)_2CuCl_4$ као новог, хомогеног катализатора омогућава лаку, ефикасну и јефтину реакцију при благим експерименталним условима. Штавише, овде је представљена прва примена ове комплексне соли у органској синтези икада. Добијени производи су високе чистоће, и могу се лако изоловати из реакционе смеше у добрим или чак одличним приносима. Такође, у односу на класичне Бигинелијеве реакционе услове, ова метода има предности јер се постижу виши приноси и експериментална једноставност. Да би се илустровао заједнички каталитички ефект Cu^{2+} и $PhNH_3^+$, два кључна корака Бигинелијеве реакције су испитана на молекулском нивоу помоћу М06 функционала.

(Примљено 28. октобра 2014, ревидирано 13. фебруара, прихваћено 13. фебруара 2015)

REFERENCES

1. I. S. Zorkun, S. Saraç, S. Çelebi, K. Erol, *Bioorg. Med. Chem.* **14** (2006) 8582
2. R. V. Chikhale, R. P. Bhole, P. B. Khedekar, K. P. Bhusari, *Eur. J. Med. Chem.* **44** (2009) 3645
3. O. Alam, S. A. Khan, N. Siddiqui, W. Ahsan, S. P. Verma, S. J. Gilani, *Eur. J. Med. Chem.* **45** (2010) 5113
4. C. A. Sehon, G. Z. Wang, A. Q. Viet, K. B. Goodman, S. E. Dowdell, P. A. Elkins, S. F. Semus, C. Evans, L. J. Jolivette, R. B. Kirkpatrick, E. Dul, S. S. Khandekar, T. Yi, L. L. Wright, G. K. Smith, D. J. Behm, R. J. Bentley, C. P. Doe, E. Hu, D. Lee, *J. Med. Chem.* **51** (2008) 6631
5. A. D. Patil, N. V. Kumar, W. C. Kokke, M .F. Bean, A. J. Freyer, C. De Brosse, S. Mai, A. Truneh, D. J. Faulkner, B. Carte, A. L. Breen, R. P. Hertzberg, R. K. Johnson, J. W. Westley, B. C. M. Potts, *J. Org. Chem.* **60** (1995) 1182
6. H. Y. K. Kaan, V. Ulaganathan, O. Rath, H. Prokopcová, D. Dallinger, C. O. Kappe, F. Kozielski, *J. Med. Chem.* **53** (2010) 5676
7. C. M. Wright, R. J. Chovatiya, N. E. Jameson, D. M. Turner, G. Zhu, S. Werner, D. Huryn, J. M. Pipas, B. W. Day, P. Wipf, J. L. Brodsky, *Bioorg. Med. Chem.* **16** (2008) 3291
8. O. C. Agbaje, O. O. Fadeyi, S. A. Fadeyi, L. E. Myles, C. O. Okoro, *Bioorg. Med. Chem. Lett.* **21** (2011) 989
9. B. R. P. Kumar, G. Sankar, R. B. N. Baig, S. Chandrashekaran, *Eur. J. Med. Chem.* **44** (2009) 4192
10. D. A. Ibrahim, A. M. El-Metwally, *Eur. J. Med. Chem.* **45** (2010) 1158
11. R. W. Lewis, J. Mabry, J. G. Polisar, K. P. Eagen, B. Ganem, G. P. Hess, *Biochemistry* **49** (2010) 4841
12. A. N. Chiang, J.-C. Valderramos, R. Balachandran, R. J. Chovatiya, B. P. Mead, C. Schneider, S. L. Bell, M. G. Klein, D. M. Huryn, X. S. Chen, B. W. Day, D. A. Fidock, P. Wipf, J. L. Brodsky, *Bioorg. Med. Chem.* **17** (2009) 1527
13. S. N. Mokale, S. S. Shinde, R. D. Elgire, J. N. Sangshetti, D. B. Shinde, *Bioorg. Med. Chem. Lett.* **20** (2010) 4424
14. A. R. Trivedi, V. R. Bhuva, B. H. Dholariya, D. K. Dodiya, V. B. Kataria, V. H. Shah, *Bioorg. Med. Chem. Lett.* **20** (2010) 6100
15. L. Ismaili, A. Nadaradjane, L. Nicod, C. Guyon, A. Xicluna, J.-F. Robert, B. Refouvelet, *Eur. J. Med. Chem.* **43** (2008) 1270
16. X. Zhu, G. Zhao, X. Zhou, X. Xu, G. Xia, Z. Zheng, L. Wang, X. Yang, S. Li, *Bioorg. Med. Chem. Lett.* **20** (2010) 299
17. J. Lloyd, H. J. Finlay, K. Atwal, A. Kover, J. Prol, L. Yan, R. Bhandaru, W. Vaccaro, T. Huynh, C. S. Huang, M. Conder, T. Jenkins-West, H. Sun, D. Li, P. Levesque, *Bioorg. Med. Chem. Lett.* **19** (2009) 5469

18. J. Lloyd, H. J. Finlay, W. Vacarro, T. Hyunh, A. Kover, R. Bhandaru, L. Yan, K. Atwal, M. L. Conder, T. Jenkins-West, H. Shi, C. Huang, D. Li, H. Sun, P. Levesque, *Bioorg. Med. Chem. Lett.* **20** (2010) 1436
19. J. C. Barrow, P. G. Nantermet, H. G. Selnick, K. L. Glass, K. E. Rittle, K. F. Gilbert, T. G. Steele, C. F. Homnick, R. M. Freidinger, R. W. Ransom, P. Kling, D. Reiss, T. P. Broten, T. W. Schorn, R. S. Chang, S. S. O'Malley, T. V. Olah, J. D. Ellis, A. Barrish, K. Kassahun, P. Leppert, D. Nagarathnam, C. Forray, *J. Med. Chem.* **43** (2000) 2703
20. P. Biginelli, *Gazz. Chim. Ital*. *23* (1893) 360
21. S. Sandhu, J. S. Sandhu, *Arkivoc* (2012) 66
22. Z. Quan, Z. Zhang, Y. Da, X. Wang, Chin*. J. Org. Chem.* **29** (2009) 876
23. K. K. Pasunooti, H. Chai, C. N. Jensen, B. K. Gorityala, S. Wang, X. W. Liu, *Tetrahedron Lett.* **52** (2011) 80
24. M. Wang, Z. Song, H. Jiang, H. Gong, *Prep. Biochem. Biotechnol.* **40** (2010) 101
25. M. M. Aghayan, A. Moradi, M. Bolourtchian, *J. Iran. Chem. Soc.* **7** (2010) 269
26. D. C. Wang, H.M. Guo, G. R. Qu, *Synth. Commun.* **40** (2010) 1115
27. C. J. Liu, J. D. Wang, *Molecules* **14** (2009) 763
28. I. Suzuki, Y. Suzumura, K. Takeda, *Tetrahedron Lett.* **47** (2006) 7861
29. P. Karthikeyan, S. A. Aswar, P. N. Muskawar, P. R. Bhagat, S. S. Kumar, *J. Organomet. Chem.* **723** (2013) 154
30. M. Dewan, A. Kumar, A. Saxena, A. De, S. Mozumdar, *PLoS One* **7** (2012) 43078
31. J. L. Suman, J. K. Joseph, B. Sain, *Catal. Lett.* **115** (2007) 52
32. G. Mukut, P. Dipak, J. S. Sandhu, *Synlett* **2** (2004) 235
33. M. Lei, L. Ma, L. Hu, *Synth. Commun.* **41** (2011) 3071
34. A. Kamal, T. Krishnaji, M. A. Azhar, *Catal. Commun.* **8** (2007) 1929
35. R. V. Yarapathi, S. Kurva, S. Tammishetti, *Catal. Commun.* **5** (2004) 511
36. H. R. Kalita, P. Phukan, *Catal. Commun.* **8** (2007) 179
37. F. Tamaddon, Z. Razmi, A. A. Jafari, *Tetrahedron Lett.* **51** (2010) 1187
38. E. S. Putilova, G. V. Kryshtal, G. M. Zhdankina, N. A. Troitskii, S. G. Zlotin, *Russ. J. Org. Chem.* **41–44** (2005) 512
39. D. S. Bose, M. Sudharshan, S. W. Chahvan, *Arkivoc* (2005) 228
40. P. K. Larsen, *Acta Chem. Scand., A* **28** (1974) 194
41. Gaussian 09, Revision A.1, Gaussian, Inc., Wallingford, CT, 2009
42. Y. Zhao, G. D. Truhlar, *Acc. Chem. Res.* **41** (2008) 157
43. Y. Zhao, G. D. Truhlar, *Theor. Chem. Acc.* **120** (2008) 215
44. D. Rappoport, F. J. Furche, *Chem. Phys.* **133** (2010) 134105
45. J. Tomasi, B. Mennucci, R. Cammi, *Chem. Rev*. **105** (2005) 2999
46. J. E. Carpenter , F. J. Weinhold, *J. Mol. Struct.: THEOCHEM* **169** (1988) 41
47. E. D. Glendening, J. K. Badenhoop, A. E. Reed, J. E. Carpenter, J. A. Bohmann, C. M. Morales, F. Weinhold, *NBO 5.9*, Theoretical Chemistry Institute, University of Wisconsin, Madison, WI, 2009
48. A. E. Reed, L. A. Curtiss, F. Weinhold, *Chem. Rev.* **88** (1988) 899
49. B. S. Furniss. A. J. Hannaford, P. W. G. Smith, A. R. Tatchell, *Vogel's Text Book of Practical Organic Chemsiry*, 5th ed., Addison Wesley Longman, Harlow, Essex, 1989
50. C. Reichardt, *Solvents and Solvent Effects in Organic Chemistry*, 3rd ed., Wiley–VCH, Weinheim, Germany, 2004
51. R. W. Taft, M. Kamlet, *J. Am. Chem. Soc.* **76** (1976) 2886
52. M. J. Kamlet, R. W. Taft, *J. Am. Chem. Soc.* **76** (1976) 377.

Journal of the Serbian Chemical Society
JSCS@tmf.bg.ac.rs • www.shd.org.rs/JSCS

J. Serb. Chem. Soc. *80* (5) S147–S165 (2015) *Supplementary material*

SUPPLEMENTARY MATERIAL TO

Double catalytic effect of $(PhNH_3)_2CuCl_4$ in a novel, highly efficient synthesis of 2-oxo- and thioxo-1,2,3,4-tetrahydopyrimidines

NENAD JANKOVIĆ*[#], ZORICA BUGARČIĆ and SVETLANA MARKOVIĆ

University of Kragujevac, Faculty of Science, Department of Chemistry, Radoja Domanovića 12, 34 000 Kragujevac, Serbia

J. Serb. Chem. Soc. 80 (5) (2015) 595–604

COPIES OF ^{1}H- AND ^{13}C-NMR SPECTRA

*Ethyl 6-methyl-4-(3-nitrophenyl)-2-oxo-1,2,3,4-tetrahydropyrimidine-5-carboxylate (**7a**)*

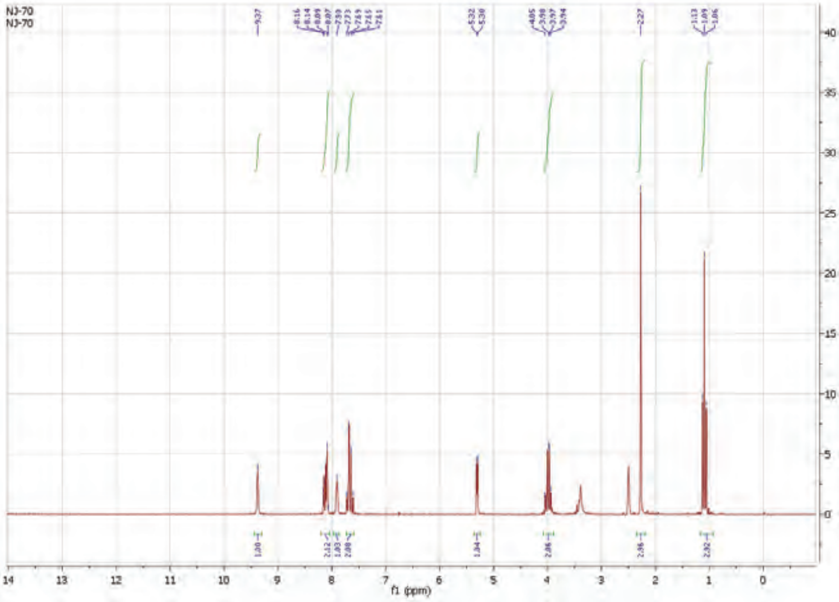

Fig. S-1. ^{1}H-NMR spectrum for **7a**.

---

* Corresponding author. E-mail: nenad.jankovic@kg.ac.rs

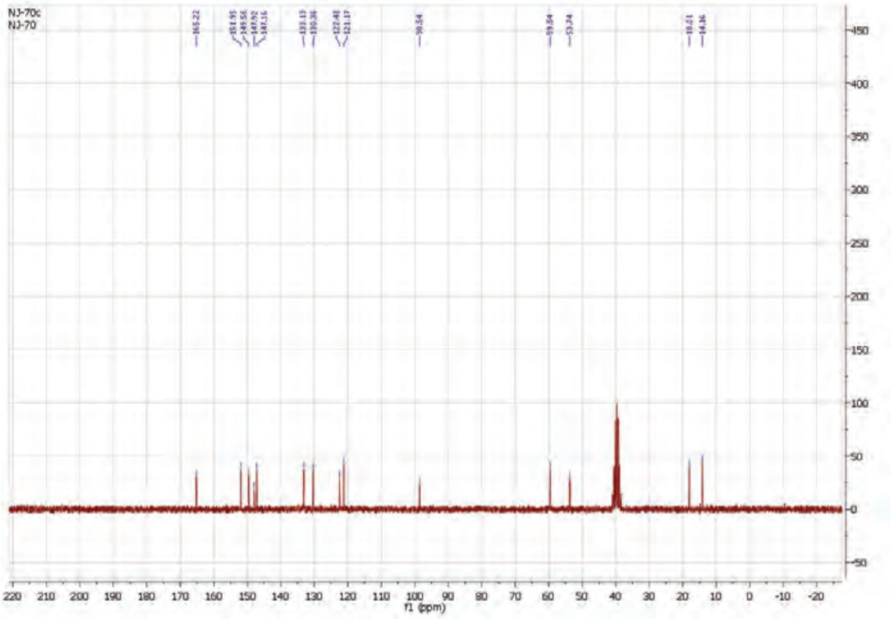

Fig. S-2. ^{13}C-NMR spectrum for **7a**.

*Ethyl 6-methyl-2-oxo-4-phenyl-1,2,3,4-tetrahydropyrimidine-5-carboxylate (**7b**)*

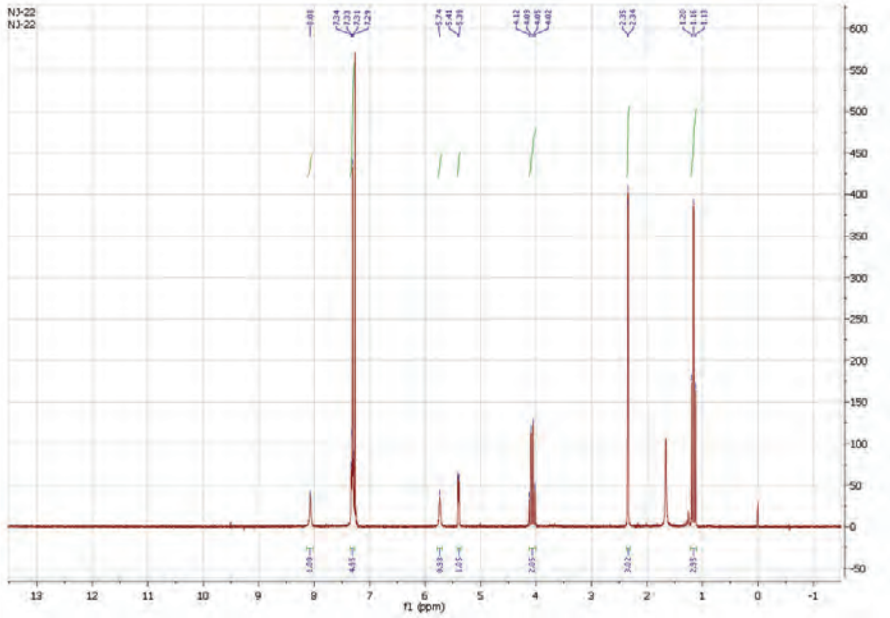

Fig. S-3. ^{1}H-NMR spectrum for **7b**.

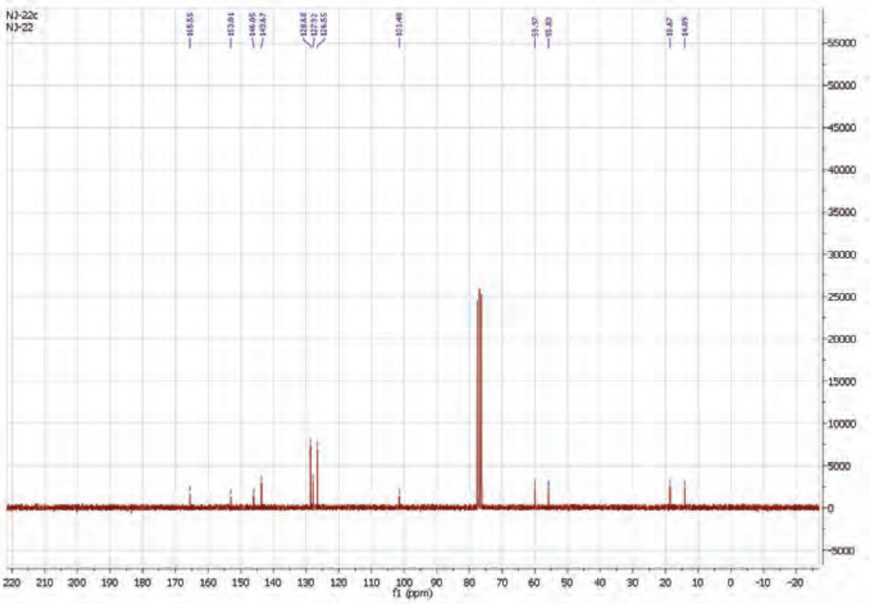

Fig. S-4. ^{13}C-NMR spectrum for **7b**.

*Ethyl 4-(4-hydroxy-3-methoxyphenyl)-6-methyl-2-oxo-1,2,3,4-tetrahydropyrimidine-5-carboxylate (**7c**)*

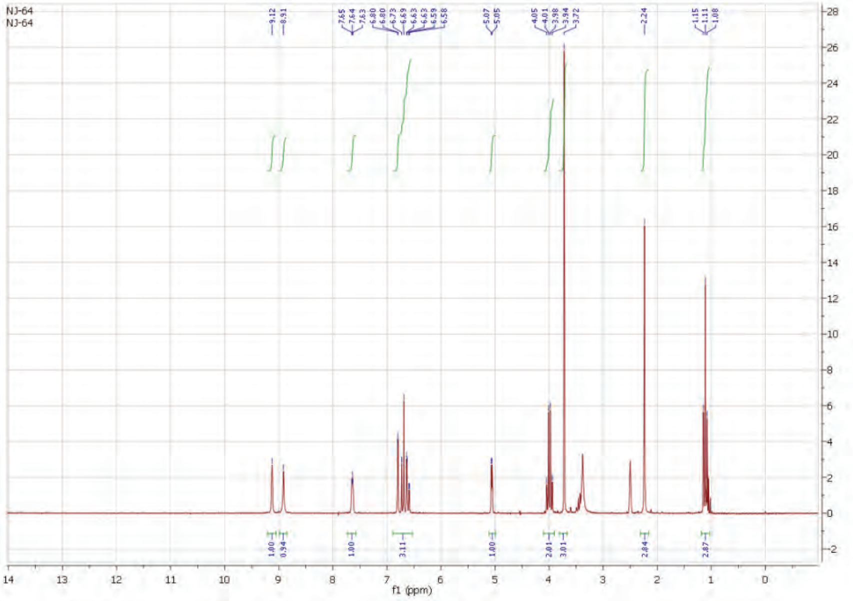

Fig. S-5. ^{1}H-NMRspectrum for **7c**.

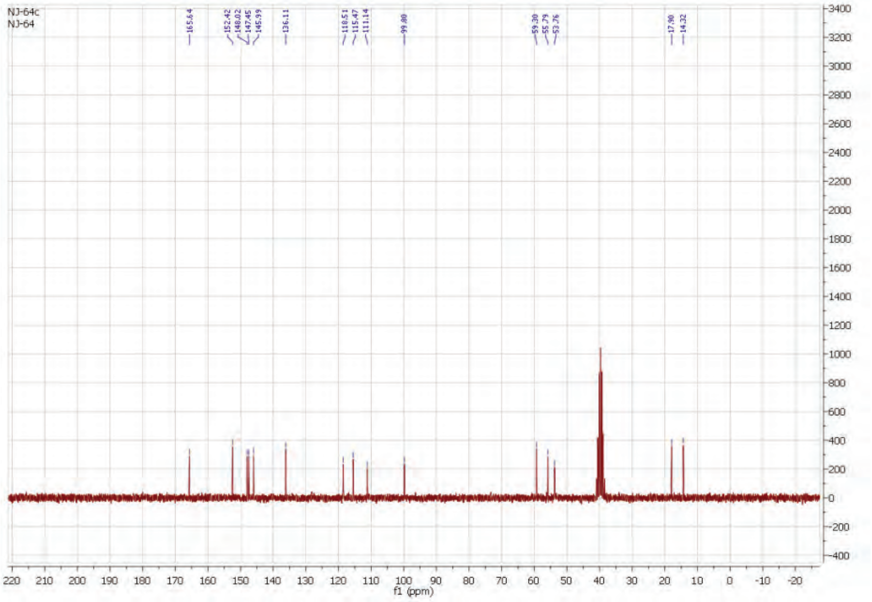

Fig. S-6. ^{13}C-NMR spectrum for **7c**.

*Ethyl 6-methyl-2-oxo-4-[(Z)-2-phenylvinyl]-1,2,3,4- tetrahydropyrimidine-5-carboxylate (**7d**)*

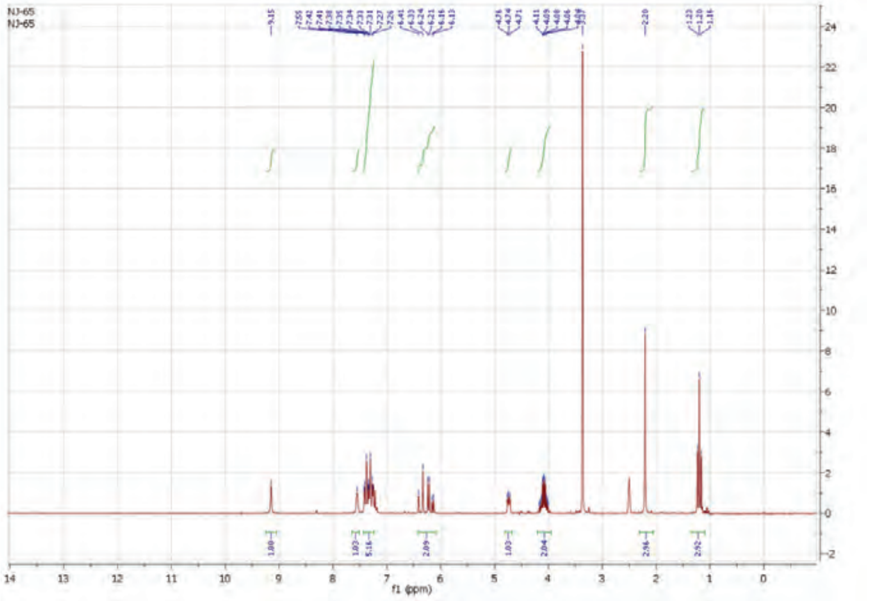

Fig. S-7. ^{1}H-NMR spectrum for **7d**.

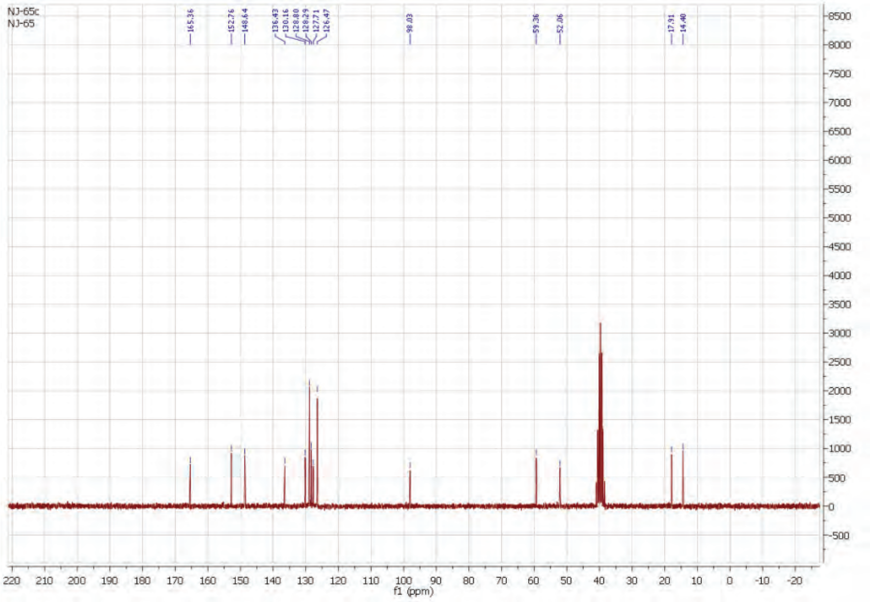

Fig. S-8. ^{13}C-NMR spectrum for **7d**.

*Ethyl 6-methyl-4-phenyl-2-thioxo-1,2,3,4-tetrahydropyrimidine-5-carboxylate (**7e**)*

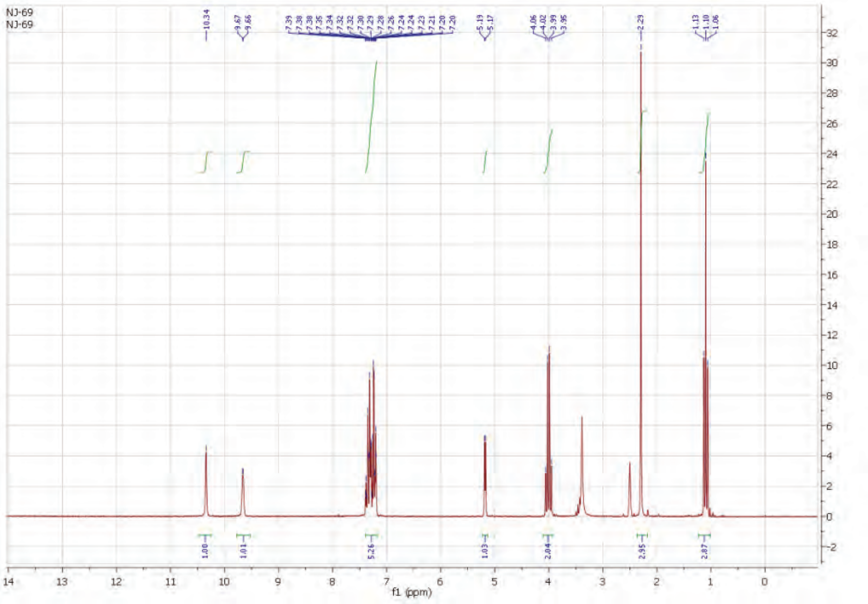

Fig. S-9. ^{1}H-NMR spectrum for **7e**.

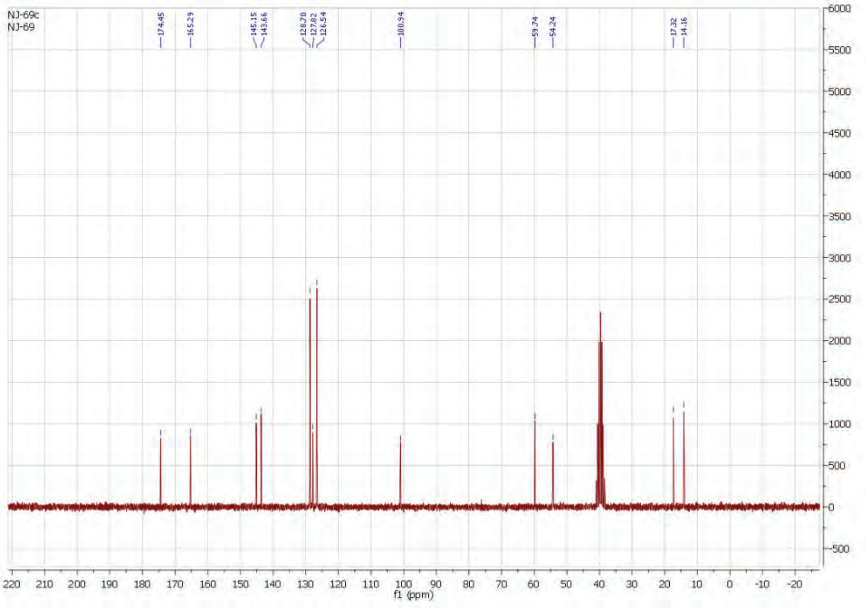

Fig. S-10. ^{13}C-NMR spectrum for **7e**.

*Ethyl 4-(4-hydroxy-3-methoxyphenyl)-6-methyl-2-thioxo-1,2,3,4-tetrahydropyrimidine-5-carboxylate (**7f**)*

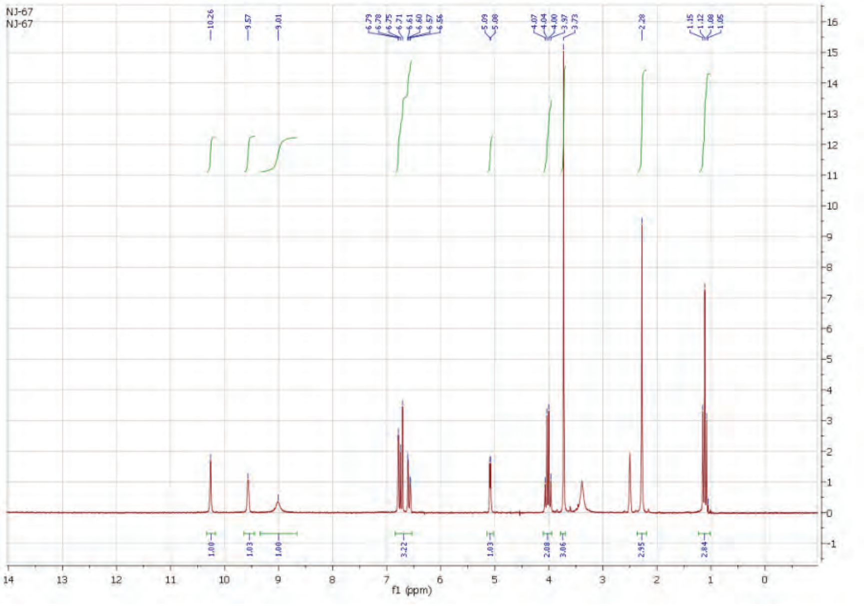

Fig. S-11. ^{1}H-NMR spectrum for **7f**.

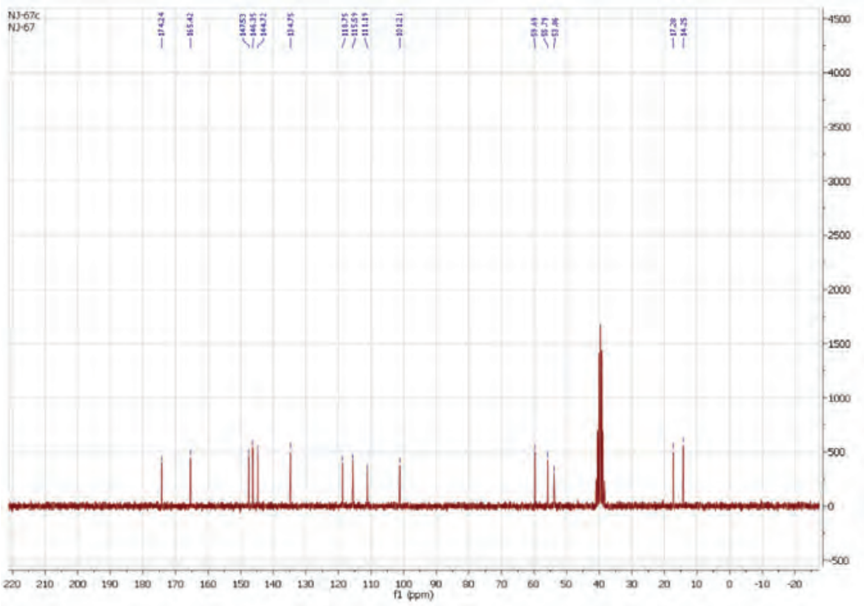

Fig. S-12. ^{13}C-NMR spectrum for **7f**.

*Methyl 6-methyl-2-oxo-4-phenyl-1,2,3,4-tetrahydropyrimidine-5-carboxylate (**7h**)*

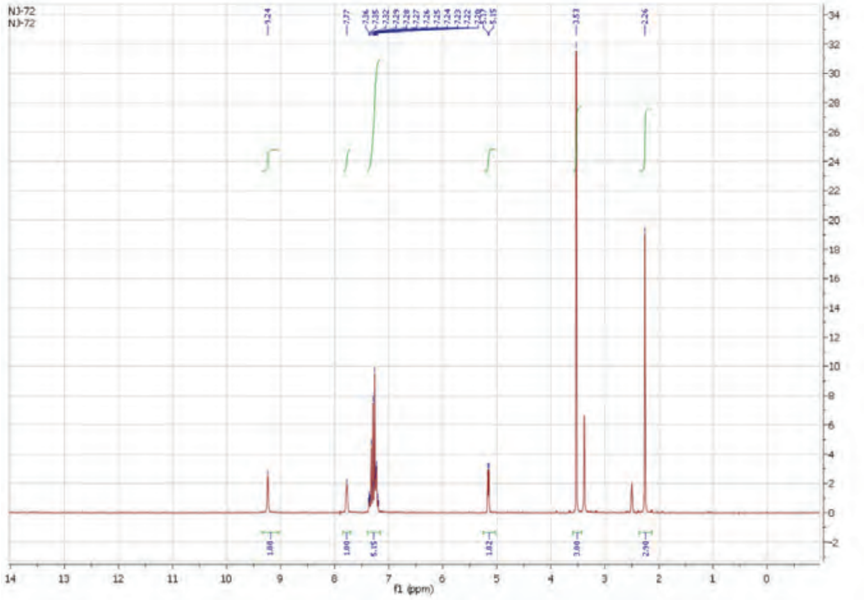

Fig. S-13 ^{1}H-NMR spectrum for **7h**.

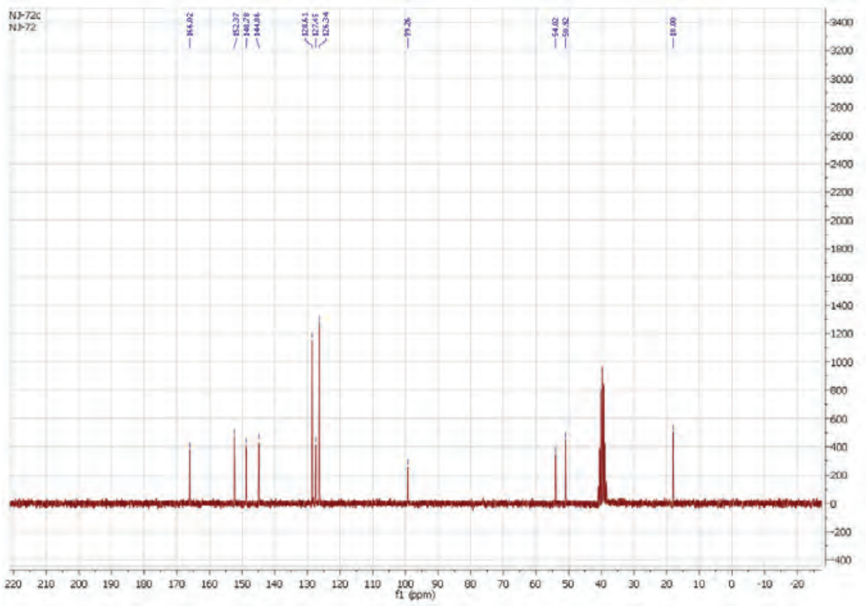

Fig. S-14. ^{13}C-NMR spectrum for **7h**.

*Methyl 4-(4-hydroxy-3-methoxyphenyl)-6-methyl-2-oxo-1,2,3,4-tetrahydropyrimidine-5-carboxylate (**7i**)*

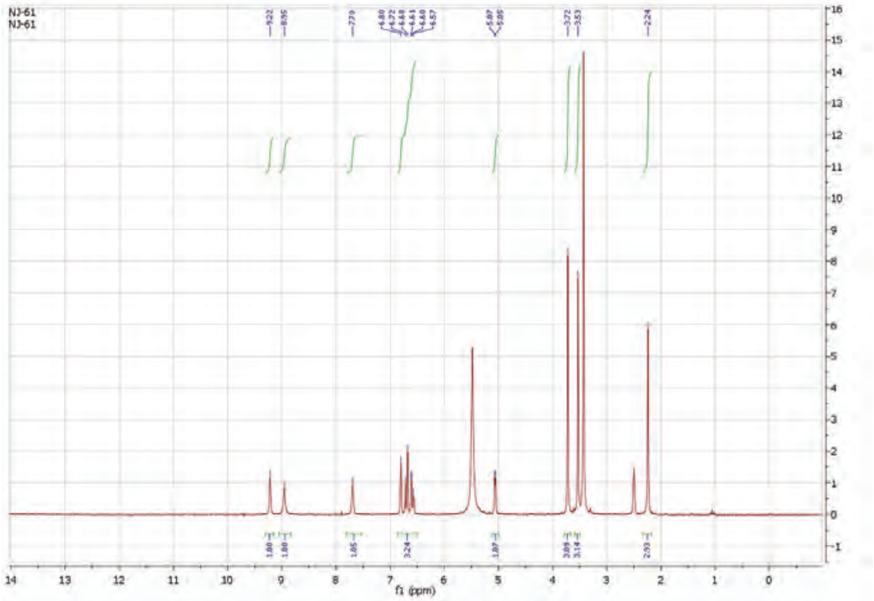

Fig. S-15. ^{1}H-NMR spectrum for **7i**.

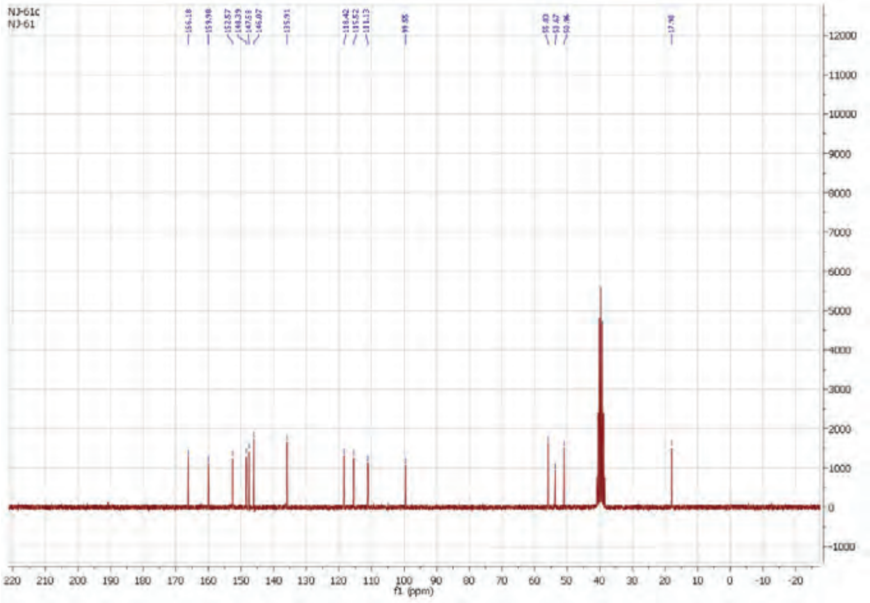

Fig. S-16. ^{13}C-NMR spectrum for **7i**.

*Methyl 6-methyl-2-oxo-4-[(*E*)-2-phenylvinyl]-1,2,3,4-tetrahydropyrimidine-5-carboxylate (**7j**)*

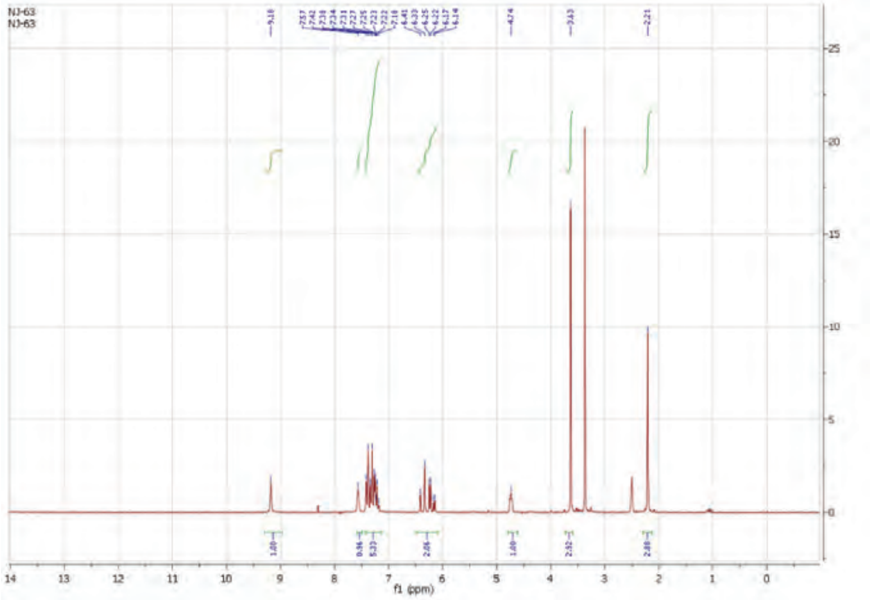

Fig. S-17. ^{1}H-NMR spectrum for **7j**.

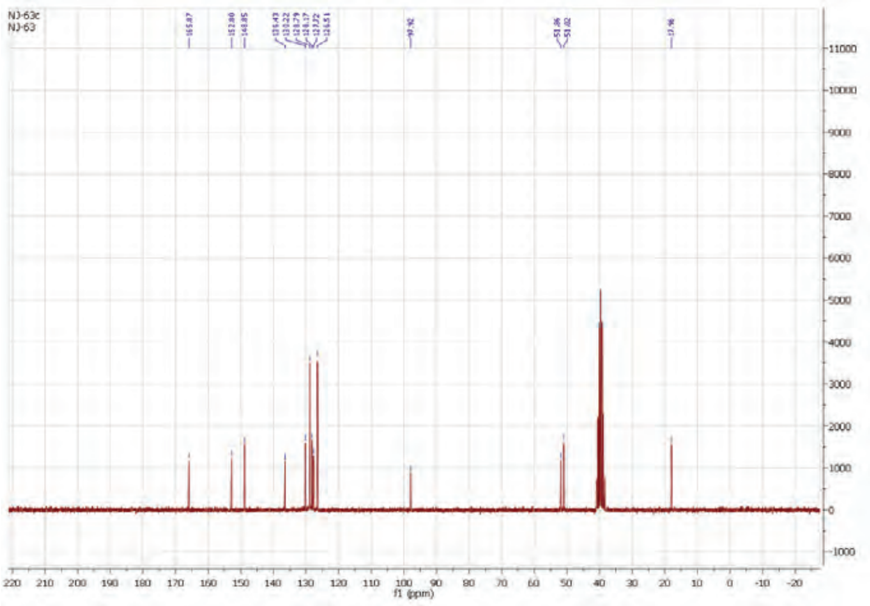

Fig. S-18. ^{13}C-NMR spectrum for **7j**.

*Methyl 6-methyl-4-(3-nitrophenyl)-2-oxo-1,2,3,4-tetrahydropyrimidine-5-carboxylate (**7k**)*

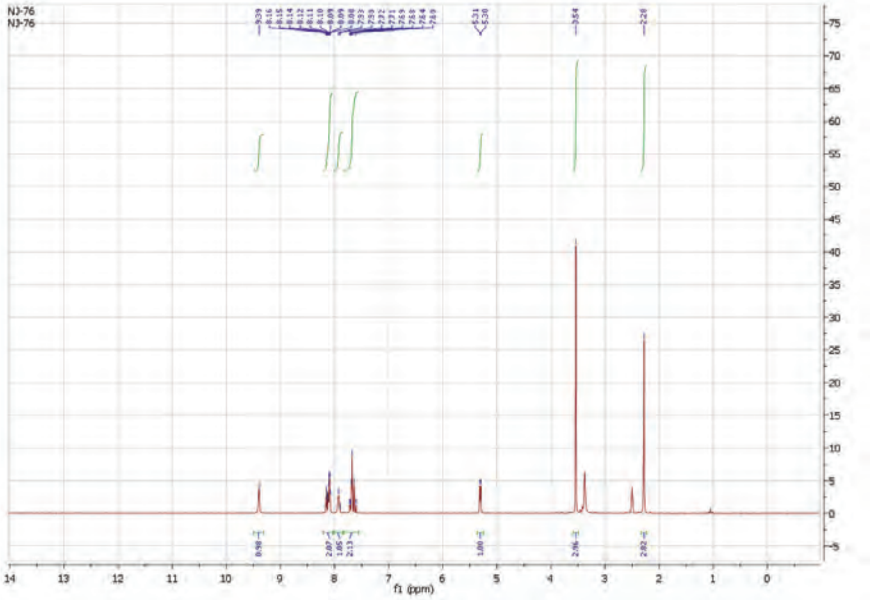

Fig. S-19. ^{1}H-NMR spectrum for **7k**.

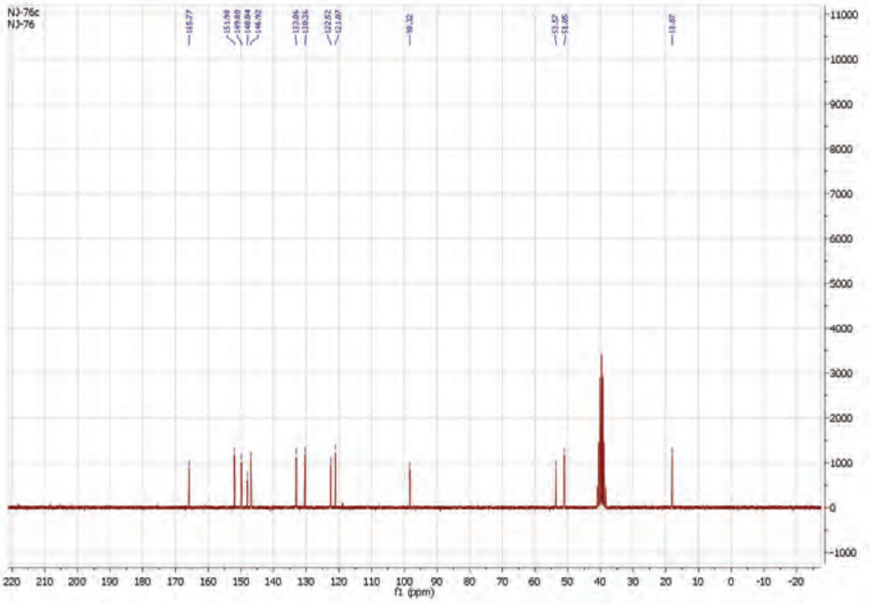

Fig. S-20. ^{13}C-NMR spectrum for **7k**.

*Methyl 4-(2-furyl)-6-methyl-2-oxo-1,2,3,4-tetrahydropyrimidine-5-carboxylate (**7l**)*

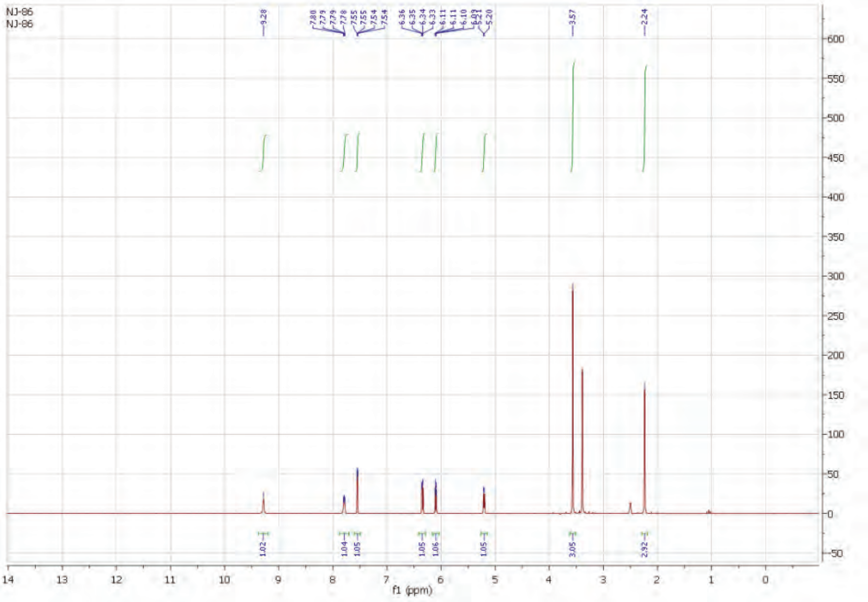

Fig. S-21. ^{1}H-NMR spectrum for **7l**.

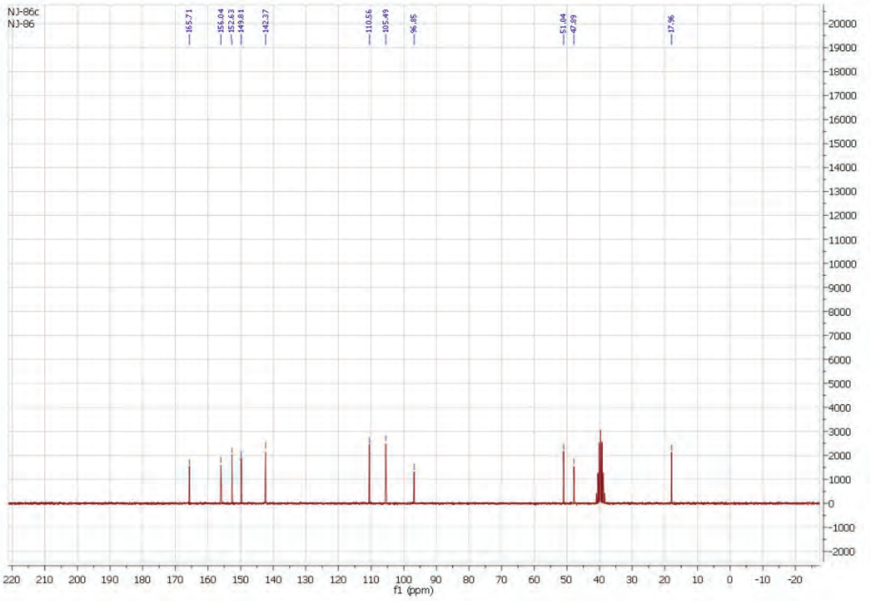

Fig. S-22. ^{13}C-NMR spectrum for **7l**.

*Methyl 4-(4-hydroxy-3-methoxyphenyl)-6-methyl-2-thioxo-1,2,3,4-tetrahydropyrimidine-5-carboxylate (**7m**)*

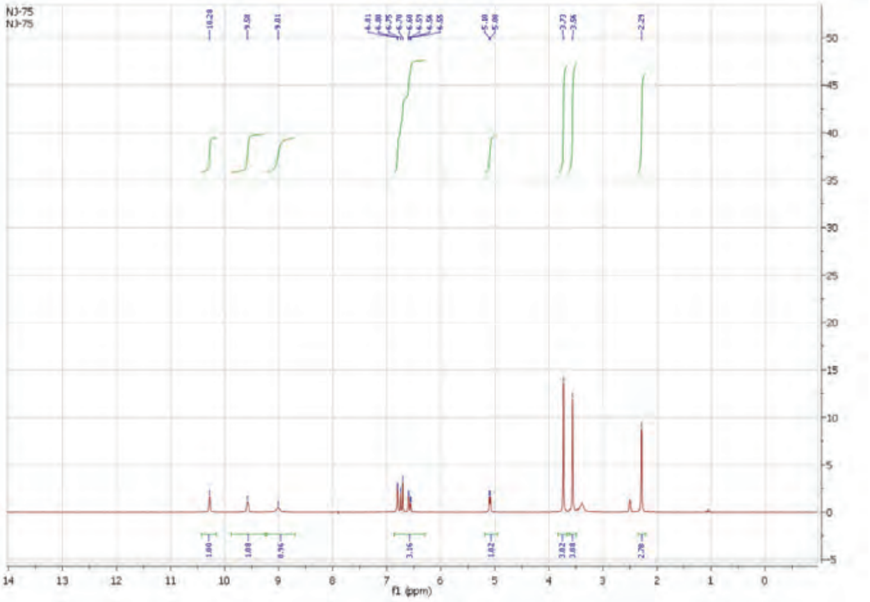

Fig. S-23. ^{1}H-MR spectrum for **7m**.

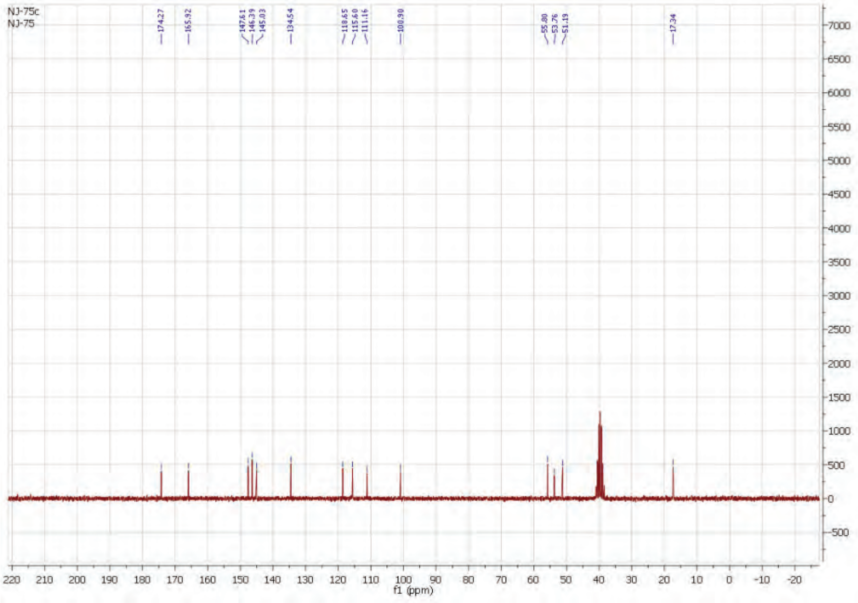

Fig. S-24. ^{13}C-NMR spectrum for **7m**.

*Methyl 6-methyl-4-phenyl-2-thioxo-1,2,3,4-tetrahydropyrimidine-5-carboxylate (**7n**)*

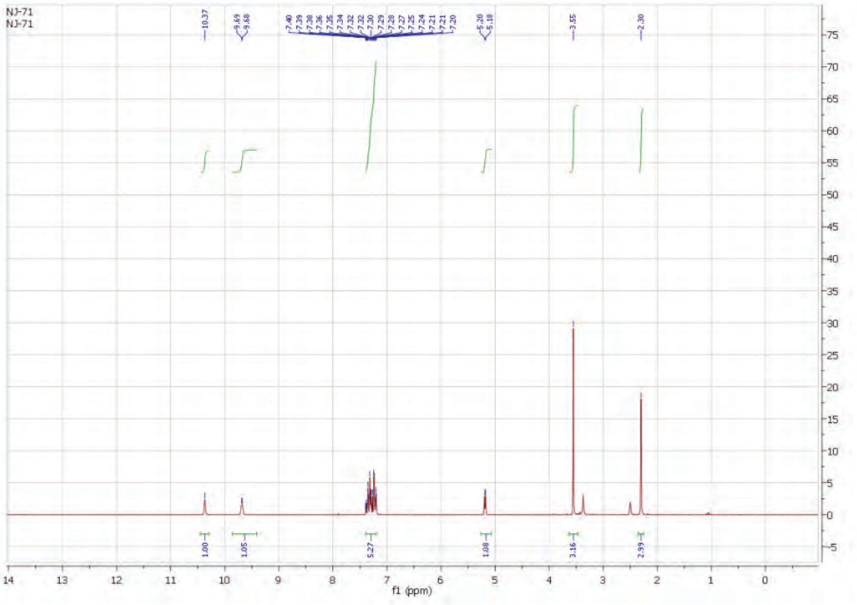

Fig. S-25. ^{1}H-NMR spectrum for **7n**.

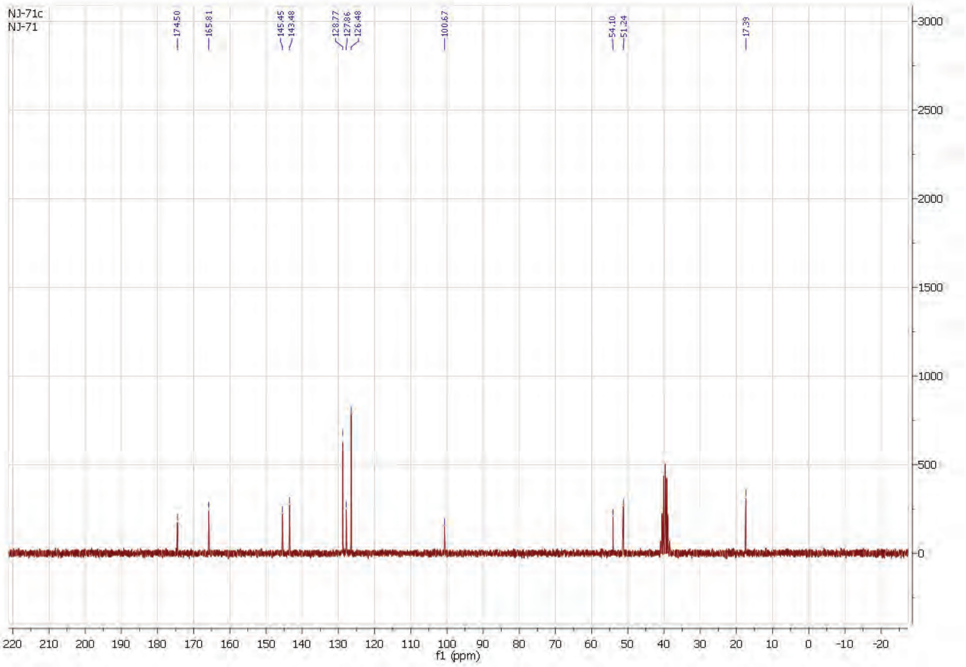

Fig. S-26. ^{13}C-NMR spectrum for **7n**.

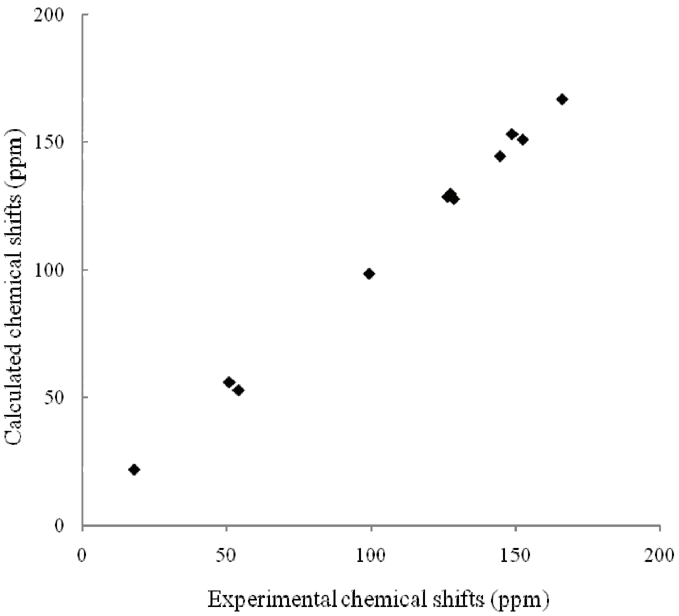

Fig. S-27. Plot of the calculated *versus* experimental chemical shifts of the carbon atoms of **7h** in DMSO.

ANALYTICAL AND SPECTRAL DATA FOR COMPOUNDS **7a–n**

*Ethyl 6-methyl-4-(3-nitrophenyl)-2-oxo-1,2,3,4-tetrahydropyrimidine-5-carboxylate (**7a**).* M.p.: 227–229 °C (Lit. 230–232 °C[1]); Anal. Calcd. for $C_{14}H_{15}N_3O_5$: C, 55.08; H, 4.95; N, 13.76 %. Found: C, 55.15; H, 5.01; N, 13.79 %; IR (KBr, cm^{-1}): 3324, 3085, 2961, 1701, 1684, 1624, 1527, 1446, 1315.1, 1300, 1261, 1221, 1086; ^{1}H-NMR (200 MHz, DMSO-d_6, δ / ppm): 1.07 (3H, *t*, J = 7.1 Hz, CH_3), 2.27 (3H, *s*, CH_3), 4.00 (2H, *m*, CH_2O), 5.28 (1H, *d*, J = 3.4 Hz, CH), 7.64–7.69 (2H, *m*, Ar), 7.90 (1H, *bs*, NH), 8.07–8.15 (2H, *m*, Ar), 9.37 (1H, *bs*, NH); ^{13}C-NMR (50 MHz, DMSO-d_6, δ / ppm): 14.2, 18.2, 53.7, 59.5, 98.6, 121.2, 122.5, 130.4, 133.1, 147.2, 147.9, 149.6, 151.9, 165.2.

*Ethyl 6-methyl-2-oxo-4-phenyl-1,2,3,4-tetrahydropyrimidine-5-carboxylate (**7b**).* M.p.: 201–204 °C (Lit. 204 °C[1]); Anal. Calcd. for $C_{14}H_{16}N_2O_3$: C, 64.60; H, 6.19; N, 10.76 %. Found: C, 64.62; H, 6.22; N, 10.86 %; IR (KBr, cm^{-1}): 3333, 3220, 3107, 2951, 1696, 1667, 1651, 1340, 1239, 1094; ^{1}H-NMR (200 MHz, DMSO-d_6 / δ ppm): 1.16 (3H, *t*, J = 7.1 Hz, CH_3), 2.34 (3H, *s*, CH_3), 4.06 (2H, *q*, J = 7.1 Hz, CH_2O), 5.39 (1H, *d*, J = 2.3 Hz, CH), 5.74 (1H, *bs*, NH), 7.26–7.34 (5H, *m*, Ar), 8.07 (1H, *bs*, NH); ^{13}C-NMR (50 MHz, DMSO-d_6, δ / ppm): 14.0, 18.6, 55.8, 59.9, 101.4, 126.6, 127.9, 128.7, 143.7, 146.1, 153.0, 165.6.

*Ethyl 4-(4-hydroxy-3-methoxyphenyl)-6-methyl-2-oxo-1,2,3,4-tetrahydropyrimidine-5-carboxylate (**7c**).* M.p.: 233–236 °C (Lit. 233–235 °C[1]); Anal. Calcd. for $C_{15}H_{18}N_2O_5$: C, 58.82; H, 5.92; N, 9.15 %. Found: C, 58.94; H, 5.94; N, 9.18 %; IR (KBr, cm^{-1}): 3450, 3246, 3122, 1698, 1645, 1513, 1277, 1222, 1093; ^{1}H-NMR (200 MHz, DMSO-d_6, δ / ppm): 1.11 (3H, *t*, J = 7.3 Hz, CH_3), 2.23 (3H, *s*, CH_3), 3.73 (3H, *s*, CH_3O), 4.01 (2H, *q*, J = 7.1 Hz, CH_2O), 5.06 (1H, *d*, J = 3.2 Hz, CH), 6.58–6.80 (3H, *m*, Ar), 7.64 (1H, *bs*, NH), 8.91 (1H, *s*, OH), 9.12 (1H, *bs*, NH); ^{13}C-NMR (50 MHz, DMSO-d_6, δ / ppm): 14.3, 17.9, 53.7, 55.8, 59.3, 99.8, 111.1, 115.5, 118.5, 136.1, 146.0, 147.5, 148.1, 152.4, 165.7.

*Ethyl 6-methyl-2-oxo-4-[(*E*)-2-phenylvinyl]-1,2,3,4- tetrahydropyrimidine-5--carboxylate (**7d**).* M.p.: 235–237 °C (Lit. 234–236 °C[4]); Anal. Calcd. for $C_{16}H_{18}N_2O_3$: C, 67.12; H, 6.34; N, 9.78 %. Found: C, 67.10; H, 6.35; N, 9.82 %; IR (KBr, cm^{-1}): 3232, 3087, 2975, 2891, 1722, 1687, 1654, 1526, 1493, 14525, 1339, 1072; ^{1}H-NMR (200 MHz, DMSO-d_6, δ / ppm): 1.19 (3H, *t*, CH_3), 2.21 (3H, *s*, CH_3), 4.11 (2H, *m*, CH_2O), 4.72 (1H, *d*, J = 2.8 Hz, CH), 6.13–6.41 (2H, *m*, 2×CH=), 7.22–7.42 (5H, *m*, Ar), 7.55 (1H, *bs*, NH), 9.14 (1H, *bs*, NH); ^{13}C-NMR (50 MHz, DMSO-d_6, δ / ppm): 14.4, 17.9, 52.0, 59.3, 98.1, 126.5, 127.7, 128.3, 128.8, 130.2, 136.4, 148.7, 152.7, 165.4.

*Ethyl 6-methyl-4-phenyl-2-thioxo-1,2,3,4-tetrahydropyrimidine-5-carboxylate (**7e**).* M.p.: 206–207 °C (Lit. 208–209 °C[4]); Anal. Calcd. for $C_{14}H_{16}N_2O_2S$: C, 60.85; H, 5.84; N, 10.14 %. Found: C, 60.86; H, 5.88; N, 10.18 %; IR (KBr, cm^{-1}): 3324, 3170, 2980, 1666, 1572, 1464, 1370, 1326, 1283, 1192, 1175, 1114, 1002; ^{1}H-NMR (200 MHz, DMSO-d_6, δ / ppm): 1.09 (3H, *t*, J = 7.1 Hz, CH_3), 2.29 (3H, *s*, CH_3), 4.02 (2H, *q*, J = 7.1 Hz CH_2O), 5.18 (1H, *s*, J = 3.7 Hz, CH), 7.19–7.35 (5H, *m*, Ar), 9.66 (1H, *d*, J = 1.9 Hz, NH), 10.34 (1H, *bs*, NH); ^{13}C-NMR (50 MHz, DMSO-d_6, δ / ppm): 14.2, 17.3, 54.2, 59.7, 100.9, 126.5, 127.8, 128.7, 143.7, 145.2, 165.3, 174.5.

*Ethyl 4-(4-hydroxy-3-methoxyphenyl)-6-methyl-2-thioxo-1,2,3,4-tetrahydropyrimidine-5-carboxylate (**7f**)*. M.p: 205–208 °C (Lit. 206–208 °C[2]); Anal. Calcd. for $C_{15}H_{18}N_2O_4S$: C, 55.88; H, 5.63; N, 8.69 %. Found: C, 55.92; H, 5.67; N, 8.70 %; IR (KBr, cm^{-1}): 3417, 3154, 2999, 2960, 1678, 1593, 1575, 1518, 1461, 1194, 1113; ^{1}H-NMR (200 MHz, DMSO-d_6, δ / ppm): 1.15 (3H, *t*, J = 7.1 Hz, CH_3), 2.28 (3H, *s*, CH_3), 3.72 (3H, *s*, CH_3O), 4.04 (2H, *q*, J = 7.0 Hz, CH_2O), 5.08 (1H, *d*, J = 3.6 Hz, CH), 6.56–6.79 (3H, *m*, Ar), 9.01 (1H, *s*, OH), 9.56 (1H, *bs*, NH), 10.25 (1H, *bs*, NH); ^{13}C-NMR (50 MHz, DMSO-d_6, δ / ppm): 14.2, 17.3, 53.9, 55.8, 59.7, 101.2, 111.1, 115.6, 118.7, 134.8, 144.7, 146.4, 147.5, 165.4, 174.3.

*Ethyl 4-(2-furyl)-6-methyl-2-oxo-1,2,3,4-tetrahydropyrimidine-5-carboxylate (**7g**)*. M.p.: 206–207 °C (Lit. 208–209 °C[1]); Anal. Calcd. for $C_{12}H_{14}N_2O_4$: C, 57.59; H, 5.64; N, 11.19 %. Found: C, 57.62; H, 5.64; N, 11.23 %; IR (KBr, cm^{-1}): 3315, 3118, 1708, 1672, 1651, 1432, 1339, 1239, 1088; ^{1}H-NMR (200 MHz, DMSO-d_6, δ / ppm): 1.15 (3H, *t*, J = 7.2 Hz, CH_3), 2.34 (3H, *s*, CH_3), 4.06 (2H, *q*, J = 7.0 Hz, CH_2O), 5.15 (1H, *d*, J = 3.2 Hz, CH), 6.18–6.21 (1H, *m*, Ar), 6.30–6.34 (1H, *m*, Ar), 7.58–7.61 (1H, *m*, Ar), 7.94 (1H, *bs*, NH), 9.08 (1H, *bs*, NH); ^{13}C-NMR (50 MHz, DMSO-d_6, δ / ppm): 14.5, 18.7, 53.3, 56.6, 96.4, 105.4, 110.7, 143.7, 149.5, 152.7, 156.0, 165.4.

*Methyl 6-methyl-2-oxo-4-phenyl-1,2,3,4-tetrahydropyrimidine-5-carboxylate (**7h**)*. M.p.: 210–213 °C (Lit. 212–213 °C[3]); Anal. Calcd. for $C_{13}H_{14}N_2O_3$: C, 63.40; H, 5.73; N, 11.37 %. Found: C, 63.44; H, 5.73; N, 11.39 %; IR (KBr, cm^{-1}): 3365, 3221, 3078, 3020, 2925, 1749, 1708, 1654, 1423, 1074; ^{1}H-NMR (200 MHz, DMSO-d_6, δ / ppm): 2.26 (3H, *s*, CH_3), 3.53 (3H, *s*, CH_3O), 5.15 (1H, *d*, J = 3.4 Hz, CH), 7.22–7.32 (5H, *m*, Ar), 7.77 (1H, *bs*, NH), 9.24 (1H, *bs*, NH); ^{13}C-NMR (50 MHz, DMSO-d_6, the calculated values are given in brackets, δ / ppm): 18.0 (21.8), 50.9 (56.0), 54.0 (52.8), 99.3 (98.3), 126.4 (128.4), 127.4 (129.6), 128.6 (127.6), 144.7 (144.3), 148.8 (153.1), 152.4 (150.9), 166.0 (166.7).

*Methyl 4-(4-hydroxy-3-methoxyphenyl)-6-methyl-2-oxo-1,2,3,4-tetrahydropyrimidine-5-carboxylate (**7i**)*. M.p.: 253–255 °C (Lit. 253–254 °C[5]); Anal. Calcd. for $C_{14}H_{16}N_2O_5$: C, 57.53; H, 5.52; N, 9.58 %. Found: C, 57.54; H, 5.53; N, 9.60 %; IR (KBr, cm^{-1}): 3363, 3230, 3069, 3033, 2941, 1746, 1707, 1647, 1430, 1107; ^{1}H-NMR (200 MHz, DMSO-d_6, δ / ppm): 2.24 (3H, *s*, CH_3), 3.53 (3H, *s*, CH_3O), 3.72 (3H, *s*, CH_3O), 5.06 (1H, *d*, J = 3.2 Hz, CH), 6.57–6.81 (3H, *m*, Ar), 7.69 (1H, *bs*, NH), 8.95 (1H, *s*, OH), 9.22 (1H, *bs*, NH); ^{13}C-NMR (50 MHz, DMSO-d_6, δ / ppm): 17.9, 50.1, 55.8, 99.5, 111.1, 115.5, 118.4, 135.9, 146.1, 147.6, 148.4, 152.6, 159.9, 166.2.

Methyl 6-methyl-2-oxo-4-[(E)*-2-phenylvinyl]-1,2,3,4-tetrahydropyrimidine--5-carboxylate (**7j**)*. M.p.: 229–231 °C (Lit. 229–232 °C[5]); Anal. Calcd. for $C_{15}H_{16}N_2O_3$: C, 66.16; H, 5.92; N, 10.29 %. Found: C, 66.19; H, 5.96; N, 10.29 %; IR (KBr, cm^{-1}): 3245, 3116, 2952, 1722, 1712, 1685, 1645, 1434, 1249, 1099; ^{1}H-NMR (200 MHz, DMSO-d_6, δ / ppm): 2.20 (3H, *s*, CH_3), 3.63 (3H, *s*, CH_3O), 4.74 (1H, *d*, *J* = 3.2 Hz, CH), 6.14–6.41 (2H, *m*, 2×CH=), 7.22–7.41 (5H, *m*, Ar), 7.55 (1H, *bs*, NH), 9.12 (1H, *bs*, NH); ^{13}C-NMR (50 MHz, DMSO-d_6, δ / ppm): 17.9, 51.1, 51.8, 97.9, 126.5, 127.7, 128.2, 128.8, 130.2, 136.4, 148.9, 152.8, 165.9.

*Methyl 6-methyl-4-(3-nitrophenyl)-2-oxo-1,2,3,4-tetrahydropyrimidine-5--carboxylate (**7k**)*. M.p.: 281–283 °C (Lit. 280–283 °C[6]); Anal. Calcd. for $C_{13}H_{13}N_3O_5$: C, 53.61; H, 4.49; N, 14.42 %. Found: C, 53.62; H, 4.49; N, 14.45 %; IR (KBr, cm^{-1}): 3177, 2980, 1710, 1654, 1590, 1521, 1462, 1340, 1274, 1180, 1100; ^{1}H-NMR (200 MHz, DMSO-d_6, δ / ppm): 2.28 (3H, *s*, CH_3), 3.54 (3H, *s*, CH_3O), 5.30 (1H, *d*, *J* = 3.4 Hz, CH), 7.64–7.69 (2H, *m*, Ar), 7.90 (1H, *bs*, NH), 8.07–8.15 (2H, *m*, Ar), 9.37 (1H, *bs*, NH); ^{13}C-NMR (50 MHz, DMSO-d_6, δ / ppm): 18.0, 51.1, 53.6, 98.3, 121.0, 122.5, 130.4, 133.1, 146.9, 148.0, 149.8, 151.9, 165.8.

*Methyl 4-(2-furyl)-6-methyl-2-oxo-1,2,3,4-tetrahydropyrimidine-5-carboxylate (**7l**)*. M.p.: 207–209 °C (Lit. 208–209 °C[7]); Anal. Calcd. for $C_{11}H_{12}N_2O_4$: C, 55.93; H, 5.12; N, 11.85 %. Found: C, 55.95; H, 5.15; N, 11.86 %; IR (KBr, cm^{-1}): 3245, 3118, 2975, 2940, 1709, 1701, 1650, 1435, 1318, 1296, 1234, 1100; ^{1}H-NMR (200 MHz, DMSO-d_6, δ / ppm): 2.24 (3H, *s*, CH_3), 3.56 (3H, *s*, CH_3O), 5.20 (1H, *d*, *J* = 3.3 Hz, CH), 6.08–6.11 (1H, *m*, Ar), 6.33–6.36 (1H, *m*, Ar), 7.54–7.56 (1H, *m*, Ar), 7.97 (1H, *t*, NH), 9.28 (1H, *bs*, NH); ^{13}C-NMR (50 MHz, DMSO-d_6, δ / ppm): 17.9, 47.8, 51.1, 96.8, 105.5, 110.6, 142.4, 149.8, 152.6, 156.1, 165.7.

*Methyl 4-(4-hydroxy-3-methoxyphenyl)-6-methyl-2-thioxo-1,2,3,4-tetrahydropyrimidine-5-carboxylate (**7m**)*. M.p.: 257–260 °C (Lit. 258–260 °C[8]); Anal. Calcd. for $C_{14}H_{16}N_2O_4S$: C, 54.53; H, 5.23; N, 9.08 %. Found: C, 54.55; H, 5.28; N, 9.10 %; IR (KBr, cm^{-1}): 3411, 3164, 3002, 1692, 1661, 1584, 1519, 1435, 1344, 1287, 1197; ^{1}H-NMR (200 MHz, DMSO-d_6, δ / ppm): 2.28 (3H, *s*, CH_3), 3.56 (3H, *s*, CH_3O), 3.73 (3H, *s*, CH_3O), 5.08 (1H, *d*, *J* = 3.7 Hz, CH), 6.55–6.80 (3H, *m*, Ar), 9.01 (1H, *s*, OH), 9.57 (1H, *bs*, NH), 10.28 (1H, *bs*, NH); ^{13}C-NMR (50 MHz, DMSO-d_6, δ / ppm): 17.3, 51.2, 53.8, 55.7, 100.9, 111.2, 115.6, 118.7, 134.5, 145.0, 146.4, 147.6, 165.9, 174.3.

*Methyl 6-methyl-4-phenyl-2-thioxo-1,2,3,4-tetrahydropyrimidine-5-carboxylate (**7n**)*. M.p.: 207–210 °C (Lit. 237–239 °C[9]); Anal. Calcd. for

$C_{13}H_{14}N_2O_2S$: C, 59.52; H, 5.38; N, 10.68 %. Found: C, 59.52; H, 5.44; N, 10.71 %; IR (KBr, cm^{-1}): 3315, 3183, 2996, 1664, 1643, 1579, 1457, 1346, 1288, 1202, 1113; ^{1}H-NMR (200 MHz, DMSO-d_6, δ / ppm): 2.30 (3H, *s*, CH_3), 3.55 (3H, *s*, CH_3), 5.18 (1H, *d*, J = 3.8 Hz, CH), 7.20–7.39 (5H, *m*, Ar), 9.66 (1H, *d*, J = 2.0 Hz, NH), 10.36 (1H, *bs*, NH); ^{13}C-NMR (50 MHz, DMSO-d_6, δ / ppm): 17.4, 51.2, 54.1, 100.6, 126.5, 127.8, 128.8, 143.5, 145.4, 165.8, 174.5.

Table S-I. Cartesian coordinates of the product **7h**

Element	Coordinates		
C	–0.28524400	0.28629100	–0.98404300
C	1.02321100	0.06946900	–0.26491800
C	1.57184000	1.07011100	0.46901700
H	–1.25697000	1.98503200	–1.82013500
H	1.35716700	3.05638100	1.01588500
H	–0.21774700	–0.18955800	–1.96932900
C	–1.47976900	–0.31974600	–0.27008100
C	–2.43738400	–1.01671100	–0.99917600
C	–1.66766700	–0.14437700	1.09919900
C	–3.56931000	–1.52776400	–0.37641200
H	–2.29007800	–1.16391200	–2.06711900
C	–2.79802800	–0.65129700	1.72443700
H	–0.92142000	0.38888400	1.68378000
C	–3.75251600	–1.34352800	0.98750100
H	–4.30723500	–2.07331300	–0.95681300
H	–2.93396500	–0.50967300	2.79245600
H	–4.63519300	–1.74228700	1.47820400
N	0.95308300	2.30356800	0.47429900
N	–0.48858600	1.71740100	–1.21830100
C	–0.03605800	2.70345500	–0.41449400
O	–0.40880200	3.86389900	–0.45997400
C	1.56397200	–1.27559300	–0.42334000
O	0.99671600	–2.14735400	–1.05169400
O	2.75068300	–1.47736700	0.16662000
C	3.30637400	–2.78283400	0.02491000
H	3.47821400	–3.01760600	–1.02809900
H	4.25256400	–2.76457500	0.56323000
H	2.64282600	–3.53560900	0.45639800
C	2.80631900	1.01544400	1.30600400
H	2.82750500	0.12461300	1.93216300
H	3.69687300	0.98433100	0.67204200
H	2.87275800	1.89956300	1.94410800

REFERENCES

1. R. Ghosh, S. Maiti, A. Chakraborty, *J. Mol. Catal., A* **217** (2004) 47
2. D. L. da Silva, S. A. Fernandes, A. A. Sabino, A. de Fatima, *Tetrahedron Lett.* **52** (2011) 6328

3. W. K. Su, J. J. Li, Z. G. Zheng, Y. C. Shen, *Tetrahedron Lett.* **46** (2005) 6037
4. Y. Ma, C. Qian, L. Wang, M. Yang, *J. Org. Chem.* **65** (2000) 3864
5. K. Ahmed, T. Azhar, M. Ameruddin, *Catal. Commun.* **8** (2007) 1929
6. H. Abibi, H. Alah, M. Beygzadeh, *Catal. Commun.* **8** (2007) 2119
7. F. Shirini, K. Marjani, H. T. Hahzomi, *Arkivoc* (2007) 51
8. C. Mukhopadyay, A Patta, B. K. Banik, *Heterocycles* **71** (2007) 181
9. C. Ramalingan, Y.-W. Kwak, *Tetrahedron* **64** (2008) 5023.

Journal of
the Serbian
Chemical Society
version electronic

JSCS-info@shd.org.rs • www.shd.org.rs/JSCS

J. Serb. Chem. Soc. 80 (5) 605–612 (2015)
JSCS–4741

UDC 547.595.4+547.269.3+546.41'46'47:
547.466.1+542.913:66.094.522:615.277
Original scientific paper

Aminopeptidase N inhibition could be involved in the anti-angiogenic effect of dobesilates

OLDŘICH FARSA[1]*, ŠÁRKA SEDLÁKOVÁ[1], JANA PODLIPNÁ[2]
and JAROSLAV MAXA[2]

[1]*Department of Chemical Drugs, Faculty of Pharmacy, University of Veterinary and Pharmaceutical Sciences Brno, Palackého 1/3, 61242 Brno, Czech Republic and* [2]*Official Laboratory for Medicines Control, Institute for State Control of Veterinary Biologicals and Medicines, Hudcova 56a, 62100 Brno-Medlánky, Czech Republic*

(Received 28 November 2013, revised and accepted 31 March 2014)

Abstract: Calcium, magnesium and zinc 2,5-dihydroxybenzenesulfonates (dobesilates) were synthesized by sulfonation of hydroquinone with sulfuric acid under mild conditions. To form the salts, neutralization with calcium carbonate followed by cation exchange by means of magnesium or zinc sulfates was performed. The dobesilates were characterized by standard spectral methods and by AAS for metal content and then tested for inhibitory activity against aminopeptidase N. The calcium and magnesium 2,5-dihydroxybenzenesulfonates exhibited rather weak inhibitory activity to aminopeptidase N, as demonstrated by the IC_{50} values of 978.0 and 832.1 μmol L^{-1}, respectively, while zinc 2,5-dihydroxybenzenesulfonate reached a more significant inhibitory activity characterized by an IC_{50} value of 77.4 μmol L^{-1}. The results of the inhibition activity suggest that the inhibition of aminopeptidase N could play a role in the anti-angiogenic activity of 2,5-dihydroxybenzenesulfonates.

Keywords: 2,5-dihydroxybenzenesulfonic acid salts; effect on CD13 activity; neovascularization; carcinogenesis; vasculopathies.

INTRODUCTION

Angiogenesis or the formation of new blood vessels is a process that rarely occurs in healthy adult tissues. It is typical either for growing embryonic tissues or for pathological conditions, such as carcinogenesis or proliferative vasculopathies, including diabetic retinopathy of nephropathy. The formation of new blood vessels or tubes capable of fulfilling their function in neoplasms is crucial for the survival, growth and metastasis of most solid tumors. Consequently, inhibition of angiogenesis is considered a promising approach in cancer treatment, and the design of novel angiogenesis inhibitors is currently underway.

---

* Corresponding author. E-mail: farsao@vfu.cz

doi: 10.2298/JSC131128032F

Angiogenesis is a complex multi-stage process, which is controlled by the balance between angiogenic factors and angiogenesis inhibitors.[1] The main factors that have been demonstrated to participate in angiogenesis regulation are growth factors, such as members of the vascular endothelial growth factor (VEGF) family, fibroblast growth factors (FGF), epidermal growth factors (EGF), platelet-derived growth factors (PDGF) and transforming growth factors (TGF). All these signaling proteins up-regulate angiogenesis. Interferon-gamma--inducible protein 10 (IP-10), which is an antagonist of VEGF, can serve as an example of the body's own angiogenesis inhibitor.[2] Some proteolytic enzymes also support angiogenesis. Among them, at least three aminopeptidases were reported to contribute to neovascularization. Aminopeptidases are ectopeptidases that cleave the N-terminal amino acid from a peptide chain. They are also metalloenzymes, as they are able to bind one or two divalent metal cations, such as Zn^{2+}, Co^{2+} or Mn^{2+}. Additionally, they exhibit broader or narrower substrate specificity. Methionine aminopeptidase type 2, containing a coordinated Co^{2+} and two zinc-aminopeptidases, adipocyte-derived leucine aminopeptidase (A--LAP) and aminopeptidase N (APN) were reported to be involved in angiogenesis control.[1] This paper discusses the effect of dobesilates on APN activity. APN (EC 3.4.11.2) is identical to CD13 antigen, which has been identified as a cell-surface marker for malignant myeloid cells.[3] It was also recognized as a cell entry receptor of some coronaviruses. In these viruses, the envelope spike glycoprotein mediates the attachment of the virus particles to APN and subsequent cell entry, which can be blocked by neutralizing antibodies.[4] It was also reported that bestatin, the most well-known APN inhibitor, stopped the invasion of tumor cells into reconstituted basement membrane.[5,6] Recently, studies on APN-null mice revealed impaired neoangiogenesis in model systems without cancer cells.[7] Moreover, it was demonstrated that a decrease of APN activity in tumor tissue results in a reduction in both the density and size of newly formed blood vessels.[8] VEGF, a key angiogenesis regulator, triggers the expression of APN at an early stage of tumor growth.[9] Similarly, the basic fibroblast growth factor (bFGF) and its downstream Ras-dependent signals, which mediate the formation of the endothelial cells network, induce APN expression in endothelial cells.[10] However, the precise mechanism by which APN regulates angiogenesis remains unclear.

Dobesilates are salts of 2,5-dihydroxybenzenesulfonic acid (**1**) with divalent or monovalent metal cations. They were first reported as early as 1880.[11] Calcium dobesilate (**2**) has been used for decades for the prevention and treatment of diabetic retinopathy,[12] nephropathy, chronic venous insufficiency,[13] hemorrhoids[14] and other related conditions. Potassium dobesilate (**3**) was successfully used for the treatment of actinic keratosis in an open-label clinical study.[15] **3** and magnesium dobesilate (**4**) were reported as the experimental drugs used in several *in vitro* studies.[16,17] Except in an early study of Seyda,[11] zinc dobesilate (**5**) has only been mentioned in a U.S. patent.[18] Except for **2**, data in the literature concerning spectral and other identification information of dobesilates are poor. The anti-angiogenic activity of dobesilates was demonstrated in a mouse gelatin sponge assay using acidic fibroblast growth factor (aFGF) as an inducer of neovascularization. Here, **2** remarkably reduced vessel ingrowths in FGF-containing subcutaneous sponges in mice.[19] Another study showed that **2** inhibited angiogenesis in both choroidal explants cultured in collagen gels and the choroids of live diabetic rats. This effect was accompanied by inhibition of VEGF production in this tissue.[20] Furthermore, inhibition of neovascularization by dobesilates was discussed several times regarding its effectiveness in the treatment of angiopathies, neoplasms and other diseases in which angiogenesis plays an important role, such as chorioretinopathy,[21] malignant glioma[22] and rosacea.[23]

The aim of this study was to determine whether dobesilates inhibit APN and whether the subsequent APN inhibition plays a role in the antiangiogenic activity of dobesilates.

EXPERIMENTAL

All melting points were determined on a Büchi 535 melting point apparatus (Büchi, Flawil, Switzerland) and are uncorrected. The IR spectra were measured on a Nicolet Impact FTIR spectrometer using the ATR technique. The ^{1}H- and ^{13}C-NMR spectra were recorded on a 200 MHz Gemini 2000 instrument (Varian, Palo Alto, CA, USA) using DMSO-d_6 as the solvent at 200 MHz or 50 MHz, respectively. The UV–Vis spectra were recorded on an Agilent 8453 diode array UV–Vis spectrophotometer (Agilent Technologies, Waldbronn, Germany). The content of metals was determined by atomic absorption spectroscopy (AAS) on a NovAA 350 atomic absorption spectrophotometer (Analytik Jena, Jena, Germany) using the flame technique.

Dobesilates

Hydroquinone (15 g, 0.136 mol) was added portionwise under stirring into 60 mL of 95 % sulfuric acid over 1 h. Stirring was continued until the starting material was completely dissolved. The temperature during this process did not exceed 45 °C. This solution of crude 2,5-dihydroxybenzenesulfonic acid (**1**) in sulfuric acid was poured under stirring into 1500 mL of water and 150 g (1.5 mol) of calcium carbonate was then added portionwise under vigorous stirring. Stirring continued for an additional 15 min at room temperature. Then, the suspension was shortly heated to a boil and immediately filtered by suction filtration. The filtrate containing crude **2** was then divided into three equal volume portions.

*Calcium dobesilate (2).*The first portion was slowly concentrated by evaporation on a vacuum evaporator at a temperature that did not exceed 42 °C. A white precipitate that formed during evaporation was filtered off. The filtrate was evaporated to dryness. The residue was dried under reduced pressure (0.7 kPa) at 40–42 °C over diphosphorus pentaoxide for 7 days. The obtained calcium 2,5-dihydroxybenzenesulfonate (**2**) was identified by ^{1}H-NMR as the pentahydrate.

Magnesium dobesilate (4). Anhydrous magnesium sulfate (4.38 g, 0.0360 mol) was added under stirring to the second portion of the solution of crude **2** at room temperature. The mixture was stirred for an additional 30 min and then heated to boiling for a short period of time. The formed calcium sulfate precipitate was removed by suction filtration of the hot suspension. The filtrate was slowly concentrated by evaporation on a vacuum evaporator at a temperature that did not exceed 42 °C. The white precipitate that formed during the evaporation was filtered off. The filtrate was evaporated to dryness. The residue was dried under reduced pressure (0.7 kPa) at 40–42 °C over diphosphorus pentaoxide for 7 days. The obtained magnesium 2,5-dihydroxybenzenesulfonate (**4**) was identified by ^{1}H-NMR as the decahydrate.

*Zinc dobesilate (**5**)*. Zinc sulfate heptahydrate (6.53 g, 0.0230 mol) was added under stirring to the third portion of the solution of crude **2** at room temperature. The mixture was stirred for an additional 30 min and then heated to boiling for a short period. The formed calcium sulfate precipitate was removed by suction filtration of the hot suspension. The filtrate was slowly concentrated by evaporation on a vacuum evaporator at a temperature that did not exceed 42 °C. The white precipitate that formed during evaporation was filtered off. The filtrate was evaporated to dryness. The residue was dried under reduced pressure (0.7 kPa) at 40–42 °C over diphosphorus pentaoxide and protected from light for 7 days. The obtained zinc dobesilate (**5**) was identified by ^{1}H-NMR as the octahydrate.

Some physical, analytical and spectral data for the examined dobesilates are given in Supplementary material to this paper.

Biochemistry

Enzyme assay. Both L-leucine-*p*-nitroanilide, C.A.S. 4178-93-2, a substrate for APN, and APN, EC 3.4.11.2, were purchased from Sigma, USA. The other employed chemicals were of analytical or biochemical grade. The absorbance values at 405 nm, which is the absorption maximum of 4-nitroaniline, a product of substrate hydrolysis catalyzed by APN, were determined on a Helios Beta UV–Vis spectrophotometer equipped with a seven-position carousel (Unicam, UK). Every measurement was performed in triplicate. The results of the assays were evaluated and the IC_{50} values were calculated using QCExpert 2.5 statistical software (Trilobyte, Czech Republic). The colorimetric assay of enzyme inhibition was performed according to a previously described procedure that is considered a standard analytical method for this purpose,[24] although some alternative approaches, including RP–HPLC with fluorescence detection, have also been successfully tested.[25] The absorbance data together with the gradually increasing concentrations of dobesilates and their logarithms are given in Table I. The concentrations of dobesilates were recalculated into the concentrations of the anhydrous substances.

TABLE I. Absorbances of samples of dobesilates incubated with APN with gradually increasing concentrations of dobesilates

c(**2**)/10^{-3} mol L^{-1}	A(**2**)	c(**4**)/10^{-3} mol L^{-1}	A(**4**)	c(**5**)/10^{-4} mol L^{-1}	A(**5**)
0.000	0.965	0.000	0.965	0.000	0.965
0.720	0.959	0.605	0.753	0.189	0.956
0.823	0.929	0.691	0.702	0.283	0.918
0.926	0.747	0.777	0.610	0.377	0.782
1.029	0.366	0.864	0.537	0.472	0.682
1.131	0.071	0.950	0.344	0.566	0.656
1.233	0.050	1.040	0.158	0.660	0.533
–	–	–	–	0.755	0.460

RESULTS AND DISCUSSION

Chemistry

The target compounds were synthesized according to the steps outlined in Scheme 1. Calcium dobesilate (**2**) was prepared by sulfonation of hydroquinone under mild conditions followed by neutralization with calcium carbonate. It also served as an intermediate for the preparation of both magnesium and zinc dobesilates, which were produced from reactions of the appropriate metal sulfates with solutions of **2** under precipitation of the less soluble calcium sulfate. The synthesized compounds were characterized by melting points, IR, ^{1}H- and ^{13}C-NMR spectral data and metal content determined by AAS. Although these three dobesilates are not completely novel compounds, satisfactory spectral characteristics of two of them, **4** and **5**, have not hitherto been reported. Furthermore, the hydrates of **2**, **4** and **5** have also not been previously reported.

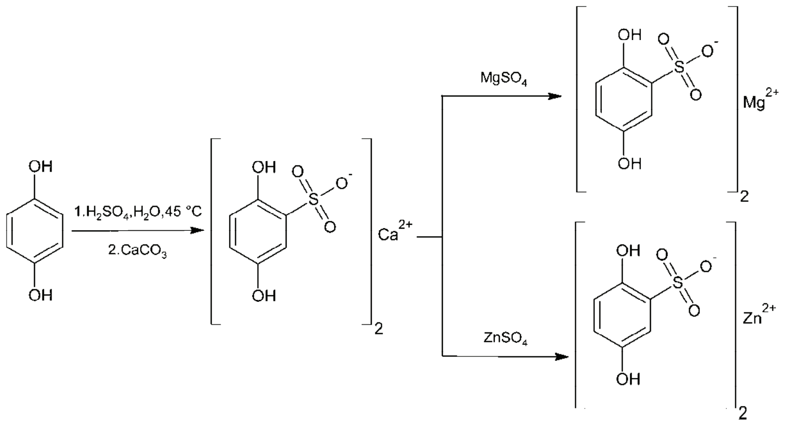

Scheme 1. Synthesis of salts of 2,5-dihydroxybenzenesulfonic acid.

The characterization data for **2**, **4** and **5** are given in the Supplementary material to this paper.

Enzyme assay

The linear regression analysis of the relationship of mean absorbance values at 405 nm with the dobesilate concentration, re-calculated into the concentration of anhydrous dobesilate, resulted in the following equations:

$$\log c(\mathbf{2}) = -0.2024A - 2.9120;\ R = 0.959 \quad (1)$$

$$\log c(\mathbf{4}) = -0.3688A - 2.9019;\ R = 0.943 \quad (2)$$

$$\log c(\mathbf{5}) = -1.1097A - 3.5761;\ R = 0.975 \quad (3)$$

The values of IC_{50} were then calculated as the concentration corresponding to 50 % of the maximum absorbance values.[26] IC_{50} values of 978.0, 832.1 and 77.4 μmol L^{-1} were obtained for **2**, **4** and **5**, respectively. Thus, **5** showed the highest inhibitory activity. Compared to the most active APN inhibitors, **2** and **4** could be characterized as weak APN inhibitors, but the IC_{50} of **5** has a comparable order of magnitude with the values for known active compounds, such as the short-chain peptide bestatin, which, determined on the same pig kidney APN, reached 16 μmol L^{-1}.[27] These results suggest that the involvement of APN inhibition in the anti-angiogenic activity of dobesilates is possible because Zn^{2+} is available in blood plasma and divalent cations are freely interchangeable. As far as the mechanism of inhibition of APN by dobesilates is concerned, their inhibitory effect cannot be attributed to the replacement of Zn^{2+} in the active center of the enzyme with other divalent cations[28] because **5** has a greater inhibitory effect than **4** and **2**. The removal of Zn^{2+} from the active center through its simple complexation by the free phenolic groups of 2,5-dihydroxybenzenesulfonate also seems improbable. This does not occur even in compounds with the *o*-configuration of hydroxyls, which are much more suitable for such complexation, such as the flavonoid quercetin.[29] The Zn^{2+} is bound by His383, His387 and Glu406 residues, which belong to the active site of APN.[30,31] Zn^{2+} and Glu406 form a regular carboxylate ion pair, while donor–acceptor bonds exist between Zn^{2+} and the imidazole nitrogens of both His residues. These coordination bonds could be disrupted by the formation a 2,5-dihydroxybenzenesulfonate ion pair on a particular basic nitrogen of the His imidazole ring by interaction with any dobesilate. By coordination, the dobesilate metal cation can then interact with other suitable amino acid residues within the catalytic site, such as Arg, His, Tyr and Asp or Glu. This interaction could lead to a decrease in catalytic activity. The mode of the inhibitory action of dobesilates on APN could also be based on their reduction activity, as they are hydroquinone derivatives and can be readily oxidized to appropriate 1,4-benzoquinone derivatives – 3,6-dioxocyclohexa-1,4-diene-1-sulfonates. The possibility and reversibility of this reaction has been repeatedly demonstrated by cyclic voltammetry using various types of electrodes.[32] This oxidation must be accompanied by a complementary reduction, such as a change in a disulfide bridge between two cysteine residues into two independent thiol groups. Such bridges occur in APN between Cys758 and Cys765 and between Cys795 and Cys831.[4] Their removal could lead to the disruption of the tertiary structure of the enzyme protein, which could lead to decreased activity.

CONCLUSIONS

In the present paper, the synthesis of calcium (**2**), magnesium (**4**) and zinc (**5**) 2,5-dihydroxybenzenesulfonates is described. The results of inhibitory activity assays against APN showed that **2** and **4** are only weak inhibitors of this enzyme while **5** has medium inhibitory activity.

SUPPLEMENTARY MATERIAL

Some physical, analytical and spectral data for the examined dobesilates are available electronically from http://www.shd.org.rs/JSCS/, or from the corresponding author on request.

ИЗВОД

ИНХИБИЦИЈА АМИНОПЕПТИДАЗЕ N ЈЕ МОЖДА УКЉУЧЕНА У АНТИ-АНГИОГЕНИ ЕФЕКАТ ДОБЕЗИЛАТА

OLDŘICH FARSA[1], ŠÁRKA SEDLÁKOVÁ[1], JANA PODLIPNÁ[2] и JAROSLAV MAXA[2]

[1]*Department of Chemical Drugs, Faculty of Pharmacy, University of Veterinary and Pharmaceutical Sciences Brno, Palackého 1/3, 61242 Brno, Czech Republic* и [2]*Official laboratory for medicines control, Institute for State Control of Veterinary Biologicals and Medicines, Hudcova 56a, 62100 Brno-Medlánky, Czech Republic*

Сулфоновање хидрохинона сумпорном киселином и реакцијом одговарајућих соли добијени су калцијум- , магнезијум- и цинк-2,5-дихидроксибензенсулфонати (добезилати). Калцијумова со је добијена директном реакцијом киселине и калцијум-карбоната, док су магнезијумова и цинкова со добијене после јонске измене употребом магнезијум- или цинк-сулфата. Добезилати су окарактерисани стандардним спектроскопским поступцима и AAS за садржај јона метала и испитана им је инхибиторна активност према аминопептидази N. Калцијум- и магнезијум-2,5-дихидроксибензенсулфонати показују слабу инхибиторну активност према аминопептидази N, са IC_{50} вредностима 978,0 и 832,1 μmol L^{-1}, редом, док цинк-2,5-дихидроксибензенсулфонат показује знатно бољу инхибиторну активност, са IC_{50} од 77,4 μmol L^{-1}. Инхибиторне активности указују да инхибиција аминопептидазе N може да буде важна у анти-ангиогеној активности 2,5-дихидроксибензенсулфоната.

(Примљено 28. новембра 2013, ревидирано и прихваћено 31. марта 2014)

REFERENCES

1. Y. Sato, *Biol. Pharm. Bull.* **27** (2004) 772
2. J. M. Heinzman, S. L. Brower, J. E. Bush, *Cancer Cell Int.* **8** (2008) 11
3. M. A. Shipp, A. T. Look, *Blood* **82** (1993) 1052
4. J. Reguera, C. Santiago, G. Mudgal, D. Ordono, L. Enjuanes, J. M. Casasnovas, *PLoS Pathog.* **8** (2012) E1002859
5. J. Yoneda, I. Saiki, H. Fujii, F. Abe, Y. Kojima, I. Azuma, *Clin. Exp. Metastasis* **10** (1992) 49
6. I. Saiki, H. Fujii, J. Yoneda, F. Abe, M. Nakajima, T. Tsuruo, I. Azuma, *Int. J. Cancer* **54** (1993) 137
7. R. Rangel, Y. Sun, L. Guzman-Rojas, M. G. Ozawa, J. Sun, R. J. Giordano, C. S. Van Pelt, P. T. Tinkey, R. R. Behringer, R. L. Sidman, W. Arap, R. Pasqualini, *Proc. Natl. Acad. Sci. USA* **104** (2007) 4588
8. L. Guzman-Rojas, R. Rangel, A. Salameh, J. K. Edwards, E. Dondossola, Y. G. Kim, A. Saghatelian, R. J. Giordano, M. G. Kolonin, F. I. Staquicini, E. Koivunen, R. L. Sidman, W. Arap, R. Pasqualini, *Proc. Natl. Acad. Sci. USA* **109** (2012) 1637
9. S. V. Bhagwat, J. Lahdenranta, R. Giordano, W. Arap, R. Pasqualini, L. H. Shapiro, *Blood* **97** (2001) 652
10. S. V. Bhagwat, N. Petrovic, Y. Okamoto, L. H. Shapiro, *Blood* **101** (2003) 1818
11. A. Seyda, *Ber. Dtsch. Chem. Ges.* **16** (1883) 687
12. O. Farsa, in *Diabetic retinopathy*, M. S. Ola, Ed., InTech, Rijeka, 2012, p. 305
13. T. Tejerina, E. Ruiz, *Gen. Pharmacol.* **31** (1998) 357

14. V. Lohsiriwat, *World J. Gastroenterol.* **18** (2012) 2009
15. P. Cuevas Sánchez, W. Espinoza, C. Pérez, J. Angulo, G. Giménez-Gallego, *Eur. J. Med. Res.* **16** (2011) 67
16. C. V. Suschek, H. Kolb, V. V. Kolb-Bachofen, *Int. J. Angiol.* **8** (1999) S21
17. J. Brunet, J. C. Farine, R. P. Garay, P. Hannaert, *Fundam. Clin. Pharmacol.* **12** (1998) 205
18. J. Esteve Soler, (J. Esteve Soler), US 4,146,646 (1979)
19. P. Cuevas, I. Sanchez, R. M. Lozano, G. Gimenez-Gallego, *Eur. J. Med. Res.* **10** (2005) 369
20. S. Lameynardie, C. Chiavaroli, P. Travoc, R. P. Garay, N. Parés-Herbuté, *Eur. J. Pharm.* **510** (2005) 149
21. P. Cuevas, L. A. Outeirino, C. Azanza, J. Angulo, G. Giménez-Gallego, *Eur. J. Med. Res.* **17** (2012) 22
22. A. D. Norden, J. Drappatz, P. Y. Wen, *Lancet Neurol.* **7** (2008) 1152
23. P. Cuevas, J. Angulo, G. Giménez-Gallego, *BMJ Case Rep.* (2011), doi: 10.1136/ /bcr.08.2011.4579
24. J. C. M. Hafkenscheid, in *Methods of Enzymatic Analysis,* Vol. 5, H. U. Bergmeyer, Ed., VCH Verlag, Weinheim, 1984, p. 11
25. X. Xiong, A. Barathi, R. W. Beuermann, D. T. H. Tan. J. *Chromatogr., B* **796** (2003) 63
26. J. L. Sebaugh, *Pharm. Stat.* **10** (2011) 128
27. R. Matsas, S. L. Stephenson, J. Hryszko, A. J. Kenny, A. J. Turner. *Biochem. J.* **231** (1985) 445
28. U. Femfert, G. Pfleiderer, *FEBS Lett.* **14** (1971) 89
29. J. Parellada, G. Suárez, M. Guinea, *J. Enzyme Inhib.* **13** (1998) 347
30. A. J. Turner, in *Handbook of proteolytic enzymes*, N. D. Rawlings, A. J. Barett, J. F. Woesner, Eds., Elsevier, New York, 2004, p. 289
31. N. D. Rawlings, A. J. Barrett, A. Bateman, *Nucleic Acids Res.* **40** (2012) D343
32. J. Zheng, Y. Zhang, P. Yang, *Talanta* **73** (2007) 920.

Journal of the Serbian Chemical Society
JSCS@tmf.bg.ac.rs • www.shd.org.rs/JSCS
J. Serb. Chem. Soc. 80 (5) S166–S167 (2015)
Supplementary material

SUPPLEMENTARY MATERIAL TO

Aminopeptidase N inhibition could be involved in the anti-angiogenic effect of dobesilates

OLDŘICH FARSA[1]*, ŠÁRKA SEDLÁKOVÁ[1], JANA PODLIPNÁ[2]
and JAROSLAV MAXA[2]

[1]Department of Chemical Drugs, Faculty of Pharmacy, University of Veterinary and Pharmaceutical Sciences Brno, Palackého 1/3, 61242 Brno, Czech Republic and [2]Official Laboratory for Medicines Control, Institute for State Control of Veterinary Biologicals and Medicines, Hudcova 56a, 62100 Brno-Medlánky, Czech Republic

J. Serb. Chem. Soc. 80 (5) (2015) 605–612

SOME PHYSICAL, ANALYTICAL AND SPECTRAL DATA FOR THE EXAMINED DOBESILATES

Calcium 2,5-dihydroxybenzenesulfonate (**2**). Yield: 94 %; white solid; m.p.: 189–191 °C; Ca content (AAS) calcd. for $C_{12}H_{20}CaO_{15}S_2$: 7.88 %. Found: 8.06 %; IR (ATR, cm^{-1}): 703 (C–S– stretching), 860 (CH bending of aromatic ring), 1338, 1445 (SO_2 stretching), 1495 (C=C stretching of aromatic ring), 1644 (C=C stretching of aromatic ring), 3010 (CH stretching of aromatic ring), 3248 (OH stretching); ^{1}H-NMR (200 MHz, DMSO-d_6, δ / ppm): 5.51 (14H, *bs*, 4 OH + 5 H_2O), 6.60 (4H, *m*, aromatic), 6.87 (2H, *m*, aromatic); ^{13}C-NMR (50 MHz, DMSO-d_6, δ / ppm): 149.17 (C), 146.11 (C), 130.92 (C), 118.32 (CH), 116.94 (CH), 113.08 (CH); UV–Vis (H_2O, λ_{max} / nm): 220, 299.

Magnesium 2,5-dihydroxybenzenesulfonate (**4**). Yield: 72 %; white solid; m.p.: > 279 °C; Mg content (AAS) calcd. for $C_{12}H_{30}MgO_{20}S_2$: 4.17. Found: 4.38; IR (ATR, cm^{-1}): 730 (C–S– stretching) 877 (CH bending of aromatic ring), 1331, 1449 (SO_2 stretching), 1500 (C=C stretching of aromatic ring), 1663 (C=C stretching of aromatic ring), 3376 (OH stretching); ^{1}H-NMR (200 MHz, DMSO-d_6, δ / ppm): 4.00 (24H, *bs*, 4 OH + 10H_2O), 6.59 (4H, *m*, aromatic), 6.87 (2H, *t*, J = 1.7 Hz, aromatic); ^{13}C-NMR (50 MHz, DMSO-d_6, δ / ppm): 149.18 (C), 146.11 (C), 133.20 (C), 118.29 (CH), 116.94 (CH), 113.08 (CH); UV–Vis (H_2O, λ_{max} / nm): 220, 294.

Zinc 2,5-dihydroxybenzenesulfonate (**5**). Yield: 80 %; pale yellow solid; m.p.: 171–173 °C under decomposition; Zn content (AAS) calcd. for $C_{12}H_{26}O_{18}S_2Zn$: 11.13. Found: 11.65; IR (ATR, cm^{-1}): 703 (C–S– stretching),

---

* Corresponding author. E-mail: farsao@vfu.cz

871 (CH bending of aromatic ring), 1327, 1469 (SO_2 stretching), 1494 (C=C stretching of aromatic ring), 1655 (C=C stretching of aromatic ring), 3010 (CH stretching of aromatic ring), 3242 (OH stretching); ^{1}H-NMR (200 MHz, DMSO-d_6, δ / ppm): 3.97 (20H, *bs*, 4 OH + 8 H_2O), 6.59 (4H, *m*, aromatic), 6.86 (2H, *m*, aromatic); ^{13}C-NMR (50 MHz, DMSO-d_6, δ / ppm): 149.16 (C), 146.11 (C), 131.00 (C), 118.27 (CH), 116.92 (CH), 113.07 (CH); UV-Vis (H_2O, λ_{max} / nm): 220, 301.

Journal of the Serbian Chemical Society
version electronic

JSCS-info@shd.org.rs • www.shd.org.rs/JSCS

J. Serb. Chem. Soc. 80 (5) 613–625 (2015)
JSCS–4742

UDC 547.964.2+546.33’226:54.121:536.7+
544.4:541.121
Original scientific paper

Evidence of *β*-sheet structure induced kinetic stability of papain upon thermal and sodium dodecyl sulfate denaturation

BRANKICA RAŠKOVIĆ[#], NIKOLINA BABIĆ, JELENA KORAĆ
and NATALIJA POLOVIĆ*[#]

Department of Biochemistry, Faculty of Chemistry, University of Belgrade,
Studentski trg 12–16, 11158 Belgrade, Serbia

(Received 1 September, revised 11 December, accepted 16 December 2014)

Abstract: Papain is a protease that consists of *α*-helical and *β*-sheet domains that unfold almost independently. Both, considerable thermal stability and sodium dodecyl sulfate (SDS) resistance of papain have been shown. However, the ability of each domain to unfold upon thermal and SDS denaturation has never been studied. This work shows that fruit papain has slightly higher resistance to thermal inactivation when compared to that of stem papain with a rather high activation energy (E_a) of 223±16 kJ mol^{-1} and a T_m50 value of 79±2 °C. The SDS resistance of fruit papain was estimated by SDS–PAGE analysis and activity staining. It was noted that, in the presence of SDS the protein remained active, unless heat energy was applied in order to unfold papain. Furthermore, it was proven *via* Fourier transform infrared spectroscopy (FT--IR) that an *α*-helical domain of fruit papain is more prone to unfolding at elevated temperatures and in the presence of SDS then a *β*-sheet rich domain. Thermal denaturation of papain without detergent present led to accelerated formation of aggregation specific intermolecular *β*-sheets as compared to native protein. The presented results are of both fundamental and practical importance.

Keywords: thermal inactivation; SDS resistance; secondary structure; FT-IR spectroscopy.

INTRODUCTION

Papain is a cysteine protease (EC 3.4.22.2) with broad substrate specificity and numerous applications. The preprotein consists of 345 amino acids and it is secreted as zymogen.[1] After cleavage of the activation peptide, the mature enzyme contains 212 amino acid residues that are organized in two domains. The *N*-terminal domain has mainly *α*-helical structure, while the C-terminal domain

---

[*] Corresponding author. E-mail: polovicn@chem.bg.ac.rs
[#] Serbian Chemical Society member.
doi: 10.2298/JSC140901007R

has an antiparallel β-sheet fold.[2] Commercial papain can be isolated from latex (stem) or papaya fruit. Both commercial enzymatic preparations have broad substrate specificity.[3]

Papain is extensively used as meat tenderizer,[4] in dental caries removal procedures,[5] for preparation of clinically relevant antibody fragments,[6] as a cell dissociation/debris removal agent[7] and as a component in cosmetic preparations.[8] Papain has been used in the detergent industry since the enzyme shows high activity and broad specificity for hydrolysis of peptide bonds.[9] Furthermore, the enzymes from the papain family are known to be sodium dodecyl sulfate (SDS) resistant[10] and very stable enzymes at elevated temperatures.[11]

Elucidation of the basis for the extreme temperature and SDS stability of proteins is both of fundamental and practical importance. Recent studies suggested that a rigid β-sheet fold, which leads to low structural flexibility of a protein, could be responsible for the SDS and protease resistance and might also be responsible for thermal stability of a protein.[10] Since papain has both α-helical and β-sheet domains, the aim of this study was to check if any of the domains was more prone to SDS denaturation by monitoring the changes in the secondary structures of the protein at elevated temperatures and in the presence of SDS. The kinetic parameters of the thermal inactivation of fruit papain were also estimated.

EXPERIMENTAL

Papain purification

Fruit papain was purified from a commercial papain preparation (BDH, London, England). Papain was extracted from the dry powder with 100 mM Tris buffer pH 8 containing 100 mM NaCl and 1 mM ethylenediaminetetraacetic acid disodium salt (EDTA) for 30 min at 10 °C. The extract was centrifuged for 15 min at 4000×*g* at 10 °C and the obtained supernatant was further used. Papain was precipitated from supernatant by addition of 2 volumes of ice-cold acetone followed by incubation at –20 °C for 30 min. The precipitate was separated by centrifugation at 10,000×*g* for 5 min. at 4 °C, dried and resuspended in 100 mM Tris buffer pH 8 containing 100 mM NaCl and 1 mM EDTA for further purification. Covalent chromatography was performed on Thiol-sepharose 4B (GE Healthcare, Uppsala, Sweden). The matrix was equilibrated in 100 mM Tris buffer pH 8.0 containing 100 mM NaCl and 1 mM EDTA (20 column volumes (CV)) first, and then the sample was applied. Unbound proteins were eluted with 20 CV of 100 mM Tris buffer pH 8 containing 100 mM NaCl and 1 mM EDTA, while bound protein was eluted by addition of 10 mM L-cysteine to the starting buffer. The homogeneity of purified protein was analyzed by sodium dodecyl sulfate polyacrylamide gel electrophoresis (SDS–PAGE). The concentration of the purified protein was determined using the Bradford method. Bovine serum albumin (BSA) was used as the standard.[12]

Papain activity measurement

The proteolytic activity of the purified papain was tested using BAPNA (N^{α}-benzoyl-DL-arginine 4-nitroanilide hydrochloride, Sigma–Aldrich, Steinheim, Germany) as a substrate in a 96-well microplate (Sarstedt, Numbrecht, Germany) as described in Raskovic *et al.*[13] Briefly, substrate solution, 100 µL of 1mM BAPNA in citrate buffer (50 mM pH 6 with 2 mM EDTA and 10 mM L-cysteine) was mixed with an aqueous papain solution (25 µL) and incubated at 25 °C. After 60 min, the reaction was stopped by the addition of glacial acetic acid and absorbance at 405 nm was measured.

Thermal inactivation curve

Papain solution (0.5 mg mL^{-1} in 100 mM Tris buffer pH 8 containing 100 mM NaCl, 1 mM EDTA and 10 mM L-cysteine) was incubated at different temperatures ranging from 15 to 100 °C for 30 min. Samples were allowed to cool to room temperature, and percentage of residual activity was determined in each sample using BAPNA. Measurements were performed in triplicate. The percentage residual activity was calculated relative to the sample that was incubated at 40 °C (maximal activity).

Determination of inactivation rate

Papain solutions were incubated at 60 or 80 °C and aliquots removed at specific intervals (1 min up to 2 h). After cooling to room temperature, the residual activity was measured using the BAPNA assay. The measurements were performed in triplicate.

Determination of the inactivation constants

Inactivation rate constants for papain were determined at four different temperatures selected from the declining part of the inactivation curve (75, 80, 85 and 90 °C). Papain solutions were incubated at an appropriate temperature, and aliquots were taken at specific intervals, ranging between 1 and 30 min. After cooling to room temperature, the samples were assayed with BAPNA. The residual activity was determined in comparison to the activity of the sample before incubation at the respective temperature. A plot of logarithmic residual activity *vs.* incubation time (expressed in minutes) was produced in order to calculate the rate constants for the inactivation of papain. Rate constant values were calculated from the slopes of the following linear regression:

$$\log (100A/A_{\max}) = -(k/2.303)t \tag{1}$$

where A represents the measured absorbance at 405 nm after certain period of incubation; $A_{\max}$ represents the maximal absorbance before incubation; k represents inactivation rate constant; and t represents the incubation time.[14]

Arrhenius plot. Activation energy of papain inactivation was determined by plotting the inactivation constants on the Arrhenius plot. Activation energy was calculated from the slope of Arrhenius plot ($\ln (k / \text{min}^{-1})$ *vs.* T^{-1} / K^{-1}) in accordance with the equation:

$$\ln k = -E_a/RT + C \tag{2}$$

where R represents the universal gas constant (8.314 J mol^{-1} K^{-1}), and T represents absolute temperature in K. Slopes and their standard errors were obtained from the linear regression curves.[15]

SDS–PAGE and activity staining

Papain samples for SDS–PAGE and activity staining analysis were prepared by mixing 0.5 mg mL^{-1} protein solution in 100 mM Tris buffer pH 8 containing 100 mM NaCl, 1 mM EDTA and 10 mM L-cysteine with adequate volume of reducing sample buffer (60 mM Tris buffer pH 6.8 containing 25 % glycerol, 1 % SDS, 14.4 mM 2-mercaptoethanol, and 0.1 % bromophenol blue) followed by 30 min incubation at various temperatures (60, 65, 70, 75, 80, 85 and 90 °C). The amount of protein loaded on the gel was 15 µg and 0.1 µg in the case of SDS–PAGE and activity staining, respectively. In the case of SDS–PAGE analysis, the samples were resolved in a discontinuous buffer system with a 4 % stacking gel and 10 % resolving gel in a Hoefer Dual Gel Mighty Small SE 245 vertical electrophoresis system

(Hoefer, Holliston, MA, USA) according to Laemmli.[16] In order to detect in-gel proteolytic activity of papain after SDS–PAGE, zymograms were run according to Felicioli *et al*. with some modifications.[17] Briefly, protein samples were applied onto a 10 % resolving gel copolymerized with 0.1 % gelatin. After electrophoresis, the gel was incubated in a 100 mM Tris, pH 8 with 100 mM NaCl and 1 mM EDTA for 16 h, followed by staining with Coomassie Brilliant Blue R-250 (Serva, Heidelberg, Germany).

Fourier transform infrared spectroscopy (FT-IR)

Infrared spectra were recorded for various papain samples (incubated for a period of 30 minutes at 25, 60 or 90 °C, with or without the addition of 1 % SDS, the same SDS concentration as in the reducing sample buffer for SDS–PAGE), utilizing Fourier transform infrared spectroscopy with attenuated total reflectance (ATR) at 1 cm^{-1} resolution (Nicolet 6700 FT-IR, software OMNIC, version 7.0, Thermo Scientific, USA). Papain samples (15 µg) were applied onto a Smart accessory with a diamond crystal (Smart Orbit, Thermo Scientific, USA). The solvent was evaporated under a nitrogen stream in order to obtain a thin ATR film. For each spectrum, 64 scans were collected. The spectrum of the buffer was subtracted from the spectrum of the protein since even water vapor can interfere with the protein absorbance. Criterion for the correctness of subtraction was a flat baseline between 1800 and 2000 cm^{-1}.[18]

Spectral analysis. Resolution enhanced spectra were generated by Fourier self-deconvolution function using 13 cm^{-1} for the full bandwidth at half height (FWHH) and 2.4 for the resolution enhancement factor as described in the study of Byler and Susi.[19] Second-derivative spectra were generated by a seven-point Savitsky–Golay derivative. The positions of the secondary structure peaks were identified from the second-derivative spectra and assigned to specific secondary structures, as described previously.[19,20] Aggregation specific bands were identified from low frequency bands.[21-23]

To compare the secondary structure transition in the papain samples incubated for 30 min at 25, 60 or 90 °C, with or without the addition of 1 % SDS, the ratio between the band intensities from the corresponding frequencies of a specific secondary structure and the amide II band maximum, identified at 1520 cm^{-1}, was calculated as described before.[24,25]

RESULTS AND DISCUSSION

Cooperative thermal inactivation of papain

Fruit papain was purified 8-fold from a commercial preparation in order to remove any inactive protein and colored low molecular weight compounds, which could interfere with the activity estimation assay (Fig. 1). In order to examine the dependence of papain activity and temperature, the residual activity of papain was observed at different temperatures using BAPNA as a substrate. Temperature range was 15–100 °C. After 30 min of incubation at a given temperature, the absorbance of the product was read and an inactivation curve was constructed (Fig. 2). The percentage residual activity was expressed in relation to the activity at 40 °C (maximal activity). The T_m50 value was found to be 79±2 °C, which is comparable to the T_m50 value of around 80 °C determined by differential scanning calorimetry.[11,26] In the incubation temperature region from 60 to 90 °C, the residual activity was reduced from 95 to only 1 %. In this part of the inactivation curve, cooperative loss of activity could be clearly observed due to denaturation of the protein. Since papain domains unfold almost independently,[26] it seems that loss of activity could be attributed to the transition of one domain. Active site residues (Cys-25, His-159 and Asn-178) are located in the cleft formed between these two domains, thus the destabilization of one domain could lead to inactivation.[11]

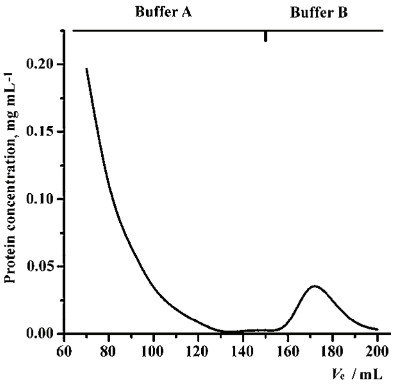

Fig. 1. Chromatographic separation of papain on a thiol-sepharose column. The column was equilibrated with 100 mM Tris buffer pH 8.0 containing 100 mM NaCl and 1 mM EDTA (Buffer A) followed by elution of unbound proteins with the same buffer and elution of papain with the same buffer containing 10 mM cysteine (Buffer B). The chromatography was run at a flow rate of 0.8 mL min^{-1}.

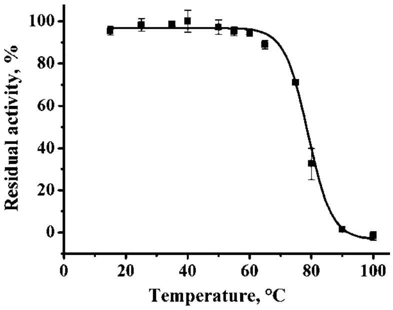

Fig. 2. Thermal inactivation curve of papain determined using BAPNA as a substrate. For creating the curve, A_{405} was monitored as a function of temperature over the appropriate temperature range (15–100 °C). The residual activity was calculated as the percentage of the maximal activity measured at 40 °C.

Papain inactivation rate at 60 and 80 °C

The term kinetic stability is used to describe proteins that are trapped in a specific conformation because of an unusually high unfolding barrier that results in very slow unfolding rates.[11] Since inactivation of papain coincided with transition of its tertiary structure, the overall kinetic stability of papain was estimated from its inactivation rates at different temperatures. Papain was incubated at 60 and 80 °C and at specific intervals starting from 1 min up to 2 h, aliquots were removed and the proteolytic activity against BAPNA was assayed. At 80 °C, the activity decline followed first order exponential kinetics (Fig. 3B). When inactivation curve of papain at 60 °C was determined, no decline of activity was registered, indicating stability of the enzyme at 60 °C (Fig. 3A) in the observed time range.

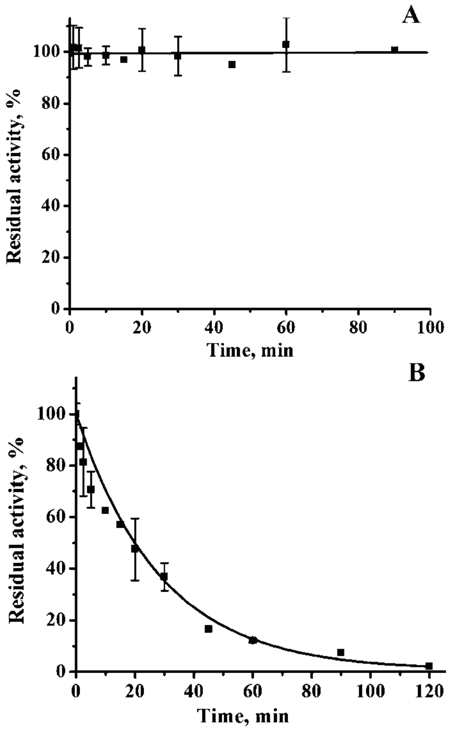

Fig. 3. Kinetics of papain inactivation at: A) 60 and B) 80 °C.

Thermal inactivation of papain

Thermal inactivation of papain was kinetically investigated in the temperature range 75–90 °C. The results are shown in Fig. 4.

First-order exponential curves for dependence of residual activity of papain on incubation time at temperatures in the range 75–90 °C were linearized by plotting the logarithm of the residual activity as a function of incubation time (Fig. 4A). The inactivation rate constants (k / min^{-1}) were calculated from the linear regression analysis and are given in Table I.

The inactivation rate constants increased approximately 20-fold in the temperature range 75–90 °C. Effect of temperature on inactivation rate is illustrated by Arrhenius plot shown in Fig. 4B.

Temperature dependence of the thermal inactivation of papain, expressed by the activation energy (E_a / kJ mol^{-1}) value, is given in Table I. Fruit papain exhibited slightly higher thermal inactivation resistance when compared to stem papain (the obtained E_a value for fruit papain was 223±16 kJ mol^{-1}, while for stem papain, it was 214±42 kJ mol^{-1}).[27] Recently, it was shown that latex and fruit papain differ in both stability and their catalytic properties under acidic conditions and in the presence of ethanol.[3] There is a possibility that fruit and stem papains are not the same enzyme but are isoenzymes. In the case of some other laticiferous plants (*e.g.*, *Ananas comosus*), different enzymatic profiles could be detected in the stem latex and the fruit regarding molecular weight, amino acid composition, substrate specificity, *etc*. Thus, stem and fruit bromelains, which belong to the papain family of proteases, could be considered as isoenzymes.[28]

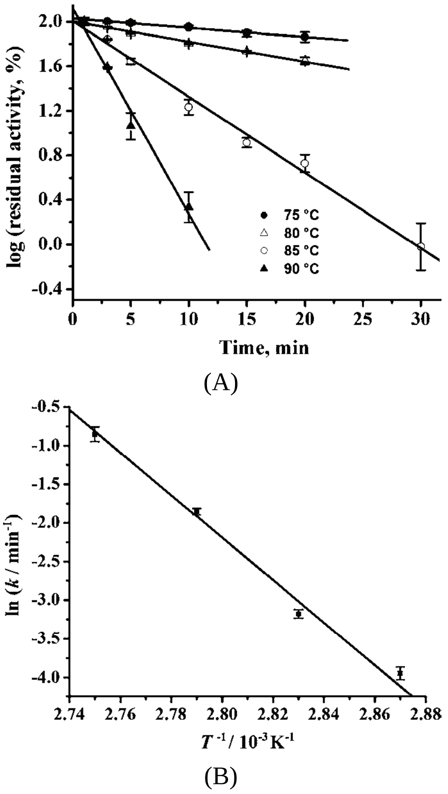

(A)

(B)

Fig. 4. A) Thermal inactivation of papain in the range between 75 to 90 °C. B) Arrhenius plot showing the temperature dependence of the rate constant of papain inactivation.

TABLE I. Inactivation rate constants (k / min^{-1}) of papain incubated at different temperatures

Temperature, °C	75	80	85	90	E_a / kJ mol^{-1}
k / min^{-1}	0.019±0.002	0.042±0.002	0.157±0.007	0.43±0.04	223±16

The E_a value of papain (223±16 kJ mol^{-1}) was considerably higher when compared to enzymes that are less stable in regards to temperature and presence of SDS. The E_a values for several enzymes having overall temperature stability below 50 °C and notorious instability in the presence of SDS were found to be 121,[29] 88[30] and 167 kJ mol^{-1},[31] for carbonic anhydrase, urease and amylase, respectively. In the case of proteolytic enzymes, the inactivation E_a value is very similar to the E_a value of fruit papain. For example, ficin has an inactivation E_a of 210±22 kJ mol^{-1}.[27]

Papain resistance to SDS

Activity staining (Fig. 5) showed that papain was stable at elevated temperatures (up to 60 °C) in the presence of SDS. At the temperatures higher than 60 °C, a gradual loss of activity was observed. Shift in SDS–PAGE mobility of the native (and active) papain in comparison to the denatured one could be explained by the resistance of papain to SDS denaturation. Since native papain showed resistance to SDS, its net negative charge during electrophoresis was decreased in comparison to the net negative charge of denatured papain (mainly originating from the sulfate group of the detergent).[10] It is noteworthy that papain expressed similar thermal stability regardless of the presence of SDS (Figs. 2 and 5). Since such extraordinary SDS stability of proteins was discussed in terms of the kinetic stability of the *β*-sheet towards SDS unfolding,[10] the propensities of changes of the certain secondary structure elements in the papain molecule upon incubation at elevated temperatures with and without added detergent were explored in the present study.

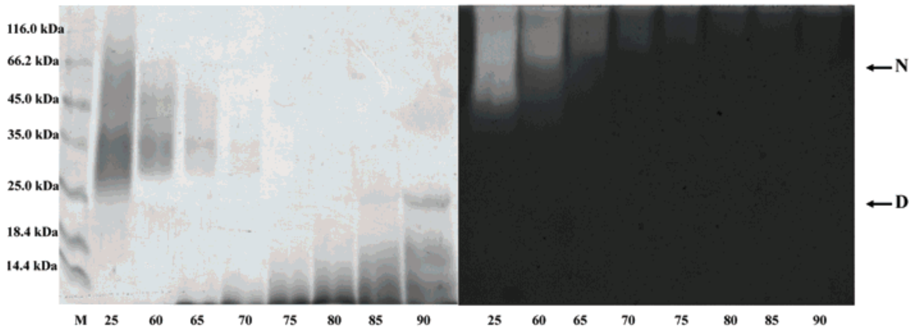

Fig. 5. SDS–PAGE analysis and activity staining towards gelatin of papain incubated at 25 °C and at temperatures from 60 to 90 °C in the presence of 1 % SDS. N – native papain; D – denatured papain.

Changes in secondary structures of papain

FT-IR spectroscopy was employed for monitoring the changes in the secondary structures. The IR spectra of papain incubated at elevated temperatures with or without SDS are shown in Figs. 6 and 7.

FT-IR spectroscopy is well-established method for the analysis of the secondary structures of proteins. The mostly used spectral region for secondary structure analysis is the amide I band (frequency limits: 1600–1700 cm^{-1}), which is almost entirely due to the C=O stretching vibrations of the peptide bonds.[32] Specific maxima within amide I region were identified from second-derivative spectra and assigned to secondary structures: *α*-helix 1654 cm^{-1} and *β*-sheet 1632 cm^{-1} according to Byler and Susi.[19] Goormaghtigh *et al.*[20] reported that 1641 cm^{-1} is a random coil specific frequency for papain, while Byler and Susi,[19] found it at 1646 cm^{-1}. In the present study, the random coil band was identified at 1643 cm^{-1}. An aggregation specific intermolecular *β*-sheet conformation was identified at a low frequency at around 1612 cm^{-1}.[21–23]

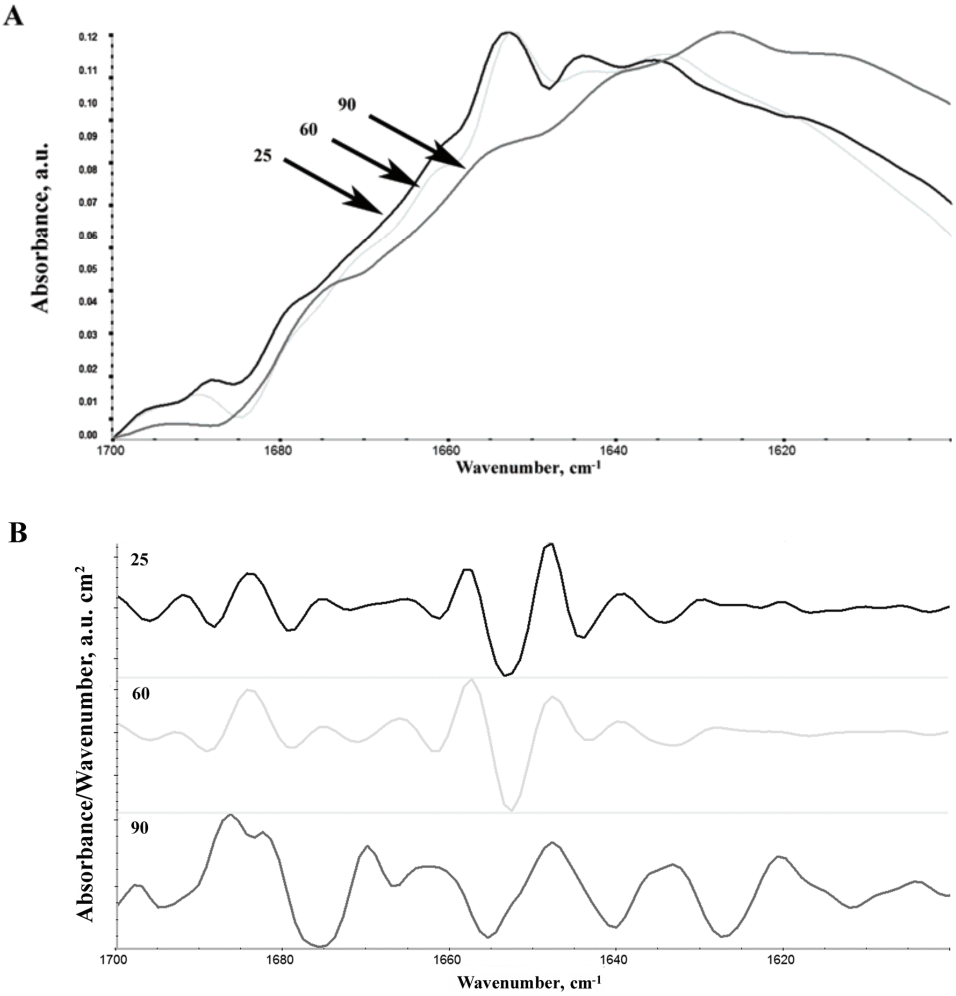

Fig. 6. A) Fourier self-deconvolution IR spectra and B) second derivative spectra of papain incubated at 25, 60 and 90 °C.

Changes in band intensity ratios of certain secondary structures identified within amide I region and amide II band in the IR spectra of papain incubated at elevated temperatures with or without added SDS are shown in Fig. 8.

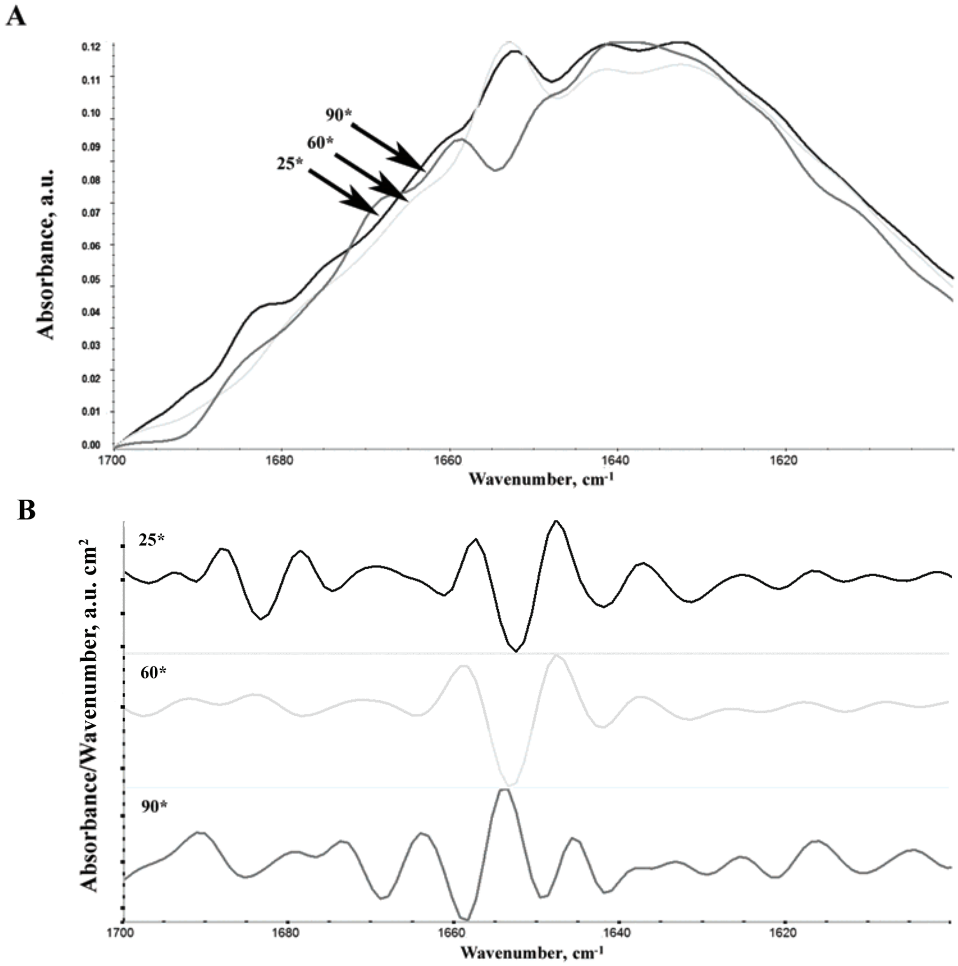

Fig. 7. A) Fourier self-deconvolution IR spectra and B) second derivative spectra of papain incubated at 25, 60 and 90 °C with addition of SDS (25*, 60* and 90*).

Denaturation of papain induced by heat (90 °C) led to lowered contents of native-like structures (ordered: *α*-helix; and unordered – random coil), while it accelerated the formation of an aggregation specific intermolecular *β*-sheet (Fig. 8). Several authors reported that frequencies 1614–1622 cm^{-1} and sometimes above 1680 cm^{-1} are aggregation specific frequencies in all *α*-helix rich,[22,33] *β*-sheet rich proteins,[21] and mixed fold proteins,[23] and that they appear due to the formation of intermolecular antiparallel *β*-sheets prior to aggregation. It was shown in the case of several proteins, including myoglobin,[22] transthyretin,[34] *β*-lactoglobulin,[21] human growth hormone, human interferon-*α*-2b[22] and chymotrypsinogen A[23] that heat denaturation induced changes in the amide I region, corresponding to shift of the intensities of frequency bands of native-like structures toward aggregation specific *β*-sheet frequency bands. Furthermore, the formation of the aggregates was lowered in the presence of SDS at elevated temperatures (60 and 90 °C, Fig. 8). However, in the case of added detergent it is apparent that elevated temperatures (especially at 90 °C) accelerated the formation of unordered structures, while lowering the content of *α*-helix structures. Changes in the *β*-sheets induced by the presence of SDS were not so pronounced, indicating that denaturation of papain by a combination of heat and detergent started within the *α*-helical domain. Lowered stability of the *α*-helical domain of papain in comparison to the *β*-sheet domain was recently reported in case of acid denaturation of papain.[35]

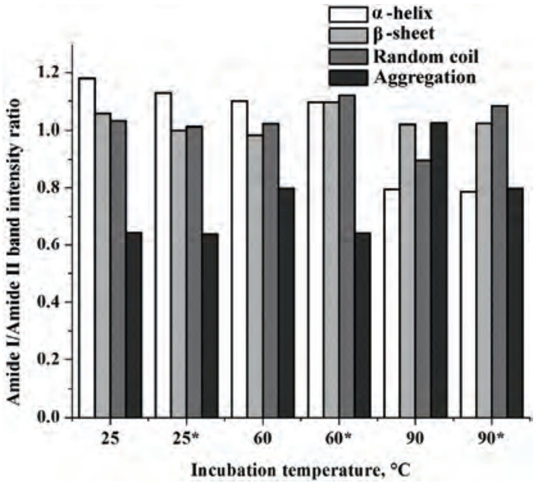

Fig. 8. Changes in intensity ratios of secondary structure specific bands in the IR spectra of papain incubated at 25, 60 and 90 °C (25, 60 and 90) and with addition of SDS (25*, 60* and 90*). The amide I/ amide II band intensity ratios were calculated using the intensity of secondary structure specific band in the amide I region (1654 cm^{-1} *α*-helix; 1632 cm^{-1} *β*-sheet; 1643 cm^{-1} random coil; 1612 cm^{-1} aggregation specific intermolecular *β*-sheet) and the amide II maximum intensity at 1520 cm^{-1}.

The explanation of SDS resistance of kinetically stable proteins is based on two assumptions. SDS binding appears to rely on transitions between protein conformations, moments of weakness in which the protein is susceptible to SDS binding, thus leading to entrapment.[10] On the other hand, kinetically stable proteins are characterized by unusually low structural flexibility, which lead to suppression of partial unfolding.[36] Thus, kinetically stable proteins, papain among them, infrequently assume open conformations and therefore are resistant to SDS unless provided with energy in the form of heat. With the exception of the papain family of proteases, most of the kinetically stable and SDS resistant proteins exhibit a tight *β*-sheet fold and tend to oligomerize.[10] However, despite having mixed *α*/*β* fold, papain is not the exception to the rule. The obtained results suggest that the *α*-helical domain of papain is more prone to unfolding at elevated temperatures and in the presence of SDS than the *β*-sheet rich domain.

CONCLUSIONS

In this study, for the first time, the differential SDS resistance of the α-helical N-terminal domain of papain and the β-sheet rich C-terminal domain is reported. Denaturation of papain by a combination of heat and SDS led to a reduction of the IR band assigned to α-helix, while preserving the β-sheet content. However, regardless of fruit papain denaturation at 90 °C, the protein exhibited considerable thermal stability and SDS resistance.

Acknowledgements. This work was financially supported by the Ministry of Education, Science and Technological Development of the Republic of Serbia, Grant No. 172049.

ИЗВОД

ДОМЕН БОГАТ β-ПЛОЧИЦАМА ЈЕ ОДГОВОРАН ЗА КИНЕТИЧКУ СТАБИЛНОСТ ПАПАИНА ПРИ ДЕНАТУРАЦИЈИ ИЗАЗВАНОЈ ПОВИШЕНОМ ТЕМПЕРАТУРОМ И НАТРИЈУМ-ДОДЕЦИЛ-СУЛФАТОМ

БРАНКИЦА РАШКОВИЋ, НИКОЛИНА БАБИЋ, ЈЕЛЕНА КОРАЋ и НАТАЛИЈА ПОЛОВИЋ

Катедра за биохемију, Хемијски факултет, Универзитет у Београду, Студентски трг 12–16, 11158 Београд

Папаин је протеаза која у својој структури поседује два домена од којих је један богат α-хеликсом, а други β-плочицом. Ова два домена се при денатурацији готово независно развијају. За папаин изолован из стабла папаје показана је знатна температурна стабилност, као и отпорност на натријум-додецил-сулфат (SDS). Међутим, подложност сваког од домена да се развијају услед денатурације изазване повишеном температуром или SDS, још увек није проучена. У овом раду је показано да папаин из плода папаје испољава благо повишену отпорност на термалну инактивацију у поређењу са папаином из стабла папаје са прилично високом вредношћу енергије активације (E_a) која износи 223±16 kJ mol^{-1} и T_m50 вредношћу од 79±2 °C. SDS–PAGE анализом и зимограмом одређена је отпорност папаина плода папаје на SDS. Изгледа да протеин задржава активност у присуству SDS-а све док се не обезбеди довољна количина енергије у виду топлоте која ће довести до развијања протеина. Употребом Фурије трансформисане инфрацрвене спектроскопије (FT-IR) показано је да је домен папаина плода папаје богат α-хеликсом подложнији развијању на повишеним температурама и у присуству SDS од домена богатог β-плочицама. Термална денатурација протеина без присуства детергента доводи до бржег формирања интермолекулске β-плочице специфичне за агрегацију протеина када се упореди са нативним протеином. Приказани резултати поседују фундаментални значај, али су веома важни и у контексту комерцијалне примене папаина.

(Примљено 1. септембра, ревидирано 11. децембра, прихваћено 16. децембра 2014)

REFERENCES

1. R. E. Mitchel, I. M. Chaiken, E. L. Smith, *J. Biol. Chem.* **245** (1970) 3485
2. I. G. Kamphuis, K. H. Kalk, M. B. A. Swarte, J. Drenth, *J. Mol. Biol.* **179** (1984) 233
3. M. Esti, I. Benucci, C. Lombardelli, K. Liburdi, A. M. V. Garzillo, *Food Bioprod. Process.* **91** (2013) 595
4. J. Weiss, M. Gibis, V. Schuh, H. Salminen, *Meat Sci.* **86** (2010) 196
5. M. C. Lopes, R. C. Mascarini, B. M. C. G. da Silva, F. M. Flório, R. T. Basting, *J. Dent. Child.* **74** (2007) 93

6. R. Flanagan, A. Jones, *Drug Saf.* **27** (2004) 1115
7. O. Kaiser, P. Aliuos, K. Wissel, T. Lenarz, D. Werner, G. Reuter, A. Kral, A. Warnecke, *PLoS One* **8** (2013) e80490
8. Y. C. Sim, S. G. Lee, D. C. Lee, B. Y. Kang, K. M. Park, J. Y. Lee, M. S. Kim, I. S. Chang, J. S. Rhee, *Biotechnol. Lett.* **22** (2000) 137
9. S. S. Khaparde, R. S. Singhal, *Bioresour. Technol.* **78** (2001) 1
10. M. Manning, W. Colon, *Biochemistry* **43** (2004) 11248
11. H. A. Sathish, P. R. Kumar, V. Prakash, *Int. J. Biol. Macromol.* **41** (2007) 383
12. M. M. Bradford, *Anal. Biochem.* **72** (1976) 248
13. B. Raskovic, O. Bozovic, R. Prodanovic, V. Niketic, N. Polovic, *J. Biosci. Bioeng.* **118** (2014) 622
14. G. E. Anthon, D. M. Barrett, *J. Agric. Food Chem.* **50** (2002) 4119
15. G. E. Anthon, Y. Sekine, N. Watanabe, D. M. Barrett, *J. Agric. Food Chem.* **50** (2002) 6153
16. U. K. Laemmli, *Nature* **227** (1970) 680
17. R. Felicioli, B. Garzelli, L. Vaccari, D. Melfi, E. Balestreri, *Anal. Biochem.* **244** (1997) 176
18. S. E. Glassford, B. Byrne, S. G. Kazarian, *Biochim. Biophys. Acta, Protein Struct. Mol. Enzymol.* **1834** (2013) 2849
19. M. D. Byler, H. Susi, *Biopolymers* **25** (1986) 469
20. E. Goormaghtigh, V. Cabiaux, J. M. Ruysschaert, *Eur. J. Biochem.* **193** (1990) 409
21. X. L. Qi, C. Holt, D. McNulty, D. T. Clarke, S. Brownlow, G. R. Jones, *Biochem. J.* **324** (1997) 341
22. D. Ami, A. Natalello, G. Taylor, G. Tonon, S. M. Doglia, *Biochim. Biophys. Acta, Protein Struct. Mol. Enzymol.* **1764** (2006) 793
23. A. A. Ismail, H. H. Mantsch, P. T. T. Wong, *Biochim. Biophys. Acta, Protein Struct. Mol. Enzymol.* **1121** (1992) 183
24. J. Buijs, W. Norde, J. W. T. Lichtenbelt, *Langmuir* **12** (1996) 1605
25. T. H. Lee, S. Y. Lin, *Process Biochem. (Oxford, UK)* **46** (2011) 2163
26. S. Solís-Mendiola, A. Rojo-Domínguez, A. Hernández-Arana, *Biochim. Biophys. Acta, Protein Struct. Mol. Enzymol.* **1203** (1993) 121
27. G. I. Katsaros, P. Katapodis, P. S. Taoukis, *J. Food Eng.* **91** (2009) 42
28. S. Ota, E. Muta, Y. Katahira, Y. Okamoto, *J. Biochem.* **98** (1985) 219
29. B. Kanbar, E. Ozdemir, *Biotechnol. Progress* **26** (2010) 1474
30. W. D. Savage, L. S. Wei, J. W. Sutherland, S. J. Schmidt, *J. Food Sci.* **60** (1995) 164
31. J. K. P. V. Yadav, *J. Biosci.* **34** (2009) 377
32. A. Barth, C. Zscherp, *Q. Rev. Biophys.* **35** (2002) 369
33. F. Meersman, L. Smeller, K. Heremans, *Biophys. J.* **82** (2002) 2635
34. Y. Cordeiro, J. Kraineva, M. C. Suarez, A. G. Tempesta, J. W. Kelly, J. L. Silva, R. Winter, D. Foguel, *Biophys. J.* **91** (2006) 957
35. R. Fosado-Quiroz, A. Rojo-Domínguez, *Protein J.* **30** (2011) 184
36. S. S. Jaswal, J. L. Sohl, J. H. Davis, D. A. Agard, *Nature* **415** (2002) 343.

Journal of the Serbian Chemical Society
JSCS-info@shd.org.rs • www.shd.org.rs/JSCS

J. Serb. Chem. Soc. *80* (5) 627–637 (2015)
JSCS–4743

UDC 547.313.3+547.295.91+547.828:
541.515:620.266.1:616.36:616.853
Original scientific paper

Edaravone, a free radical scavenger, protects liver against valproic acid induced toxicity

NEZIHA HACIHASANOGLU CAKMAK and REFIYE YANARDAG*

Department of Chemistry Faculty of Engineering, Istanbul University,
34320, Avcilar-Istanbul, Turkey

(Received 12 August, revised 10 December, accepted 22 December 2014)

Abstract: Valproic acid (VPA) is a well-established anticonvulsant drug that has been increasingly used in the treatment of many forms of generalized epilepsy. Edaravone (EDA, 3-methyl-1-phenyl-2-pyrazolin-5-one) is a potent free radical scavenger. In this study, the aim was to investigate the effects of EDA on VPA-induced hepatic damage. Male Sprague Dawley rats were divided into four groups. Group I was control animals. Group II was control rats given valproic acid (500 mg kg^{-1} day^{-1}) for seven days. Group III was given only EDA (30 mg kg^{-1} day^{-1}) for seven days. Group IV was given VPA+EDA (at the same dose and in the same time). EDA and VPA were administered intraperitoneally. On the 8th day of the experiment, blood samples and liver tissue were taken. Serum aspartate and alanine aminotransferase, alkaline phosphatase and bilirubin levels, liver myeloperoxidase, xanthine oxidase, adenosine deaminase, Na^+/K^+ATPase, sorbitol dehydrogenase, glutamate dehydrogenase, DT-diaphorase, arginase and thromboplastic activities, lipid peroxidation, protein carbonyl levels were increased whereas paraoxonase and biotinidase activities and glutathione levels were decreased in the VPA group. Application of EDA with VPA protected against VPA-induced effects. These results demonstrated that administration of EDA is potentially beneficial to reduce hepatic damage in VPA-induced hepatotoxicity, probably by decreasing oxidative stress.

Keywords: edaravone; hepatotoxicity; hepatic enzymes; rat; valproic acid; free radicals.

INTRODUCTION

Valproic acid (2-propylpentanoic acid, VPA) is one of the most widely prescribed antiepileptic drugs (AEDs) worldwide, and is also used against migraine, cluster headaches and bipolar psychiatric disorders.[1] In addition, VPA has a wide range of therapeutic applications in many cancer types, including breast

---

* Corresponding author. E-mail: refiyeyanardag@yahoo.com

doi: 10.2298/JSC140812123C

cancer, glioma, acute myelogenous leukemia, thyroid cancer, endometrial carcinoma and neuroblastoma[2] and human immune deficiency virus infection.[3] VPA shows important potential adverse effects, including weight gain, hepatotoxicity, pancreatitis, skin rash, hair loss, antifolate activity, teratogenicity, bone marrow suppression and hyperammononemic encephalopathy.[4–7] One of the most important clinical adverse effects ascribed to VPA therapy is hepatic failure.[6] Various studies showed protection against VPA-induced hepatotoxicity by antioxidants, including α-tocopherol, *N*,*N′*-diphenylphenylenediamine[8] and vitamin U.[9]

Edaravone (3-methyl-1-phenyl-2-pyrazolin-5-one, MCI-186; EDA) is a newly developed free radical scavenger for clinical use that can quench free radical reaction by trapping a variety of free radical species.[10] It can act as a hydroxyl radical scavenger[11,12] and has antioxidant effects against both the hydroxyl radical and iron-dependent lipid peroxidation.[13,14] Several experimental studies reported that EDA may have noteworthy effects on hepatic ischemia – reperfusion injury.[15,16]

The purpose of the present study was to evaluate the ability of EDA to protect hepatic tissue against VPA-induced toxicity.

EXPERIMENTAL

Animals and experimental design

Male Sprague Dawley rats were used in this study. The animals were 2.5–3 months old and clinically healthy. All the experimental procedures were approved by the Istanbul University Local Ethics Committee on Animal Research. The rats were randomly divided into four groups. Group I (n = 8) was intact control animals. Group II (n = 10) was given only VPA (500 mg kg^{-1} day^{-1}) for seven days. Group III (n = 10) was given only EDA (30 mg kg^{-1} day^{-1}) for seven days and lastly, Group IV (n = 10) was given VPA+EDA (at the same dose and in the same time). EDA and VPA were given by intraperitoneally. On the 8th day of the experiment, all of the animals were fasted overnight and then sacrificed under anesthesia. Blood and liver tissue were taken from the animals.

Biochemical assays

In this study, biochemical investigations were made on serum and liver tissues from all groups. Liver tissue samples were washed with 0.9 % saline and kept frozen until the day of the experiments. Serum aspartate (AST) and alanine aminotransferase (ALT) activities were estimated by the Reitman and Frankel methods.[17] Serum alkaline phosphatase (ALP) activity was assayed by two points methods.[18] Serum total and direct bilirubin levels were determined by the method of Jendrassik and Grof.[19] Liver tissues were taken from animals, homogenized in 0.9 % saline to make a 10 % (w/v) homogenate. The homogenates were centrifuged and used for determination of the protein, glutathione (GSH), lipid peroxidation (LPO), protein carbonyl (PC) levels and enzyme activities. GSH levels were determined according to the Beutler method using Ellman’s reagent.[20] LPO levels were estimated by the Ledwozyw method.[21] PC levels were measured by the method of Levine.[22] The myeloperoxidase (MPO) activity was determined according to Wei and Frenkel,[23] paraoxonase (PON1) according to Furlong *et al*.,[24] xanthine oxidase (XO) according to Corte and Stirpe,[25] adenosine deaminase (ADA) according to the Karker method,[26] Na^+/K^+ATPase according to Ridderstap and Bonting,[27] biotinidase according to Wolf *et al.*,[28] sorbitol dehydrogenase (SDH) according to Bergmeyer *et al.*,[29] glutamate dehydrogenase (GLDH) according to Ellis and Goldberg,[30] DT-diaphorase (DTD) according to Ernster *et al.*[31] and arginase according to Geyer and Dabich.[32] The thromboplastic activity (TF) was determined by the method of Ingram and Hills.[33] The protein content in the supernatants was estimated by the Lowry method using bovine serum albumin as standard.[34]

Statistical analysis

The biochemical results were analyzed by one-way ANOVA followed by the Duncan/Newman-Keuls multiple comparison test. The values are expressed as mean ± *SD*. Values of p less than 0.05 were considered significant.

RESULTS

The serum AST, ALT and ALP activities are given in Table I. The serum AST, ALT and ALP activities were significantly increased in the VPA group compared to the control group ($^ap < 0.05$, $^cp < 0.005$, Table I). Administration of EDA significantly decreased the AST, ALT and ALP activities in the VPA group ($^bp < 0.005$, $^dp < 0.05$, Table I). The serum total and direct bilirubin were analyzed to evaluate hepatic injury. The serum total and direct bilirubin were significantly increased in the VPA group as compared to the control group ($^cp < 0.005$, Table I). EDA given to the VPA group lowered the serum total and direct bilirubin levels in a significant manner when compared to the VPA group ($^bp < 0.005$, $^ep < 0.005$, Table I).

TABLE I. Serum aspartate aminotransferase (AST / U L^{-1}), alanine aminotransferase (ALT / U L^{-1}) and alkaline phosphatase (ALP / U L^{-1}) activities and serum total and direct bilirubin levels for all groups; mean±*SD*; $^ap < 0.05$ *vs*. control group, $^bp < 0.005$ *vs*. VPA group; $^cp < 0.005$ *vs*. control group; $^dp < 0.05$ *vs*. VPA group; $^ep < 0.005$ *vs*. VPA group

Group	AST	ALT	ALP	Total bilirubin µmol L^{-1}	Direct bilirubin µmol L^{-1}
Control	144.77±38.72	53.49±17.89	104.28±27.74	5.81±1.48	1.40±0.42
Control+EDA	171.28±36.38	54.12±12.11	125.96±15.61	5.32±1.39	1.35±0.53
VPA	207.57±41.16^a	87.62±19.89^c	177.44±45.11^c	11.27±3.48^c	2.49±0.61^c
VPA+EDA	148.57±27.81^b	59.54±9.47^b	108.77±42.63^d	5.64±1.93^b	1.33±0.62^e
p_{ANOVA}	0.004	0.001	0.002	0.0001	0.001

Hepatic glutathione (GSH), lipid peroxidation (LPO) and protein carbonyl (PC) levels are presented in Table II. The GSH levels were significantly decreased in the VPA group ($^ap < 0.05$). Administration of EDA significantly protected against the reduction in GSH levels in the EDA-treated VPA (VPA+EDA) group in comparison to the VPA group ($^bp < 0.05$, Table II). Hepatic LPO and PC levels were significantly increased in the VPA group compared to control group ($^ap < 0.05$). Administration of EDA showed significant protection against oxidation in the LPO and PC levels in the EDA-treated VPA group compared to the VPA group ($^bp < 0.05$, Table II). The MPO activity in the hepatic tissue was significantly elevated in the VPA group. This can demonstrate enhanced infiltration of neutrophils to the hepatic tissue (${}^{c}p < 0.0005$). Administration of EDA significantly decreased the hepatic MPO levels (${}^{d}p < 0.0005$) in the VPA group. The hepatic PON activity was significantly decreased in the VPA group (${}^{e}p < 0.005$). EDA inhibited these decreases significantly (${}^{b}p < 0.05$, Table II).

TABLE II. Liver glutathione (GSH / nmol mg^{-1} prot.), lipid peroxidation (LPO nmol MDA mg^{-1} prot.) and protein carbonyl (PC / nmol mg^{-1} prot.) levels and myeloperoxidase (MPO / U g^{-1} tissue) and paraoxonase (PON / mU mg^{-1} prot.) activities for all groups; mean±*SD*; ${}^{a}p < 0.05$ *vs*. control group, ${}^{b}p < 0.05$ *vs*. VPA group; ${}^{c}p < 0.0005$ *vs*. control group; ${}^{d}p < 0.0005$ *vs*. VPA group; ${}^{e}p < 0.005$ *vs*. VPA group

Group	GSH	LPO	PC	MPO	PON
Control	33.31±7.6	0.75±0.26	1.91±1.08	0.67±0.085	9.03±0.50
Control+EDA	36.61±8.77	0.86±0.51	2.50±1.34	0.62±0.0067	10.18±3.13
VPA	24.14±4.88^{a}	2.38±1.26^{a}	4.96±2.51^{a}	0.83±0.0051^{c}	6.54±1.48^{e}
VPA+EDA	33.60±6.94^{b}	0.86±0.54^{b}	1.88±0.92^{b}	0.65±0.10^{d}	12.31±4.66^{b}
p_{ANOVA}	0.017	0.001	0.003	0.0001	0.029

The hepatic XO and ADA activities were significantly increased in the VPA group (${}^{a}p < 0.005$, ${}^{c}p < 0.05$, Table III). Administration of EDA significantly decreased the hepatic XO and ADA activities (${}^{b}p < 0.05$, Table III). The activity of Na^{+}/K^{+}ATPase, indicating the functional transport capacity of the hepatic cells, was increased in the VPA group compared with control group (${}^{c}p < 0.05$). However the EDA-treated VPA group had significantly decreased hepatic Na^{+}/K^{+}ATPase activity (${}^{d}p < 0.005$, Table III). Hepatic biotinidase activity was significantly decreased in the VPA group as compared to the control group (${}^{a}p < 0.005$), whereas biotinidase activity in the hepatic tissue was significantly increased in the EDA-treated VPA group as compared with VPA group (${}^{b}p < 0.05$, Table III). Hepatic SDH was significantly increased in the VPA groups as compared to the controls (${}^{a}p < 0.005$). On the other hand, EDA administration to the VPA group resulted in a significant decrease in SDH activity in comparison to the VPA group (${}^{e}p < 0.005$, Table III).

TABLE III. Liver xanthine oxidase (XO / mU mg^{-1} prot.), adenosine deaminase (ADA / mU mg^{-1} prot.), sodium potassium ATPase (Na^{+}/K^{+}ATPase, µmol P mg^{-1} prot., 10 min), biotinidase (nmol min mg^{-1} prot.) and sorbitol dehydrogenase (SDH / mU mg^{-1} prot.) activities for all groups; mean±*SD*; ${}^{a}p < 0.005$ *vs*. control group, ${}^{b}p < 0.05$ *vs*. VPA group; ${}^{c}p < 0.05$ *vs*. control group; ${}^{d}p < 0.005$ *vs*. VPA group; ${}^{e}p < 0.005$ *vs*. VPA group

Group	XO	ADA	Na^{+}/K^{+}ATPase	Biotinidase	SDH
Control	1.81±0.51	2.31±0.66	0.159±0.052	0.035±0.006	0.938±0.311
Control+EDA	3.16±1.91	10.18±1.13	0.129±0.041	0.031±0.011	0.960±0.158
VPA	6.71±3.75^{a}	5.09±3.03^{c}	0.298±0.160^{c}	0.022±0.006^{a}	3.86±2.11^{a}
VPA+EDA	3.20±2.43^{b}	2.40±0.88^{b}	0.126±0.053^{d}	0.034±0.012^{b}	1.30±0.73^{e}
p_{ANOVA}	0.001	0.003	0.001	0.003	0.0001

The hepatic GLDH, DTD and arginase activities were significantly increased in VPA group compared to control group ($^a p < 0.05$, $^c p < 0.005$). EDA significantly decreased the GLDH, DTD and arginase activities in the VPA groups as compared with the VPA group ($^b p < 0.05$, $^d p < 0.005$, Table IV). The TF activity was increased in the VPA group ($^a p < 0.05$) but was significantly decreased by EDA administration ($^b p < 0.05$, Table IV).

TABLE IV. Liver glutamate dehydrogenase (GLDH/mU mg^{-1} prot.), DT-diaphorase (nmol min mg^{-1} prot.), arginase (μmol urea mg^{-1} prot.) and thromboplastic activities (TF/s) for all groups; mean±*SD*; $^a p < 0.05$ *vs*. control group, $^b p < 0.05$ *vs*. VPA group; $^c p < 0.005$ *vs*. control group; $^d p < 0.005$ *vs*. VPA group

Group	GLDH	DT-Diaphorase	Arginase	TF
Control	0.25 ± 0.09	5.55 ± 1.76	0.42 ± 0.14	209.63 ± 91.19
Control+EDA	0.31 ± 0.014	6.41 ± 2.21	0.47 ± 0.20	196.10 ± 51.74
VPA	1.085 ± 0.748^a	11.89 ± 2.99^c	0.87 ± 0.43^a	121.40 ±27.52^a
VPA+EDA	0.483 ± 0.323^b	7.19 ± 2.91^d	0.53± 0.24^b	172.10 ±51.80^b
p_{ANOVA}	0.0001	0.0001	0.012	0.012

DISCUSSION

One of the most sensitive and dramatic indicators of hepatocyte injury is the release of intracellular enzymes, such as AST, ALT and ALP. The increase in the activities of these enzymes in serum during VPA administration, is thus indicative of hepatocellular damage.[35] In this study, treatment with EDA significantly reversed the alterations in the status of these enzymes to normal levels, probably due to its highly effective free radical scavenger activity,[36] thus, maintaining the hepatocellular membrane integrity.

Serum bilirubin is a potential marker for hepatic dysfunction and any abnormal increase in the levels of bilirubin in serum denotes hepatobiliary disease and hepatocellular dysfunction.[37] In the present study, the elevated levels of bilirubin observed in the VPA group corresponded to extensive hepatic damage. Its accumulation is a measure of binding, conjugation and excretory capacity of hepatocytes.[38] Recent reports showed that EDA exhibits excellent efficacy in both hepatic ischemia–reperfusion and acute hepatic injury in rat models.[39] Accordingly, in this study, EDA prevented the increases of the total and direct bilirubin levels.

It is well known that GSH is involved in the protection of normal cellular structure and function by maintaining redox homeostasis, quenching free radicals, and participating in detoxification reactions. Several studies reported the implication of an increased generation of free radicals and oxidative stress in the toxic mechanism of VPA.[40,41] The present study showed significantly decreased levels of GSH in the liver of VPA treated rats, as compared to the control. This decrease in GSH level may be due to increased utilization of GSH to scavenge toxic intermediates. Administration of EDA significantly increased the hepatic GSH levels in the group given VPA, showing a protective effect.

LPO results from excessive reactive oxygen species (ROS) and it was shown that VPA induced LPO production in rat hepatocyte cultures.[8,42] Tong *et al*.[40] reported that hepatic LPO levels were elevated on day 14 in VPA therapy. Another study demonstrated that a single dose of VPA in rats leads to an elevation in plasma and liver of the endogenous lipid peroxidation marker.[43] According to the present study, VPA increased LPO levels of liver compared with the control group. Similar to this result, Sokmen *et al*. reported significantly increased hepatic LPO levels in VPA treated rats.[9] However administration of EDA prevented these changes.

PC levels are the most commonly used markers of protein oxidation.[44] There is increasing evidence for the involvement of toxic carbonyls in numerous human diseases.[45] The present study showed the PC levels were significantly increased. The increased production of PC indexed the enhanced oxidative stress caused by VPA. EDA prevented the enhancement of the PC levels and restored the liver cells to their normal physiological state.

When neutrophils are stimulated by various stimulants, MPO, as well as other tissue-damaging substances, is released from these cells.[46] In the present study, VPA treatment caused significant increases in hepatic MPO activity. These results suggested that VPA induced neutrophil-dependent oxidative damage. EDA inhibited oxidative injury and decreased MPO activities. The protective effect of EDA on hepatic injury was mediated in part by blocking tissue neutrophil infiltration.

PON1 is another antioxidant enzyme closely associated with high-density lipoproteins. It is a calcium-dependent esterase that detoxifies lipid peroxides, and is widely distributed in many tissues, including liver, brain, lung, heart, kidneys and small intestines.[47] Increased oxidative stress was shown to reduce PON1 synthesis *in vivo* and *in vitro*.[48] Varoglu *et al*.[49] demonstrated that serum PON1 activity was decreased in epileptic patients rather than in the control subjects. In another study, the administration of vitamin U significantly increased hepatic PON1 activity in rats treated with VPA.[9] In the present study, PON1 activity was significantly lower in the VPA group. The decrease in PON1 activity is directly related to the degree of hepatic damage. Administration of EDA significantly increased hepatic PON1 activity in rats treated with VPA.

XO is one of the most important enzyme sources of the superoxide radical and catalyses the conversion of hypoxanthine and xanthine to uric acid. It is a major potential source of ROS. Free radical generation by mediation of XO enzyme in tissue is triggered by a large increase in the formation of its substrates inosine and hypoxanthine.[50] The present study showed that VPA administration increases XO activity in rat liver. This increase in XO activity on VPA treatment may enhance the generation of ROS and may partly be responsible for the increased lipid peroxidation and oxidative injury. However, EDA treatment may prevent hepatotoxicity by decreasing XO activity.

ADA catalyzes the irreversible deamination of adenosine and deoxyinosine to inosine and deoxyinosine respectively.[51] It was reported that ADA has an important role in acute immune inflammatory reactions, and its serum level has been used as a biochemical marker for inflammation and disease.[52] A recent study showed that VPA administration increased ADA activity in rat liver.[9] In the VPA group, in the present study, elevated hepatic ADA activity indicated hepatic damage. Additionally, the reduced ADA activity in the VPA plus EDA group showed significant improvement in the hepatic tissue.

ATPases are lipid-dependent enzymes involved in active transport processes and have been implicated in the pathogenesis of hepatic cell injury.[53] Enhanced susceptibility of membranes to oxidative stress can lead to loss of protein thiol, thereby changing the functions of membrane.[54] In the present study, increased hepatic Na^+/K^+ATPase activity was observed in VPA-supplemented rats. It was originally postulated that the increase in Na^+/K^+ATPase in the liver after VPA administration was due to increased oxidative phosphorylation and oxygen consumption to supply ATP for ATPase activity. On administering EDA, the $Na^+/$ $/K^+$ATPase activity was significantly decreased in hepatic tissue.

Biotinidase is synthesized mainly by the liver and then secreted into the blood[55] and is decreased in the plasma of both humans and experimental animals with hepatic cirrhosis. Pispa[56] noted a 50 % decrease in biotinidase activity, and a 30 % decrease in serum activity of partially hepatectomized rats. Nagamine *et al*.[57] implicated biotinidase deficiency in chronic hepatic disease. It was reported in several studies that chronic VPA use could alter the biotinidase enzyme activity in humans[58] and rats.[59] The decrease in the liver biotinidase activity may be due to the inhibition of the biosynthetic and secretory capacity of the liver after administration of a toxic dose of VPA. The present study showed that VPA administration decreased the biotinase activity in rat liver. In our study, administration of EDA significantly increased liver biotinidase activity in rats treated with VPA, showing again a restoration in hepatic tissue.

SDH catalyzes the conversion of sorbitol to fructose in the presence of NAD. SDH is a specific indicator of hepatocellular injury in rodents and has a reported value in humans.[60] In the present study, hepatic SDH activity was increased due to liver injury. The increased activities of SDH are a sensitive index of hepatic injury as demonstrated in rats intoxicated with VPA. However, EDA treatment significantly decreased the SDH activity. A decrease of liver SDH activity indicates improvement of hepatic injury.

GLDH, a key enzyme in amino acid oxidation and urea production, has several features that make it attractive as a potential biomarker of drug-induced hepatocellular toxicity.[61] Cotariu *et al.*[35] showed that VPA induces dose-dependent changes in the hepatic GLDH activity. In this study, the GLDH activity was increased depending on the liver injury induced by VPA. Elevations in GLDH activity could be the result of enzyme release from cellular membranes due to hepatocellular necrosis. EDA treatment significantly decreased the enzymatic activity and thus prevented the hepatic injury.

DTD is a cytosolic enzyme that is localized mainly in the liver, kidney and gastrointestinal tract.[31] DTD, which is a flavoprotein, catalyzes the two-electron reduction and detoxification of quinones and their derivatives.[62] DTD protein forms homodimers and reduces quinones to hydroquinones in a way that prevents the one electron reduction of quinones, which results in the production of ROS. An increase in the activity of DTD may also correspond to an increase in oxidative stress. In the present study, VPA increased the activity of DTD, suggesting a response to increased oxidative stress. EDA treatment normalized the DTD activity.

Arginase is highly liver specific making it a candidate biomarker that shows higher specificity compared to the hepatic enzymes.[63] Arginase activity was reported to be increased in chronic hepatic damage by thioacetamide.[64] In the present study, there was an increase in the activity of arginase in the liver of the VPA group. Administration of EDA restored the arginase activity to a normal level in the hepatic tissue, indicating an improving effect in hepatic injury.

TF is an important coagulation factor that initiates extrinsic blood coagulation with FVII. It is a cell membrane component, and its activity was measured by the prothrombin time test.[65] Shortened clot formation time indicates increased TF activity that could easily be changed by alterations in the membrane composition or lipid peroxidation composition of the membrane due to oxidative stress.[66–68] In the present study, VPA-induced injury increased the TF activity in the hepatic tissue. This increase could be attributed to inflammation of the hepatic membrane. Anti-inflammatory effects of EDA were previously reported.[69,70] EDA treatment reversed the increased TF activity in the liver of rat receiving VPA therapy, due to the anti-inflammatory effect of EDA.

EDA has potent hydroxyl radical scavenging activity. In various experimental models, EDA was reported to protect several organs, such as the brain, heart[71] and liver[72] from free radical-mediated injuries.

This is the first study that evaluates the protective effects of EDA against VPA-induced hepatic damage in experimental animals. In conclusion, the results indicate that VPA-induced hepatotoxicity is associated with increased oxidative stress. EDA shows protection against this damage. The protective effect of EDA observed in the present study is due to the scavenging of free radicals. Therefore, it is suggested that EDA could be potentially useful for the prevention of hepatic toxicity during epileptic disease.

ИЗВОД

ЕДАРАВОН ШТИТИ ЈЕТРУ ОД ТОКСИЧНОГ ДЕЈСТВА ВАЛПРОИНСКЕ КИСЕЛИНЕ УКЛАЊАЈУЋИ СЛОБОДНЕ РАДИКАЛЕ

NEZIHA HACIHASANOGLU CAKMAK и REFIYE YANARDAG

Department of Chemistry, Faculty of Engineering, Avcilar-Istanbul University, Turkey

Валпроинска киселина (VPA) је добро познати антиконвулзивни лек који се користи за терапију епилепсије, а едаравон (EDA, 1-фенил-3-метил-2-пиразолин-5-он) је потентан хватач слободних радикала. У овом раду је испитиван ефекат EDA на јетру оштећену применом VPA. Пацови мушког пола су подељени у четири групе. Групу I су чиниле контролне животиње. Пацовима у групи II је давана VPA (500 mg kg^{-1} по дану) током седам дана. Животињама у групи III је даван само EDA (30 mg kg^{-1} по дану) током седам дана. Пацовима у групи IV је комбиновано давано VPA+EDA (у дозама и временском периоду као и осталима). EDA и VPA су уношени интраперитонеално. Осмог дана од почетка експеримента, животињама су вађени узорци крви и јетре. Концентрације или активности следећих параметара су биле повећане у групи II: а) серумска аспартат- и аланин-аминотрансфераза, алкална фосфатаза и билирубин, као и б) јетрена мијелопероксидаза, ксантин-оксидаза, аденозин-деаминаза, Na^+/K^+ATPаза, сорбитол-дехидрогеназа, глутамат-дехидрогеназа, ДТ-дијафораза, аргиназа, тромбопластична активност, липидни пероксиди и протеински карбонили. Истовремено су смањене активности параоксоназе и биотинидазе, као и концентрација глутатиона. Применом EDA омогућена је заштита од ефеката VPA. Ови резултати указују да је коришћењем EDA могуће умањити оштећење јетре индуковано применом VPA, вероватно преко смањења оксидативног стреса.

(Примљено 12. августа, ревидирано 10. децембра, прихваћено 22. децембра 2014)

REFERENCES

1. C. U. Johannessen, S. I. Johannessen, *CNS Drug Rev.* **9** (2003) 199
2. M. Berretta, F. Di Benedetto, L. Dal Maso, B. Cacopardo, G. Nasti, G. Facchini, A. Bearz, M. Spina, E. Garlassi, V. De Re, F. Fiorica, A. Lleshi, U. Tirelli, *Anti-Cancer Drugs* **24** (2012) 212
3. G. Lehrman, I. B. Hogue, S. Palmer, C. Jennings, C. A. Spina, A. Wiegand, A. L. Landay, R. W. Coombs, D. D. Richman, J. W. Mellors, J. M. Coffin, R. J. Bosch, D. M. Margolis, *Lancet* **366** (2005) 549
4. S. J. Wallace, *Drug Saf.* **15** (1996) 378
5. J. H. Lewis, H. J. Zimmerman, C. T. Garrett, E. Rosenberg, *Hepatology* **2** (1982) 870
6. E. Perucca, *Epilepsy Res.* **52** (2002) 25
7. E. Perucca, *CNS Drugs* **16** (2002) 695
8. K. N. Buchi, P. D. Gray, D. E. Rollins, K. G. Tolman, *J. Clin. Pharmacol.* **24** (1984) 148
9. B. B. Sokmen, S. Tunali, R. Yanardag, *Food Chem. Toxicol.* **50** (2012) 3562
10. H. Yoshida, K. Sasaki, Y. Namiki, N. Sato, N. Tada, *Atherosclerosis* **179** (2005) 97
11. A. Mizuno, K. Umemura, M. Nakashima, *Gen. Pharmacol.* **30** (1998) 575
12. S. Arumugam, R. A. Thandavarayan, P. T. Veeraveedu, T. Nakamura, W. Arozal, F. R. Sari, V. V. Giridharan, V. Soetikno, S. S. Palaniyandi, M. Harima, K. Suzuki, M. Nagata, M. Kodama, K. Watanabe, *J. Cell Mol. Med.* **16** (2012) 2176
13. T. Watanabe, S. Yuki, M. Egawa, H. Nishi, *J. Pharmacol. Exp. Ther.* 2**68** (1994) 1597
14. H. Yagi, S. Horinaka, H. Matsuoka, *J. Cardiovasc. Pharmacol.* **46** (2005) 46

15. T. Abe, M. Unno, H. Takeuchi, T. Kakita, Y. Katayose, T. Rikiyama, T. Morikawa, M. Suzuki, S. Matsuno, *J. Gastrointest. Surg.* **8** (2004) 604
16. M. Ninomiya, M. Shimada, N. Harada, S. Shiotani, S. Hiroshige, Y. Soejima, T. Suehiro, K. Sugimachi, *Transplantation* **74** (2002) 1470
17. S. Reitman, S. Frankel, *Am. J. Clin. Pathol.* **28** (1957) 56
18. K. Walter, C. Schutt, in *Methods of enzymatic analysis*, Vol. 2, H. U. Bergmeyer Ed., Verlag Chemie, Boca Raton, FL, 1974, p. 856
19. L. Jendrassik, P. Grof, *Biochem.* **297** (1938) 82
20. E. Beutler, *Red cell metabolism*: *A manual of biochemical methods*, Grune and Stratton, New York, 1975, p. 67
21. A. Ledwozyw, W. I. Michalak, A. Stepien, A. Kadziolka, *Clin. Chim. Acta* **155** (1986) 275
22. R. L. Levine, D. Garland, C. N. Oliver, A. Amici, I. Climent, A. G. Lenz, B. W. Ahn, S. Shaltiel, E. R. Stantman, *Methods Enzymol.* **186** (1990) 464
23. H. Wei, K. Frenkel, *Cancer Res.* **51**(1991) 4443
24. C. E. Furlong, R. J. Richter, S. J. Seidel, *Am. J. Hum. Genet*. **43** (1988) 230
25. D. E. Corte, F. Stirpe, *Biochem. J.* **108** (1968) 349
26. H. Karker, *Scand. J. Clin. Lab. Invest.* **16** (1964) 570
27. A. S. Ridderstap, S. L. Bonting, *Am. J. Physiol.* **217** (1969) 1721
28. B. Wolf, J. Hymes, G. S. Heard, *Methods Enzymol*. **184** (1990) 103
29. H. U. Bergmeyer, M. Grassi, H. E. Walter, *Methods of enzymatic analysis*, 3rd ed., Vol. 2, VCH, Weinheim, 1983, p. 309
30. G. Ellis, D. M. Goldberg, *Clin. Chem.* **18** (1972) 523
31. L. Ernster, L. Danielson, M. Ljunggren, *Biochim. Biophys. Acta* **58** (1962) 171
32. J. W. Geyer, D. Dabich, *Anal. Biochem*. **39** (1971) 412
33. G. I. C. Ingram, M. Hills, *Thromb. Haemostasis* **36** (1976) 237
34. O. H. Lowry, N. J. Rosebrough, A. L. Farr, R. J. Randall, *J. Biol. Chem.* **193** (1951) 265
35. D. Cotariu, S. Evans, J. L. Zaidman, *Enzyme* **34** (1985) 196
36. V. Yamamoto, T. Kuwahara, K. Watanabe, *Redox Rep.* **2** (1996) 333
37. P. Martin, L. S. Friedman, in *Handbook of liver disease*, Vol. 1–14, L. S. Friedman, E. B. Keefe, Eds., Churchill Livingstone, Philadelphia, PA, 1992
38. D. Nandi, R. C. Patra, D. Swarup, *Food Chem. Toxicol*. **44** (2006) 1579
39. K. Tsuji, A. H. Kwon, H. Yoshida, Z. Qiu, M. Kaibori, T. Okumura, Y. Kamiyama, *J. Hepatol.* **42** (2005) 94
40. V. Tong, X. W. Teng, T. K. Chang, F. S. Abbott, *Toxicol. Sci.* **86** (2005) 427
41. E. N. Defoort, P. M. Kim, L. M. Winn, *Mol. Pharmacol.* **69** (2006) 1304
42. M. Jurima-Romet, F. S. Abbott, W. Tang, H. S. Huang, L. W. Whitehouse, *Toxicology* **112** (1996) 69
43. V. Tong, X. W. Teng, S. Karagiozov, T. K. Chang, F. S. Abbott, *Free Rad. Biol. Med.* **38** (2005) 1471
44. E. R. Stadtman, R. L. Levine, *Ann. N. Y. Acad. Sci.* **899** (2000) 191
45. B. S. Berlett, E. R. Stadtman, *J. Biol. Chem.* **272** (1997) 20313
46. A. J. Kettle, C. C. Winterbourn, *Redox Rep,* **3** (1997) 3
47. M. Senti, M. Tomas, M. Fito, T. Weinbrenner, M. Covas, J. Sala, R. Masia, J. Marrugat, *J. Clin. Endocrinol. Metab.* **88** (2008) 5422
48. O. Rozenberg, M. Aviram, *Biochem. Biophys. Res. Commun.* **351** (2006) 92
49. A. O. Varoglu, A. Yildirim, R. Aygul, O. L. Gundogdu, Y. N. Sahin, *Clin. Pharmacol.* **33** (2010) 155

50. D. A. Parks, D. N. Granger, *Acta Physiol. Scand. Suppl*. **548** (1986) 87
51. G. Cristalli, S. Costanzi, C. Lambertucci, G. Lupidi, S. Vittori, R. Volpini, E. Camaioni, *Med. Res. Rev*. **21** (2001) 105
52. R. A. Sari, S. Tays, O. Yilmaz, N. Bakan, *Clin. Exp. Rheumatol.* **21** (2003) 87
53. M. F. Rahman, M. K. Siddiqui, K. Jamil, *Ecotoxicol. Environ. Saf.* **47** (2000) 125
54. M. Adhirai, R. Selvam, *Jpn. J. Med. Sci. Biol.* **50** (1997) 9
55. R. E. Grier, G. S. Heard, P. Watkins, B. Wolf, *Clin. Chim. Acta* **186** (1990) 397
56. J. Pispa, *Ann. Med. Exp. Biol. Fenn.* **43** (1965) 1
57. T. Nagamine, S. Saito, S. Yamada, T. Arai, K. Takehara, T. Fukui, *Scand. J. Gastroenterol.* **28** (1993) 899
58. Y. Yilmaz, H. A. Tasdemir, M. S. Paksu, *Eur. J. Pediatr. Neurol.* **13** (2009) 439
59. N. Korkmazer, S. Vurucu, E. Demirkaya, B. Unay, M. Kul, R. Akin, E. Gokçay, *Brain Dev*. **28** (2006) 515
60. A. A. Khayrollah, Y. Y. Al-Tamer, M. Taka, L. Skursky, *Ann. Clin. Biochem.* **19** (1982) 35
61. P. J. O'Brien, M. R. Slaughter, S. R. Polley, K. Kramer, *Lab. Anim.* **36** (2002) 313
62. R. J. Riley, P. Workman, *Biochem. Pharmacol.* **43** (1992) 1657
63. F. Ashamiss, Z. Wierzbicki, A. Chrzanowska, D. Scibior, M. Pacholczyk, M. Kosieradzki, B. Lagiewska, Z. Porembska, W. Rowinski, *Ann. Transplant.* **9** (2004) 58
64. H. Murayama, M. Ikemoto, Y. Fukuda, S. Tsunekawa, A. Nagata, *Clin. Chim. Acta* **375** (2007) 63
65. F. Isik, T. Tunali Akbay, A. Yarat, Z. Genc, R. Pisiriciler, E. Caliskan-Ak, S. Cetinel, A. Altıntas, G. Sener, *Dig. Dis. Sci*. **56** (2011) 721
66. E. Bachlie, *Br. J. Haematol*. **110** (2010) 248
67. S. Danese, A. Papa, S. Saibeni, A. Repici, A. Malesci, M. Vecchi, *Am. J. Gastroenterol*. **102** (2007) 174
68. C. Anthoni, J. Russell, K. C. Wood, K. Y. Stokes, T. Vowinkel, D. Kirchhofer, D. N. Granger, *J. Expl. Med.* **204** (2007) 1595
69. T. Yang, Y. F. Mao, S. Q. Liu, J. Hou, Z. Y. Cai, J. Y. Hu, X. Ni, X. M. Deng, X. Y. Zhu, *Eur. J. Pharmacol*. **630** (2010) 152
70. S. Tajima, M. Soda, M. Bando, M. Enomoto, H. Yamasawa, S. Ohno, T. Takada, E. Suzuki, F. Gejyo, Y. Sugiyama, *Respirology* **13** (2008) 646
71. T. W. Wu, L. H. Zeng, J. Wu, K. P. Fung, *Life Sci*. **71** (2002) 2249
72. Y. Okatani, A. Wakatsuki, H. Enzan, Y. Miyahara, *Eur. J. Pharmacol*. **465** (2003) 163.

Journal of the Serbian Chemical Society
JSCS-info@shd.org.rs • www.shd.org.rs/JSCS

J. Serb. Chem. Soc. 80 (5) 639–649 (2015)
JSCS–4744

UDC 547.233’821+546.96+547.544:
57–188:615.281
Original scientific paper

A study on tailor made ruthenium sulphoxide complexes: Synthesis, characterization and application

RIPUL MEHROTRA*•, SATYENDRA N. SHUKLA and PRATIKSHA GAUR

Coordination Chemistry Research Lab, Department of Chemistry, Govt. Model Science College Jabalpur (MP) 482001, India

(Received 4 July, revised 11 August, accepted 31 August 2014)

Abstract: In this study, a dinucleating spacer incorporating two 2-aminopyridine units was used to prepare seven novel dinuclear compounds. These molecules were characterized by elemental analyses, conductivity measurements, magnetic susceptibility, FT-IR, FAB-Mass, electronic, ^{1}H-NMR and ^{13}C{^{1}H}-NMR spectral studies. The complex [{*trans,mer*-RuCl$_2$(DMSO)$_3$}$_2$(μ-5,5′-methylenebis(2-aminopyridine))]·2DMSO (**2**) was also characterized through ^{1}H-^{1}H COSY NMR. There are mainly three different formulations, [{*cis,fac*-RuCl$_2$(SO)$_3$}$_2$(μ-MBAP)]·2SO; [{*trans,mer*-RuCl$_2$(SO)$_3$}$_2$(μ-MBAP)]·2SO and [{*trans*-RuCl$_4$(SO)}$_2$(μ-MBAP)]$^{2-}$ [X]$_2$$^+$; where SO = DMSO / TMSO; MBAP = 5,5′-methylenebis(2-pyridinamine) and [X]$^+$ = [(DMSO)$_2$H]$^+$, Na$^+$ or [(TMSO)H]$^+$. The coordination was found through cyclic nitrogen of the pyridine ring in an octahedral environment for both metal centres. The chemical behaviour of [{*cis,fac*-RuCl$_2$(DMSO)$_3$}$_2$(μ-5,5′-methylenebis(2-pyridinamine))]·2DMSO (**1**) and (**2**) in aqueous solution with respect to time was observed by conductivity measurements and UV–Vis spectrophotometry. All complexes were found to possess prominent antibacterial activity against *Escherichia coli* in comparison to chloramphenicol and gatifloxacin.

Keywords: 2-aminopyridine; antibacterial; dinuclear; ruthenium; spacer; sulphoxide.

INTRODUCTION

Metal complexes were found valuable for the design and development of synthetic restriction enzymes and new drugs because of their ability to bind with DNA.[1] In the past decade, ruthenium complexes have generated interest due to their potential application as chemotherapeutic agents.[2] Several ruthenium compounds were proven to have antitumour activity.[3–6] After introduction of two

---

* Corresponding author. E-mail: ripul.mehrotra@gmail.com

• Present Address: Department of Chemistry and Polymer Science, Stellenbosch University, Private Bag X1, Matieland, 7602, South Africa.

doi: 10.2298/JSC140704086M

ruthenium compounds [indH] *trans*-[$RuCl_4(ind)_2$] (ind = indazole, KP1019) and [imH] *trans*-[$RuCl_4$(DMSO-*S*)(im)] (im = imidazole, NAMI-A), into clinical trials,[7,8] substantial attraction explored this field and a number of mononuclear analogue with different *N*-containing heterocyclic ligands were synthesized and tested for their *in vitro* antimicrobial and antitumour activity.[9–12]

As well as mononuclear analogues, dinuclear compounds have also been recognized with increased size, variety of molecular shapes and consisting of two discrete metal centres connected *via* a spacer of various lengths, type and composition.[13–18] The rational design and synthesis of new compounds with an organized molecular framework and functional feature is the major goal of a researcher. 2-Aminopyridine, functionally closed in biological systems and also able to form self-complementary intermolecular interactions, was chosen. The compounds bearing two 2-aminopyridyl moieties separated by linkers of different shapes and lengths (devoid any other functionality) might give a new look to synthesized molecules.[19] These findings suggested the preparation of 5,5′-methylenebis(2-aminopyridine) [MBAP],[20] with the anticipation of some noteworthy contribution. Thus, the aim of the present study was to synthesize and characterize dinuclear ruthenium sulphoxide complexes with the anticipation of a better pharmacological conclusion.

EXPERIMENTAL

$RuCl_3\cdot 3H_2O$ (Merck), 2-aminopyridine (Himedia, India), tetramethylenesulphoxide (TMSO, Lancaster, UK) and Muller Hinton agar (Himedia) were used as received. Analytical grade dimethyl sulphoxide (DMSO, Merck), formaldehyde (Merck) and routine solvents were used for synthetic purposes without further purification.

Instrumentation

The electronic absorption spectra were recorded with a Shimadzu-1700 UV–Vis spectrophotometer equipped with a PC. Conductivity measurements were realised at 25 °C using an EI-181 conductivity bridge with a dipping type cell. The FT-IR spectra were recorded in KBr pellets on a Shimadzu-8400 PC, FT-IR spectrophotometer in the 4000–400 cm^{-1} range and the far-IR spectra of the complexes were recorded using polyethylene pellets in the 500–100 cm^{-1} region on a Nicolet Mega-550 FT-IR instrument. The ^1H-, ^{13}C- and ^1H––^1H COSY NMR spectra were recorded in D_2O on a Bruker Avance-400 NMR spectrometer. The Gouy's method was employed for the measurements of magnetic susceptibility. Hg[$Co(NCS)_4$] was used as a standard. Diamagnetic correction was made using the Pascal constant. Elemental analyses (CHN) were performed on an Elementra Vario EL III elemental analyzer. FAB-MS spectra were recorded on Jeol SX-102 mass spectrometer.

Preparation of the complexes

Appropriate quantities of precursor ([*cis*,*fac*-$RuCl_2$(*S*-DMSO)$_3$(*O*-DMSO)] (**1a**),[21] [*trans*-$RuCl_2$(DMSO-*S*)$_4$] (**2a**),[4] [$(DMSO)_2H]^+$ [*trans*-Ru(DMSO-*S*)$_2Cl_4]^-$ (**3a**)[5] or Na^+[*trans*--Ru(DMSO-*S*)$_2Cl_4]^-$ (**4a**)[5] was dissolved in the minimum volume (≈ 0.2 mL) of DMSO, or [*cis*-$RuCl_2$(TMSO-*S*)$_4$] (**5a**),[22] [*trans*-$RuCl_2$(TMSO-*S*)$_4$] (**6a**)[22] or $[(TMSO)H]^+$ [*trans*--Ru(TMSO-*S*)$_2Cl_4]^-$ (**7a**)[22] in TMSO (≈0.2 mL) and was mixed with a solution of MBAP in acetone (10 mL) in a 1:1 ratio. The reaction mixture was stirred at room temperature for 3 h, followed by the addition of another mole of precursor (dissolved in ≈0.2 mL DMSO/TMSO). The reaction mixture was kept under reflux for 3–12 h. The volatile fraction was allowed to evaporate under vacuum and the obtained solids were washed with acetone / diethyl ether (1:2, *V*/*V*) solvent mixture. The impure product was re-crystallized by vapour diffusion of diethyl ether into a DCM solution at room temperature to afford yellow solids. The products were isolated by filtration, washed with diethyl ether and vacuum dried.

In vitro *antibacterial activity*

The complexes **1**–**7**, their precursors **1a**–**7a** and MBAP were screened for antibacterial properties against *Escherichia coli* MTCC 1304 at a concentration 2.5 μg mL^{-1} in water by the agar well diffusion method as described by Mehrotra *et al.*[23] In brief, overnight grown bacterial cells (≈ 10^5 colony forming unit) were spread on Mueller–Hinton (MH) agar plates using a sterile cotton swab. Uniform wells (diameter of 6.0 mm) were created in the agar slab by using a cork borer. 50 μL of test and control solutions were placed in respective wells. Solutions, 0.25 μg mL^{-1} of chloramphenicol (CM) and gatifloxacin (GT) were used as positive controls and MBAP in water as the negative control. All plates were incubated at 37 °C for 48 h followed by 4 °C incubation for 20 min. All plates were observed for the zone of inhibition.

*Minimum inhibitory concentration (*MIC*) determination*

The *MIC* values for complexes **1**–**7** were determined against *E. coli*. The successive dilution method reported by Mehrotra *et al.*[24] was used for *MIC* evaluation. In brief, the complexes were serially diluted to 25.0–0.0 μg mL^{-1} in MH broth. The 5.7log (number of cells) were inoculated in respective dilutions. All the tubes were incubated at 37 °C for 24 h. The *MIC* was considered as concentrations of higher dilution tube in which bacterial growth was absent.

Statistical analysis

Statistical analysis was performed by one-way analysis of variance (ANOVA) using GraphPad Prism 6 (version 6.04 (Trial) for Windows; GraphPad Software, Inc., CA). Differences were considered statistically significant at P values < 0.05.

RESULTS AND DISCUSSION

Synthesis and physiochemical characterization

The complexes **1**–**7** were obtained through tailored synthesis. The reaction was planned with selected Ru(II/III) sulphoxide precursors and MBAP (spacer), in acetone medium. The desired products were isolated as solids and purified through vapour diffusion of Et_2O into a DCM solution at room temperature. The attempts to obtain crystals failed and the obtained solid was only a precipitate. All complexes were stable in air at room temperature and soluble in water, chloroform, acetone, MeCN, DCM and DMSO.

The physical, analytical and spectral data for complexes **1**–**7** are given in the Supplementary material to this paper.

Empirical formulas for **1**–**7** were in good agreement with elemental data. The determined molecular weights were supported by FAB-MS spectra. The molar conductivities for complexes **1**, **2**, **5** and **6**, observed between 52 and 68

Ω^{-1} mol^{-1} dm^3 cm^{-1} in water, were within the range suggested for non-electrolytes. However, for **3**, **4**, and **7**, the values were comparatively high (between 122 and 130 Ω^{-1} mol^{-1} dm^3 cm^{-1}), indicating the ionic nature of these complexes.[5,25]

Spectral studies

Infrared spectral study. In FTIR spectrum of MBAP, the absorption band at 3487 cm^{-1}, assigned to ν(N–H),[20] did not show any appreciable shift in the spectra of **1**–**7**, confirming the non-participation of the (N–H) nitrogen in the coordination. The bands between 1609 and 1430 cm^{-1}, assigned to cyclic C=C and C=N stretching mode in MBAP,[20] were found shifted (by 30–60 cm^{-1}) on the positive scale in the spectra of the complexes. These bands were also less intense, indicating that both metal centres were symmetrically coordinated to the cyclic nitrogen of MBAP (spacer).[18] The appearance of the ν(Ru–N) band at 280 cm^{-1} was further support of metal ligand binding.[16]

The bands appearing in the range 1090–1136 cm^{-1} were assigned to ν(SO). In the spectra of **1**–**3**, an additional band was observed at about 1055 cm^{-1}, due to uncoordinated DMSO. In the spectra of **5**–**7**, the strong band of free TMSO appeared near 1028 cm^{-1}.[25,26] The ν(Ru–Cl) stretching mode was observed at around 330 cm^{-1} and the ν(Ru–S) mode at about 402 cm^{-1}. In complexes **3** and **7**, the broad signal registered at 730 cm^{-1} along with another sharp signal at 1056 cm^{-1} in DMSO and at 1029 cm^{-1} in the TMSO analogue indicates the presence of hydrogen bonded DMSO/TMSO in these complexes.[5,25]

Electronic spectral study. Complexes **1**, **2**, **5** and **6** were diamagnetic (low spin d^6, $S = 0$), as expected for low spin Ru(II) compounds. Four bands appeared in the spectra. In the visible region, two weak absorption bands with low extinction coefficient were observed between 662 and 580 nm, and 480 and 390 nm. These bands were assigned to the transitions $^1A_1g \rightarrow {}^1T_1g$ and $^1A_1g \rightarrow {}^1T_2g$, respectively. The band at about 350 nm was probably due to a metal ligand charge transfer transition (MLCT). Moreover, the higher energy absorption band at around 300 nm was due to $\pi \rightarrow \pi^*$ intraligand transitions in the coordinated π-acidic imine ligand.[27,28]

Complexes **3**, **4** and **7** were paramagnetic with magnetic moments of 1.87––1.89 μ_B per ruthenium centre, (low spin d^5, $S = 1/2$) as expected for low spin Ru(III) complexes. In the spectra, three bands were registered between 482 and 472, 446 and 430, and 302 and 301 nm. The intense absorption band around 430 nm coupled with a less intense transition at 470 nm was ascribed to a charge transfer transition from chloride to the Ru(III) ion. This is a typical identification for the $RuCl_4^-$ unit.[29] In complexes **3** and **7**, the weak absorption band at 300 nm was due to the protonated sulphoxide cation.[27,28]

NMR spectral studies The NMR study for **1**–**7** was found not very helpful since only small swings in the chemical shift were reported. However, in the ^{1}H-NMR spectra of **1**, **2**, **5** and **6**, broad signals for four NH_2 protons were observed between δ 5.49–5.43 ppm, and at almost the same position as observed in MBAP,[20] confirming the non-involvement of the NH_2 group in the coordination. A sharp signal for two methylenic protons appeared in the range δ 2.99–2.73 ppm and for six heteroaromatic protons observed between δ 7.94–6.93 ppm. In the ^{13}C{^{1}H}NMR spectra, signals for the methylenic carbon were observed between δ 40.3–39.4 ppm and for Ar-C between δ 149.9–110.1 ppm.[30]

Three singlets (intensity ratio 1:1:1) observed in the ^{1}H-NMR spectrum of **1**, (Fig. S-1 of the Supplementary material to this paper) indicated three different environments for the methyl protons of DMSO. The signals at δ 3.50 and 3.48 ppm were both assigned to twelve CH_3 protons of DMSO *trans* to Cl, and were in the diastereotopic arrangement to each other.[17] However, the signal centred at δ 3.40 ppm was assigned to twelve DMSO protons *trans* to the pyridine nitrogen.[25,31,32] The appearance of three signals at δ 45.7, 45.3 and 44.3 ppm in the ^{13}C-NMR spectrum of **1** (Fig. S-2 of the Supplementary material) supported the ^{1}H-NMR data. The signals at δ 45.7 and 45.3 ppm were assigned to the methyl carbon *trans* to Cl and at δ 44.3 ppm to the methyl carbon of DMSO *trans* to the pyridine nitrogen.

In ^{1}H-NMR spectra of **5**, four sets of signals were registered. The multiplet centered at δ 4.01 and 3.98 ppm (for eight protons each) were assigned to the S–CH_2 protons of TMSO *trans* to Cl and diastereotopic to each other.[17,25] The multiplet centred at δ 3.57 ppm (for eight protons) were assigned to two S–CH_2 protons situated *trans* to the pyridine nitrogen for both metal centres. However, the multiplet at δ 2.30 ppm was assigned to twenty-four protons of S–C–CH_2 groups. The relative intensity of these four signals was 1:1:1:3.[17,33] Similar conclusions were drawn from the ^{13}C-NMR data of **5**. The signals at δ 57.8 and 57.7 ppm were assigned to the (S–C) carbon of TMSO *trans* to Cl, and at δ 55.6 ppm *trans* to the pyridine nitrogen. The signals observed at δ 27.1, 26.9 and 25.7 ppm were assigned to the (S–C–C) carbons of TMSO.[33]

In the ^{1}H-NMR spectrum of **2**, two singlets appeared with an intensity ratio of 1:2, indicating two different environments for the CH_3 protons. The singlet at δ 3.49 ppm was assigned to twelve DMSO protons *trans* to the pyridine nitrogen and at δ 3.37 ppm to twenty-four DMSO protons *trans* to each other. In the ^{1}H–^{1}H COSY NMR spectrum of **2** (Fig. S-3 of the Supplementary material), no cross peaks were noticed in the sulphoxide region, indicating there was no connectivity between the methyl carbons of DMSO. Similar conclusions were derived from the ^{13}C-NMR results for **2**, (Fig. S-4 of the Supplementary material), in which two signals for the (S–C) carbon of DMSO were observed at δ 46.7 and 44.9 ppm.[32,33]

Similarly, complex **6** exhibited three sets of multiplets centred at *δ* 3.54, 3.51 and 2.32 ppm. The signals centred at *δ* 3.54 and 3.51 ppm were assigned to S–CH$_2$ protons and that at *δ* 2.32 ppm to S–C–CH$_2$ protons of TMSO. The intensity ratios for these three signals were 1:2:3. Therefore, it could be concluded that one TMSO unit was *trans* to the pyridine nitrogen and other two were *trans* to each other, in an octahedral environment for both metal centres.[33,34] This conclusion was further supported by the ^{13}C-NMR spectral study. The signal centred at *δ* 57.2 ppm was assigned to the (S–C) carbon of TMSO *trans* to pyridine nitrogen and the signal for S–C carbon *trans* to each other was observed at *δ* 56.3 ppm. Moreover, for the S–C–C of TMSO, the signals appeared at *δ* 27.4 and 26.8 ppm.[33,34]

In ^{1}H-NMR spectra of **1** and **2**, an additional singlet observed at about *δ* 2.75 ppm was due to free S–CH$_3$, while in **5** and **6**, the signals for the free S–CH$_2$ and S–C–CH$_2$ groups were centred at *δ* 2.54 and 2.21 ppm, respectively. This conclusion was further supported by ^{13}C{^{1}H}NMR data, where in **1** and **2**, the signal at about *δ* 37.6 ppm was due to free (S–C) carbons of DMSO; while in **5** and **6**, the presence of free TMSO was evidenced by signals at *δ* 54.4 and 24.1 ppm.[14,22] Thus, the NMR results were in support the IR data and confirmed the presence of uncoordinated DMSO/TMSO in the Ru(II) complexes. Moreover, this feature was also in confirmation with elemental results and mass spectral studies. Thus, based on spectroscopic and elemental studies, the most plausible structure of the Ru(II) complexes **1**, **2**, **5** and **6** are presented in Fig. 1.

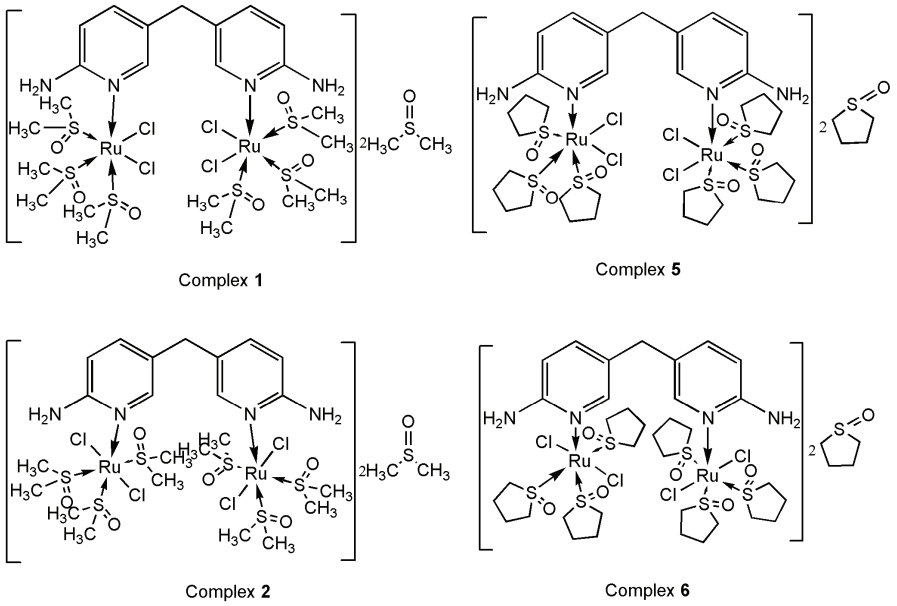

Complex **1**

Complex **5**

Complex **2**

Complex **6**

Fig. 1. Structures of Ru(II) complexes **1**, **2**, **5** and **6**.

The signals in the NMR spectra of **3**, **4** and **7** were too broad due to intervention of the paramagnetic ion. Thus, it was not possible to use NMR as a diagnostic tool for the Ru(III) complexes.[16,25] Hence, the binding mode was concluded based on FT-IR, UV–Vis, CHN analyses and FAB-MS. The most probable structures are shown in Fig. 2.

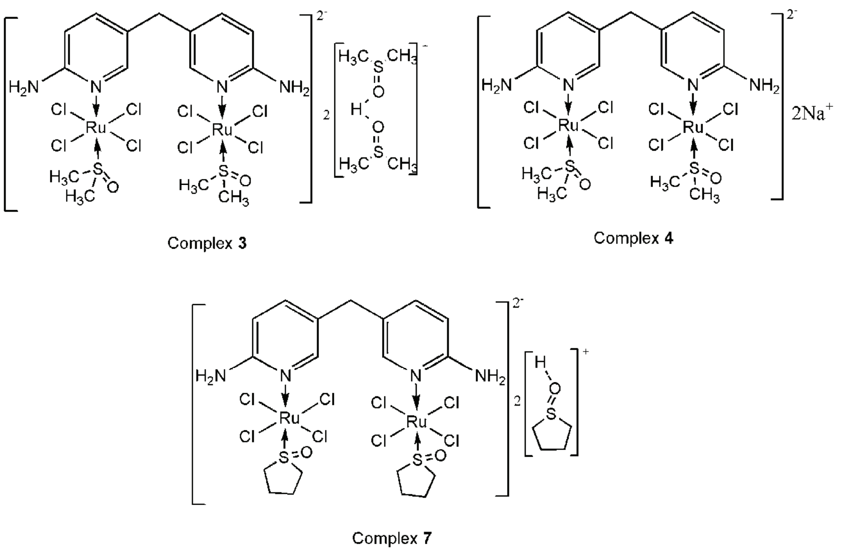

Fig. 2. Structures of Ru(III) complexes **3**, **4** and **7**.

*Chemical behaviour of complexes **1** and **2** in aqueous solution*

The chemical behaviours of complexes **1** and **2** in aqueous solution were studied by repetitive electronic absorption and conductivity measurements. The conductivity for light protected solutions of **1** (10^{-3} M) slowly increased from a non electrolytic to a 1:1 electrolytic range (68 to 102 Ω^{-1} mol^{-1} dm^{3} cm^{-1} at 25 °C) due to the release of Cl^{-} over 12 h. The chloride dissociation step was confirmed spectrophotometrically. In the electronic spectra of complex **1**, significant changes in the 300–440 nm range were registered with respect to time (Fig. 3A). The clear isosbestic points (324 and 362 nm) suggested the conversion of the parent complex to the corresponding aqua species.[35]

However, complex **2** once dissolved immediately released one of the *trans* DMSO (at each ruthenium centre) due to the strong trans influence that was followed by the slow release of Cl^{-}. The conductivity determined for **2** (10^{-3} M) increased in time at a lower rate than that of **1**. The release of Cl^{-} is in agreement with the lower *trans* effect of chloride with respect to DMSO.[4] A molar conductance of 108 Ω^{-1} mol^{-1} dm^{3} cm^{-1} was obtained after 24 h at 25 °C, characteristic for a 1:1 electrolyte. This observation was in support of hydrolytic step and formation of aqua species, which was verified by UV–Vis spectrophotometer (Fig. 3B). However, on long-standing periods (4 days), the conductivity was found to increase at a very slow rate up to values characteristic for 2:1 electrolytes.

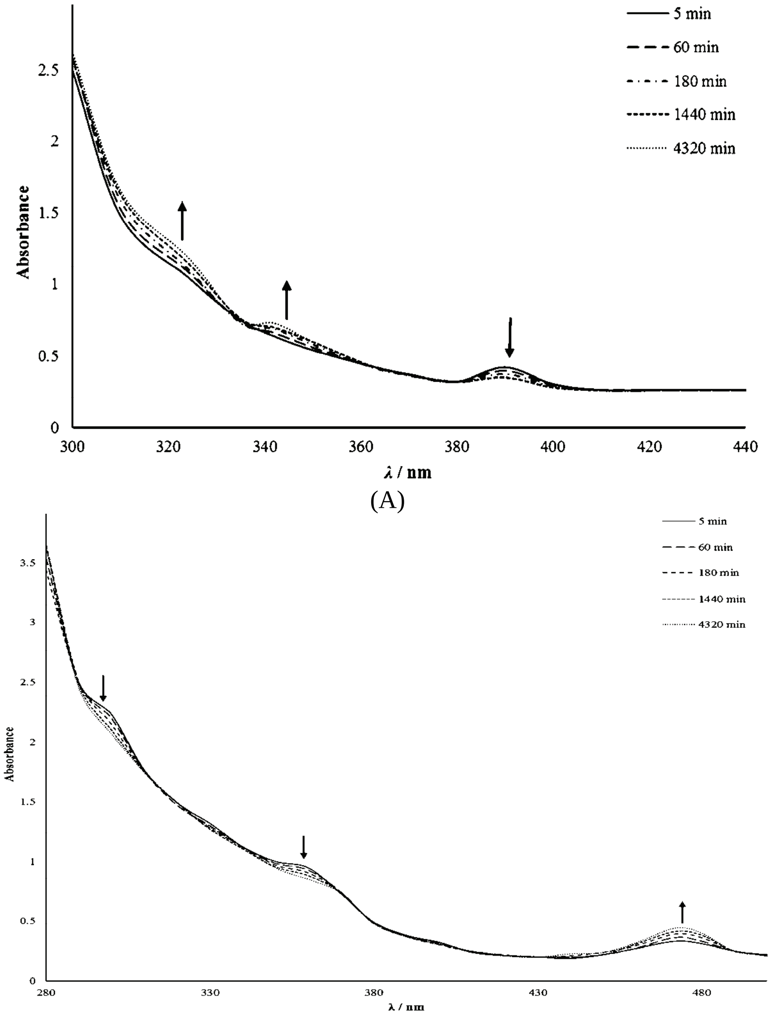

(A)

(B)

Fig. 3. Time evolution of the UV–Vis spectra of **1** (A) and **2** (B) in H_2O at 25 °C.

The chemical behaviour of complexes **1** and **2** are presented in Figs. S-5 and S-6 of the Supplementary material, respectively.

Antibacterial assay and determination of MIC *values*

A significant increase ($P < 0.0001$) in the zone of inhibition (26 mm) was observed for **7** against *E. coli* as compared with GT (Fig. 4B). The zone of inhibition for **4** was 17 mm ($P < 0.0001$); for **3**, 16 mm ($P < 0.05$); for **6**, 12 mm ($P < 0.05$); for **5**, 10 mm ($P < 0.0001$); for **2**, 8 mm ($P < 0.0001$) and for **1**, 6 mm ($P < 0.0015$). The enhanced antibacterial activities of **1**–**7** as compared to the control (MBAP in water) was probably due to the increased liphophilicity of the complexes causing permeability barrier breakdown and enzyme binding inhibition leading to cell death.[23]

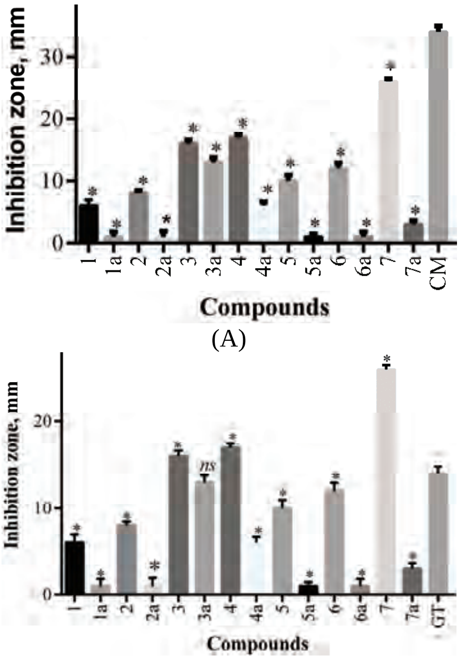

(A)

(B)

Fig. 4. Effect of the precursors **1a**–**7a** and **1**–**7** on the inhibition zone at a concentration 2.5 μg mL^{-1} against *E. coli* in comparison to chloramphenicol, CM (A), and gatifloxacin, GT (B). The values of the zones of inhibition were obtained by subtracting control (MBAP in water). Statistics points are the average values of three independent experiments (mean ± standard deviation; $n = 3$). *: $P < 0.05$; *ns* = not significant.

The results of antibacterial activity are in agreement with MIC evaluation. It was shown that Ru(III) compounds **3**, **4** and **7** were found to be more active to inhibit *E. coli* at *MIC* of 0.31 μg/mL (Table I) in comparison to respective precursors.

TABLE I. *MIC* evaluation (μg/mL) of **1**–**7** and market drugs against *E. coli*

1	**2**	**3**	**4**	**5**	**6**	**7**	Chloramphenicol (CM)	Gatifloxacin (GT)
0.62	0.62	0.31	0.31	0.62	1.25	0.31	0.25	0.25

CONCLUSIONS

Seven dinuclear Ru(II/III) complexes were synthesized by the reaction of a spacer, MBAP and the building block, ruthenium sulphoxide precursors. All compounds were characterized based on spectroscopic techniques and were found novel due to their specific structure and biological action against *E. coli*.

The use of ruthenium medicinal chemistry could be interesting as a potentially less toxic alternative to platinum. The results reported herein indicate that ruthenium complexes show potent antibacterial action. They may find importance in the future due to other aspects of biological activity in the age of superbugs. Their characterization, chemical reactivity and inherent activity give a new look to ruthenium-based pharmaceuticals.

SUPPLEMENTARY MATERIAL

Physical, analytical and spectral data for the synthesised complexes are available electronically from http://www.shd.org.rs/JSCS/, or from the corresponding author on request.

Acknowledgement. We are thankful to the Head, Department of Chemistry, Govt. Model Science College, Jabalpur for providing the laboratory facilities. Thanks are also due to SAIF, CDRI, Lucknow for the CHN analyses, and mass and NMR spectra. RM is thankful to Dr. J. J. Ahire, Postdoc Fellow, University of Stellenbosch, South Africa, for his kind help in the statistical analysis.

ИЗВОД

ИСПИТИВАЊЕ НОВИХ РУТЕНИЈУМОВИХ СУЛФОКСИДНИХ КОМПЛЕКСА: СИНТЕЗА, КАРАКТЕРИЗАЦИЈА И ПРИМЕНА

RIPUL MEHROTRA, SATYENDRA N. SHUKLA и PRATIKSHA GAUR

Coordination Chemistry Research Lab, Department of Chemistry, Govt. Model Science College
Jabalpur (MP) 482001, India

У овом раду, једињење који садржи две 2-аминопиридинске јединице је коришћено као мосни лиганд за синтезу седам нових динуклеарних комплекса рутенијума(II/III). Ови комплекси су окарактерисани помоћу елементалне микроанализе, кондуктометријских, магнетних, FT-IR, FAB-масених, електронских, ^{1}H- и ^{13}C{^{1}H}NMR мерења. Поред тога, [{*trans,mer*-RuCl$_2$(DMSO)$_3$}$_2$(*μ*-5,5′-метиленбис(2-пиридинамин-κ*N*^{1}))]·2DMSO комплекс **2** је окарактерисан помоћу ^{1}H–^{1}H COSY NMR спектроскопије. Нађено је да постоје три различите комплексне врсте које се могу представити на следећи начин: [{*cis,fac*-RuCl$_2$(SO)$_3$}$_2$(*μ*-MBAP)]·2SO, [{*trans,mer*-RuCl$_2$(SO)$_3$}$_2$(*μ*-MBAP)]·2SO и [{*trans*-RuCl$_4$(SO)}$_2$(*μ*-MBAP)]$^{2-}$ $[X]_2^+$; где су SO = DMSO/TMSO, MBAP = 5,5'-метиленбис(2-аминопиридин) и [X]$^+$ = [(DMSO)$_2$H]$^+$, Na$^+$ или [(TMSO)H]$^+$. На основу кондуктометријских мерења и UV–Vis спектрофотометрије испитиванао је хемијско понашање комплекса [{*cis,fac*-RuCl$_2$(DMSO)$_3$}$_2$(*μ*-5,5'-метиленбис(2- пиридинамин-κ*N*^{1}))]·2DMSO (**1**) и комплекса **2** у раствору у току различитих временских интервала. Нађено је да сви испитивани комплекси показују значајну антибактеријску активност на *Escherichia coli* у односу на хлорамфеникол и гатифлоксацин.

Примљено 4. јула, ревидирано 11. августа, прихваћено 31. августа 2014)

REFERENCES

1. D. Ossipov, P. I. Pradeep, M. Holmer, J. Chattopadhyaya, *J. Am. Chem. Soc.* **27** (2001) 3551
2. E. Alessio, *Bioinorganic Medicinal Chemistry*, Wiley–VCH Verlag, Weinheim, 2011, p. 68
3. A. H. Velders, A. Bergamo, E. Alessio, E. Zangrando, J. G. Haasnoot, C. Casarsa, M. Cocchietto, S. Zorzet, G. Sava, *J. Med. Chem.* **47** (2004) 1110

4. E. Alessio, G. Mestroni, G. Nardin, W. M. Attia, M. Calligaris, G. Sava, S. Zorzet, *Inorg. Chem.* **27** (1988) 4099
5. E. Alessio, G. Balducci, M. Calligaris, G. Costa, W. M. Attia, G. Mestroni, *Inorg. Chem.* **30** (1991) 609
6. A. Yadav, T. Janaratne, A. Krishnan, S. S. Singhal, S. Yadav, A. S. Dayoub, D. L. Hawkins, S. Awasthi, F. M. MacDonnell, *Mol. Cancer Ther.* **12** (2013) 643
7. C. G. Hartinger, M. A. Jakupec, S. Z. Seifried, M. Groessl, A. Egger, W. Berger, H. Zorbas, P. J. Dyson, B. K. Keppler, *Chem. Biodivers.* **5** (2008) 2140
8. J. M. R. Lakhai, D. V. Bongard, D. Pluim, J. H. Beijnen, J. H. M. Schellens, *Clin. Cancer Res.* **10** (2004) 3717
9. E. Alessio, M. Calligaris, M. Iwamoto, L. G. Marzilli, *Inorg. Chem.* **35** (1996) 2538
10. A. G. Ortiz, P. U. Maheswari, M. Siegler, A. L. Spekb, J. Reedijk, *New J. Chem.* **37** (2013) 3450
11. A. Rilak, I. Bratsos, E. Zangrando, J. Kljun, I. Turel, Z. D. Bugarcic, E. Alessio, *Inorg. Chem.* **53** (2014) 6113.
12. E. Alessio, E. Iengo, E. Zangrando, S. Geremia, P. A. Marzilli, M. Calligaris, *Eur. J. Inorg. Chem.* (2000) 2207
13. E. Iengo, G. Mestroni, S. Geremia, M. Calligaris, E. Alessio, *J. Chem. Soc., Dalton Trans.* (1999) 3361
14. S. N. Shukla, P. Gaur, A. Dubey, S. Mathews, R. Mehrotra, *J. Coord. Chem.* **65** (2012) 602
15. O. V. Gijte, A. A. Kirsch-De-Mesmaeker, *J. Chem. Soc., Dalton Trans.* (1999) 951
16. R. Mehrotra, S. N. Shukla, P. Gaur, *J. Coord. Chem.* **65** (2012) 176
17. E. Alessio, *Chem. Rev.* **104** (2004) 4203
18. R. S. Srivastava, F. R. Fronczek, L. M. Romero, *Inorg. Chim. Acta* **357** (2004) 2410
19. I. Bensemann, M. Gdaniec, T. Polonski, *New J. Chem.* **26** (2002) 448
20. S. N. Shukla, P. Gaur, R. Mehrotra, R. S. Srivstava, *E – J. Chem.* **9** (2012) 593.
21. I. P. Evans, A. Spencer, G. Wilkinson, *J. Chem. Soc., Dalton Trans.* (1973) 204
22. E. Alessio, B. Milani, G. Mestroni, M. Calligaris, P. Faleschini, W. M. Attia, *Inorg. Chim. Acta* **177** (1990) 255
23. R. Mehrotra, S. N. Shukla, P. Gaur, A. Dubey, *Eur. J. Med. Chem.* **50** (2012) 149
24. R. Mehrotra, S. N. Shukla, P. Gaur, *Med. Chem. Res.* **21** (2012) 4455
25. S. N. Shukla, P. Gaur, R. Mehrotra, M. Prasad, H. Kaur, M. Prasad, R. S. Srivastava, *J. Coord. Chem.* **62** (2009) 2556
26. J. A. Davis, *Adv. Inorg. Chem. Radiochem.* **24** (1981) 115
27. U. C. Sarma, R. K. Poddar, *Polyhedron* 7 (1988) 1737.
28. A. B. P. Lever, *Inorganic Electronic Spectroscopy*, 2nd ed., Elsevier Amsterdam, 1984, p. 168
29. B. R. James, R. H. Morris, *Can. J. Chem.* **58** (1980) 399
30. R. M. Silverstein, G. C. Bassler, T. C. Morrill, *Spectrometric Identification of Organic Compounds*, Wiley, New York, 1991, p. 219
31. A. M. S. Silva, J. A. S. Cavaleiro, G. Tarrago, C. Marzin, *New J. Chem.* (1999) 329
32. S. N. Shukla, P. Gaur, H. Kaur, M. Prasad, R. Mehrotra, R. S. Srivastava, *J. Coord. Chem.* **61** (2008) 441
33. F. D. Rochon, P. C. Kong, L. Girard, *Can. J. Chem.* **64** (1986) 1897
34. J. H. Price, A. N. Williamson, R. F. Schramm, B. B. Wayland, *Inorg. Chem.* **11** (1972) 1280
35. I. Bratsos, D. Urankar, E. Zangrando, P. G. Kalou, J. Kosmrlj, E. Alessio, I. Turel, *J. Chem. Soc., Dalton Trans.* **40** (2011) 5188.

Journal of the Serbian Chemical Society
JSCS@tmf.bg.ac.rs • www.shd.org.rs/JSCS

J. Serb. Chem. Soc. 80 (5) S168–S172 (2015)   *Supplementary material*

SUPPLEMENTARY MATERIAL TO

A study on tailor made ruthenium sulphoxide complexes: Synthesis, characterization and application

RIPUL MEHROTRA*, SATYENDRA N. SHUKLA and PRATIKSHA GAUR

Coordination Chemistry Research Lab, Department of Chemistry, Govt. Model Science College Jabalpur (MP) 482001, India

J. Serb. Chem. Soc. 80 (5) (2015) 639–649

PHYSICAL, ANALYTICAL AND SPECTRAL DATA FOR THE SYNTHESISED COMPLEXES

*[{*Cis,fac-*RuCl$_2$(DMSO)$_3$}$_2$(*μ*-5,5'-methylenebis(2-aminopyridine))]·2DMSO (**1**)*. Yield: 86.7 %; yellowish brown solid; m.p.: 112 °C; Anal. Calcd. for $C_{27}H_{60}N_4S_8O_8Cl_4Ru_2$ (FW: 1169.21): C, 27.73; H, 5.17; N, 4.79; S, 21.94 %. Found: C, 27.69; H, 5.21; N, 4.72; S, 21.88 %; IR (KBr, cm^{-1}): 3485 (N–H stretching of NH_2 group), 2860, 2830 (C–H stretching of CH_2), 1650, 1634, 1552, 1490 (C=C and C=N stretching of ring), 1281 (C–N stretching of C–NH_2), 1096, 1050 (SO stretching bands of sulphoxide), 404 (Ru–S stretching), 336, 331 (Ru–Cl stretching), 282 (Ru–N stretching); ^{1}H-NMR (400 MHz, D_2O, δ / ppm): 7.94–6.93 (6H, *m*, Ar-H); 5.46 (4H, *brs*, NH_2); 3.50 (12H, *s*, CH_3), 3.48 (12H, *s*, CH_3), 3.40 (12H, *s*, CH_3), 2.78 (12H, *s*, CH_3); 2.73 (2H, *s*, CH_2); ^{13}C{^{1}H}-NMR (400 MHz, D_2O, δ / ppm): 146.8–110.1 (Ar-C); 45.7, 45.3, 44.3, 37.8 (SC); 39.8 (CH_2); MS (*m*/*z*): 1170 $(M+H)^+$; UV–Vis (MeCN) (λ_{max} / nm (ε / mol^{-1} dm^3 cm^{-1})): 590 (100), 390 (410), 324 (550), 228 (780). Conductivity (H_2O, 25 °C, Δm / Ω^{-1} mol^{-1} dm^3 cm^{-1}): 68.

*[{*Trans,mer-*RuCl$_2$(DMSO)$_3$}$_2$(*μ*-5,5'-methylenebis(2-aminopyridine))]·2DMSO (**2**)*. Yield: 91.2 %; golden yellow powder; m.p.: 123 °C; Anal. Calcd. for $C_{27}H_{60}N_4S_8O_8Cl_4Ru_2$ (FW: 1169.21): C, 27.73; H, 5.17; N, 4.79; S, 21.94 %. Found: C, 27.82; H, 5.20; N, 4.76; S, 21.86 %; IR (KBr, cm^{-1}): 3490 (N–H stretching of NH_2 group), 2842, 2835 (C–H stretching of CH_2), 1651, 1626, 1550, 1480 (C=C and C=N stretching of ring), 1283 (C–N stretching of C–NH_2), 1101, 1058 (SO stretching bands of sulphoxide), 402 (Ru–S stretching), 334, 330 (Ru–Cl stretching), 278 (Ru–N stretching); ^{1}H-NMR (400 MHz, D_2O, δ / ppm): 7.92–7.03 (6H, *m*, Ar-H); 5.43 (4H, *brs*, NH_2); 3.49 (12H, s, CH_3), 3.37 (24H, *s*, CH_3), 2.71 (12H, *s*, CH_3); 2.84 (2H, *s*, CH_2); ^{13}C{^{1}H}-NMR (400 MHz, D_2O,

---

* Corresponding author. E-mail: ripul.mehrotra@gmail.com.

δ / ppm): 147.6–112.1 (Ar-C); 46.7, 44.9, 37.6 (SC); 39.4 (CH_2); MS (*m*/*z*): 1170 $(M+H)^+$; UV–Vis (MeCN) (λ_{max} / nm (ε / mol^{-1} dm^3 cm^{-1})): 630 (46), 472 (620), 360 (806), 300 (705). Conductivity (H_20, 25 °C, Δm / Ω^{-1} mol^{-1} dm^3 cm^{-1}): 52.

$[(DMSO)_2H]_2^+[\{$trans-$Ru(DMSO)Cl_4\}_2$(μ-*5,5'-methylenebis(2-aminopyridine*))$]^{2-}$ (**3**). Yield: 91.7 %; yellow powder; m.p.: 153 °C; Anal. Calcd. for $C_{23}H_{50}N_4S_6O_6Cl_8Ru_2$ (FW: 1156.77): C, 23.88; H, 4.36; N, 4.84; S, 16.63 %. Found: C, 23.79; H, 4.34; N, 4.78; S, 16.70 %; IR (KBr, cm^{-1}): 3485 (N–H stretching of NH_2 group); 2860, 2843 (C–H stretching of CH_2), 1671, 1620, 1546, 1468 (C=C and C=N stretching of ring), 1278 (C–N stretching of C–NH_2), 1100, 1056 (SO stretching bands of sulphoxide); 730 $[(DMSO)_2H]^+$, 405 (Ru–S stretching), 337, 331 (Ru–Cl stretching), 270 (Ru–N stretching); MS (*m*/*z*): 1175 $(M+H)^+$; UV–Vis (MeCN, $\lambda_{max,}$ / nm (ε / mol^{-1} dm^3 cm^{-1})): 476 (802), 446 (960), 302 (706); Conductivity (H_2O, 25 °C, Δm / Ω^{-1} mol^{-1} dm^3 cm^{-1}): 128; Magnetic moment ($\boldsymbol{\mu}_{eff}$ / μ_B): 1.87.

$(Na)_2^+[\{$trans-$Ru(DMSO)Cl_4\}_2$(μ-*5,5'-methylenebis(2-aminopyridine*))$]^{2-}$ (**4**). Yield: 88.2 %; yellowish green solid; m.p.: > 220 °C; Anal. Calcd. for $C_{15}H_{24}N_4S_2O_2Cl_8Na_2Ru_2$ (FW: 888.22): C, 20.28; H, 2.72; N, 6.31; S, 7.22 %. Found: C, 20.22; H, 2.68; N, 6.27; S, 7.28 %; IR (KBr, cm^{-1}): 3480 (N–H stretching of NH_2 group); 2860, 2847 (C–H stretching of CH_2), 1646, 1630, 1560, 1465 (C=C and C=N stretching of ring), 1286 (C–N stretching of C–NH_2), 1090 (SO stretching bands of sulphoxide), 399 (Ru–S stretching), 331, 327 (Ru–Cl stretching), 276 (Ru–N stretching); MS (*m*/*z*): 911 $(M+Na)^+$; UV–Vis (MeCN, λ_{max} / nm (ε / mol^{-1} dm^3 cm^{-1})): 482 (780), 442 (901), 301 (709). Conductivity (H_2O, 25 °C, Δm / Ω^{-1} mol^{-1} dm^3 cm^{-1}): 130; Magnetic moment ($\boldsymbol{\mu}_{eff}$ / / μ_B): 1.89.

$[\{$Cis,fac-$RuCl_2(TMSO)_3\}_2$(μ-*5,5'-methylenebis(2-aminopyridine*))]·2TMSO (**5**). Yield: 91.2 %; golden yellow powder; m.p.: 146 °C; Anal. Calcd. for $C_{43}H_{76}N_4S_8O_8Cl_4Ru_2$ (FW: 1377.50): C, 37.49; H, 5.56; N, 4.07; S, 18.62 %. Found: C, 37.53; H, 5.49; N, 4.11; S, 18.59 %; IR (KBr, cm^{-1}): 3490 (N–H stretching of NH_2 group); 2870, 2823 (C–H stretching of CH_2), 1656, 1638, 1522, 1475 (C=C and C=N stretching of ring), 1284 (C–N stretching of C–NH_2), 1120, 1028 (SO stretching bands of sulphoxide), 403 (Ru–S stretching), 334, 330 (Ru–Cl stretching), 282 (Ru–N stretching); ^{1}H-NMR (400 MHz, D_2O, δ / ppm): 7.71–7.11 (6H, *m*, Ar-H); 5.49 (4H, *brs*, NH_2); 4.01 (8H, *m*, SCH_2), 3.98 (8H, *m*, SCH_2), 3.57 (8H, *m*, SCH_2), 2.54 (8H, *m*, SCH_2); 2.99 (2H, *s*, CH_2); 2.30 (24H, *m*, $SCCH_2$), 2.19 (8H, *m*, $SCCH_2$); $^{13}C\{^1H\}$NMR (400 MHz, D_2O, δ / ppm): 146.4–115.9 (Ar-C); 57.8, 57.7, 55.6, 54.4 (SC); 39.6 (CH_2); 27.1, 26.9, 25.7, 24.1 (SC**C**); MS (*m*/*z*): 1378 $(M+H)^+$; UV–Vis (MeCN, λ_{max} / nm (ε / mol^{-1} dm^3 cm^{-1})): 580 (35), 410 (450), 326 (682), 230 (744). Conductivity (H_2O, 25 °C, Δm / Ω^{-1} mol^{-1} dm^3 cm^{-1}): 62.

*[{*Trans,mer-*RuCl$_2$(TMSO)$_3$}$_2$(*μ-*5,5'-methylenebis(2-aminopyridine))]·2TMSO* ***(6)***. Yield: 84.5 %; golden yellow powder; m.p.: 158 °C; Anal. Calcd. for $C_{43}H_{76}N_4S_8O_8Cl_4Ru_2$ (FW: 1377.50): C, 37.49; H, 5.56; N, 4.07; S, 18.62 %. Found: C, 37.47; H, 5.60; N, 4.09; S, 18.57 %; IR (KBr, cm^{-1}): 3475 (N–H stretching of NH_2 group), 2845, 2840 (C–H stretching of CH_2), 1650, 1637, 1572, 1463 (C=C and C=N stretching of ring), 1283 (C–N stretching of C–NH_2), 1098, 1031 (SO stretching bands of sulphoxide), 407 (Ru–S stretching), 337, 331 (Ru–Cl stretching), 286 (Ru–N stretching); ^{1}H-NMR (400 MHz, D_2O, δ / ppm): 7.63–6.99 (6H, *m*, Ar-H); 5.45 (4H, *brs*, NH_2); 3.54 (8H, *m*, SCH_2), 3.51 (16H, *m*, SCH_2), 2.55 (8H, *m*, SCH_2); 2.32 (24H, *m*, $SCCH_2$), 2.21 (8H, *m*, $SCCH_2$); 2.92 (2H, *s*, CH_2); ^{13}C{^{1}H}NMR (400 MHz, D_2O, δ / ppm): 149.9–114.8 (Ar-C); 57.2, 56.3, 54.5 (SC); 40.3 (CH_2); 27.4, 26.8, 24.3 (SC**C**); MS (*m*/*z*): 1378 (M+H)$^+$; UV–Vis (MeCN, λ_{max} / nm (ε / mol^{-1} dm^3 cm^{-1})): 662 (42), 480 (502), 360 (760), 302 (880). Conductivity (H_2O, 25 °C, Δ*m* / Ω^{-1} mol^{-1} dm^3 cm^{-1}): 68.

*[(TMSO)H]$_2$$^+$[{*trans-*Ru(TMSO)Cl$_4$}$_2$(*μ-*5,5'-methylenebis(2-aminopyridine))]$^{2-}$* ***(7)***. Yield: 83.7 %; yellow red powder; m.p.: > 220 °C; Anal. Calcd. for $C_{27}H_{46}N_4S_4O_4Cl_8Ru_2$ (FW: 1104.66): C, 29.35; H, 4.20; N, 5.07; S, 11.61 %. Found: C, 29.40; H, 4.23; N, 5.11; S, 11.66 %; IR (KBr, cm^{-1}): 3495 (N–H stretching of NH_2 group), 2850, 2810 (C–H stretching of CH_2), 1641, 1631, 1550, 1482 (C=C and C=N stretching of ring), 1280 (C–N stretching of C–NH_2), 1136, 1029 (SO stretching bands of sulphoxide), 735 [(TMSO)H]$^+$, 402 (Ru–S stretching), 338, 333 (Ru–Cl stretching), 280 (Ru–N stretching); UV–Vis (MeCN, λ_{max} / nm (ε / mol^{-1} dm^3 cm^{-1})): 472 (600), 430 (780), 301 (861); MS (*m*/*z*): 1105(M+H)$^+$; Conductivity (H_2O, 25 °C, Δ*m* / Ω^{-1} mol^{-1} dm^3 cm^{-1}): 122; Magnetic moment ($\boldsymbol{\mu}_{eff}$ / μ_B): 1.88.

THE SPECTRA AND CHEMICAL BEHAVIOR

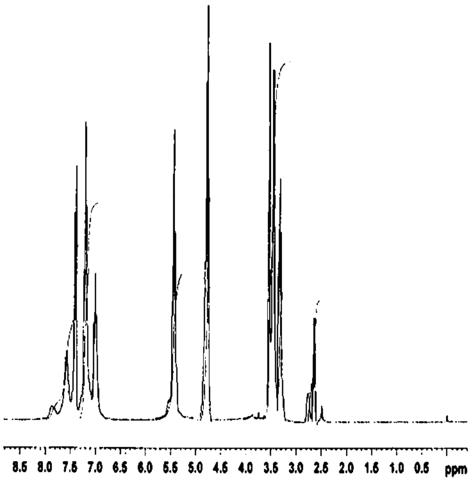

Fig. S-1. ^{1}H-NMR spectrum of **1**.

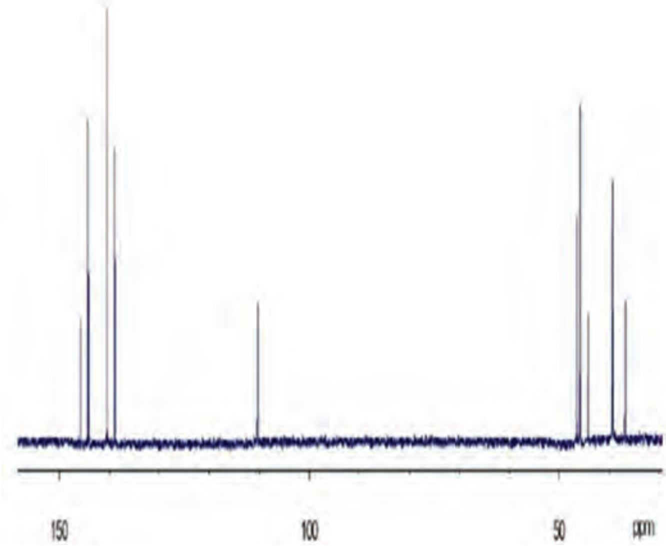

Fig. S-2. ^{13}C-NMR spectrum of **1**.

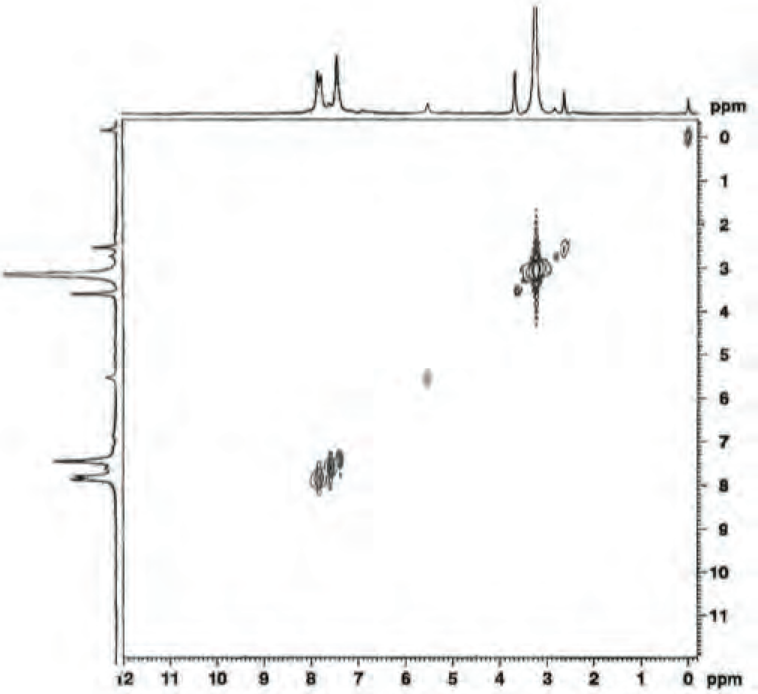

Fig. S-3. ^{1}H–^{1}H COSY NMR spectrum of **2**.

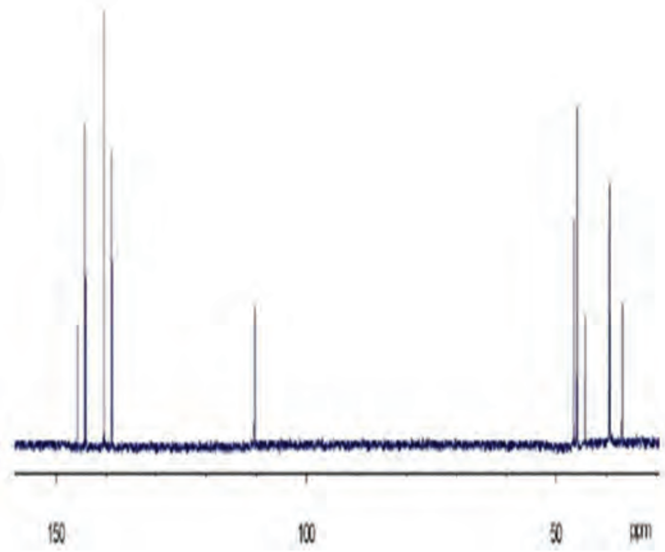

Fig. S-4. 13C-NMR spectrum of **2**.

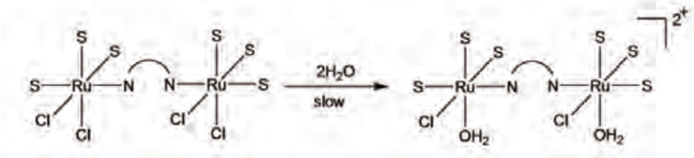

Fig. S-5. Chemical behaviour of **1** in aqueous solution.

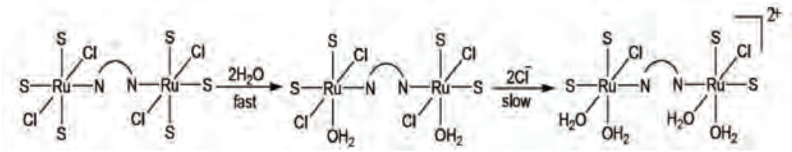

Fig. S-6. Chemical behaviour of **2** in aqueous solutions.

Journal of the Serbian Chemical Society
Version electronic
JSCS-info@shd.org.rs • www.shd.org.rs/JSCS

J. Serb. Chem. Soc. *80* (5) 651–658 (2015)
JSCS–4745

UDC 547–311+546.161–32+544.351–145.82:
547.312
Original scientific paper

Solvent effect on ternary complexes formed by oxirane and hydrofluoric acid

BOAZ G. OLIVEIRA*

Institute of Environmental Sciences and Sustainable Development (ICADS), Federal University of Bahia, 47801-100, Barreiras – BA, Brazil

(Received 23 September 2014, revised 7 January, accepted 8 January 2015)

Abstract: The solvent effect on derivatives of the $C_2H_4O\cdots HF\cdots HF$ ternary complex was investigated through the PCM approach and AGOA calculations at the B3LYP/6-311++G(d,p) level of theory. Continuous analysis was useful to verify the profiles of the hydrogen bond distances in the complex, specifically the $O\cdots H$, $F\cdots H$, and $F\cdots H^{\beta}$ contacts. From the viewpoint of AGOA, the configurations of the water molecules, followed by measurement of the discrete hydration energies, were unveiled. Through single point energy calculations, the hydration energies were determined *via* the supermolecule approach, and the values were corrected by the counterpoise correction of the basis sets superposition error (BSSE). In line with this, the analysis of the molecular electrostatic potential (*MEP*) revealed positive and negative regions, which represent the interaction sites for the water molecules regarding the oxygen and hydrogen, respectively. In an overview, the acid-catalyzed oxirane ring-opening reaction has distinct interpretations both in vacuum and in aqueous medium depending on whether the most appropriate structure of the $C_2H_4O\cdots HF\cdots HF$ trimolecular complex is taken into consideration.

Keywords: hydrogen bonds; oxirane; hydrofluoric acid; PCM; AGOA.

INTRODUCTION

Many years ago, the solvent effect on chemical and biochemical processes was studied by many research groups worldwide.[1,2] Even taking into account the polar or non-polar nature of the solvent/solute, the benchmark in solvation studies could be understood by the interactions of the solvent molecules surrounding the solute.[3] These are specific interactions with low and high concentrations of charge density and, although there are many types of intermolecular interactions,[4–10] they are often recognized as hydrogen bonds.[11] Nevertheless, it is necessary to bear in mind that the solvation process must be comprehended not

---

* E-mail: boazgaldino@gmail.com

doi: 10.2298/JSC140923002D

only by the H-bond strengths,[12,13] but also by the structure or conformation of the solute.[14]

From the theoretical viewpoint, a description of the solvent effect can be realized through the application either of continuous or discrete methods,[15,16] or even by means of a combination of both. The first one is formulated based on quantum chemical calculations[17] that are developed into a fixed reaction field that mimics a cavity fitted to cover the solute. This is limited because the specific interactions are often poorly described, in particular H-bonds. From this threshold, discrete methods are useful once each molecule of solvent is aligned into a solvation model with a description of all specific interactions,[18] which is supported by adjusted force fields instead of quantum chemical calculations. On the other hand, this procedure demands extensive processing time with high computational effort, which restricts drastically its application, mainly in compounds containing site-specific solvation.

In the past, Lynschka *et al.*[19] and Wang and co-authors[20] discussed the influence of the solvent on the H-bond regarding either its thermodynamic functions or spectroscopy parameters through comparison between a vacuum and an aqueous environment. With absence of solvent, it is well known that the H-bond strength varies drastically in conformity with the structure of the solute. For example, it could be mentioned the $C_2H_4O\cdots HF$ complex,[21] the bimolecular configuration of which is formed by one H-bond between the lone pair of electrons of oxygen and the hydrogen of the hydrofluoric acid. However, the trimolecular possibility must also be worthwhile of study, *i.e.*, $C_2H_4O\cdots HF\cdots HF$,[22] wherein three conformations with three possible H-bonds, namely $O\cdots H$, $F\cdots H$, and $F\cdots H^{\beta}$, (structures **I**, **II** and **III**, respectively) were assumed the most stable structures. Among these, the last one is the result of a secondary interaction between the fluorine and axial hydrogen atoms (H^{β}) of the hetero-ring.

Within this scenario, the main goal of this work was not devoted to an evaluation of the influence of solvent, actually water, but the manner in which the solvent behaves upon the formation of the three structures of $C_2H_4O\cdots HF\cdots HF$. It is of fundamental importance to compare the solute–solvent interaction energies on these structures with the purpose of finding systematic tendencies, as well as verify whether the recently documented calculations performed under vacuum conditions corroborates with this.[22]

COMPUTATIONAL METHODS

The first step of this theoretical study was the determination of the optimized geometries of the three structures of the $C_2H_4O\cdots HF\cdots HF$ complex, which was realized using Gaussian 03W software[23] at the B3LYP/6-311++G(d,p) level of theory. In the second step, the calculations were processed to build the solvation configurations, which were modeled through AGOA software[24] by means of reading the cube file generated in a single point calculation developed previously by the Gaussian 03W program. The computations of the interaction energies or hydration energies were determined based on the supermolecule approach.[25] The surfaces of the molecular potential were generated by gOpenMol 3.0 visualization tools.[26]

RESULTS AND DISCUSSIONS

The values in angstroms of the H-bond distances of the complexes **I**, **II** and **III**, both in vacuum or water medium, are gathered in Table I. In agreement with the results of Lyschka *et al.*,[19] it could easily be seen that all H-bonds are shortened due the influence of the water medium simulated by the PCM approach. By comparing the variations of the H-bond lengths, the $O\cdots H$ values are much more reduced than those of $F\cdots H$, *e.g.*, the values of 0.1854 and 0.1725 are longer than 0.161 and 0.1239 of the **II** and **III** complexes, respectively. Moreover, the larger reductions in the $O\cdots H$ lengths also reflect on secondary interactions.

TABLE 1. Values of the H-bond distances (Å) obtained at the B3LYP/6-311++G(d,p) level of theory in vacuum and aqueous medium simulated through the PCM protocol; values of ΔRs were computed as follows: R (vacuum) – R (PCM/water)

H-bonds and medium	Structures		
	I	**II**	**III**
$R_{O\cdots H}$ (vacuum)	1.7137[a] (1.7144)[b]	1.5513	1.5372
$R_{O\cdots H}$ (PCM/water)	1.5817[a] (1.5824)[b]	1.3659	1.3647
$\Delta R_{O\cdots H}$	–0.132[a] (0.132)[b]	–0.1854	–0.1725
$R_{F\cdots H}$ (vacuum)	–	1.7035	1.6706
$R_{F\cdots H}$ (PCM/water)	–	1.5425	1.5467
*$\Delta R_{F\cdots H}$	–	–0.1610	–0.1239
$R_{F\cdots H^{\beta}}$ (vacuum)	3.1600	–	2.7550
$R_{F\cdots H^{\beta}}$ (PCM/water)	3.3900	–	4.6308
$\Delta R_{F\cdots H^{\beta}}$	0.2300	–	1.8758

It was demonstrated that **III** is the only structure able to form the secondary interactions between the fluorine and axial hydrogen atoms ($F\cdots H^{\beta}$).[22] This can be clearly seen by the H-bond length of 2.7550 Å, which even longer than the sum of the van der Waals atomic radii for fluorine and hydrogen (2.67 Å).[27] Regardless that this distance is outside the range of the intermolecular interaction profile, $(F\cdots H)^{\beta}$ was recognized as a typical H-bond interaction. In aqueous medium, PCM calculations revealed that $(F\cdots H)^{\beta}$ is drastically enhanced by 1.8758 Å. In other words, secondary interactions do not influence the structures of complexes **I**–**III** in the aqueous medium, whereas the primary H-bonds $O\cdots H$ are sensitive to the influence of the solvent, which means that O protonation is the main route to the ring-opening reaction. Meanwhile, it is fundamental to know in which manner the water molecules act in these complexes, which could maybe be an explanation of the influence of the solvent in this type of reaction.

The clusters for the three structures **I**–**III** of the trimolecular $C_2H_4O\cdots HF\cdots HF$ complex are illustrated in the Figs S-1–S-3 of the Supplementary material to this paper. In these Figures, it can also be observed the punctual charges derived from the ChelpG protocol (Charges from Electrostatic Potentials using a Grid based method),[28] within the formalism of which is a picture of the electrostatic potential (*ESP*) fields, either negative ($MEP_{\min}$) or positive ($MEP_{\max}$), which are illustrated in Fig. S-4 of the Supplementary material. It can be seen that the water molecules are orientated towards the hydrogen atoms of oxirane as well as the fluorine atoms of hydrofluoric acid. These molecular sites possess $MEP_{\max}$ and $MEP_{\min}$ with positive values (hydrogen ChelpG charges of 0.129, 0.133, 0.120, and 0.124 eu) and negative ones (fluorine ChelpG charges of –0.420, –0.422, –0.438, –0.473, –0.481, and –0.496 eu) respectively, and due to this, the interactions and solvation occur on the oxygen atoms and hydrogen atoms, respectively.

The ChelpG charges of –0.420 and –0.422 eu in **I** indicate that the fluorine atoms (F^a and F^b) are equally solvated by water molecules. On the contrary, the fluorines in **II** and **III** are specific solvation sites. Note that the hydrogen atoms of the water molecules surround preferably the F^b atoms, as is observed especially in **II**. About the clusters in **III**, both F^a and F^b are solvated, although the first slightly by only four water molecules. However, the shapes of these clusters corroborate with two distinct circumstances regarding the chemistry of the three-membered rings. In one of them, the solvation on F^b is in line with the open ring reaction with acid (see Fig. 1), although in the present case with two

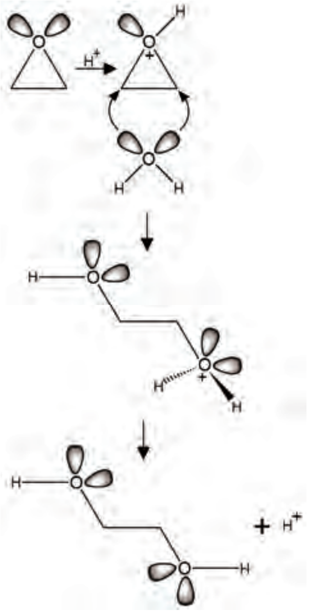

Fig. 1. Ring-opening reaction of oxirane *via* nucleophilic attack.

molecules of hydrofluoric acid, which represents an acid-catalyzed ring-opening reaction (see Fig. 2). Otherwise, the nucleophilic attack of the water molecules on the axial hydrogen atoms indicates that a SN_2 mechanism is delineated. Which of these two profile rules the oxirane open ring reaction was also one of the main goals of this work but if is not reliable, maybe in future could be.

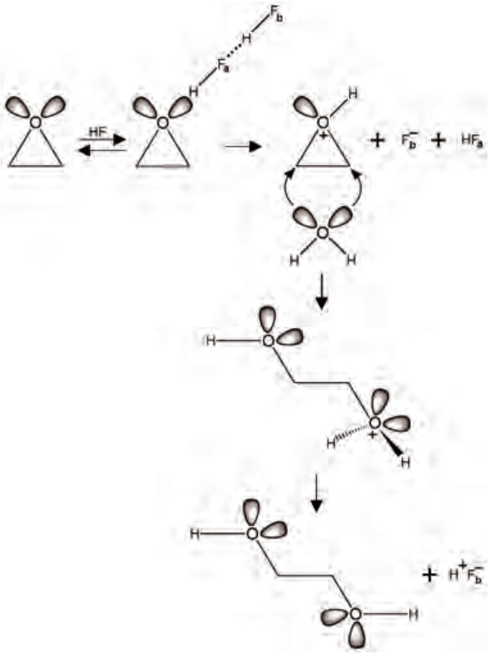

Fig. 2. Acid-catalyzed ring-opening reaction of oxirane.

A graph with all values of the hydration energies is designed in Fig. 3. The profiles of the strengths of the H-bond in **I**, **II**, and **III** are quite different. For this reason, the computation of the hydration energies by means of Eq. (1) is not a general rule:

$$E^{\mathrm{HYDRA}} = E(\text{hydrated } C_2H_4O\cdots HF\cdots HF) - E(H_2O + C_2H_4O\cdots HF\cdots HF) \quad (1)$$

As such, ideally each hydration energy should be appraised by the H-bond energies along the $C_2H_4O\cdots HF\cdots HF$ complex, *e.g.*, $O\cdots H$, $F\cdots H$, and $F\cdots H^{\alpha}$ in **III**, for instance. As the individual measurement of the H-bond energies is unapproachable,[29] it is not allowed in parts to use them to correct the hydration energies. In accordance with the different H-bond distances given in Table I, the complexes **I**–**III** are certainly formed through an unusual cooperative effect, *i.e.*, an electronic organization derived from the energy distribution among several intermolecular interactions along the supramolecular structure. However, the computations of the H-bond energies of $O\cdots F$ and $F\cdots H$ were made based on the supermolecule approach as follows:

$$CE = E_{\text{O}\cdots\text{H}} + E_{\text{F}\cdots\text{H}} \tag{2}$$

$$E_{\text{O}\cdots\text{H}} = E(\text{C}_2\text{H}_4\text{O}) - 2E(\text{HF}) \text{ and } E_{\text{F}\cdots\text{H}} = E(\text{C}_2\text{H}_4\text{O}\cdots\text{HF}) - E(\text{HF}) \tag{3}$$

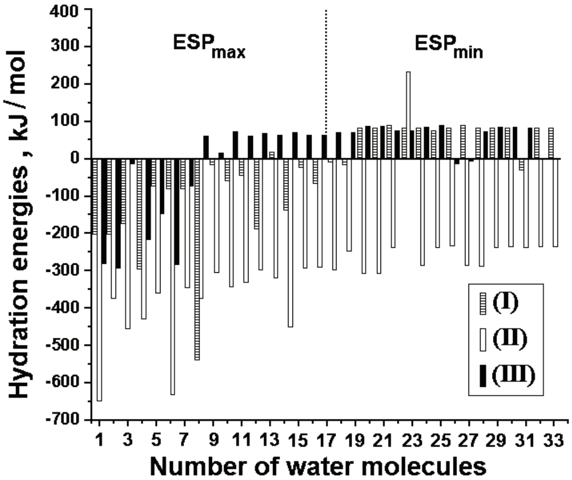

Fig. 3. Acid hydration energies of the three structures (**I**, **II** and **III**) of the $C_2H_4O\cdots HF\cdots HF$ complex.

In practice, the hydration energies could be used to predict accurately the most stable complex as well as which molecular site is the most sensitive to nucleophilic or electrophilic attack. Only to mention, these hydration values were not corrected by BSSE calculations because the counterpoise amounts are often very small. Through *MEP* analysis and after completing the calculations, the AGOA method suggests that the number of water molecules necessary for hydration of complexes **I**, **II**, and **III** are 32, 34 and 30, respectively. Regarding Fig. 3, it can be seen that **I** and **III** are the less stable structures. On the contrary, the hydration energies of **II** are much more stable, although there is one configuration located at a positive *MEP* or $MEP_{\max}$ that indicates a repulsion. This is to some extent surprising because **III** is the most stable structure in vacuum. On the other hand, the solvation of the water molecules on the hydrofluoric acid in **II** is the more appropriate to describe (see Fig. 2) a feasible mechanism for the acid-catalyzed ring-opening reaction of oxirane.

CONCLUSIONS

The acid-catalyzed ring-opening reaction of oxirane was once again studied. In this work, a theoretical survey based on PCM[30] and AGOA[31–34] calculations was presented. The influence of water as solvent was examined in terms of the H-bond properties,[62,63] in particular the distances that were reduced upon the formation of the $C_2H_4O\cdots HF\cdots HF$ complex. In line with this, it was revealed that the structure of this complex rules the specific configurations of the water molecules, and it was not necessary that such a structure was the most stable in the absence of solvent. Based on these evaluations, the acid-catalyzed ring-opening reaction of epoxy was described with shorter H-bond distances for protonation of oxirane, as well as solvation of the water molecules on the second hydrofluoric acid molecule.

SUPPLEMENTARY MATERIAL

Hydration clusters and *MEP* surfaces of the complexes **I**, **II** and **III** are available electronically from http://www.shd.org.rs/JSCS/, or from the corresponding author on request.

Acknowledgements. The author would like to thanks CAPES, CNPq, and FAPESB Brazilian Funding Agencies.

ИЗВОД

УТИЦАЈ РАСТВАРАЧА НА ТЕРНАРНЕ КОМПЛЕКСЕ ЕПОКСИДА И ФЛУОРОВОДОНИЧНЕ КИСЕЛИНЕ

BOAZ G. OLIVEIRA

Institute of Environmental Sciences and Sustainable Development, Federal University of Bahia, Barreiras, Brazil

Испитиван је утицај растварача на тернарне комплексе $C_2H_4O\cdots HF\cdots HF$, применом PCM поступка и рачунањем AGOA методом на B3LYP/6-311++G(d,p) нивоу теорије. Тиме су проверени профили водоничних веза у комплексу, посебно O···H, F···H и $F\cdots H^{\beta}$ контакт. Мерењем дискретне хидратационе енергије, праћени су положаји молекула воде. Анализом електростатичких потенцијала (*MEP*) утврђене су позитивне и негативне области, које одговарају интеракцији са молекулима воде преко кисеоника, односно водоника. На тај начин је интерпретирано киселином-катализовано отварање оксиранског прстена како у вакуму, тако и у воденом раствору.

(Примљено 24. септембра 2014, ревидирано 7. јануара, прихваћено 8. јануара 2015)

REFERENCES

1. R. A. Nome, *J. Braz. Chem. Soc.* **21** (2010) 2189
2. R. Giernoth, *Angew. Chem. Int. Ed. Eng.* **50** (2011) 11289
3. P. L. Geissler, *Ann. Rev. Phys. Chem.* **64** (2013) 317
4. B. G. Oliveira, M. L. L. A. Vasconcellos, *Inorg. Chem. Comm.* **12** (2009) 1142
5. B. G. Oliveira, M. L. L. A. Vasconcellos, *Struct. Chem.* **20** (2009) 897
6. B. G. Oliveira, M. L. L. A. Vasconcellos, R. R. Olinda, E. B. A. Filho, *Struc. Chem.* **20** (2009) 81
7. B. G. Oliveira, R. C. M. U. Araújo, J. J. Silva, M. N. Ramos, *Struc. Chem.* **21** (2010) 221
8. B. G. Oliveira, R. C. M. U. Araújo, A. B. Carvalho, M. N. Ramos, *Spectrochim. Acta A* **75** (2010) 563
9. S. L. Capim, S. R. Santana, B. G. Oliveira, G. B. Rocha, M. L. A. A. Vasconcellos, *J. Braz. Chem. Soc.* **21** (2010) 1718
10. B. G. Oliveira, R. C. M. U. Araújo, E. S. Leite, M. N. Ramos, *Int. J. Quantum Chem.* **111** (2011) 111
11. B. G. Oliveira, L. F. C. C. Leite, *J. Mol. Struct. (THEOCHEM)* **915** (2009) 38
12. B. G. Oliveira, *Comput. Theor. Chem.* **998** (2012) 173

13. B. G. Oliveira, *Phys. Chem. Chem. Phys.* **15** (2013) 37
14. B. G. Oliveira, *Struc. Chem.* **25** (2014) 745
15. M. Orozco, F. J. Luque, *Chem. Rev*. **100** (2000) 4187
16. H. M. Senn, W. Thiel, *Angew. Chem. Int. Ed. Engl*. **48** (2009) 1198
17. J. Tomasi, B. Mennucci, R. Cammi, *Chem. Rev.* **105** (2005) 2999
18. L.-P. Wang, T. Van Voorhis, *J. Chem. Theory Comput*. **8** (2012) 610
19. A. J. A. Aquino, D. Tunega, G. Haberhauer, M. H. Gerzabek, H. Lischka, *J. Phys. Chem. A* **106** (2002) 1862
20. L. Selvam, F. Chen, F. Wang, *Chem. Phys. Lett*. **500** (2010) 327
21. B. G. Oliveira, R. C. M. U. Araújo, *Can. J. Chem*. **90** (2012) 368
22. B. G. Oliveira, R. C. M. U. Araújo, F. F. Chagas, A. B. Carvalho, M. N. Ramos, *J. Mol. Model*. **14** (2008) 949
23. Gaussian 03, Revision B.04, M. J. Frisch, G. W. Trucks, H. B. Schlegel, G. E. Scuseria, M. A. Robb, J. R. Cheeseman, J. A. Montgomery, Jr., T. Vreven, K. N. Kudin, J. C. Burant, J. M. Millam, S. S. Iyengar, J. Tomasi, V. Barone, B. Mennucci, M. Cossi, G. Scalmani, N. Rega, G. A. Petersson, H. Nakatsuji, M. Hada, M. Ehara, K. Toyota, R. Fukuda, J. Hasegawa, M. Ishida, T. Nakajima, Y. Honda, O. Kitao, H. Nakai, M. Klene, X. Li, J. E. Knox, H. P. Hratchian, J. B. Cross, V. Bakken, C. Adamo, J. Jaramillo, R. Gomperts, R. E. Stratmann, O. Yazyev, A. J. Austin, R. Cammi, C. Pomelli, J. W. Ochterski, P. Y. Ayala, K. Morokuma, G. A. Voth, P. Salvador, J. J. Dannenberg, V. G. Zakrzewski, S. Dapprich, A. D. Daniels, M. C. Strain, O. Farkas, D. K. Malick, A. D. Rabuck, K. Raghavachari, J. B. Foresman, J. V. Ortiz, Q. Cui, A. G. Baboul, S. Clifford, J. Cioslowski, B. B. Stefanov, G. Liu, A. Liashenko, P. Piskorz, I. Komaromi, R. L. Martin, D. J. Fox, T. Keith, M. A. Al-Laham, C. Y. Peng, A. Nanayakkara, M. Challacombe, P. M. W. Gill, B. Johnson, W. Chen, M. W. Wong, C. Gonzalez, J. A. Pople, Gaussian, Inc., Wallingford CT, 2004
24. http://www.ufpe.br/farmacia/zaldini/agoa.html (accessed on June, 2004)
25. F. B. van Duijneveldt, J. N. Murrell, *J. Chem. Phys.* **46** (1967) 1759
26. a) L. Laaksonen, J. Mol. Graphics **10** (1992) 33; b) D. L. Bergman, L. Laaksonen, A. Laaksonen, *J. Mol. Graphics Model.* **15** (1997) 301
27. A. Bondi, *J. Phys. Chem.* **68** (1964) 441
28. C. M. Breneman, K. B. Wiberg, *J. Comput. Chem.* **11** (1990) 361
29. B. G. Oliveira, R. C. M. U. Araújo, A. B. Carvalho, M. N. Ramos, M. Z. Hernandes, K. R. Cavalcante, *J. Mol. Struct. (THEOCHEM)* **802** (2007) 91
30. A. Abkowicz-Bieńko, M. Biczysko, Z. Latajka, *Comp. Chem.* **24** (2000) 303
31. M. Z. Hernandes, J. B. P. Silva, R. L. Longo, *J. Braz. Chem. Soc.***13** (2002) 36.
32. M. L. A. A. Vasconcellos, B. G. Oliveira, L. F. C. C. Leite, *J. Mol. Struct. (THEOCHEM)* **860** (2008) 13
33. B. G. Oliveira, R. C. M. U. Araújo, A. B. Carvalho, M. N. Ramos, *Can. J. Chem.* **88** (2010) 338
34. B. G. Oliveira, R. C. M. U. Araújo, A. B. Carvalho, M. N. Ramos, *Quim. Nova* **32** (2009) 1184.

Journal of the Serbian Chemical Society
JSCS@tmf.bg.ac.rs • www.shd.org.rs/JSCS
J. Serb. Chem. Soc. 80 (5) S173–S175 (2015) *Supplementary material*

SUPPLEMENTARY MATERIAL TO

Solvent effect on ternary complexes formed by oxirane and hydrofluoric acid

BOAZ G. OLIVEIRA*

Institute of Environmental Sciences and Sustainable Development (ICADS), Federal University of Bahia, 47801-100, Barreiras – BA, Brazil

J. Serb. Chem. Soc. 80 (5) (2015) 651–658

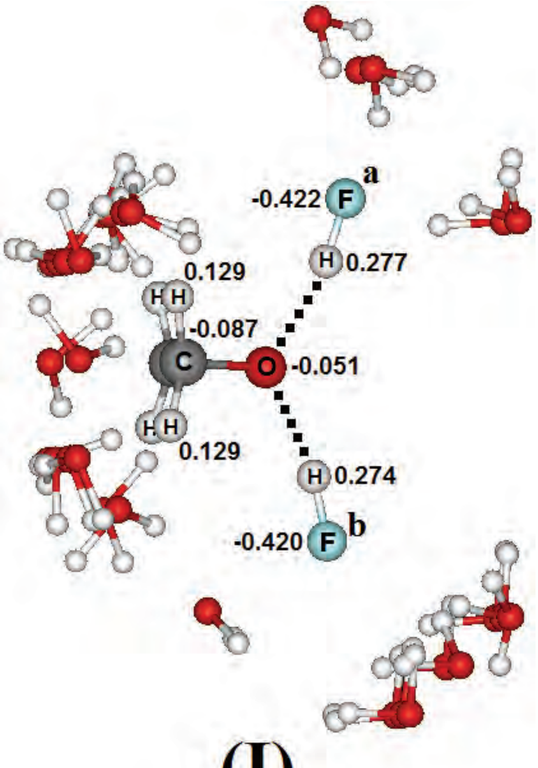

(I)

Fig. S-1. Hydration clusters on the $C_2H_4O\cdots HF\cdots HF$ complex obtained through the AGOA method.

---

* E-mail: boazgaldino@gmail.com

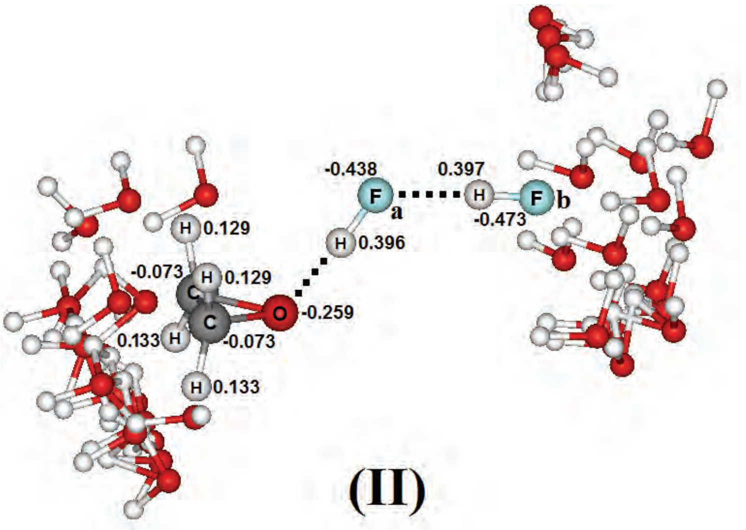

Fig. S-2. Hydration clusters on the $C_2H_4O\cdots HF\cdots HF$ complex obtained through the AGOA method.

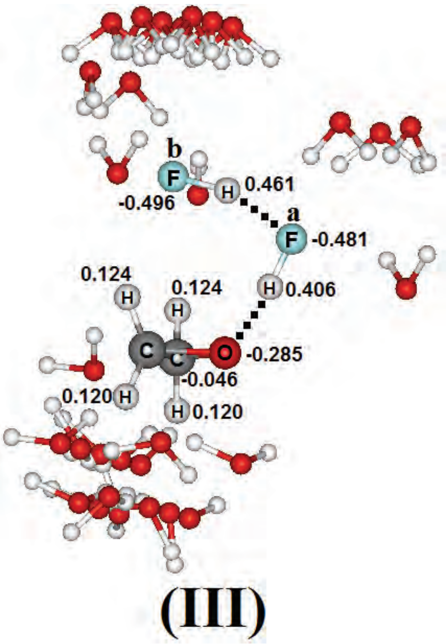

Fig. S-3. Hydration clusters on the $C_2H_4O\cdots HF\cdots HF$ complex obtained through the AGOA method.

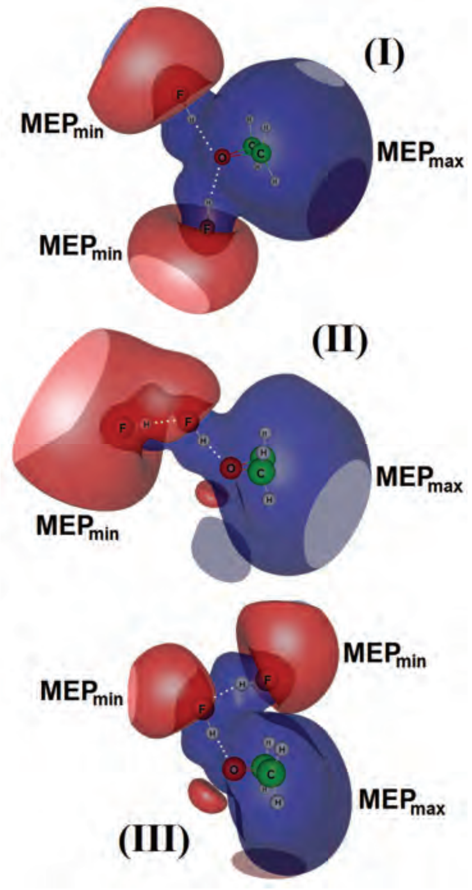

Fig. S-4. *MEP* surfaces of the complexes **I**, **II** and **III**.

Journal of the Serbian Chemical Society

JSCS-info@shd.org.rs • www.shd.org.rs/JSCS

J. Serb. Chem. Soc. 80 (5) 659–671 (2015)
JSCS–4746

UDC 547.53+532.11+54–134+533.75:519.245
Original scientific paper

Quantitative relationships for the prediction of the vapor pressure of some hydrocarbons from the van der Waals molecular surface

TUDOR OLARIU[1]*, VICENŢIU VLAIA[1], CIPRIAN CIUBOTARIU[2], DAN DRAGOŞ[1], DAN CIUBOTARIU[1] and MIRCEA MRACEC[3]**

[1]*Department of Organic Chemistry, Faculty of Pharmacy, "Victor Babes" University of Medicine and Pharmacy, P-ta Eftimie Murgu No. 2, 300041, Timisoara, Romania,* [2]*Department of Computer Sciences, University "Politehnica", P-ta Victoriei No. 2, 300006, Timisoara, Romania and* [3]*Molecular Forecast Research Center, Prof. Dr. Aurel Păunescu-Podeanu str. 125, A 4, RO-300588 Timişoara, Romania*

(Received 16 April, accepted 17 May 2014)

Abstract: A quantitative structure–property relationship (QSPR) modeling of vapor pressure at 298.15 K, expressed as log (VP / Pa) was performed for a series of 84 hydrocarbons (63 alkanes and 21 cycloalkanes) using the van der Waals (vdW) surface area, S^W / Å^2, calculated by the Monte Carlo method, as the molecular descriptor. The QSPR model developed from the subset of 63 alkanes (C_1–C_{16}), deemed as the training set, was successfully used for the prediction of the log (VP / Pa) values of the 21 cycloalkanes, which was the external prediction (test) subset. A QSPR model was also developed for a series composed of all 84 hydrocarbons. Both QSPR models were statistically tested for their ability to fit the data and for prediction. The results showed that the vdW molecular surface used as molecular descriptor (MD) explains the variance of the majority of the log (VP / Pa) values in this series of 84 hydrocarbons. This MD describes very well the intermolecular forces that hold neutral molecules together. The clear physical meaning of the molecular surface values, S^W / Å^2, could explain the success of the QSPR models obtained with a single structural molecular descriptor.

Keywords: MD – molecular descriptor; van der Waals molecular surface; Monte Carlo method; QSPR.

INTRODUCTION

Equilibrium vapor pressure is defined as the pressure exerted by a vapor in thermodynamic equilibrium with its condensed phase (solid or liquid) in a closed system under standard conditions (298.18 K and p = 100 kPa).

---

*,** Corresponding authors. E-mail: (*)olariu.t@umft.ro; (**)mirceamracec@yahoo.com

doi: 10.2298/JSC140416051O

Vapor pressure, VP, plays an important role in the study of the environmental fate, transport and distribution of the compounds in water, air and soil, as well as for engineers designing chemical processes.[1] The distribution of environmental pollutants between the soil and the atmosphere is determined by their VP. It is also used for calculating other physicochemical properties, such as liquid viscosity, enthalpy of vaporization, air–water partition coefficients, rates of evaporation and distribution coefficients for adsorption on soil.[2]

Experimental vapor pressure data are abundant for low molecular weight hydrocarbons, but the measurements can be difficult to realize, and even unreliable in certain ranges. If the experimental data are missing, the only option is to predict the vapor pressure of various compounds using a quantitative structure–property relationship (QSPR).[3] Another difficulty is related to the fact that experimental VP measurement of actual chemical products is both time-consuming and expensive. The equations of state for the calculation of vapor pressure exist, but these typically require experimental determinations at a minimum of two temperatures. Most reported QSPR studies to predict vapor pressure still depend on various empirical data, such as boiling points, critical pressures, and critical temperatures[1] but, unfortunately, boiling points as well as critical properties are often lacking, especially for heavy hydrocarbons many of them are thermally unstable in the critical region.[2] Therefore, QSPR is an alternative approach for estimating vapor pressure based on the premise that physicochemical properties can be correlated with molecular structural characteristics expressed in terms of appropriate molecular descriptors. When a quantitative structure–property relationship is found, it might also provide insight into which aspect of the molecular structures influences the property. Such insight may facilitate a systematic approach to the design of new molecules with more desirable properties.[1]

Earlier, a QSPR study of boiling points of a series of alkanes based on comparative analysis of the molecular vdW space and topological space of these compounds with the aid of 36 molecular descriptors: 16 generalized topological distance matrix indices (GTDIs), 11 topological distance indices (TDIs) known in the literature (seven obtained from eigenvalues/eigenvectors of distance matrix), and 9 van der Waals molecular descriptors has been reported.[4]

Herein, it is supposed that the molecular van der Waals surfaces of hydrocarbons are responsible of their vapor pressure values. Intermolecular forces hold neutral molecule to each other. These forces involve attraction of charges of opposite signs. The attractive forces between the molecules of a non-polar compound, such as alkanes and cycloalkanes, are called van der Waals (vdW) forces. They are of the induced dipole–induced dipole type (dispersion forces),[4] and they act only at very short distances, between the parts of different molecules that are in close contact, *i.e.*, between the surfaces of molecules. These vdW forces holding non-polar molecules together are weak and of very short range. Therefore, within the class of hydrocarbons, the larger is the molecule, the larger is its surface, the stronger are the intermolecular forces, and, hence, the lower will the VP value be.

The aim of this paper is to propose a statistically validated QSPR model for vapor pressure prediction of 84 saturated hydrocarbons (63 alkanes and 21 cycloalkanes) and to develop a QSPR model for the series 63 alkanes that will be used to predict the log (*VP* / Pa) values for the series of 21 cycloalkanes. The models were based mainly of the vdW molecular surface, S^{W} / Å^2, which was used as a unique molecular descriptor. Regression analysis[5] was applied for the development of the QSPR models log (*VP* / Pa) *vs*. S^{W} / Å^2. The S^{W} values of these hydrocarbons were estimated with IRS software.[6] IRS (Investigation Receptor Space) implements numerical algorithms developed based on the Monte Carlo (MC) method for computation of various vdW molecular characteristics – the so-called molecular descriptors (MDs) – used for the study of relationships between the molecular structure and a variety of properties of chemical compounds.[4,7–17]

EXPERIMENTAL DATA

The experimental data used in this QSPR study were taken from the literature.[18] The values of experimental vapor pressures at 298.15 K were expressed as log (*VP* / Pa). The structures included 63 alkanes and 21 cycloalkanes. The data set containing the 63 alkanes was used as a training set (see Table S-I of the Supplementary material to this paper). In order to validate the predictive ability of the training set model (see, below, relation (7)), the series of 21 cycloalkanes (Table S-I) was used as an external prediction set. The values of log (*VP* / / Pa) for all hydrocarbons are systematized in Table S-I, together with the corresponding vdW surface, S^{W} / Å^2, values calculated by means of the Monte Carlo method with IRS software.[6] Table S-I also contains the predicted log (*VP* / Pa) values with the linear Model (7) and the errors, Δ, calculated as difference between experimental and the corresponding predicted log (*VP* / Pa) values.

Methods

The analysis of the relationship between the vapor pressure of the hydrocarbons in Table S-I and their molecular structure was performed using regression analysis as a statistical tool for the development of reliable QSPR models.

Below, the Monte Carlo integration algorithm implemented in IRS and used for the calculation of hydrocarbon surface areas (S^{W}) in Table S-I is presented, together with some general aspects of the regression analysis and statistics used for the validation of the developed QSPR models.

Molecular van der Waals surface. The space occupied by an alkane molecule (interacting with the other molecules) can be described within the frame of the "hard sphere approximation" as follows: each atom of a molecule is represented by an isotropic sphere having the centre in the equilibrium position of the atom and a radius equal to its vdW radius, r^{w}. Consequently, a molecular vdW envelope, $\mathbf{\Gamma}$, can be defined as the external surface resulting from the intersection of all vdW spheres. This envelope embeds a 3D space of volume V^{W} and surface S^{W}. The points (x,y,z) disposed within the envelope **Γ** satisfy one and only one of the following inequalities:

$$(X_i-x)^2+(Y_i-y)^2+(Z_i-z)^2\le(r_i^{\mathrm{W}})^2 \quad i=1,2,\ldots,m \tag{1}$$

The point (X_i,Y_i,Z_i) represent the center of an atomic sphere i (i = 1,…,m), and m represents the number of atoms in a molecule M.

The molecular van der Waals envelope, **Γ**, defined by relation (1), is a surface. The calculation of the area of this surface should be made by means of the MC method.[7,11,19]

The MC algorithm[7,11] used for the calculation of the S^{W} value for the alkanes and cycloalkanes in Table S-I implies the random generation of a uniform grid (composed of n_{t} points) on each sphere i (i = 1,2,…,m) of the molecule M. After the generation of the total number of points on the surface (n_{t}), the detection of those points (n_{e}) that do not satisfy the inequalities in (1) follows. For every "hard sphere" i, the outer part of its surface, S_i^{W}, is computed:

$$S_i^{\mathrm{W}}=\frac{(n_{\mathrm{e}})_i}{n_{\mathrm{t}}}4\pi\left(r_i^{\mathrm{W}}\right)^2 \tag{2}$$

The final surface of hydrocarbon molecules in Table S-I is computed as the sum of the exterior surface, S_i^{W}, of each sphere:

$$S^{\mathrm{W}}=\sum_{i=1}^{m}S_i^{\mathrm{W}} \tag{3}$$

As was seen,[7-10,16,17] the vdW radius is a successful concept for the computation of molecular size and shape descriptors, even if in a quantum chemical description the electron cloud has no well-defined boundary surface. The values of the surface area of alkanes and cycloalkanes in Table S-I were computed using the Bondi vdW radii measured from various physicochemical properties.[20]

Regression analysis. Regression analysis is generally realized by a correlation equation of the following type:[6]

$$y_n=\beta_1x_1+\beta_2x_{n2}+\cdots+\beta_px_{p1}+z_n=\left(x_{n1},\cdots,x_{np}\right)\beta+z_n \tag{4}$$

where y_n are the VP values and the matrix **X** = (x_{n1},…,x_{np}) contains the predictor variables, *i.e.*, the structural parameters (MDs) of the compounds from the studied series.

Linear regression provides estimates and other inferential results for the (statistical) parameters $\beta = (\beta_1, \beta_2,\ldots,\beta_{\mathrm{p}})^{\mathrm{T}}$ in the model (4). In this model, the random variable y_n, which represents the response for the case n, n = 1,2,…,N, which has a deterministic part and a stochastic part. The deterministic part, $(x_{\mathrm{n1}},\ldots,x_{\mathrm{np}})\beta$, depends on the parameter β and on the predictor or regression variables x_{np}, p = 1,2,…,P. The stochastic part, represented by the random variable z_n, is a disturbance that perturbs the response for that case. The superscript $^{\mathrm{T}}$ denotes the transpose of a matrix.

The model for N cases can be written as follows:

$$\mathbf{Y}=\mathbf{X}\beta+\mathbf{Z} \tag{5}$$

where **Y** is the vector of random variables represented the experimental data one may obtains, **X** is the $N\times P$ matrix of regression variables, *i.e.*, the molecular structural parameters and/or the physical and chemical properties (especially for QSAR studies) and **Z** is the vector of variables representing the disturbances; one assumes that **Z** is normally distributed. The maximum likelihood estimate $\hat{\beta}$ is the value of β that minimizes $S(\beta)$:

$$S\left(\beta\right) = \mathbf{Y} - \mathbf{X}\beta^2 = \sum_{n=1}^{N}\left[y_n - \left(\sum_{p=1}^{P} x_{np}\beta_p\right)\right]^2 \tag{6}$$

This β is called the least squares estimate and can be written: $\beta = (\mathbf{X}^{\mathrm{T}}\mathbf{X})^{-1}\mathbf{X}^{\mathrm{T}}\mathbf{Y}$.

Once the QSPR model is built, its goodness of fit is evaluated by means of the following statistical parameters: the correlation coefficient (r) and the coefficient of determination (r^2), adjusted for the degree of freedom r^2_{adj}, which is also called explained variance, (*EV*). The uncertainty in the model was noted as the standard error (s), and the reliability in the model was expressed by *F*- (Fisher) and *t*-(Student) statistics. The *t*-test was used to determine the 95 % confidence limits of the developed QSPR model.[7]

The statistical fit should not be confused with the ability of a model to make predictions. Therefore, the leave-one-out (LOO) and the leave-*n*-out (L-*n*-O) cross-validation methods to estimate the predictive ability of the obtained QSPR model, using the cross-validation coefficient (also called coefficient of predictions), q^2, and the squared correlation coefficient between the predicted and experimental properties, R^2 (see Fig. 2) was used.[21,22] In the LOO procedure, a value of $q^2 > 0.5$ is acceptable.[21]

Finally, the chance correlation in the developed QSPR was been checked by scrambling the VP response values (*Y*-scrambling) and trying to build a model using the scrambled data. This procedure was then repeated, say, 100 times and the r^2 values were checked against that for the actual QSPR: if only one of the r^2 values from the scrambled data is as high as that from actual QSPR, then there is 1 % risk that the real QSPR is a chance correlation.[23]

In this study, only S^{W} was used as a MD of the molecular size of hydrocarbon molecules. Consequently, the matrix **X** of the predictor variables contains a single MD, $\mathbf{X} = (S^{\mathrm{W}})$, and the above Eq. (4) is a simple linear model.

RESULTS AND DISCUSSIONS

Hitherto, the proposed vapor pressure QSPRs were limited to predicting VP at a constant temperature, using five or more linear correlation models based on topostructural, topochemical, and geometrical type descriptors.[18] The interpretation of these QSTRs was difficult in terms of an interaction model between the molecular entities because, commonly, the physical meaning of topological indices was not clear.

Here, a simple linear model is presented, which was developed based on the vdW surface area of hydrocarbons, S^{W}. It is known that vdW forces act at very short distances and are responsible for the intermolecular forces manifested between non-polar molecules, such as hydrocarbons. Consequently, it may be supposed that these forces act between the surfaces of molecules. S^{W} is a molecular feature that could explain the intermolecular interactions that occur in the physical process of the vaporization of a given chemical substance at a specified temperature.

All statistical calculations were realized by means of MobyDigs software.[23] First, the *VP* / Pa values for the hydrocarbons in Table S-I of the Supplementary material were used as experimental values in the training set. The cycloalkanes in Table S-I of the Supplementary material were used as an external prediction (test) set. The values of surface area, S^{W} / Å^2, of alkanes and cycloalkanes in Table S-I were calculated with in house developed IRS software.[6] Secondly, the entire set of alkanes and cycloalkanes (in Table S-I) was used as test set, and the obtained QSPR model was analyzed for its predictive ability by the cross-validation procedures described above.

The range of vapor pressure values measured at 298.15 K was about 8 logarithmic Pa units (see Table S-I). The values of vdW surface varied from 48.54 Å^2 (the smallest studied hydrocarbon molecule, methane) to 377.78 Å^2 (the largest studied alkane molecule, *n*-hexadecane). The range of S^{W} values was about 330 Å^2, and the ratio between the maximal and minimal values was also about 8. Consequently, one logarithmic unit corresponds to about (40 Å^2). Therefore, the discrimination capability of the S^{W} molecular descriptor for this QSPR study was good.

The training process involves using a dataset with known values, and learning a model from that dataset. However, it is possible that models fit the training dataset very well, but they may fail to predict new data points. Such over-fitting of the training data will most likely yield a model that cannot be generalized and, therefore, would not be useful. Thus, an algorithm and its associated parameters must be validated before they are used to predict new data. This process involves segmenting the entire data set into two subsets. One set is used for training and the other for testing the model.

By correlating the vapor pressures at 298.15 K (A = log (*VP* / Pa), with the vdW surface areas (S^{W} / Å^2) for the 63 alkanes in Table S-I, used as the training set, the following linear QSPR model was obtained:

$$\log\left(VP/\ \mathrm{Pa}\right)=8.237\left(\pm 0.0779\right)-0.0242\left(\pm 0.0004\right)S^{\mathrm{W}} \tag{7}$$

$$N = 63;\ r^2 = 0.986;\ r^2_{\mathrm{adj}} = 0.985;\ s = 0.173;\ F = 4072.5$$

The QSPR Model (7) has good statistical quality for fitting the calculated VP values to the experimental ones. Thus, 98.5 % of the variance of experimental *VP* values is explained by this model, the confidence limits of the model parameters are less than 4 %, and the standard error is less than 3 % of the domain of log (*VP* / / Pa). The parameters of model (7) are significantly different from the zero value. This model was tested to evaluate its predictive ability, as shown below.

The robustness of Model (7) and its internal predictive ability were evaluated by both the q^2 cross validation coefficient based on the leave-one-out (LOO) and bootstrap procedures. In the bootstrap technique, M n-dimensional groups are randomly selected from the original data set in Table S-Ia. The model obtained on the first selected objects is used to predict the remaining values, and then q^2 is calculated for each model. The bootstrapping was repeated 100 times for each validated model. The values of cross validation coefficients for LOO $\left(q^2_{\text{LOO}}\right)$ and bootstrapping $\left(q^2_{\text{BOOT}}\right)$ procedures are given in Table I.

TABLE I. Statistics corresponding to the QSPR Linear Model (7); they were obtained by LOO $\left(q^2_{\text{LOO}}\right)$, bootstrapping $\left(q^2_{\text{BOOT}}\right)$, and Y-scrambling $\left(r^2_{\text{Y-scr}}, q^2_{\text{Y-scr}}\right)$ procedures, and the standard deviations (errors) of the predicted (*SDEP*) and calculated (*SDEC*) values; the values were obtained by cross-validation with MobyDigs software[23]

Eq.	q^2_{LOO}	q^2_{BOOT}	$r^2_{\text{Y-scr}}$	$q^2_{\text{Y-scr}}$	*SDEP*	*SDEC*
(7)	0.983	0.982	–0.037	–0.108	0.181	0.170
(8)	0.988	0.987	–0.039	–0.106	0.144	0.140
(9)	0.929	0.927	–0.035	–0.085	0.341	0.331

Model (7) was also checked for reliability, robustness and chance correlation by applying the Y-scrambling method of the MobyDigs computer programs.[23] The basis of the Y-scrambling technique is the permutation concept, in which new models are recalculated for randomly reordered experimental vapor pressure values A_i = log (VP_i / Pa), i = 1,2,…,63, and the corresponding values of the cross-validation coefficients, $q^2_{\text{Y-scr}}$, were computed. These new models should have significantly lower $q^2_{\text{Y-scr}}$ values than the proposed ones because of the linear relationship between the predictor variables that describe the molecular structure (molecular surface S^{W} of the hydrocarbons in Table I) and the response A is broken. This is proof of the validity of the proposed model because it can be reasonably concluded that the originally proposed model was not obtained by chance correlation. For Model (7), the A *vs.* S^{W} Y-scrambling procedure was performed by A scrambling with 100 iterations. The values of the statistical parameters obtained by applying the *Y*-scrambling method to the data in Table S-I are summarized in Table I.

In this way, the QSPR Model (7) was statistically validated. It was then used to predict the log (*VP* / Pa) values not only for the alkanes, but also for the log (*VP* / Pa) values of the cycloalkanes in Table S-I. It is important to emphasize that the results of cross-validation and bootstrapping procedures presented above only assess the internal predictive ability of the developed Model (7), and this fact validates the use of this model to predict the values of alkanes (see A_{pred} values in Table S-I). Analyses of the deviations of the calculated (predicted) log (*VP* / Pa) values in Table S-I allowed the consideration of the point represented by methane (C1) as an outlier. The linear equation resulting when this point was eliminated from correlation is the following:

$$\log\left(VP/\text{ Pa}\right) = 8.106\left(\pm 0.137\right) - 0.0236\left(\pm 0.0007\right)S^{\text{W}} \tag{8}$$

$$n = 62;\ r^2 = 0.988;\ r^2_{\text{adj}} = 0.988;\ s = 0.143;\ F = 5075.3$$

The results of the predictive ability of the QSPR Model (8) are also presented in Table I. By elimination of this point, the goodness of fit, the reliability and the robustness of the QSPR Model (7) were not significantly improved. The point corresponding to the methane is not a real outlier because there is no reason to eliminate it from the correlation. An outlier usually indicates a data point that is not at all typical for the rest of the data set and/or does not operates by the same mechanism. In this case, methane is the first term of the homologous series of alkanes and all hydrocarbon molecules are hydrophobic. Probably methane is an outlier because it is not polar, while the other molecules are slightly polar. Therefore, one may suppose that the intermolecular forces responsible of their vapor pressure are, in essence, of the same type.

An external predictive ability of the linear Model (7) would provide a more rigorous evaluation of the capability of the model to predict log (*VP* / Pa) values for chemicals with unknown VP values. In this investigation, Model (7) was externally validated on a series of structurally different compounds, namely the cyclic hydrocarbons presented in Table S-I. The predicted log (*VP* / Pa) values for the series of 21 cycloalkanes calculated with Eq. (7) are also given in Table S-I, together with their deviations from the corresponding measured log (*VP* / Pa) values.

It is known that alkane molecules are characterized by staggered conformations, which is most stable conformation because the carbon–hydrogen bonds of the vicinal non-bonded atoms are as far removed from each other as possible and, on the contrary, the eclipsed conformation is the least stable conformation because the C–H bonds are close to one another. In fact, the eclipsed conformations should be viewed as transition states between the staggered conformations, and they are very short lived. The supplementary energy of the eclipsed conformations is called torsional strain. The most stable of the staggered conformers is called the ANTI (A) conformer. However, beginning with *n*-butane, other staggered conformers exist, which are called GAUCHE (G) conformers. ANTI and GAUCHE conformers do not have the same energy because of steric strain (Fig. 1).

At room temperature, the barrier energy between staggered and eclipsed conformations is very small. Therefore, there is enough thermal energy in the surroundings to allow the conformational isomers to interconvert many times per second. Obviously, the more stable the conformation, the greater the number of molecules that will be in that conformation.

The S^{W} / Å^2 values of alkane molecules are calculated only for the most extended *anti* conformation. This fact could explain the small differences between the experimental and predicted (calculated) values of log (*VP* / Pa) for the same alkane molecule in Table S-I. Thus, neglecting the smallest molecule, CH_4 (C1), the maximum deviation of the predicted log (*VP* / Pa) values was –0.446, which represents less than 6 % from the range of experimentally measured log (*VP* / Pa) values. It could be concluded that Model (7) predicts well the log (*VP* / Pa) values of alkanes, within the limits of the accuracy and precision of experimental measurements. This fact may be very well observed in Fig. 2 that contains the linear relationship between the experimental and the predicted log (*VP* / Pa) values for the 63 hydrocarbons in Table S-Ia, calculated with Eq. (7).

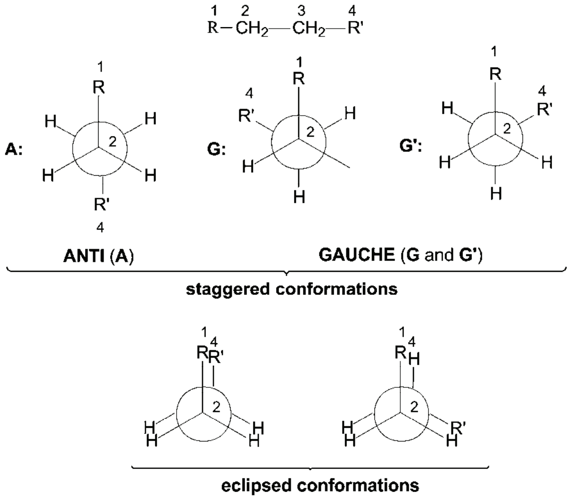

Fig. 1. Newman projection of the staggered and eclipsed conformation of an alkane molecule.

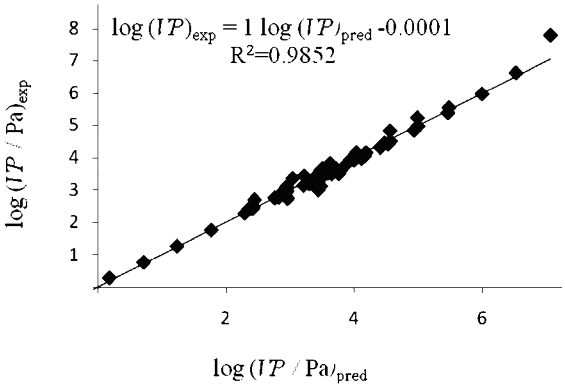

Fig. 2. Experimental log (*VP* / Pa) values *vs*. the predicted values for the alkanes in the training set.

A systematic deviation of the predicted log(*VP* / Pa) values of the cycloalkanes could be observed in Table S-I. This is, probably, due to the difference in the structural three-dimensional (3D) characteristics of the acyclic and cyclic hydrocarbons, respectively, which were reflected in the variation of their surface area values between the members of each homologous series. The deviations in the predicted log (*VP* / Pa) values of the cycloalkanes from the regression line

Eq. (7) are, obviously, greater than those for the alkanes. The regression line between the experimental values and predicted log (*VP* / Pa) values for the cycloalkanes, calculated using Eq. (7), is presented in Fig. 3.

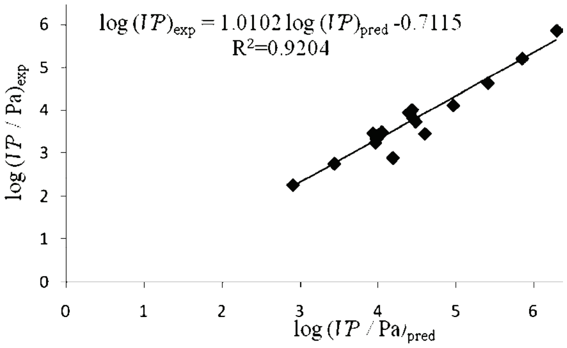

Fig. 3. Experimental values *vs*. predicted log(*VP* / Pa) values for the cycloalkanes in the test set.

To explain these results, the energetic aspects of cycloalkane molecules have to be taken into consideration. There are three kinds of internal strain that can destabilize a cyclic compound: angle strain, torsional strain and steric strain. Deviation of bond angles from the tetrahedral bond angle (109°29′) generates angle strain. Torsional strain is caused by repulsion between the bonding electrons of adjacent non-bonded atoms or substituents. Steric strain is produced by the approach of atom groups to a distance less than to their vdW distance. Cyclic molecules bend and twist in order to achieve a final structure that minimizes these strains. These steric requirements could be a reason for the observed systematic deviations of the predicted log (*VP* / Pa) values. A short analysis of this subject is given in Table II.

The increments of a methylene group corresponding to alkane and cycloalkane molecules are approximately constant, as may be seen in Table II. This is just the difference in the surface area between the vicinal compounds from the corresponding homologous series. On the contrary, the difference in the surface area of a methylene group (CH_2) between the alkanes and cycloalkanes with the same number of carbon atoms in the molecule (see the corresponding values in Table II) varies considerably from cyclopropane 12.317 Å^2 to cyclooctane 34.812 Å^2. This fact could explain the constant deviations of all the cycloalkanes log (*VP* / Pa) values predicted with the QSPR Model (7), developed based on the surface area of alkanes in Table S-I. The cycloalkane molecules are more compact; this fact is reflected much more in their surface area, less than that the surface area of alkane molecules with the same number of carbon atoms.

Taking into consideration the entire series of alkanes and cycloalkanes in Table S-I, the obtained QSPR linear model was the following:

$$\log\left(VP/\ \mathrm{Pa}\right) = 7.7709\left(\pm 0.1309\right) - 0.0226\left(\pm 0.0007\right) S^{\mathrm{W}} \qquad (9)$$

$$n = 84;\ r^2 = 0.933;\ r^2_{\rm adj} = 0.932;\ s = 0.3348;\ F = 1142.4$$

TABLE II. The variation of the surface area of a methylene group ($S^{\rm W}_{\rm CH_2}$): a) between the vicinal terms of the homologous series of alkanes; b) between the vicinal members of the homologous series of cycloalkanes; c) among the alkanes and cycloalkanes with the same number of carbon atoms in the molecule; $S^{\rm W}_{\rm CH_2} = S^{\rm W}({\rm C}n{+}1) - S^{\rm W}({\rm C}n)$, $n = 1,2,\ldots,16$; $S^{\rm W}_{\rm CH_2} = S^{\rm W}({\rm CyC}n{+}1) - S^{\rm W}({\rm CyC}n)$, $n = 1,2,\ldots,8$; $S^{\rm W}_{\rm CH_2} = S^{\rm W}({\rm C}n) - S^{\rm W}({\rm CyC}n)$, $n = 3,4,\ldots,8$

No.	C*n*	$S^{\rm W}$ / Å^2	$S^{\rm W}_{\rm CH_2}$ / Å^2	No.	CyC*n*	$S^{\rm W}$·/ Å^2	$S^{\rm W}_{\rm CH_2}$ / Å^2	$S^{\rm W}_{\rm CH_2}$ / Å^2
56	C1	48.541	–	1	CyC3	80.531	–	12.317
1	C2	70.896	22.355	2	CyC4	98.905	18.374	15.926
2	C3	92.848	21.952	3	CyC5	117.025	18.120	19.591
3	C4	114.831	21.983	4	CyC6	135.333	18.308	23.256
5	C5	136.616	21.785	5	CyC7	150.489	15.156	29.966
8	C6	158.589	21.973	6	CyC8	167.417	16.928	34.812
21	C8	202.229	21.774					
38	C9	224.104	21.875					
57	C10	246.018	21.914					
58	C11	267.742	21.724					
59	C12	289.892	22.150					
60	C13	311.469	21.577					
61	C14	333.608	22.139					
62	C15	355.375	21.767					
63	C16	377.377	22.002					

Model (9) has the ability to fit well the experimental vapor pressure values of both the alkanes and cycloalkanes in Table S-I (84 compounds). The predictive power of this model was estimated with the statistics summarized in Table I. The values of the coefficients of prediction, $q^2_{\rm LOO}$ and $q^2_{\rm BOOT}$, are significantly greater than the limit value, $q^2 = 0.500$. These facts are reflected in Fig. 4, which presents the regression line between the experimental vapor pressure values, log (*VP* / Pa)$_{\rm exp}$, and the corresponding predicted values, log (*VP* / Pa)$_{\rm pred}$, which were calculated using Eq. (9).

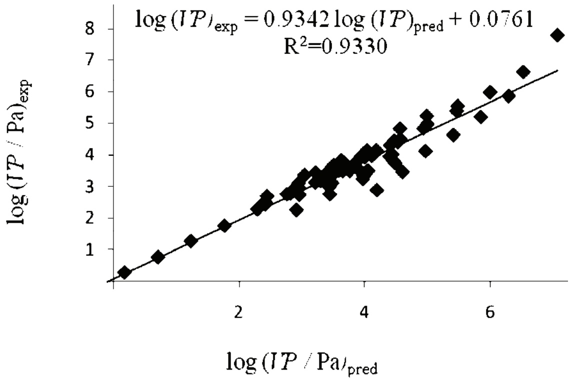

Fig. 4. Experimental log (*VP* / Pa) values *vs.* predicted values for the entire series of hydrocarbons in Table S-I.

CONCLUSIONS

The most important objective of this study was to investigate the usefulness of the vdW molecular surface area, S^{W} / Å^2, as a molecular descriptor for QSPR studies.

A QSPR approach using S^{W} values as the MD was successfully applied to a series of 84 hydrocarbons (alkanes and cycloalkanes) with vapor pressure values measured at 298.15 K, log (*VP* / Pa). QSPR equations with this single theoretical molecular descriptor of the vdW molecular space, S^{W}, were obtained for two subsets comprised of 63 alkanes (training set) and 21 cycloalkanes (prediction set). The S^{W} / Å^2 values were calculated solely from the three-dimensional chemical structures of the compounds with a Monte Carlo algorithm implemented in in-house developed software Investigation of Receptor Space (IRS), and have a clear physical meaning corresponding to intermolecular interactions. All the developed QSPR models were tested with good results for their ability of prediction and fitting the data according to the corresponding statistics.

The log (*VP* / Pa) values of cycloalkanes were predicted well by the QSPR model developed for the subset of alkanes as the training set. The observed small systematic deviations of these values from the linear equation obtained for the training set were explained by the difference in the structural 3D characteristics in the series of cyclic and acyclic hydrocarbons, respectively. This difference was measured by the S^{W} / Å^2 values between the members of each homologous series. A general QSPR model for all 84 hydrocarbons was also proposed.

This study shows that a QSPR model could be obtained by means of a single molecular descriptor when this MD has a definite physical meaning.

SUPPLEMENTARY MATERIAL

Vapor pressure data sets for alkanes and cycloalkanes are available electronically from http://www.shd.org.rs/JSCS/, or from the corresponding author on request.

ИЗВОД

КВАНТИТАТИВНЕ РЕЛАЦИЈЕ ЗА НАПОН ПАРЕ НЕКИХ УГЉОВОДОНИКА ИЗ ПОЗНАВАЊА ВАН ДЕР ВАЛСОВЕ МОЛЕКУЛСКЕ ПОВРШИНЕ

TUDOR OLARIU[1], VICENŢIU VLAIA[1], CIPRIAN CIUBOTARIU[2], DAN DRAGOŞ[1], DAN CIUBOTARIU[1]
и MIRCEA MRACEC[3]

[1]*Faculty of Pharmacy, "Victor Babes" University, Timisoara, Romania,* [2]*Department of Computer Sciences, University "Politehnica", Timisoara, Romania u* [3]*Molecular Forecast Research Center, Timişoara, Romania*

Извршено је QSPR моделовање напона паре на 298.15 K, у облику log (*VP* / Pa), за 84 угљоводоника (63 алкана иу 21 циклоалкана). Као молекулски дескриптор употребљене су ван дер Валсове (*van der Waals*, vdW) површине, S^{W} / Å^2, израчунате методом Монте Карло. QSPR модел је развијен на подскупу од 63 алкана (C_1–C_{16}), а затим је успешно примењен за предвиђање log (*VP* / Pa)-вредности 21 циклоалкана. Један други QSPR модел је конструисан на бази свих 84 угљоводоника. Оба QSPR модела су статистички тестирани. Резултати показују vdW молекулска површина може да објасни највећи део log (*VP* / Pa)-вредности, и на тај начин да објасни међумолекулске силе које де-

лују између неутралних молекула. Јасан физички смисао молекулске површине, S^{W} / Å^{2}, може да објасни успешност QSPR модела са једним јединим молекулским дескриптором.

(Примљено 16. априла, прихваћено 17. маја 2014)

REFERENCES

1. C. Liang, D. A. Gallagher, *J. Chem. Inf. Comput. Sci.* **38** (1998) 321
2. D. Yaffe, Y. Cohen, *J. Chem. Inf. Comput. Sci.* **41** (2001) 463
3. H. E. McClelland, P. Jurs, *J. Chem. Inf. Comput. Sci.* **40** (2000) 967
4. D. Ciubotariu, M. Medeleanu, V. Vlaia, T. Olariu, C. Ciubotariu, D. Dragos, C. Seiman, *Molecules* **9** (2004) 1053
5. N. R. Draper, H. Smith, *Applied Regression Analysis*, Wiley, New York, 1981
6. IRS Computer program, http://irs.cheepee.ro/ (accessed in May, 2015)
7. D. Ciubotariu, *PhD Thesis*, Polytechnic Institute of Bucharest, Bucharest, 1987
8. I. Niculescu-Duvaz, D. Ciubotariu, Z. Simon, N. Voiculetz, in *Modeling of Cancer Genesis and Prevention*, N. Voiculetz, A. T. Balaban, I. Niculescu-Duvaz, Z. Simon, Eds., CRC Press, Boca Raton, FL, 1991, p. 157
9. A. Chiriac, D. Ciubotariu, Z. Simon, *Quantitative Structure – Activity Relationship (QSAR). The MTD Method*, Mirton, Timisoara, 1996
10. D. Ciubotariu, V. Gogonea, M. Medeleanu, in *QSPR/QSAR Studies by Molecular Descriptors*, M. V. Diudea, Ed., NOVA Science Publishers, Huntington, New York, 2000, p. 281
11. V. Gogonea, D. Ciubotariu, E. Deretey, I. Iorga, M. Medeleanu, *Rev. Roum. Chim.* **36** (1991) 465
12. D. Ciubotariu, V. Gogonea, E. Deretey, A. Chiriac, Z. Simon, *Reprint, Univ. Timisoara, Ser. Chim.* **3**, 1987
13. V. Gogonea, A. Motsenigos, D. Ciubotariu, E. Delete, A. Chiriac, Z. Simon, *Reprint, Univ. Timişoara, Fac. St. Nat. Ser. Chim.* **1**, 1987
14. M. Medeleanu, D. Dragoş, T. Olariu, V. Vlaia, C. Ciubotariu, C. Seiman, D. Ciubotariu, *Chem. Bull. Politehnica Univ.* **49** (2004) 8
15. C. Ciubotariu, M. Medeleanu, D. Ciubotariu, *Chem. Bull. Politehnica Univ. Timisoara*, **51 (**2006) 13
16. D. Ciubotariu, V. Vlaia, C. Ciubotariu, T. Olariu, M. Medeleanu, in *Quantum Frontiers of Atoms and Molecules*, M. V. Putz, Ed., Nova Science Pub., Huntington, New York, 2010, p. 629
17. D. Ciubotariu, V. Vlaia, C. Ciubotariu, T. Olariu, M. Medeleanu, in *Carbon Bonding and Structures. Advances in physics and chemistry*, M. V. Putz, Ed., Springer, Dordrecht, 2011, p. 337
18. A. R. Katritzky, S. H. Slavov, D. A. Dobchev, M. Karelson, *Comput. Chem. Eng.* **31** (2007) 1123
19. S. M. Ermakov, *Metoda Monte Carlo şi probleme înrudite*, Ed. Tehnică, Bucureşti, Romania, 1976 (in Romanian)
20. A. J. Bondi, *J. Phys. Chem.* **68** (1964) 441
21. K. H. Esbensen, *Multivariate Data Analysis-In Practice*, CAMO Process AS, Oslo, 2004
22. P. Gedeck, B. Rohde, C. Bartel, *J. Chem. Inf. Model.* **46** (2006) 1924
23. MobyDigs v.1.1, Talete srl., *via* V. Pisani, 13-20124, Milano, http://www.talete.mi.it (accessed May, 2015).

Journal of the Serbian Chemical Society
JSCS@tmf.bg.ac.rs • www.shd.org.rs/JSCS

J. Serb. Chem. Soc. 80 (5) S176–S178 (2015)
Supplementary material

SUPPLEMENTARY MATERIAL TO

Quantitative relationships for the prediction of the vapor pressure of some hydrocarbons from the van der Waals molecular surface

TUDOR OLARIU[1]*, VICENŢIU VLAIA[1], CIPRIAN CIUBOTARIU[2], DAN DRAGOŞ[1], DAN CIUBOTARIU[1] and MIRCEA MRACEC[3]**

[1]Department of Organic Chemistry, Faculty of Pharmacy, "Victor Babes" University of Medicine and Pharmacy, P-ta Eftimie Murgu No. 2, 300041, Timisoara, Romania, [2]Department of Computer Sciences, University "Politehnica", P-ta Victoriei No. 2, 300006, Timisoara, Romania and [3]Molecular Forecast Research Center, Prof. Dr. Aurel Păunescu-Podeanu str. 125, A 4, RO-300588 Timişoara, Romania

J. Serb. Chem. Soc. 80 (5) (2015) 659–671

TABLE S-I. Vapor pressure data sets for: a) alkanes; b) cycloalkanes. The experimental data, A_e, are the values of vapor pressure, log (*VP* / Pa) at 298.15 K;[18] the substituents: M – methyl, E – ethyl, IPR – isopropyl, PR – propyl, BU – butyl

No	C*n* or CyC*n*	A_{exp} = log (*VP* / Pa)	S^W / Å^2	$A_{calc\ or\ pred}$ = = log (*VP* / Pa)$_{calc}^a$	Δ*A* = = A_{exp}–A_{calc}
a) C*n*, where n represents the number of carbon atoms in an alkane molecule					
1	C2	6.62	70.896	6.522	0.098
2	C3	5.97	92.848	5.992	–0.02
3	C4	5.38	114.83	5.46	–0.08
4	2M-C3	5.54	114.11	5.478	0.062
5	C5	4.83	136.62	4.933	–0.1
6	2M-C4	4.96	134.18	4.992	–0.03
7	22MM-C3	5.23	134.48	4.985	0.245
8	C6	4.3	158.59	4.402	–0.1
9	3M-C5	4.4	153.57	4.523	–0.12
10	2M-C5	4.44	155.89	4.467	–0.03
11	23MM-C4	4.49	151.86	4.565	–0.08
12	22MM-C4	4.82	152.20	4.556	0.264
13	C7	3.78	180.46	3.873	–0.09
14	3M-C6	3.91	175.30	3.998	–0.09
15	2M-C6	3.94	177.74	3.939	0.001
16	23MM-C5	3.96	170.73	4.109	–0.15
17	33MM-C5	4.04	168.74	4.157	–0.12
18	223MMM-C4	4.135	167.74	4.181	–0.05

---

*,** Corresponding authors. E-mail: (*)olariu.t@umft.ro; (**)mirceamracec@yahoo.com

TABLE S-I. Continued

No	C*n* or CyC*n*	A_{exp} = log (*VP* / Pa)	S^W / Å^2	$A_{calc\ or\ pred}$ = = log $(VP / Pa)_{calc}^a$	Δ*A* = = A_{exp}–A_{calc}
	a) C*n*, where n represents the number of carbon atoms in an alkane molecule				
19	24MM-C5	4.02	174.47	4.018	0.002
20	22MM-C5	4.14	173.79	4.034	0.106
21	C8	3.27	202.23	3.347	–0.08
22	3E-C6	3.428	195.35	3.513	–0.09
23	3M-C7	3.417	197.04	3.472	–0.06
24	34MM-C6	3.481	189.82	3.647	–0.17
25	3E3M-C5	3.486	185.25	3.757	–0.27
26	4M-C7	3.436	196.97	3.474	–0.04
27	2M-C7	3.439	199.68	3.409	0.03
28	3E2M-C5	3.503	192.53	3.582	–0.08
29	23MM-C6	3.495	193.49	3.558	–0.06
30	233MMM-C5	3.556	184.91	3.766	–0.21
31	234MMM-C5	3.55	185.75	3.745	–0.2
32	33MM-C6	3.581	190.4	3.633	–0.05
33	223MMM-C5	3.631	186.76	3.721	–0.09
34	24MM-C6	3.607	194.69	3.529	0.078
35	25MM-C6	3.606	197.02	3.473	0.133
36	22MM-C6	3.657	195.69	3.505	0.152
37	224MMM-C5	3.818	190.77	3.624	0.194
38	C9	2.77	224.1	2.818	–0.05
39	3M-C8	2.921	219.05	2.94	–0.02
40	4M-C8	2.959	218.84	2.945	0.014
41	2M-C8	2.927	221.45	2.882	0.045
42	2233MMMM-C5	3.103	196.87	3.476	–0.37
43	3E24MM-C5	3.126	207.95	3.209	–0.08
44	26MM-C7	3.094	218.95	2.943	0.151
45	3E22MM-C5	3.177	204.41	3.294	–0.12
46	225MMM-C6	3.347	215.04	3.037	0.31
47	2244MMMM-C5	3.427	207.63	3.216	0.211
48	2233MMMM-C6	2.73	218.45	2.955	–0.23
49	22MM-C8	2.686	239.68	2.441	0.245
50	2M-C9	2.4	243.38	2.352	0.048
51	335-MMMC7	2.746	226.57	2.758	–0.01
52	33EE-C5	2.988	198.61	3.434	–0.45
53	3M-C9	2.421	240.97	2.41	0.011
54	4M-C9	2.49	240.81	2.414	0.076
55	5M-C9	2.468	240.83	2.414	0.054
56	C1	7.79	48.541	7.063	0.727
57	C10	2.27	246.02	2.288	–0.02
58	C11	1.745	267.74	1.763	–0.02
59	C12	1.252	289.89	1.227	0.025

TABLE S-I. Continued

No	C*n* or CyC*n*	A_{exp} = log (*VP* / Pa)	S^{W} / Å^2	$A_{\mathrm{calc\ or\ pred}}$ = = log (*VP* / Pa)$_{\mathrm{calc}}^{\mathrm{a}}$	Δ*A* = = A_{exp}–A_{calc}
a) C*n*, where n represents the number of carbon atoms in an alkane molecule					
60	C13	0.755	311.47	0.705	0.05
61	C14	0.27	333.61	0.17	0.1
62	C15	–0.183	355.38	–0.36	0.173
63	C16	–0.7	377.38	–0.89	0.188
b) CyC*n*, where *n* represents the number of carbon atoms in the cycle (Cy) of a cycloalkane molecule					
1	CyC3	5.85	80.531	6.289	–0.439
2	CyC4	5.195	98.905	5.845	–0.65
3	CyC5	4.62	117.025	5.407	–0.787
4	CyC6	4.11	135.333	4.964	–0.854
5	CyC7	3.45	150.489	4.598	–1.148
6	CyC8	2.876	167.417	4.189	–1.313
7	E-CyC5	3.727	155.334	4.481	–0.754
8	E-CyC6	3.23	176.719	3.964	–0.734
9	IPR-CyC5	3.332	176.106	3.978	–0.646
10	IPR-CycloC6	2.747	198.422	3.439	–0.692
11	1,1MM-CyC5	4.006	157.207	4.435	–0.429
12	1,1MM-CyC6	3.48	173.535	4.041	–0.561
13	BU-CyloC6	2.243	220.344	2.909	–0.666
14	*cis*-1,2MM-CyC5	3.799	156.622	4.450	–0.651
15	*trans*-1,2MM-CyC5	3.931	158.805	4.397	–0.466
16	*cis*-1,3MM-CyC6	3.457	177.856	3.936	–0.479
17	*trans*-1,3MM-CyC6	3.371	175.33	3.997	–0.626
18	cis-1,3MM-Cy5	3.945	158.861	4.395	–0.45
19	*trans*-1,3MM-CyC5	3.934	158.507	4.404	–0.47
20	*cis*-1,4MM-CyC6	3.379	175.575	3.991	–0.612
21	*trans*-1,4MM-CyC6	3.481	173.064	4.052	–0.571

[a] Calculated (A_{calc}) values of log *VP* with Eq. (7) for the training set; predicted values (A_{pred}) of log *VP* with Eq. (7), developed for training set composed of alkanes in part a)

Journal of the Serbian Chemical Society
JSCS-info@shd.org.rs • www.shd.org.rs/JSCS

J. Serb. Chem. Soc. 80 (5) 673–683 (2015) UDC 532.783+547.655.1+541.57:547.26’11
JSCS–4747 *Original scientific paper*

Unsymmetrical banana-shaped liquid crystalline compounds derived from 2,7-dihydroxynaphthalene

AUREL SIMION[1], COSMIN-CONSTANTIN HUZUM[1], IRINA CARLESCU[1],
GABRIELA LISA[1], MIHAELA BALAN[2] and DAN SCUTARU[1]*

[1]*Faculty of Chemical Engineering and Environmental Protection, Gheorghe Asachi Technical University of Iasi, 71 D. Mangeron St., 700050 – Iaşi, Romania and* [2]*Petru Poni Institute of Macromolecular Chemistry, Aleea Grigore Ghica Voda 41A, 700487-Iasi, Romania*

(Received 25 July, revised 16 December, accepted 23 December 2014)

Abstract: The synthesis and characterization of new asymmetric bent-core compounds derived from 2,7-dihydroxynaphthalene with various connecting groups between the aromatic rings and alkyloxy terminal substituents at the end of the long arm are presented. Some 1,4-disubstituted phenylene rings with an azo or ester linkage between them have been used as calamitic pro-mesogen units. The synthetic strategies to obtain the final esteric derivatives involved the esterification of 7-(benzyloxy)naphthalen-2-ol with 4-((4-(alkyloxy)phenyl)-azo)benzoyl chlorides or with 4-((4-(alkyloxy)benzoyl)oxy)benzoic acids in the presence of dicyclohexylcarbodiimide (DCC) and 4-(dimethylamino)pyridine (DMAP). The mesomorphic properties were assigned by optical polarizing microscopy and differential scanning calorimetry. All the compounds showed mesomorphic properties of the enantiotropic or monotropic type, the liquid crystalline behavior depending on the linking group between the phenylene rings. Thermogravimetric studies evidenced that all compounds were stable in the range of the existence of mesophases.

Keywords: liquid crystals; asymmetric bent-core; 2,7-naphthalenediol.

INTRODUCTION

Although classical liquid crystals are widely used in a variety of applications, especially in displays, significant research has been performed on non-conventional, bent-core liquid crystals in order to establish structure–property relationships. The first mention of the existence of mesogenic properties exhibited by non-linear compounds was reported in 1929 by Vorländer for isophthalic acid derivatives, which showed nematic phases.[1] The research on bent-core liquid crystals (BCLC) was taken and further extended by Matsunaga and co-workers.[2–5] The field of bent-core liquid crystals has greatly advanced since

---

* Corresponding author. E-mail: dscutaru@ch.tuiasi.ro

doi: 10.2298/JSC140725126S

1996, when Niori showed that because of limitation of the rotational freedom in the mesophase, bent-shaped compounds are able to organize into a compact arrangement and exhibit spontaneous polarization, which leads to ferroelectric properties.[6]

The bent-shaped molecular structure is provided for by proper selection of a central core with an adequate bent angle and by covalent connection of two mesogenic units to this. The positions used for a bent connection are at 1,3-, 2,6-, 2,7- or 1,3′- for benzene, pyridine, naphthalene or biphenyl, respectively. Such structures induce a bent angle of about 120°. While the mesophases exhibited by such compounds are similar to those displayed by classical calamitic liquid crystals, some characteristic B phases are usually present in such structures. Thus, while compounds based on 1,2-disubstituted benzene or 2,3-disubstituted naphthalene as the central core provide an angle of about 60° and display only conventional nematic and smectic phases,[2,4] 2,7-disubstituted naphthalenes lead to derivatives that exhibit typical banana phases.[7–10]

The substitution of the central core could be symmetrical or non-symmetrical. Compared to symmetrical structures, the non-symmetrical ones induce a lowering of the transition temperatures. Most of the banana-shaped compounds contain five aromatic rings connected through various linking groups. Increasing of the number of phenyl rings enhances the core rigidity and tends to increase the transition temperatures, whereas terminal alkyl tails induce flexibility (which lowers the phase transition temperatures) and permits the formation of B phases.

The presence of a 2,7-disubstituted naphthalene unit as the central core in banana-shaped compounds was first reported in 1999 by Shen *et al.*[11] and Pelzl *et al.*[12] While the compounds reported by Shen *et al.* did not show mesomorphic properties, those reported by Pelzl *et al.* showed a B_1 phase. Further studies on such compounds focused on the introduction of azomethine linking groups, which exhibited smectic[13–15] or nematic and B phases.[16–18]

In this paper, the synthesis, structural characterization and mesomorphic properties of two new classes of liquid crystalline compounds based on a non-symmetrical 2,7-disubstituted naphthalene core and containing esteric or azo linking groups in the pro-mesogenic moiety are reported.

EXPERIMENTAL

Materials, instruments and methods

Benzyl chloride, 2,7-dihydroxynaphthalene (Aldrich), potassium iodide, potassium carbonate (Fluka), tetrabutylammonium hydrogensulfate (TBAHS) (Aldrich), 1,3-dicyclohexylcarbodiimide (DCC) (Fluka), 4-(dimethylamino)pyridine (DMAP) (Fluka) and silica gel-60 (Merck) were used as received. Acetone and dichloromethane were refluxed over phosphorus pentaoxide (Merck) and distilled before use. Other solvents and chemicals were used without further purification. 7-(Benzyloxy)naphthalen-2-ol (**1**),[19] 4-((4-(alkyloxy)benzoyl)oxy)benzoic acids (**3a**–**e**),[20] 4-((4-(alkyloxy)phenyl)azo)benzoic acids[21] and 4-((4-alkyl)oxyphenyl)azo)-benzoyl chlorides (**2a**–**e**)[22] were synthesized according to literature procedures.

Nuclear magnetic resonance (NMR) spectra were recorded on a Bruker Avance DRX 400 MHz spectrometer. Chemical shifts are reported in ppm relative to tetramethylsilane (TMS) as internal standard. The mass spectra were recorded on a quadrupole-time of flight mass spectrometer equipped with an electrospray ion source (Agilent 6520 Accurate Mass Q-ToF LC/MS). FT-IR spectra were recorded on a Nicolet Magna 550 FT-IR spectrometer (NaCl crystal window).

The transition temperatures were determined using a Linkam heating stage connected with a Linksys 32 temperature control unit in conjunction with an Axioscop 40 Zeiss polarizing optical microscope (POM) and Qimaging/Retiga-1000R camera for image capture. The transitions were confirmed by DSC analysis (Mettler Toledo DSC1). Heating and cooling cycles were run at rates of 10 °C min^{-1} under a nitrogen atmosphere. The samples were measured in closed lid aluminum pans. Mesophase type was assigned by visual comparison (under the microscope) with known phase standards.[23]

All the thermal analysis were run under the same conditions, on 2.8 – 4.3 mg samples, on a Mettler-Toledo TGA SDTA851 derivatograph under a dynamic N_2 atmosphere, with a flow rate of 20 ml min^{-1} and a heating rate of 10 °C min^{-1} from 25 to 900 °C. In order to obtain comparable data, constant operational parameters were employed for all samples.

The melting points were recorded using a melting point meter Krüss Optotronic KSPI-N and are uncorrected.

*General method for the preparation of 7-(benzyloxy)naphthalen-2-yl 4-((4-(alkyloxy)phenyl)-diazenyl)benzoates (**4a**–**e**)*

Compounds **4a**–**e** were prepared by adapting a literature method.[24] A mixture of 7-(benzyloxy)naphthalen-2-ol (0.20 g, 0.799 mmol), 4-((4-(alkyl)oxyphenyl)azo)benzoyl chloride (0.877 mmol), potassium carbonate (0.14 g, 1.00 mmol), tetrabutylammonium hydrogensulfate (0.006 g, 0.017 mmol) in dichloromethane (150 mL) and water (40 mL) was vigorously stirred for 24 h at room temperature. The organic layer was separated, washed several times with distilled water, dried over anhydrous magnesium sulfate and concentrated on rotaevaporator. The compounds were separated by column chromatography on silica gel using a mixture of dichloromethane:hexane 20:1 as eluent. Orange products were obtained.

The following compounds were synthesized: 7-(benzyloxy)naphthalen-2-yl 4-((4-(hexyloxy)phenyl)diazenyl)benzoate (**4a**) using 4-((4-(hexyloxy)phenyl)azo)benzoyl chloride 0.302 g (0.877 mmol); 7-(benzyloxy)naphthalen-2-yl-4-((4-(heptyloxy)phenyl)diazenyl)benzoate (**4b**) using 4-((4-(heptyloxy)phenyl)azo)benzoyl chloride 0.315 g (0.879 mmol); 7-(benzyloxy)naphthalen-2-yl 4-((4-(octyloxy)phenyl)diazenyl)benzoate (**4c**) using 4-((4-(octyloxy)-phenyl)azo)benzoyl chloride 0.327 g (0.878 mmol); 7-(benzyloxy)naphthalen-2-yl 4-((4-(nonyloxy)phenyl)diazenyl)benzoate (**4d**) using 4-((4-(nonyloxy)phenyl)azo)benzoyl chloride 0.339 g (0.877 mmol); 7-(benzyloxy)naphthalen-2-yl 4-((4-(decyloxy)phenyl)diazenyl)-benzoate (**4e**) using 4-((4-(decyloxy)phenyl)azo) benzoyl chloride, 0.352 g (0.879 mmol).

The physical and spectral data for **4a**–**e** are given in the Supplementary material to this paper.

*General method for the preparation of 7-(benzyloxy)naphthalen-2-yl 4-((4-(alkyloxy)benzoyl)-oxy)benzoates (**5a**–**e**)*

Compounds were prepared by adapting literature data.[25] A mixture of 1 equivalent of 7-(benzyloxy)naphthalen-2-ol (0.20 g, 0.799 mmol), 1.1 equivalents of 4-((4-(alkyloxy)benzoyl)oxy)benzoic acid and 0.2 equivalents of DMAP (0.019, g 0.155 mmol), dissolved in dry dichloromethane (50 mL), was stirred for 15–20 min at room temperature, cooled to 0 °C on an ice bath and then 1.2 equivalents of DCC (0.197 g, 0.954 mmol), dissolved in dry dichloromethane (50 mL), were added dropwise. After 30 min, the ice bath was removed and the reaction mixture was stirred for 48 h at room temperature after which the precipitated *N*,*N*′-dicyclohexylurea (DCU) was filtered off. The solvent was evaporated under vacuum and the solid residue was chromatographed on silica gel using a 20:1 mixture of dichloromethane:ethyl acetate as the eluent. White products were obtained.

The following compounds were synthesized: 7-(benzyloxy)naphthalen-2-yl 4-((4-(hexyloxy)benzoyl)oxy)benzoate (**5a**) using 4-((4-(hexyloxy)benzoyl)oxy)benzoic acid (0.300 g, 0.876 mmol); 7-(benzyloxy)naphthalen-2-yl 4-((4-(heptyloxy)benzoyl)oxy)benzoate (**5b**) using 4-((4-(heptyloxy)benzoyl)oxy)benzoic acid 0.313 g (0.878 mmol); 7-(benzyloxy)-naphthalen-2-yl 4-((4-(octyloxy)benzoyl)oxy)benzoate (**5c**) using 4-((4-(octyloxy)benzoyl)-oxy)benzoic acid 0.325 g (0.877 mmol); 7-(benzyloxy)naphthalen-2-yl 4-((4-(nonyloxy)-benzoyl)oxy)benzoate (**5d**) using 4-((4-(nonyloxy)benzoyl)oxy)benzoic acid 0.339 g (0.877 mmol); 7-(benzyloxy)naphthalen-2-yl 4-((4-(decyloxy)benzoyl)oxy)benzoate (**5e**) 4-((4-(decyloxy)benzoyl)oxy)benzoic acid 0.350 g (0.878 mmol).

The physical and spectral data for 5**a**–**e** are given in the Supplementary material to this paper.

RESULTS AND DISCUSSION

The synthetic approach used to prepare the intermediate and final compounds is outlined in Scheme 1. The short arm compound (**1**) was prepared by alkylation of 2,7-dihydroxynaphthalene with benzyl chloride.[19] Depending of the chemical structure, the longer arm was coupled to the remaining hydroxyl group of the central mono-alkylated naphthalene core by two methods, which gave two series of final compounds. The first series used 4-((4-(alkyloxy)phenyl)azo)-benzoyl chlorides **2a**–**e** in the presence of potassium carbonate as base and TBAHS as phase transfer catalyst to give the target compounds **4a**–**e**. The second one coupled 4-((4-(alkyloxy)phenyl)azo)benzoic acids **3a**–**e** using DCC and DMAP to achieve the final compounds **5a**–**e**.

All the obtained compounds were purified by column chromatography using dichloromethane:hexane 20:1 (for series **4a**–**e**) or dichloromethane:ethyl acetate 20:1 (for series **5a**–**e**) as eluents. The yields were similar for both series (between 61–79 %). The structure and purity of the obtained final compounds were checked and confirmed by ^{1}H-NMR, ^{13}C-NMR, FT-IR and mass spectrometry (data given in the Supplementary material to this paper).

Thermogravimetric studies performed for both the **4a**–**e** and **5a**–**e** series evidenced very good thermal stability for all the investigated compounds, the T_{onset} values (temperatures at which the degradation processes begin) being at least 155 °C higher than the isotropization temperatures (the T_{onset} values are given in Tables I and II).

The phase transition temperatures and phase transition enthalpy changes were determined by differential scanning calorimetry (Tables I and II).

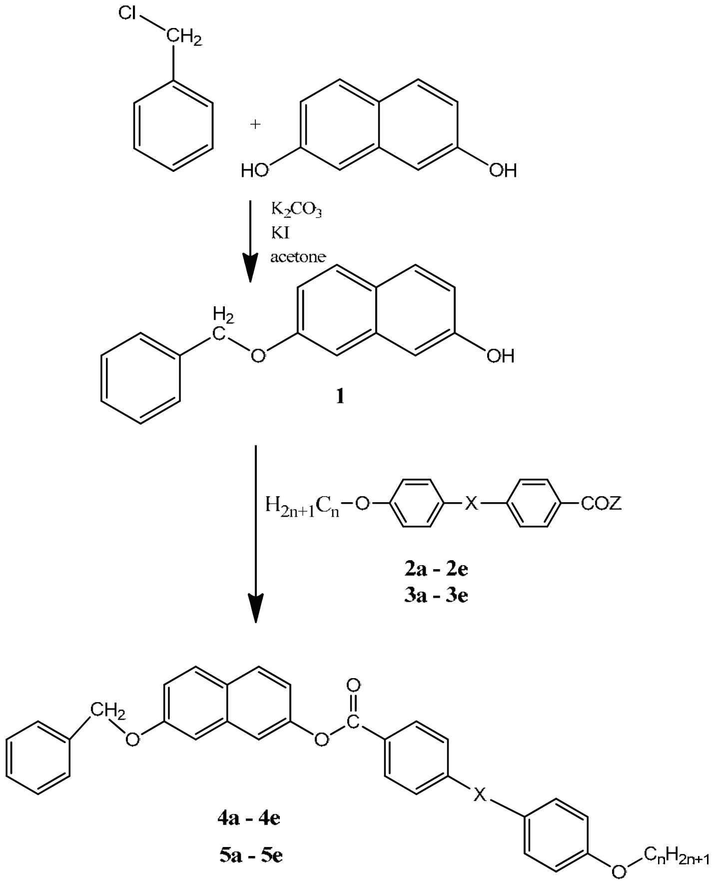

Scheme 1. Synthesis of bent-core liquid crystalline compounds; **4a**–**e**, X = –N=N–, Z = –Cl, *n* = 6–10, aq. K_2CO_3, TBAHS, CH_2Cl_2, 24 h, RT; **5a**–**e**, X = –OCO–, Z = –OH, *n* = 6–10, DCC, DMAP, CH_2Cl_2, 48 h, RT.

The first compound of the series **4**, compound **4a**, exhibited monotropic behavior, visible under polarized light between 126–95 °C. The transition isotropic liquid–liquid crystal was a very slow process and difficult to identify on the DSC curve; nevertheless, it was identified from POM observations at about 126 °C (similar behaviors were evidenced in the case of the other compounds of series **4** and **5**, Tables I and II). The microscopic analyses highlighted an interesting unidentified B type texture at 110 °C during the first cooling (Fig. 1a), which did not appear on the second cooling curve when only a classical B type texture was evidenced (Fig. 1b). The mesophase was stable in a temperature domain of 31 °C; the crystallization process started at 95 °C and the process was completed at 91 °C after a crystalline/crystalline transition.

TABLE I. Transition temperatures and associated enthalpy values of compounds **4a–e**; Cr, crystalline; LC, liquid crystal; I, isotropic; *MI*, mesophase interval; t_{onset}, the initial $_{\text{temperature}}$ at which the degradation processes begin

Cmpd.	t / °C [ΔH / J g^{-1}]									t_{onset} °C
	Heating				Cooling					
	Cr_1	Cr/LC	LC/I	*MI* / °C	I/LC	LC/Cr_3	Cr_3/Cr_2	Cr_2/Cr_1	*MI* / °C	
4a	–	–	155	–	126[a]	95	91	–	31	308
			[–87.60]			[38.07]	[1.55]			
4b	–	–	143	–	118	100	–	–	18	315
			[–77.24]		[0.51]	[79.23]				
4c	107	120	150	30	129[a]	118	82	–	11	316
	[–3.37]	[–14.06]	[–26.94]			[0.32]	[37.52]			
4d	–	110	137	27	128[a]	92	87	83	36	314
		[–6.15]	[–43.12]			[34.32]	[84.54]	[78.30]		
4e	–	113	148	35	123[a]	89	85	–	34	319
		[–30.04]	[–72.59]			[36.63]	[0.34]			

[a] Data obtained from POM

TABLE II. Transition temperatures (°C) and associated enthalpy values (J g^{-1}) of compounds **5a–e**

Cmpd.	t / °C [ΔH / J g^{-1}]									t_{onset} °C
	Heating				Cooling					
	Cr_1	Cr/LC	LC/I	*MI* / °C	I/LC	LC/Cr_3	Cr_3/Cr_2	Cr_2/Cr_1	*MI* / °C	
5a	–	122	144	22	109	84	–	–	25	336
		[–27.81]	[–63.03]		[0.44]	[62.79]				
5b	109	116	129	13	104	75	–	–	29	324
	[–6.74]	[–11.02]	[–37.22]		[0.48]	[56.08]				
5c	–	127[a]	148	21	107	83	–	–	24	331
			[–83.93]		[0.56]	[70.12]				
5d	–	–	146	–	108	87	80	–	28	334
			[–84.80]		[0.73]	[0.66]	[66.91]			
5e	–	–	136	–	108	90	68	59	49	318
			[–76.63]		[0.58]	[0.72]	[5.62]	[28.16]		

[a] Data obtained from POM

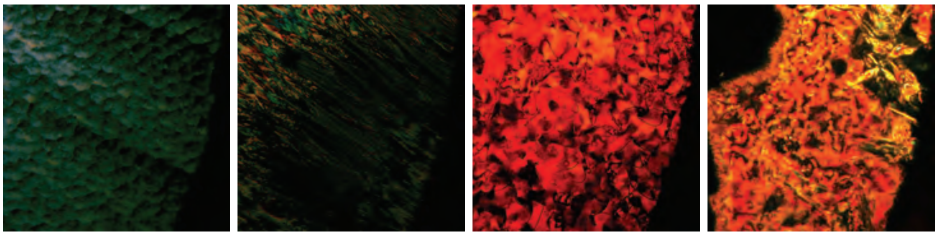

(a) (b) (c) (d)

Fig. 1. Microphotographs of the mesophase textures: a) compound **4a**, first cooling, 110 °C; b) compound **4a**, second cooling, 126 °C; c) compound **4b**, first cooling, 107 °C; d) compound **4c**, first heating, 142 °C.

The increasing of the number of carbon atoms in the alkyloxy tail from 6 (compound **4a**) to 7 (compound **4b**) lowered the isotropization temperature and the domain of the mesophase stability. The mesophase changed into a nematic type with characteristic Schlieren texture (Fig. 1c). The mesomorphic properties switched significantly for compound **4c**, which exhibited an enantiotropic liquid crystalline behavior. A nematic phase was stable for 30 °C on heating (Fig. 1d). However, the stability of the mesophase on cooling decreased when compared with the first two compounds.

The enantiotropic behavior was maintained for the next two compounds of the series, **4d** and **4e**, and the stability of mesophases on heating increased gradually, compound **4e** showing the broadest domain of about 35 °C. On cooling, compound **4d** showed liquid crystalline properties in a 36 °C temperature domain, plus a rich polymorphism during the crystallization, evidenced on the DSC curves (Fig. 2). The microscopic analysis for these compounds evidenced mesophases of nematic and B types (Fig. 3a and b).

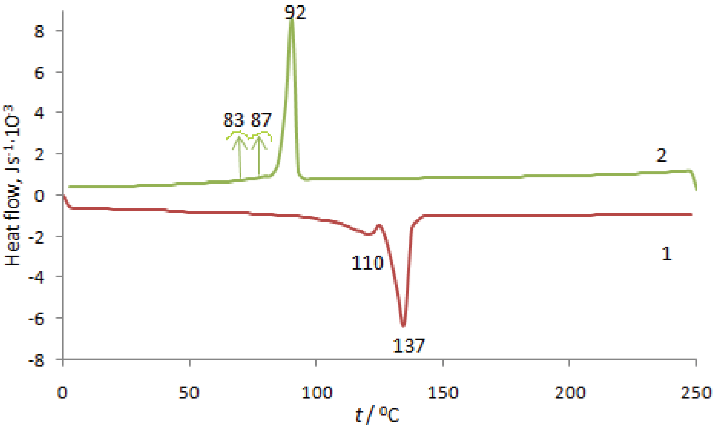

Fig. 2. DSC curves for compound **4d**: 1 – first heating, 2 – first cooling.

The first compound of the second series, **5a**, exhibited an enantiotropic behavior, with characteristic Schlieren nematic textures both on the heating and cooling cycles (Fig. 3c). The mesophase appeared late under the visual field of the microscope, the sample being extremely sensitive to any touch when it crystallized. A similar behavior was observed for compound **5b**, the isotropization point of which was lower than that of **5a** (Table II). On heating, the mesophase was of B type, while on cooling the ordering began with Schlieren nematic textures that changed into a smectic one at 87 °C (Fig. 3d).

The same behavior of the mesophase was evidenced for compound **5c** on heating. On heating, a transition crystalline to a B type mesophase was identified from POM observations at about 127 °C (Fig. 4a). On cooling, the mesophase was of nematic type with Schlieren texture that turned into a ribbon type one (Fig. 4b) near the crystallization temperature.

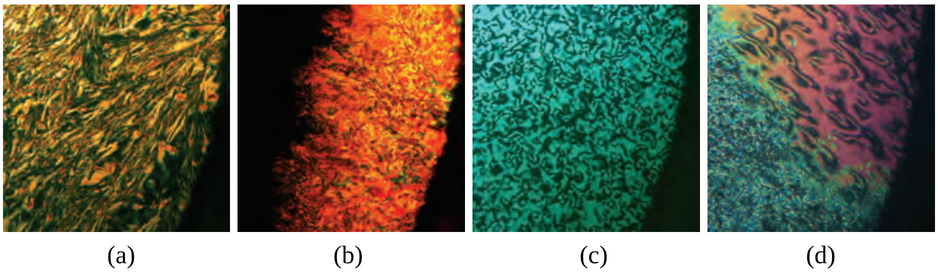
(a) (b) (c) (d)

Fig. 3. Microphotographs of the mesophase textures: a) compound **4d**, fourth cooling, 126 °C; b) compound **4e**, second cooling, 122 °C; c) compound **5a,** first cooling, 96 °C; d) compound **5b,** second cooling, 85 °C.

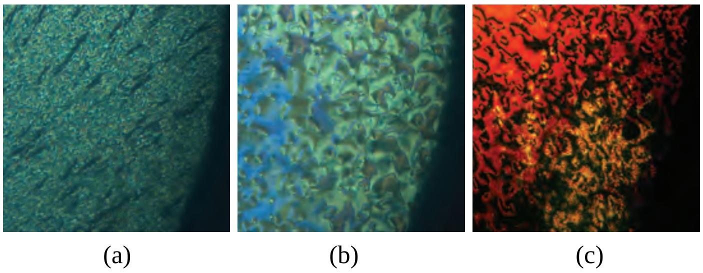
(a) (b) (c)

Fig. 4. Microphotographs of the textures: a) compound **5c**, second heating, 133 °C; b) compound **5c**, second cooling, 95 °C; c) compound **5d**, first cooling, 91 °C.

The last two compounds of the series, **5d** and **5e**, changed the mesomorphic behavior and showed liquid crystalline properties only on cooling (Fig. 4c), with several crystalline to crystalline transitions evidenced on the DSC curves (Fig. 5).

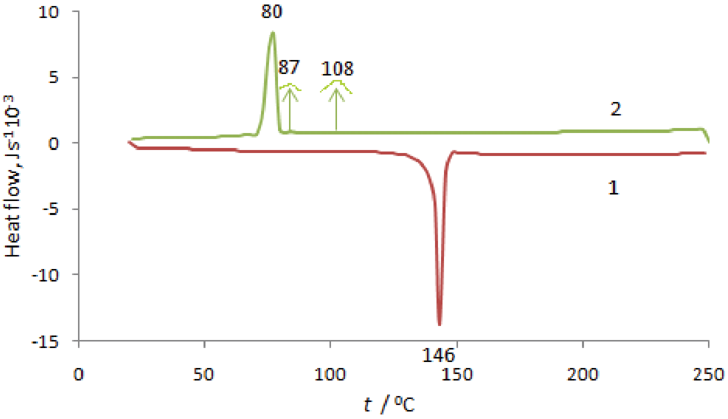

Fig. 5. DSC curves for compound **5d**: 1 – first heating, 2 – first cooling.

With only one exception (compound **4d**), there were significant differences between the isotropization temperatures and the temperatures at which the compounds entered into mesophase on cooling (between 21 and 41 °C, 9 °C for compound **4d**, Fig. 6).

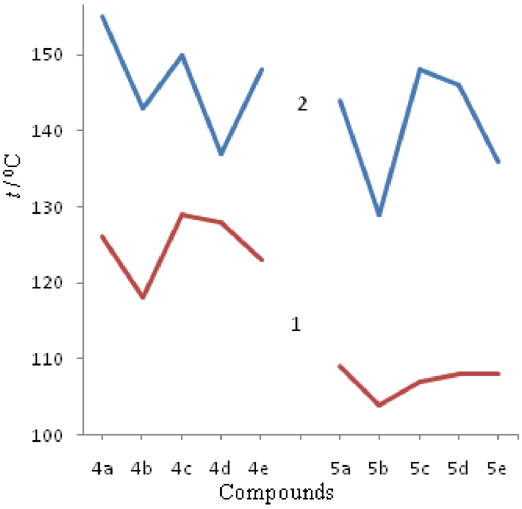

Fig 6. Comparison between the isotropization temperatures and LC temperatures (temperatures at which the compounds are entering into mesophase on cooling): 1 – LC temperatures; 2 – isotropization temperatures.

For series **4a**–**e**, an even/odd effect related to the number of carbon atoms in the tail may be evidenced (Fig. 6). In the same time, the differences between the isotropization temperatures and the LC temperatures on cooling for series **5a**–**e** were 14–22 °C higher then those for series **4a**–**e**.

CONCLUSIONS

Two new series of asymmetrical bent-core liquid crystalline compounds based on a 2,7–dihydroxynaphthalene core were synthesized and characterized. All compounds contained a benzyloxy non-mesogenic shorter flexible arm and a pro-mesogenic arm containing two benzenic rings connected by azo or ester linking groups. All the investigated compounds exhibited liquid crystalline properties, mainly of the enantiotropic type, as evidenced by optical polarizing microscopy and differential scanning calorimetry. Despite the absence of a long flexible tail in the shorter arm, the isotropization temperatures were relatively low (between 129 and 155 °C). There were no significant differences related to the transition temperatures and the stabilities of the mesophases as a function of the nature of the linking groups between the aromatic rings. The investigated compounds showed nematic and B type mesophases.

Thermogravimetric studies evidenced that all compounds were stable in the range of the existence of mesophases, the degradation processes beginning at temperatures more than 155 °C higher than the isotropization temperatures.

SUPPLEMENTARY MATERIAL

Physical and spectral data for the prepared compounds are available electronically from http://www.shd.org.rs/JSCS/, or from the corresponding author on request.

ИЗВОД

АСИМЕТРИЧНА ЈЕДИЊЕЊА ТЕЧНИХ КРИСТАЛА У ОБЛИКУ БАНАНЕ ИЗВЕДЕНА ИЗ 2,7-ДИХИДРОКСИНАФТАЛЕНА

AUREL SIMION[1], COSMIN-CONSTANTIN HUZUM[1], IRINA CARLESCU[1], GABRIELA LISA[1], MIHAELA BALAN[2]
и DAN SCUTARU[1]

[1]*Faculty of Chemical Engineering and Environmental Protection, Gheorghe Asachi Technical University of Iasi, 71 D. Mangeron St., 700050 – Iaşi, Romania* и [2]*Petru Poni Institute of Macromolecular Chemistry, Aleea Grigore Ghica Voda 41A, 700487-Iasi, Romania*

У овом раду представљена је синтеза и карактеризација нових асиметричних једињења савијеног језгра изведених из 2,7-дихидроксинафталена са различитим везивним групама између ароматичних прстенова и алкилокси терминалних супституената на крају дуге руке. Као каламитичне промезогене јединице коришћени су неки од 1,4-дисупституисаних фениленских прстенова повезаних преко азо или естарских веза. Стратегија синтезе крајњих естарских производа садржавала је естерификацију 7-(бензилокси)нафтален-2-ола употребом 4-((4-алкилокси)фенил)азо)бензоил-хлорида или 4-((4-(алкилокси)безоил)окси)бензоеве киселине у присуству дициклохексилкарбодиимида (DCCI) и 4-(диметиламино)пиридина (DMAP). Мезоморфна својства одређене су оптичком поларизационом микроскопијом и диференцијалном скенирајућом калориметријом. Сва једињења показују мезоморфне особине енантиотропног и монотропног типа, понашање течних кристала зависи од група које повезују фениленске прстенове. Термогравиметријска истраживања су показала да су сва једињења стабилна у опсегу постојања мезофаза.

(Примљено 25. јула, ревидирано 16. децембра, прихваћено 23. децембра 2014)

REFERENCES

1. D. Vorländer, A. Apel, *Ber. Dtsch. Chem. Ges.* **62** (1929) 2831
2. M. Kuboshita, Y. Matsunaga, H. Matsuzaki, *Mol. Cryst. Liq. Cryst.* **199** (1991) 319
3. Y. Matsunaga, S. Miyamoto, *Mol. Cryst. Liq. Cryst.* **237** (1993) 311
4. H. Matsuzaki, Y. Matsunaga, *Liq. Cryst.* **14** (1993) 105
5. T. Akutagawa, Y. Matsunaga, K. Yasuhara, *Liq. Cryst.* **17** (1994) 659
6. T. Niori, T. Sekine, J. Watanabe, T. Furukawa, H. Takezoe, *J. Mater. Chem.* **6** (1996) 1231
7. S. K. Lee, Y. Naito, L. Shi, M. Tokita, H. Takezoe, J. Watanabe, *Liq. Cryst.* **34** (2007) 935
8. S. K. Lee, M. Tokita, H. Takezoe, J. Watanabe, *Ferroelectrics* **365** (2008) 1
9. S. K. Lee, L. Shi, R. Ishige, S. Kang, M. Tokita, J. Watanabe, *Chem. Lett.* **37** (2008) 1230
10. S. K. Lee, X. Li, S. Kang, M. Tokita, J. Watanabe, *J. Mater. Chem.* **19** (2009) 4517
11. D. Shen, S. Diele, G. Pelzl, I. Wirth, C. Tschierske, *J. Mater. Chem.* **9** (1999) 661
12. G. Pelzl, S. Diele, W. Weissflog, *Adv. Mater.* **11** (1999) 707
13. J. Thisayukta, H. Kamee, S. Kawauchi, J. Watanabe, *Mol. Cryst. Liq. Cryst.* **246** (2000) 63
14. J. Thisayukta, Y. Nakayama, J. Watanabe, *Liq. Cryst.* **27** (2000) 1129
15. J. Thisayukta, H. Niwano, H. Takezoe, J. Watanabe, *J. Mater. Chem.* **11** (2001) 2717

16. R. Amaranatha Reddy, B. K. Sadashiva, *Liq. Cryst.* **27** (2000) 1613
17. R. Amaranatha Reddy, B. K. Sadashiva, *J. Mater. Chem.* **14** (2004) 1936
18. J. Svoboda, V. Novotna, V. Kozmik, W. Weissflog, S. Diele, G. Pelzl, *J. Mater. Chem.* **13** (2003) 2104
19. S. Balamurugan, P. Kannan, K. Yadupati, A. Roy, *J. Mol. Struct.* **1001** (2011) 118
20. N. Gimeno, M. J. Clemente, J. L. Serranno, M. B. Ros, *New J. Chem.* **33** (2009) 2007
21. E. R. Cioanca, E. L. Epure, I. Carlescu, G. Lisa, D. Wilson, N. Hurduc, D. Scutaru, *Mol. Cryst. Liq. Cryst.* **51** (2011) 537
22. G. Simion, D. F. Iuganu, I. Carlescu, D. Scutaru, *Bull. Polytech. Inst Iasi, Chem. Chem.Eng.* **57** (2011) 213
23. I. Dierking, *Textures of liquid crystals*, Wiley–VCH, Weinheim, 2003, p. 188
24. G. Simion, I. Carlescu, G. Lisa, D. Scutaru, *Rev. Chim.-Bucharest* **63** (2012) 4
25. C. C. Huzum, I. Carlescu, G. Lisa, D. Scutaru, *J. Serb. Chem. Soc.* **78** (2013) 669.

Journal of the Serbian Chemical Society
JSCS@tmf.bg.ac.rs • www.shd.org.rs/JSCS
J. Serb. Chem. Soc. 80 (5) S179–S183 (2015) *Supplementary material*

SUPPLEMENTARY MATERIAL TO

Unsymmetrical banana-shaped liquid crystalline compounds derived from 2,7-dihydroxynaphthalene

AUREL SIMION[1], COSMIN-CONSTANTIN HUZUM[1], IRINA CARLESCU[1],
GABRIELA LISA[1], MIHAELA BALAN[2] and DAN SCUTARU[1]*

[1]*Faculty of Chemical Engineering and Environmental Protection, Gheorghe Asachi Technical University of Iasi, 71 D. Mangeron St., 700050 – Iaşi, Romania and* [2]*Petru Poni Institute of Macromolecular Chemistry, Aleea Grigore Ghica Voda 41A, 700487-Iasi, Romania*

J. Serb. Chem. Soc. 80 (5) (2015) 673–683

PHYSICAL AND SPECTRAL DATA FOR THE PREPARED COMPOUNDS

7-(Benzyloxy)naphthalen-2-yl 4-((4-(hexyloxy)phenyl)diazenyl)benzoate (***4a***). Yield: 69 % (0.341 g); color: orange; m.p.: 155 °C; FT-IR (KBr, cm^{-1}): 3030 (CH Ar-H), 2932, 2857 (CH, aliphatic), 1730 (O–C=O, ester), 1500 (N=N); ^{1}H-NMR (400 MHz, $CDCl_3$, δ / ppm): 8.37 (2H, *d*, J = 8.4 Hz, Ar-H), 7.98 (2H, *d*, J = 8.4 Hz, Ar-H), 7.97 (2H, *d*, J = 8.8 Hz, Ar-H), 7.83 (1H, *d*, J = 8.8 Hz, Ar-H), 7.78 (1H, *d*, J = 8.8 Hz, Ar-H), 7.59 (1H, *d*, J = 2.0 Hz, Ar-H), 7.49 (2H, *m*, Ar-H), 7.41 (2H, *m*, Ar-H), 7.35 (1H, *d*, J = 7.5 Hz, Ar-H), 7.24–7.21 (3H, *m*, Ar-H), 7.03 (2H, *d*, J = 8.8 Hz, Ar-H), 5.18 (2H, *s*, Ar-CH_2–O–), 4.06 (2H, *t*, J = 6.6 Hz, –O–CH_2–), 1.83 (2H, *quint*, J = 6.8 Hz, –CH_2–), 1.49 (2H, *quint*, J = 7.0 Hz, –CH_2–), 1.36 (4H, *m*, aliphatic), 0.92 (3H, *t*, J = 6.8 Hz, CH_3); ^{13}C-NMR (101 MHz, $CDCl_3$, δ / ppm): 164.89, 162.49, 157.38, 155.82, 149.24, 146.86, 136.71, 135.14, 131.23, 130.50, 129.37, 129.22, 128.63, 128.06, 127.54, 127.15, 125.31, 122.53, 118.98, 118.81, 117.75, 114.83, 107.11 (1C, ester + 22C, Ar-H), 70.06 (Ar-CH_2–O–), 68.46 (–O–CH_2–), 31.55, 29.12, 25.67, 22.58, 14.02 (5C, aliphatic); MS ($CHCl_3$, *m/z*): 559.1964 [M+Na]$^{+}$.

7-(Benzyloxy)naphthalen-2-yl 4-((4-(heptyloxy)phenyl)diazenyl)benzoate (***4b***). Yield: 68 % (0.315 g); color: orange; m.p.: 143 °C; FT-IR (KBr, cm^{-1}): 3030 (CH Ar-H), 2931.79, 2855 (CH, aliphatic), 1730 (O–C=O ester), 1499 (N=N); ^{1}H-NMR (400 MHz, $CDCl_3$, δ / ppm): 8.37 (2H, *d*, J = 8.4 Hz, Ar-H), 7.98 (2H, *d*, J = 8.4 Hz, Ar-H), 7.97 (2H, *d*, J = 8.8 Hz, Ar-H), 7.84 (1H, *d*, J = 8.8 Hz, Ar-H), 7.79 (1H, *d*, J = 9.0 Hz, Ar-H), 7.59 (1H, *d*, J = 1.8 Hz, Ar-H), 7.49 (2H, *m*, Ar-H), 7.41 (2H, *m*, Ar-H), 7.36 (1H, *d*, J = 7.2 Hz, Ar-H), 7.24–7.21 (3H, *m*, Ar-H), 7.03 (2H, *d*, J = 8.8 Hz, Ar-H), 5.19 (2H, *s*, Ar-CH_2–

---

* Corresponding author. E-mail: dscutaru@ch.tuiasi.ro

–O–), 4.06 (2H, *t*, *J* = 6.6 Hz, –O–CH$_2$–), 1.84 (2H, *quint*, *J* = 7.0 Hz, –CH$_2$–), 1.49 (2H, *quint*, *J* = 7.2 Hz, –CH$_2$–), 1.36 (6H, *m*, aliphatic), 0.92 (3H, *t*, *J* = 6.4 Hz, CH$_3$); ^{13}C-NMR (101 MHz, CDCl$_3$, δ / ppm): 164.55, 162.17, 157.06, 155.50, 148.93, 146.54, 136.40, 134.83, 130.90, 130.19, 129.05, 128.90, 128.31, 127.73, 127.21, 126.83, 125.00, 122.21, 118.66, 118.49, 117.43, 114.52 (1C ester + 21C Ar-H), 69.75 (Ar-CH$_2$–O–), 68.14 (–O–CH$_2$–), 31.44, 28.84, 28.72, 25.64, 22.28, 13.76 (6C, aliphatic); MS (CHCl$_3$, *m/z*): 573.2133 [M+Na]$^+$.

7-(Benzyloxy)naphthalen-2-yl 4-((4-(octyloxy)phenyl)diazenyl)benzoate (***4c***). Yield: 79 % (0.407 g); color: orange; m.p.:150 °C; FT-IR (KBr, cm^{-1}): 3057 (CH Ar-H), 2922.15, 2855 (CH, aliphatic), 1732 (O–C=O ester), 1452 (N=N); ^{1}H-NMR (400 MHz, CDCl$_3$, δ / ppm): 8.37 (2H, *d*, *J* = 8.4 Hz, Ar-H), 7.98 (2H, *d*, *J* = 8.4 Hz, Ar-H), 7.97 (2H, *d*, *J* = 8.8 Hz, Ar-H), 7.83 (1H, *d*, *J* = 9.0 Hz, Ar-H), 7.78 (1H, *d*, *J* = 9.0 Hz, Ar-H), 7.59 (1H, *d*, *J* = 2.0 Hz, Ar-H), 7.49 (2H, *m*, Ar-H), 7.41 (2H, *m*, Ar-H), 7.35 (1H, *d*, *J* = 7.2 Hz, Ar-H), 7.24–7.21 (3H, *m*, Ar-H), 7.03 (2H, *d*, *J* = 8.8 Hz, Ar-H), 5.18 (2H, *s*, Ar-CH$_2$–O–), 4.06 (2H, *t*, *J* = 6.6 Hz, –O–CH$_2$–), 1.83 (2H, *quint*, *J* = 7.0 Hz, –CH$_2$–), 1.49 (2H, *quint*, *J* = 7.0 Hz, –CH$_2$–), 1.36 (8H, *m*, aliphatic), 0.90 (3H, *t*, *J* = 6.4 Hz, CH$_3$); ^{13}C-NMR (101 MHz, CDCl$_3$, δ / ppm): 164.87, 162.52, 157.39, 155.79, 149.25, 146.85, 136.72, 135.14, 131.22, 130.51, 129.37, 129.22, 128.63, 128.05, 127.53, 127.15, 125.34, 122.53, 118.98, 118.81, 117.75, 114.85, 107.13 (1C ester + 22C Ar-H), 70.07 (Ar-CH$_2$–O–), 68.47 (–O–CH$_2$–), 31.79, 29.33, 29.21, 29.15, 25.99, 22.64, 14.08 (7C, aliphatic); MS (CHCl$_3$, *m/z*): 587.2246 [M+Na]$^+$.

7-(Benzyloxy)naphthalen-2-yl 4-((4-(nonyloxy)phenyl)diazenyl)benzoate (***4d***). Yield: 72 % (0.381 g); color: orange; m.p: 137 °C; FT-IR (KBr, cm^{-1}): 2956.87 (CH Ar-H), 2872, 2852.71 (CH, aliphatic), 1728 (O–C=O ester), 1472 (N=N); ^{1}H-NMR (400 MHz, CDCl$_3$, δ / ppm): 8.37 (2H, *d*, *J* = 8.4 Hz, Ar-H), 7.98 (2H, *d*, *J* = 8.4 Hz, Ar-H), 7.97 (2H, *d*, *J* = 8.8 Hz, Ar-H), 7.83 (1H, *d*, *J* = 8.8 Hz, Ar-H), 7.78 (1H, *d*, *J* = 8.8 Hz, Ar-H), 7.59 (1H, *d*, *J* = 2.0 Hz, Ar-H), 7.49 (2H, *m*, Ar-H), 7.41 (2H, *m*, Ar-H), 7.35 (1H, *d*, *J* = 7.2 Hz, Ar-H), 7.24–7.21 (3H, *m*, Ar-H), 7.03 (2H, *d*, *J* = 8.8 Hz, Ar-H), 5.18 (2H, *s*, Ar-CH$_2$–O–), 4.05 (2H, *t*, *J* = 6.6 Hz, –O–CH$_2$–), 1.83 (2H, *quint*, *J* = 7.0 Hz, –CH$_2$–), 1.49 (2H, *quint*, *J* = 7.0 Hz, –CH$_2$–), 1.30 (10H, *m*, aliphatic), 0.90 (3H, *t*, *J* = 6.4 Hz, –CH$_3$); ^{13}C-NMR (101 MHz, CDCl$_3$, δ / ppm): 164.87, 162.49, 157.37, 155.81, 149.24, 146.85, 136.71, 135.13, 131.22, 130.49, 129.37, 129.21, 128.62, 128.05, 127.53, 127.14, 125.31, 122.52, 118.98, 118.80, 117.75, 114.83, 107.10 (1C ester + 22C Ar-H), 70.05 (Ar-CH$_2$–O–), 68.45 (–O–CH$_2$–), 31.86, 29.51, 29.37, 29.24, 29.14, 25.99, 22.65, 14.09 (8C, aliphatic); MS (CHCl$_3$, *m/z*): 601.2408 [M+Na]$^+$.

7-(Benzyloxy)naphthalen-2-yl 4-((4-(decyloxy)phenyl)diazenyl)benzoate (***4e***). Yield: 62 % (0.335 g); color: orange; m.p.: 148 °C; FT-IR (KBr, cm^{-1}): 2957 (CH Ar-H), 2941, 2918 (CH, aliphatic), 1732 (O–C=O ester), 1501 (N=N); ^{1}H-

-NMR (400 MHz, CDCl$_3$, δ / ppm): 8.37 (2H, *d*, *J* = 8.4 Hz, Ar-H), 7.98 (2H, *d*, *J* = 8.4 Hz, Ar-H), 7.97 (2H, *d*, *J* = 8.8 Hz, Ar-H), 7.83 (1H, *d*, *J* = 8.8 Hz, Ar-H), 7.78 (1H, *d*, *J* = 8.8 Hz, Ar-H), 7.59 (1H, *d*, *J* = 2.0 Hz, Ar-H), 7.49 (2H, *m*, Ar-H), 7.41 (2H, *m*, Ar-H), 7.35 (1H, *d*, *J* = 7.2 Hz, Ar-H), 7.24–7.21 (3H, *m*, Ar-H), 7.03 (2H, *d*, *J* = 8.8 Hz, Ar-H), 5.18 (2H, *s*, Ar-CH$_2$–O–), 4.05 (2H, *t*, *J* = 6.6 Hz, –O–CH$_2$–), 1.83 (2H, *quint*, *J* = 7.0 Hz, –CH$_2$–), 1.49 (2H, *quint*, *J* = = 7.0 Hz, –CH$_2$–), 1.29 (12H, *m*, aliphatic), 0.89 (3H, *t*, *J* = 6.4 Hz, –CH$_3$); ^{13}C--NMR (101 MHz, CDCl$_3$, δ / ppm): 164.88, 162.49, 157.38, 155.83, 149.24, 146.87, 136.72, 135.14, 131.22, 130.50, 129.37, 129.22, 128.63, 128.05, 127.53, 127.15, 125.30, 122.53, 118.98, 118.81, 117.75, 114.84, 10.12 (1C ester + 22C Ar-H), 70.07 (Ar-CH$_2$–O–), 68.46 (–O–CH$_2$–), 31.89, 29.54, 29.37, 29.30, 29.15, 25.99, 22.66, 14.10 (8C, aliphatic); MS (CHCl$_3$, *m/z*): 615.2653 [M+Na]$^+$.

7-(Benzyloxy)naphthalen-2-yl 4-((4-(hexyloxy)benzoyl)oxy)benzoate (***5a***). Yield: 69 % (0.350 g); color: white; m.p.: 144 °C; FT-IR (KBr, cm^{-1}): 3030 (CH Ar-H), 2936, 2868 (CH, aliphatic), 1732, 1728 (O–C=O ester); ^{1}H-NMR (400 MHz, CDCl$_3$, δ / ppm): 8.32 (2H, *d*, *J* = 8.8 Hz, Ar-H), 8.17 (2H, *d*, *J* = 9.0 Hz, Ar-H), 7.82 (1H, *d*, *J* = 8.8 Hz, Ar-H), 7.78 (1H, *d*, *J* = 8.8 Hz, Ar-H), 7.57 (1H, *d*, *J* = 2.0 Hz, Ar-H), 7.49 (2H, *m*, Ar-H), 7.43–7.34 (5H, *m*, Ar-H), 7.24–7.20 (3H, *m*, Ar-H), 6.99 (2H, *d*, *J* = 8.8 Hz, Ar-H), 5.18 (2H, *s*, Ar-CH$_2$–O–), 4.05 (2H, *t*, *J* = 6.6, Hz –O–CH$_2$–), 1.83 (2H, *quint*, *J* = 7.0 Hz, –CH$_2$–), 1.49 (2H, *quint*, *J* = 7.0 Hz, –CH$_2$–), 1.37 (4H, *m*, aliphatic), 0.93 (3H, *t*, *J* = 6.8 Hz, –CH$_3$); ^{13}C-NMR (101 MHz, CDCl$_3$, δ / ppm): 164.61, 164.32, 163.82, 157.36, 155.38, 149.20, 136.72, 135.13, 132.40, 131.80, 129.35, 129.19, 128.61, 128.03, 127.52, 127.12, 126.95, 122.09, 120.94, 118.95, 118.82, 117.75, 114.40, 107.09 (2C ester + 22C Ar-H), 70.04 (Ar-CH$_2$–O–), 68.36 (–O–CH$_2$–), 31.51, 29.03, 25.63, 22.56, 14.00 (5C, aliphatic); MS (CHCl$_3$, *m/z*): 575.1825 [M+Na]$^+$.

7-(Benzyloxy)naphthalen-2-yl 4-((4-(heptyloxy)benzoyl)oxy)benzoate (***5b***). Yield: 78 % (0.403 g); color: white; m.p.: 129 °C; FT-IR (KBr, cm$^{–1}$): 3068.74 (CH Ar-H), 2947, 2870 (CH, aliphatic), 1734 (O–C=O ester); ^{1}H-NMR (400 MHz, CDCl$_3$, δ / ppm): 8.32 (2H, *d*, *J* = 8.9 Hz, Ar-H), 8.16 (2H, *d*, *J* = 8.8 Hz, Ar-H), 7.82 (1H, *d*, *J* = 8.8 Hz, Ar-H), 7.78 (1H, *d*, *J* = 8.8 Hz, Ar-H), 7.57 (1H, *d*, *J* = 1.8 Hz, Ar-H), 7.49 (2H, *m*, Ar-H), 7.42–7.34 (5H, *m*, Ar-H), 7.24––7.20 (3H, *m*, Ar-H), 6.99 (2H, *d*, *J* = 8.9 Hz, Ar-H), 5.18 (2H, *s*, Ar-CH$_2$–O–), 4.05 (2H, *t*, *J* = 6.6 Hz, –O–CH$_2$–), 1.83 (2H, *quint*, *J* = 7.0 Hz, –CH$_2$–), 1.48 (2H, *quint*, *J* = 7.0 Hz, –CH$_2$–), 1.33 (6H, *m*, aliphatic), 0.91 (3H, *t*, *J* = 6.6 Hz, –CH$_3$); ^{13}C-NMR (101 MHz, CDCl$_3$, δ / ppm): 164.63, 164.34, 163.83, 157.37, 155.39, 149.21, 136.73, 135.14, 132.41, 131.82, 129.36, 129.20, 128.63, 128.05, 127.53, 127.17, 126.96, 122.10, 120.95, 118.97, 118.83, 117.76, 114.42, 107.10 (2C ester + 22C Ar-H), 70.06 (Ar-CH$_2$–O–), 68.38 (–O–CH$_2$–), 31.74, 29.08, 29.01, 25.93, 22.58, 14.06 (6 C, aliphatic); MS (CHCl$_3$, *m/z*): 589.1939 [M+Na]$^+$.

7-(Benzyloxy)naphthalen-2-yl 4-((4-(octyloxy)benzoyl)oxy)benzoate (**5c**). Yield: 61 % (0.325 g); color: white; m.p.: 148 °C; FT-IR (KBr, cm^{-1}): 3067 (CH Ar-H), 2926, 2851 (CH, aliphatic), 1738, 1734 (O–C=O ester); ^{1}H-NMR (400 MHz, CDCl$_3$, δ / ppm): 8.32 (2H, *d*, *J* = 8.7 Hz, Ar-H), 8.16 (2H, *d*, *J* = 8.8 Hz, Ar-H), 7.82 (1H, *d*, *J* = 9.0 Hz, Ar-H), 7.78 (1H, *d*, *J* = 8.8 Hz, Ar-H), 7.57 (1H, *d*, *J* = 2.0 Hz, Ar-H), 7.49 (2H, *m*, Ar-H), 7.43–7.34 (5H, *m*, Ar-H), 7.24–7.20 (3H, *m*, Ar-H), 6.99 (2H, *d*, *J* = 8.7 Hz, Ar-H), 5.18 (2H, *s*, Ar-CH$_2$–O–), 4.05 (2H, *t*, *J* = 6.6 Hz, –O–CH$_2$–), 1.83 (2H, *quint*, *J* = 7.0 Hz, –CH$_2$–), 1.48 (2H, *quint*, *J* = 6.8 Hz, –CH$_2$–), 1.31 (8H, *m*, aliphatic), 0.90 (3H, *t*, *J* = 6.4 Hz, –CH$_3$); ^{13}C-NMR (101 MHz, CDCl$_3$, δ / ppm): 164.62, 164.34 , 163.83, 157.37, 155.39, 149.22, 136.73, 135.14, 132.41, 131.82, 129.36, 129.20, 128.63, 128.05, 127.53, 127.14, 126.96, 122.10, 120.95, 118.97, 118.83, 117.76, 114.42, 107.10 (2C ester + 22C Ar-H), 70.06 (Ar-CH$_2$–O–), 68.38 (–O–CH$_2$–), 31.79, 29.31, 29.20, 29.08, 25.97, 22.64, 14.08 (7C, aliphatic); MS (CHCl$_3$, *m/z*): 603.2077 [M+Na]$^+$.

7-(Benzyloxy)naphthalen-2-yl 4-((4-(nonyloxy)benzoyl)oxy)benzoate (**5d**). Yield: 74 % (0.402 g); color: white; m.p.: 146 °C; FT-IR (KBr, cm^{-1}): 3030 (CH Ar-H), 2913, 2851 (CH, aliphatic), 1730, 1722 (O–C=O ester); ^{1}H-NMR (400 MHz, CDCl$_3$, δ / ppm): 8.32 (2H, *d*, *J* = 8.7 Hz, Ar-H), 8.16 (2H, *d*, *J* = 8.8 Hz, Ar-H), 7.82 (1H, *d*, *J* = 8.8 Hz, Ar-H), 7.78 (1H, *d*, *J* = 8.8 Hz, Ar-H), 7.57 (1H, *d*, *J* = 1.6 Hz, Ar-H), 7.49 (2H, *m*, Ar-H), 7.43–7.34 (5H, *m*, Ar-H), 7.24–7.20 (3H, *m*, Ar-H), 6.99 (2H, *d*, *J* = 8.7 Hz, Ar-H), 5.18 (2H, *s*, Ar-CH$_2$–O–), 4.05 (2H, *t*, *J* = 6.6 Hz, –O–CH$_2$–), 1.83 (2H, *quint*, *J* = 7.0 Hz, –CH$_2$–), 1.48 (2H, *quint*, *J* = 7.0 Hz, –CH$_2$–), 1.30 (10H, *m*, aliphatic), 0.90 (3H, *t*, *J* = 6.0 Hz, –CH$_3$); ^{13}C-NMR (101 MHz, CDCl$_3$, δ / ppm): 164.61, 164.33, 163.82, 157.37, 155.39, 149.21, 136.72, 135.13, 132.40, 131.81, 129.35, 129.19, 128.62, 128.04, 127.53, 127.13, 126.96, 122.09, 120.94, 118.96, 118.82, 117.75, 114.41, 107.10 (2C ester + 22C Ar-H), 70.05 (Ar-CH$_2$–O–), 68.37 (–O–CH$_2$–), 31.85, 29.49, 29.34, 29.23, 29.07, 25.96, 22.65, 14.08 (8 C, aliphatic), MS (CHCl$_3$, *m/z*): 617.2224 [M+Na]$^+$.

7-(Benzyloxy)naphthalen-2-yl 4-((4-(decyloxy)benzoyl)oxy)benzoate (**5e**). Yield: 67 % (0.376 g); color: white; m.p.: 136 °C FT-IR (KBr, cm^{-1}): 3021 (CH Ar-H), 2914, 2849 (CH, aliphatic), 1732, 1728 (O–C=O ester); ^{1}H-NMR (400 MHz, CDCl$_3$, δ / ppm): 8.32 (2H, *d*, *J* = 8.8 Hz, Ar-H), 8.16 (2H, *d*, *J* = 9.0 Hz, Ar-H), 7.82 (2H, *d*, *J* = 8.8 Hz, Ar-H), 7.78 (1H, *d*, *J* = 8.8 Hz, Ar-H), 7.57 (1H, *d*, *J* = 2.0 Hz, Ar-H), 7.49 (2H, *m*, Ar-H), 7.42–7.34 (5H, *m*, Ar-H), 7.24–7.20 (3H, *m*, Ar-H), 6.99 (2H, *d*, *J* = 8.8 Hz, Ar-H), 5.18 (2H, *s*, Ar-CH$_2$–O–), 4.05 (2H, *t*, *J* = 6.6 Hz, –O–CH$_2$–), 1.83 (2H, *quint*, *J* = 7.0 Hz, –CH$_2$–), 1.48 (2H, *quint*, *J* = 7.0 Hz, –CH$_2$–), 1.29 (12H, *m*, aliphatic), 0.89 (3H, *t*, *J* = 6.6 Hz, –CH$_3$); ^{13}C-NMR (101 MHz, CDCl$_3$, δ / ppm): 164.95, 164.66, 164.15, 157.69, 155.71, 149.53, 137.04, 135.46, 132.73, 132.14, 129.68, 129.52, 128.95, 128.37, 127.86, 127.45, 127.28, 122.42, 121.27, 119.29, 119.15, 118.07, 114.74, 107.41 (2C ester + 22C Ar-H), 70.38 (Ar-CH_2–O–), 68.70 (–O–CH_2–), 32.20, 29.86, 29.67, 29.62, 29.39, 26.28, 22.98, 14.42 (8C, aliphatic); MS ($CHCl_3$, *m/z*): 631.2366 $[M+Na]^+$.

Journal of the Serbian Chemical Society
JSCS-info@shd.org.rs • www.shd.org.rs/JSCS

J. Serb. Chem. Soc. *80* (5) 685–694 (2015)
JSCS–4748

UDC 546.881–31+541.135.5+544.6.076.2+
546.34:621.354.32
Original scientific paper

High performance of solvothermally prepared VO_2(B) as an anode for aqueous rechargeable lithium batteries

SANJA MILOŠEVIĆ[1], IVANA STOJKOVIĆ[2], MIODRAG MITRIĆ[3]
and NIKOLA CVJETIĆANIN[2]*

[1]The Vinča Institute, Department of Materials Science, University of Belgrade, P. O. Box 522, 11001 Belgrade, Serbia, [2]Faculty of Physical Chemistry, University of Belgrade, 11158 Belgrade, Serbia and [3]The Vinča Institute, Laboratory for Theoretical and Condensed Matter Physics, University of Belgrade, P. O. Box 522, 11001 Belgrade, Serbia

(Received 22 September, revised 3 December, accepted 25 December 2014)

Abstract: The VO_2(B) was synthesized *via* a simple solvothermal route at 160 °C in ethanol. The initial discharge capacity of the VO_2(B) anode, in saturated aqueous solution of $LiNO_3$, was 177 mAh g^{-1} at a current rate of 50 mA g^{-1}. After 50 cycles, the capacity fade was 4 %, but from 20th–50th cycle, no capacity drop was observed. The VO_2(B) showed very good cyclability at a current rate of even 1000 mA g^{-1} with initial discharge capacity of 92 mAh g^{-1}. The excellent electrochemical performance of VO_2(B) was attributed to the stability of micro–nano structures to a repeated intercalation/deintercalation process, very good electronic conductivity as well as the very low charge transfer resistance in an aqueous electrolyte.

Keywords: aqueous rechargeable lithium batteries; anode materials; discharge capacity; electrochemical impedance spectroscopy; electric conductivity.

INTRODUCTION

Most of the present lithium technology is based on organic electrolytes.[1] The most common of these electrolytes are expensive, toxic and flammable liquids that may cause accidents in the case of improper use.[1,2] One way to overcome the safety issue is to use aqueous electrolytes which are environmentally benign. The assembly of aqueous lithium batteries is simpler and cheaper than for their organic counterparts because it does not demand the usage of argon-filled chambers in which moisture and oxygen have to be excluded. Unfortunately, aqueous rechargeable lithium batteries (ARLBs) cannot deliver a high voltage, because their voltage is restricted by the potentials of the evolution of hydrogen and oxygen. However, aqueous electrolytes have conductivities which are

---

* Corresponding author. E-mail: nikola.cvj@ffh.bg.ac.rs

doi: 10.2298/JSC140922128M

typically two orders of magnitude higher than that of organic systems, which enables the achievement of a high rate capability. From the time when the first papers were published in 1994/5 by Dahn's group,[3–5] interest in ARLBs increased. Numerous intercalation compounds have been tested in alkaline and neutral aqueous electrolytes,[5–12] especially in the last five years.[12–21] Among them, the vanadium oxide family of compounds has attracted much attention as anodic materials for ARLBs. Due to a suitable electrode potential and tunnel structure, VO_2(B), one of the polymorphs of VO_2, was already used as the anodic material in the first ARLBs.[3,5] However, this compound was neglected in subsequent researches compared to other vanadium oxides. Transformation from bulk to nano-dimensions brought new qualities to electrode materials, such as larger surface area, shorter diffusion lengths of Li-ion, capability for buffering large volume changes and possible new storage mechanisms, leading to higher specific capacity, faster kinetics and enhanced cycle life.[1,22] This has increased the interest for VO_2(B) both as a cathodic and anodic material for organic and aqueous electrolytes based lithium batteries, respectively. In recent years VO_2(B) has been synthesized with different micro/nano-morphologies: nanowire arrays,[23] networks of nanofilaments,[24] nanobelts and nanosheets,[25–28] nanorods,[29,30] ultra-thin nanowires,[31] flower-like micro–nano structures,[13] and hollow microspheres with a nanothorn surface.[32] The majority of these morphologies have been synthesised by more or less sophisticated hydrothermal/solvothermal methods.

In this paper, the high capacity and excellent galvanostatic cyclic behaviour of solvothermally prepared VO_2(B), in saturated aqueous $LiNO_3$ solution and up to current rates of 1000 $mA\cdot g^{-1}$, is primarily demonstrated.

EXPERIMENTAL

Nanostructured VO_2(B) was synthesized *via* a simple one-step solvothermal (ST) process that was published recently.[33] Thus, without using any additives or surfactants, a mixture of vanadium pentoxide (Merck 99.99 %) and ethanol (Merck 96 %) was treated in a Teflon-lined stainless-steel autoclave at 160 °C for 24 h. The obtained blue–black powder was rinsed several times with ethanol and then dried at 50 °C.

$LiCr_{0.15}Mn_{1.85}O_4$, as the counter electrode (cathode) material for a two electrode cell, was prepared by the glycine–nitrate method (GNM).[34]

The characterization of VO_2(B) and $LiCr_{0.15}Mn_{1.85}O_4$ by X-ray diffraction (XRD) was presented in previous papers.[33,34] The morphological characterization of VO_2(B) was performed on a JEOL JSM-6390 LV scanning electron microscope (SEM). The SEM images of $LiCr_{0.15}Mn_{1.85}O_4$ corresponded to those published previouly[34] and are not presented here.

The preparation of electrodes from both materials was performed in the same way. The active material, carbon black and poly(vinylidene fluoride) in weight ratio 85:10:5 were homogeneously mixed in *N*-methyl 2-pyrrolidone. The slurry was treated for about 30 min in an ultrasonic bath, deposited on the stainless steel (SS) discs electrodes (≈6.2 cm^2) and Pt foil (2 cm^2), and dried under vacuum at 120–140 °C for at least 4 h.

Galvanostatic charging/discharging measurements were performed using a software-controlled Arbin BT-2042 device, in a two-electrode arrangement within the voltage range 0.5–1.65 V. The electrode materials applied to the SS discs were mounted in the body of a cell made from Plexiglas. The electrodes were separated with eight filter paper sheets (total thickness ≈1 mm) soaked in saturated aqueous solution of $LiNO_3$ as the electrolyte. The capacity calculations were based on the weight of the active anode material, *i.e.*, VO_2(B).

For electrical conductivity measurements, VO_2(B) powder was pressed into a pellet, 8 mm in diameter and 1.835 mm thick. Good electrical contact was realized by coating silver paste onto both contact surfaces of the pellet. The conductivity was measured by means of an Wayne Kerr B224 AC bridge at a fixed frequency of 1 kHz. The self-made two electrode conductometric cell for solid conductors was placed inside a small cylindrical oven, heated up to 120 °C, and the measurements were performed in the cooling regime.

Electrochemical impedance spectroscopy (EIS) measurements were performed in a three electrode cell (VO_2(B) deposited on Pt foil – working electrode, Pt foil – counter electrode, SCE – reference electrode) filled with a saturated aqueous solution of $LiNO_3$ using a Gamry PCI4/300 Potentiostat/Galvanostat. An AC amplitude of 5 mV was applied in the frequency range 100 kHz–0.1 Hz. The programme EIS Spectrum Analyzer, version 1.0, was used for fitting data to the equivalent circuit model.

RESULTS AND DISCUSSION

SEM images of VO_2(B) synthesized solvothermally are shown in Fig. 1. The product consisted of different nano-units, such as single nanoparticles, rods and flat particles, mutually welded in different irregularly shaped micrometre-sized structures, Fig. 1A. The shape of micro–nano structures mainly resembled those previously described in more detail.[33] Additionally, some amount of large spherical micrometre-sized particles, the surfaces of which were covered with mostly spherical particles of size mainly below 300 nm, was also observed, Fig. 1B.

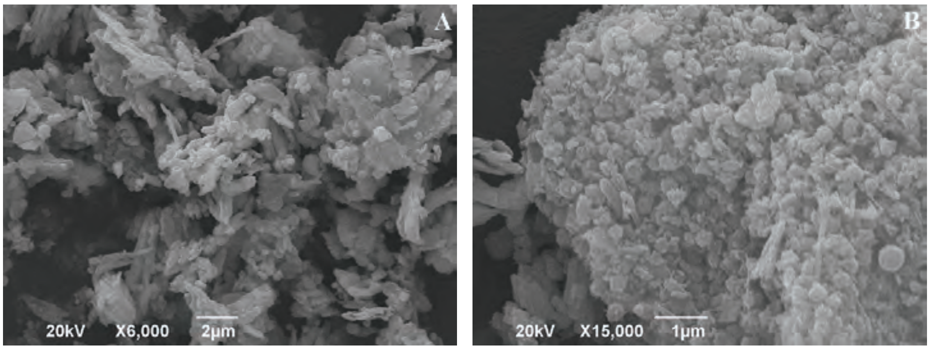

Fig. 1. SEM micrograph of VO_2(B): A) irregularly shaped particles composed from welded nano-units; B) large spherical VO_2(B) particles covered with spherical nano particles.

The voltage range, 0.5–1.65 V, for the galvanostatic charge/discharge experiments was determined based on the electrochemical performance of both VO_2(B) and $LiCr_{0.15}Mn_{1.85}O_4$ in saturated aqueous solution of $LiNO_3$, perceived by cyclic voltammetry.[33,34] Here, $LiCr_{0.15}Mn_{1.85}O_4$ was used as cathodic material instead of most commonly used $LiMn_2O_4$, because the substitution of some manganese with Cr^{3+} gives a faster cathode in saturated aqueous solution of $LiNO_3$.[34] A two-fold stoichiometric excess of the cathode material $LiCr_{0.15}Mn_{1.85}O_4$ was used in order to avoid the cathode limiting the cell performance.

Although there was no voltage plateau during discharging (Figs. S-1 snd S-2 of the Supplementary material to this paper), the discharge capacity of the VO_2(B) anode was very high and exceptionally stable, Fig. 2. In the first 50 cycles, the VO_2(B) anode was tested with a constant current of 50 mA g^{-1}, Fig. 2A, and then every next ten cycles the current was increased to 100, 150, 200, 500 and 1000 mA g^{-1}, Fig. 2B. The initial discharge capacity was 177 mAh g^{-1} at current rate 50 mA g^{-1}. The discharge capacity then increased to 182 mAh g^{-1}, and after the 5th cycle, started to decrease. After twenty cycles, the discharge capacity became constant at 170 mAh g^{-1}. The capacity fade after 50 cycles was only 4 %. The obtained value of the capacity exceeded the theoretical capacity of $Li_{0.5}VO_2$(B) (161.6 mAh g^{-1}). This could mean that surface storage participates in the overall charge storage. Figure 2B shows that VO_2(B) had a quite high

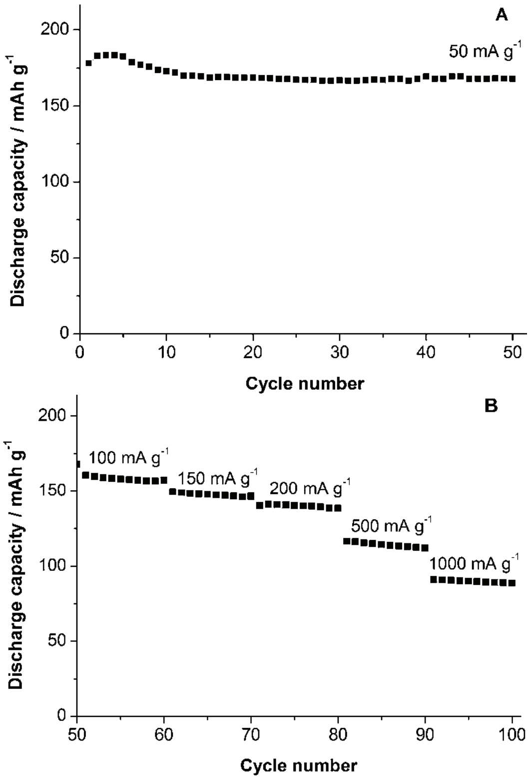

Fig. 2. Discharge capacity of VO_2(B) anode in a saturated aqueous solution of $LiNO_3$: A) at a current rate of 50 mA g^{-1} and B) at different current rates: 100, 150, 200, 500 and 1000 mA g^{-1}.

discharge capacity and retained very good cycling stability when the current rates were significantly increased. The initial discharge capacities were 161, 149, 140, 117 and 92 mAh g^{-1} at current rates 100, 150, 200, 500 and 1000 mA g^{-1}, respectively. The capacity fade after ten cycles was below 4 % in all cases. These are much better characteristics in comparison to other intercalation anode materials hitherto tested in aqueous electrolytes with similar current rates.[12–14,16,17,19] Recently, Tang *et al.* published that a hybrid of V_2O_5 and MWCNTs coated with polypyrrole as anode for ARLB had excellent cycling performance, but its reversible capacity was only 60 mAh g^{-1} at 200 mA g^{-1}.[20]

The Nyquist plot of the lithiated VO_2(B) ($Li_{0.5}VO_2$) electrode showed one depressed semicircle in the high-to-medium frequency region, which could be assigned to charge-transfer resistance (R_{ct}), and a near unity-slope line at lower frequencies, which could be considered as Warburg impedance, Fig. 3A. The data were successfully fitted in the frequency range 100 kHz–1 Hz to the equivalent circuit model shown in the inset of Fig. 3A. The charge transfer resistance amounted to only 1.8 Ω, which is six times and an order of magnitude smaller than for NiO–LiV_3O_8 and LiV_3O_8 electrode, respectively, in the same

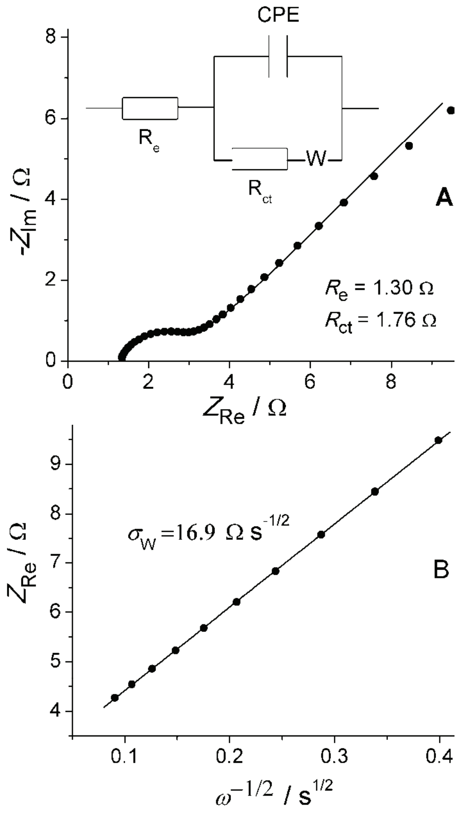

Fig. 3. EIS data of lithiated VO_2(B) electrode: A) Nyquist plot and the equivalent circuit used to fit the impedance data (R_e – resistance of electrolyte, R_{ct} – charge transfer resistance, *CPE* – constant phase element, W – Warburg impedance) and B) the Z' *vs.* $\omega^{-1/2}$ plot used for determination of D_{Li+}. ● represents data, line represents fit.

aqueous electrolyte.[19] The calculated value of R_{ct} was also approximately two orders of magnitude smaller than those obtained for similar anodes in some organic electrolytes.[35,36] The diffusion coefficient of the lithium ion was calculated from the equation:[37,19]

$$D = \frac{R^2T^2}{2A^2n^4F^4c_{\text{Li}^+}^2\sigma_{\text{W}}^2} \tag{1}$$

where σ_{W} is the Warburg coefficient, and according to the equation:[37]

$$Z_{\text{R}_\text{e}} = R_\text{e} + R_{\text{ct}} + \sigma_{\text{W}}\omega^{-1/2} \tag{2}$$

which is valid in the low-frequency region. Equation (2) represents the slope of the Z_{R_e} *vs.* $\omega^{-1/2}$ plot, Fig. 3B. The concentration of Li^+ in $\text{Li}_{0.5}\text{VO}_2$ was obtained using unit cell parameters of this monoclinic compound: a = 12.03 Å, b = 4.0 Å, c = 6.42 Å and β =1 06.6°,[38] bearing in mind that the unit cell contains eight formula-units. The crystal structure of $\text{Li}_{0.5}\text{VO}_2$ is very similar to the parent VO_2(B), which is monoclinic (space group C12/m1 – ICSD 73855), having the unit cell 9.2 % elongated in the b-axis direction.[38] By taking R = 8.314 J·mol^{-1} K^{-1}, T = 298 K, A = 2 cm^2, n = 0.5, F = 96485 C mol^{-1}, $c_{\text{Li+}}$ = 0.0224 mol·cm^{-3} and σ_{W} = 16.9 Ω s$^{-1/2}$, the calculated value of the diffusion coefficient is equal to $D_{\text{Li+}}$ = 1×10^{-12} cm^2 s^{-1}. This value is almost the same as the diffusion coefficient of Li^+ (1.69×10^{-12} cm^2 s^{-1}) in LiV_3O_8,[19] determined by the same method, but is much smaller than the diffusion coefficients of Li^+ in carbon-coated VO_2(B) nanobelts (2.6×10^{-10}–8.6×10^{-10} cm^2 s^{-1}), obtained from cyclic voltammetry experiments in an organic electrolyte.[36]

High power devices demand fast transport of electrons, therefore the electronic conductivities of cathode and anode materials for LBs is of very great importance. VO_2(B) is a semiconductor, but there is not much data about its electronic conductivity.[39,40] The temperature dependence of the specific conductivity of the VO_2(B) synthesised in this work is shown in Fig. 4. From this almost ideally linear, logarithmic-type plot, the activation energy for electric conductivity was determined to be 21.5 kJ·mol^{-1} or 0.223 eV. The room temperature electric conductivity is 4.7×10^{-3} S cm^{-1}, which is in good agreement with the value (≈1×10^{-2} S cm^{-1}) obtained by Corr. *et al.*[40] for VO_2(B) nanorods, pressed into a pellet, by four-probe resistivity measurements. This value is several orders of magnitude higher than those of some anode and cathode materials for lithium batteries, such as $\text{Li}_4\text{Ti}_5\text{O}_{12}$ (3.5×10^{-8} S cm^{-1})[41] and LiFePO_4 (10^{-9}–10^{-10} S cm^{-1}).[42]

It was shown recently that electrochemical cycling stability of some cathode[43,44] and anode[45] materials for ARLBs, mostly layer-structured compounds, abruptly decreases in the low-pH solutions due to the co-intercalation of H^+ ions. Such behaviour was not observed in this study, despite the low pH (around 3.2) of the saturated (≈9 M) aqueous solution of $LiNO_3$. The tunnel--structured VO_2(B) and the spinel-structured $LiCr_{0.15}Mn_{1.85}O_4$ used as the cathode are not, most probably, energetically favourable for the accommodation of H^+ ions. This was already confirmed, at least to some extent, for spinel-type compounds.[44]

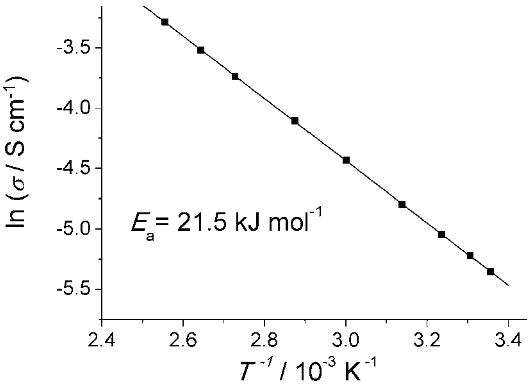

Fig. 4. Temperature dependence of the specific conductivity of VO_2(B). ● represents data, line represents fit.

Nanostructures of VO_2(B), such as nanobelts, nanorods and nanosheets, can offer a high initial capacity due to their large surface area and the short diffusion length of Li-ion. Unfortunately these nanostructures mostly suffer from significant capacity fade. Such a loss of capacity, on the one hand, is due to pulverization of the electroactive material during cycling, resulting in the loss of some amount of active mass. On the other hand, nano-sized materials have a large surface area and high surface energy that favour the formation of agglomerates and leads to the loss of the insertion capacity of Li^+.[35,46] It was already documented that 3D VO_2(B) structures such as micro/nano-flowers[13] and hollow microspheres[32] show improved electrochemical characteristics because they have collective properties from the self-assembling of nano-units into micrometre-sized structures. The VO_2(B) obtained in this study enabled the excellent performance of the ARLB, most likely due to both the micro–nano morphology and the use of a water-based electrolyte. Although the nano-units were mutually welded in irregularly shaped microstructures, they were robust enough on exposure to the aqueous electrolyte to give a stable intercalation capacity of lithium ions. These micro–nano structures also had very good electronic conductivity, but the rate of diffusion of Li^+ inside these structures, although one of the most important properties, seems not to have been a prevailing factor for the excellent electrochemical performance. The EIS data indicated that not only the high conductivity of aqueous electrolyte, but also the very low charge transfer resistance and the absence of resistive surface film seems to be responsible for the very fast insertion/extraction of lithium ions.

All the presented electrochemical experiments were performed in aerated aqueous solution, without testing the oxygen content. The elimination of dissolved oxygen may significantly improve the performance of some ARLBs.[47] However, in the presence of oxygen, carbon coating of the cathode may exceptionally improve the rate capability and cycle life, as was recently demonstrated for a VO_2(B)/$LiNO_3$(sat)/$LiFe_{1-x}V_xPO_4$–C aqueous battery.[48] The precise influence of dissolved oxygen on VO_2(B) anodes in saturated aqueous solutions of $LiNO_3$ remains to be examined in the near future.

CONCLUSIONS

The VO_2(B) was synthesised by a simple, low-cost and environmentally friendly solvothermal method. It displayed exceptional characteristics during galvanostatic cycling: the initial discharge capacity was 177, 161, 149, 140, 117 and 92 mAh g^{-1} at current rates 50, 100, 150, 200, 500 and 1000 mA g^{-1}, respectively, with a very small capacity fade. The obtained material showed very high electronic conductivity and moderately fast diffusion of lithium ions. The robust micro–nano structures of VO_2(B) in contact with the highly conductive aqueous electrolyte formed an electrode/electrolyte interface with fast charge transfer kinetics, which enabled the excellent rate performance of the anode. Further improvement of hydrothermal/solvothermal synthetic methods in obtaining strong micro–nano structures, in the first place more uniform in shape, may offer superior electrode materials for aqueous rechargeable lithium batteries.

SUPPLEMENTARY MATERIAL

Charge/discharge curves of a VO_2(B) anode are available electronically from http:// //www.shd.org.rs/JSCS/, or from the corresponding author on request.

Acknowledgements. This work was supported by the Ministry of Education, Science and Technological Development of the Republic of Serbia (Contract No. III45014).

ИЗВОД

ВИСОКЕ ПЕРФОРМАНСЕ СОЛВОТЕРМАЛНО СИНТЕТИСАНОГ VO_2(B) КАО АНОДНОГ МАТЕРИЈАЛА ЗА СЕКУНДАРНЕ ЛИТИЈУМСКЕ БАТЕРИЈЕ СА ВОДЕНИМ ЕЛЕКТРОЛИТОМ

САЊА МИЛОШЕВИЋ[1], ИВАНА СТОЈКОВИЋ[2], МИОДРАГ МИТРИЋ[3] и НИКОЛА ЦВЈЕТИЋАНИН[2]

[1]*Институт Винча, Лабораторија за материјале, Универзитет у Београду, п. пр. 522, 11001 Београд,* [2]*Факултет за физичку хемију, Универзитет у Београду, 11158 Београд 118 и* [3]*Институт Винча, Лабораторија за теорijску физику и физику кондензоване материје, Универзитет у Београду, п. пр. 522, 11001 Београд*

VO_2(B) је синтетисан једноставним солвотермалним поступком на 160 °C у етанолу. Тестиран је као анодни материјал за секундарне литијумске батерије у засићеном раствору литијум-нитрата методом галваностатског пуњења и пражњења. При специфичним јачинама струје од 50 до 1000 mA g^{-1} VO_2(B) је показао висок почетни капацитет при пражњењу од 177 до 92 mAh g^{-1}, уз веома мали пад капацитета. Високе перформансе овог материјала потичу од стабилности робусних микро–нано структура према великом броју интеркалација/деинтеркалација јона литијума као и од добре електронске проводљивости и малог отпора преносу наелектрисања.

(Примљено 22. септембра, ревидирано 3. децембра, прихваћено 25 децембра 2014)

REFERENCES

1. B. Scrosati, J. Garche, *J. Power Sources* **195** (2010) 2419
2. D. Wainwright, *Mat. Tech.* **11** (1996) 9
3. W. Li, J. R. Dahn, D. Wainwright, *Science* **264** (1994) 1115
4. W. Li, W. R. McKinnon, J. R. Dahn, *J. Electrochem. Soc.* **141** (1994) 2310
5. W. Li, J. R. Dahn, *J. Electrochem. Soc.* **142** (1995) 1742
6. G. X. Wang, S. Zhong, D. H. Bradhurst, S. H. Dou, H. K. Liu, *J. Power Sources* **74** (1998) 198
7. J. Kohler, H. Makahira, H. Uegaito, H. Inoue, M. Toki, *Electrochim. Acta* **46** (2000) 59
8. Y. Wang, Y. Xia, *Electrochem. Commun.* **7** (2005) 1138
9. G. J. Wang, H. P. Zhang, L. J. Fu, B. Wang, Y. P. Wu, *Electrochem. Commun.* **9** (2007) 1873
10. G. J. Wang, N. H. Zhao, L. C. Yang, Y. P. Wu, H. Q. Wu, R. Holze, *Electrochim. Acta* **52** (2007) 4911
11. G. J. Wang, L. J. B. Wang, N. H. Zhao, Y. P. Wu, R. Holze, *J. Appl. Electrochem.* **38** (2008) 579
12. C. Z. Wu, Z. P. Hu, W. Wang, M. Zhang, J. L. Yang, Y. Xie, *Chem Commun.* (2008) 3891
13. S. Zhang, Y. Li, C. Wu, F. Zheng, Y. Xie, *J. Phys. Chem. C* **113** (2009) 15058
14. I. Stojković, N. Cvjetićanin, I. Pašti, M. Mitrić, S. Mentus, *Electrochem. Commun.* **11** (2009) 1512
15. X.-H. Liu, T. Saito, T. Doi, S. Okada, J. Yamaki, *J. Power Sources* **189** (2009) 706
16. I. Stojković, N. Cvjetićanin, M. Mitrić, S. Mentus, *Electrochim. Acta* **56** (2011) 6469
17. M. Zhao, Q. Zheng, F. Wang, W. Dai, X. Song, *Electrochim. Acta* **56** (2011) 3781
18. H. Heli, H. Yadegari, A. Jabbari. *Mat. Chem. Phys.* **126** (2011) 476
19. L. Liu, M. Zhou, X. Wang, F. Tian, H. Guo, B. Shen, T. Hu, *J. Electrochem. Soc.* **159** (2012) A1230
20. W. Tang, X. Gao, Y. Zhu, Y. Yue, Y. Shi, Y. Wu, K. Zhu, *J. Mater. Chem.* **22** (2012) 20143
21. V. S. Nair, Y. L. Cheah, S. Madhavi, *J. Electrochem. Soc.* **161** (2014) A256
22. C. K. Chan, H. Peng, R. D. Twesten, K. Jarausch, X. F. Zhang, Y. Cui, *Nano Lett.* **7** (2007) 490
23. X. Chen, X. Wang, Z. Wang, J. Wan, J. Liu, Y. T. Qian, *Nanotechnology* **15** (2004) 1685
24. E. Baudrin, G. Sudant, D. Larcher, B. Dunn, J.-M. Tarascon, *Chem. Mater.* **18** (2006) 4369
25. G. Li, K. Chao, H. Peng, K. Chen, Z. Zhang, *Inorg. Chem.* **46** (2007) 5787
26. F. Sediri, N. Gharbi, *Mater. Lett.* **63** (2009) 15
27. J. Li, Z. Su, B. Yang, S. Cai, Z. Dong, J. Ma, R. Li, *J. Phys. Chem. Solids* **71** (2010) 407
28. G. Zakharova, I. Hellmann, V. Volkov, C. Taschner, A. Bachmatiuk, A. Leonhardt, R. Klingeler, B. Büchner, *Mater. Res. Bull.* **45** (2010) 1118
29. Ch. V. Subba Reddy, E. H. Walker Jr., S. A. Wicker Sr., Q. L. Williams, R. R. Kalluru, *Curr. Appl. Phys.* **9** (2009) 1195
30. F. J. Quites, H. O. Pastore, *Mater. Res. Bull.* **45** (2010) 892
31. G. Armstrong, J. Canales, A. R. Armstrong, P. Bruce, *J. Power Sources* **178** (2008) 723

32. H. Liu, Y. Wang, K. Wang, E. Hosono, H. Zhou, *J. Mater. Chem.* **19** (2009) 2835
33. S. Miliošević, I. Stojković, S. Kurko, J. Grbović-Novaković, N. Cvjetićanin, *Ceram. Int.* **38** (2012) 2313
34. N. Cvjetićanin, I. Stojković, M. Mitrić, S. Mentus, *J. Power Sources* **174** (2007) 1117
35. M. M. Rahman, J.-Z. Wang, N. H. Idris, Z. Chen, H. Liu, *Electrochim. Acta* **56** (2010) 693
36. X. Rui, D. Sim, C. Xu, W. Liu, H. Tan, K. Wong, H. H. Hng, T. M. Lim, Q. Yan, *RSC Adv.* **2** (2012) 1174
37. A. J. Bard, L. R. Faulkner, *Electrochemical methods: Fundamentals and applications*, 2nd ed., Wiley, New York, 2001, p. 383
38. P. A. Christian, F. J. Di Salvo Jr., D. W. Murphy, US Patent 4228226 (1980)
39. J. Liu, Q. Li, T. Wang, D. Yu, Y. Li, *Angew. Chem. Int. Ed.* **43** (2004) 5048
40. S. A. Corr, M. Grossman, Y. Shi, K. R. Heier, G. D. Stucky, R. Seshadri, *J. Mater. Chem.* **19** (2009) 4362
41. M. Vujković, I. Stojković, M. Mitrić, S. Mentus, N. Cvjetićanin, *Mater. Res. Bull.* **48** (2013) 218
42. S.-Y. Chung, J. T. Bloking, Y.-M. Chiang, *Nat. Mater.* **1** (2002) 123
43. X. Gu, J.-L. Liu, J.-H. Yang, H.-J. Xiang, X.-G. Gong, Y.-Y. Xia, *J. Phys. Chem. C* **115** (2011) 12672
44. Q. Shu, L. Chen, Y. Xia, X. Gong, X. Gu, *J. Phys. Chem., C* **117** (2013) 6929
45. L. Bai, J. Zhu, X. Zhang, Y. Xie, *J. Mater. Chem.* **22** (2012) 16957
46. J. Huang, X. Wang, J. Liu, X. Sun, L. Wang X. Xe, *Int. J. Electrochem. Sci.* **6** (2011) 1709
47. J.-Y. Luo, W.-J. Cui, P. He, Y.-Y. Xia, *Nat. Chem.* **2** (2010) 760
48. M. Vujković, D. Jugović, M. Mitrić, I. Stojković, N. Cvjetićanin, S. Mentus, *Electrochim. Acta* **109** (2013) 835.

Journal of the Serbian Chemical Society
JSCS@tmf.bg.ac.rs • www.shd.org.rs/JSCS
J. Serb. Chem. Soc. 80 (5) S184–S185 (2015)
Supplementary material

SUPPLEMENTARY MATERIAL TO

High performance of solvothermally prepared VO_2(B) as an anode for aqueous rechargeable lithium batteries

SANJA MILOŠEVIĆ[1], IVANA STOJKOVIĆ[2], MIODRAG MITRIĆ[3]
and NIKOLA CVJETIĆANIN[2]*

J. Serb. Chem. Soc. 80 (5) (2015) 685–694

The charging/discharging curves of VO_2(B) anode are shown in Figs. S-1 and S-2. The difference between the first and the second charging at a current rate of 50 mA g^{-1} indicates a large initial irreversible capacity loss, Fig. S-1. The charging and discharging become very stable after twenty cycles, which is reflected in the almost overlapping overall curves in the following cycles. The change in the profile of the charge and discharge curves due to the increase in the current rate is shown in Fig. S-2.

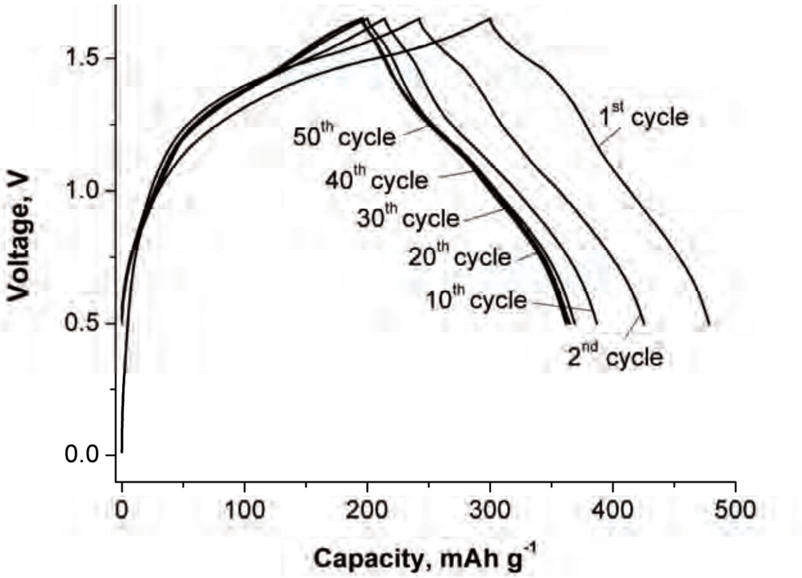

Fig. S-1. Charge/discharge curves of a VO_2(B) anode in saturated aqueous solution of $LiNO_3$ at a current rate of 50 mA g^{-1}.

---

* Corresponding author. E-mail: nikola.cvj@ffh.bg.ac.rs

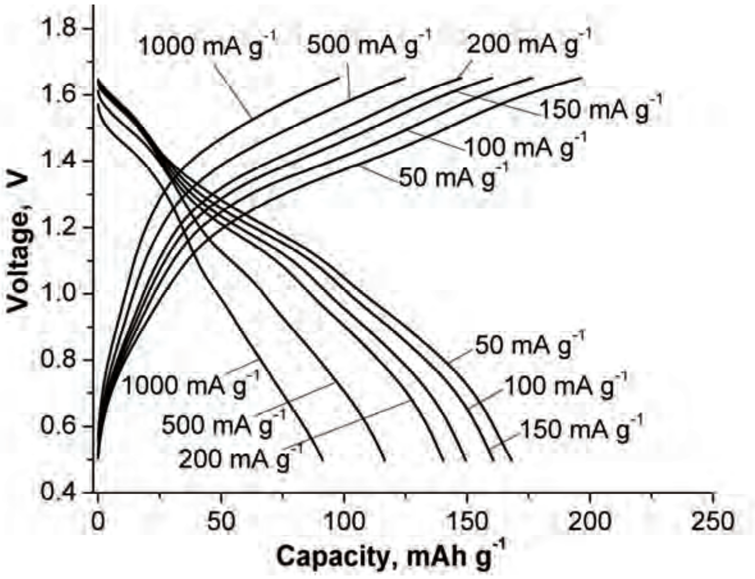

Fig. S-2. Charge/discharge curves of a VO_2(B) anode at different current rates: 50 mAg^{-1} (the last cycle) and 100, 150, 200, 500 and 1000 mA g^{-1} (the first cycle).

Journal of the Serbian Chemical Society
JSCS-info@shd.org.rs • www.shd.org.rs/JSCS

J. Serb. Chem. Soc. 80 (5) 695–704 (2015)
JSCS–4749

UDC 547.262+66.021.2.063.8:66.09.001.57:
544.032.4
Original scientific paper

Solubility of atenolol in ethanol + water mixtures at various temperatures

SAMIN HAMIDI[1] and ABOLGHASEM JOUYBAN[2,3]*

[1]*Liver and Gastrointestinal Diseases Research Center, Tabriz University of Medical Sciences, Tabriz, Iran,* [2]*Drug Applied Research Center and Faculty of Pharmacy, Tabriz University of Medical Sciences, Tabriz 51664, Iran and* [3]*Pharmaceutical Engineering Laboratory, School of Chemical Engineering, College of Engineering, University of Tehran, P. O. Box 11155/4563, Tehran, Iran*

(Received 17 June, revised 17 September, accepted 18 September 2014)

Abstract: The experimental solubility of atenolol in ethanol + water mixtures at different temperatures (298.2, 303.2, 308.2 and 313.2 K) was reported. The solubility was calculated using five numerical methods. First, the Jouyban–Acree model (method I), its combination with the van't Hoff equation (method II) and the extended version of the Jouyban–Acree model with Abraham parameters (method III) were employed. The minimum number of data points (N) were used to train the Jouyban–Acree model ($N = 11$) and its combination with the van't Hoff equation ($N = 22$), then the obtained parameters of the models were used to calculate the solubilites at other temperatures (methods IV and V). The accuracies of the calculated solubilites were evaluated by computing mean percentage deviation (*MPD*). The obtained *MPD*s (±standard deviation) for methods I–V were 5.6±7.1, 5.1±4.6, 34.1±28.0, 10.0±9.6 and 6.6±4.8 %, respectively.

Keywords: mixed solvent; simulation; Jouyban–Acree model.

INTRODUCTION

Drugs are mostly hydrophobic compounds therefore their limited aqueous solubility is the most challenging problem in drug development that causes their poor bioavailability. Many published works could be found regarding the improvement of the low bioavailability of poorly soluble drugs including solubilization techniques. Among the broad variety of methods proposed for enhancing drug solubility, the addition of pharmaceutical cosolvents is the most widely used technique for drugs in aqueous media.[1–3] Furthermore, the solubility enhancement of poorly soluble drugs can be achieved by the changes of temperature,[4]

---

* Corresponding author. E-mail: ajouyban@hotmail.com; jouyban@ut.ac.ir
doi: 10.2298/JSC140617095H

which is a useful technique in recrystalization studies. Several methods have been proposed to explain the solubility enhancement of organic compounds as well as its temperature dependence.[5,6]

Atenolol (Fig. 1) is a well-known drug used in pharmacotherapy of cardiovascular diseases, such as hypertension and stable angina pectoris. Furthermore, it reduces mortality in patients with hypertension and is prescribed in the treatment of patients with myocardial infarction.[7] On the other hand, the poorly aqueous soluble drug needs a high dose to reach therapeutic plasma concentrations. It is well recognized that an injectable liquid formulation provides high doses of drugs in small volumes.[8] Although atenolol is one of the most frequently used anti-hypertensive drugs, information on its solubility, which is one of the important physicochemical properties, is not abundant.

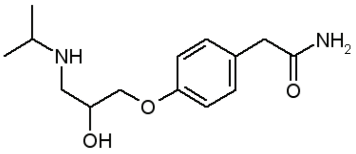

Fig. 1. Chemical structure of atenolol.

Solubility data are acquired in the pharmaceutical industry as well as in formulation processes. Concerning variations of solubility with cosolvent concentration and temperature, as the most important variables, the experimental measurements of solubilities become a laborious and time-consuming procedure. Several mathematical models were developed to predict the solubility of drugs beside their experimental measurements in mixed solvents.[2,5,9] The Jouyban–Acree model is one of the well-established models that provides the most accurate computations for the solubility of drugs concerning temperature and solvent composition. It is represented as:[10]

$$\log C_{\mathrm{m},T}^{\mathrm{sat}} = w_1 \log C_{1,T}^{\mathrm{sat}} + w_2 \log C_{2,T}^{\mathrm{sat}} + \frac{w_1 w_2}{T} \sum_{i=0}^{2} J_i (w_1 - w_2)^i \tag{1}$$

in which $C_{\mathrm{m},T}^{\mathrm{sat}}$ is the solute solubility in the solvent mixtures at temperature T, w_1 and w_2 are the mass fractions of solvent 1 and solvent 2 in the absence of solute, $C_{1,T}^{\mathrm{sat}}$ and $C_{2,T}^{\mathrm{sat}}$ imply the solubility of the solute in the neat solvents 1 and 2, respectively, and J_i denotes the constants of the model, which are computed by regression analysis.

Solubility data at different temperatures in a mono-solvent can be predicted using the van't Hoff equation.[11] The required data are solubilities at the lowest and highest temperatures ($\log C_T^{\mathrm{sat}}$):

$$\log C_T^{\mathrm{sat}} = A + \frac{B}{T} \tag{2}$$

where A and B are model constants calculated using the least square method.

A combination of the Jouyban–Acree model and van't Hoff equation[12] was used to calculate the solubility of pharmaceuticals in solvent mixtures at different temperatures without employing any further experimental values as independent variable. Thus:

$$\log C_{\mathrm{m},T}^{\mathrm{sat}} = w_1\left(A_1 + \frac{B_1}{T}\right) + w_2\left(A_2 + \frac{B_2}{T}\right) + \frac{w_1 w_2}{T}\sum_{i=0}^{2} J_i (w_1 - w_2)^i \tag{3}$$

The solubility of drugs is influenced by the interactions in the solutions between the solvents and the solute, represented by physical and chemical parameters similar to those proposed by Acree and Abraham.[13] The Abraham model includes five parameters for each solute and six solvent coefficients, which were previously calculated for a number of solvents.[14] The general Abraham model is:

$$\log\left(\frac{C_\mathrm{s}}{C_\mathrm{w}}\right) = c + eE + sS + aA + bB + vV \tag{4}$$

where C_s and C_w are the solubilities of the solute (in molarities) in the organic solvent and water, respectively. E is the excess molar refraction, S is the dipolarity/polarizability of the solute, A denotes the hydrogen-bond acidity of the solute, B indicates the hydrogen-bond basicity of the solute and V is the McGowan volume of the solute. Thus, E, S, A, B and V are the Abraham solute parameters and c, e, s, a, b and v are the Abraham solvent coefficients. The Abraham solute parameters for atenolol which were used in the following computations are 1.45, 1.89, 0.55, 1.75 and 2.18 for E, S, A, B and V, respectively.[15]

The Jouyban–Acree model and the Abraham solvation parameters could be combined for predicting the solubility of drugs in mixed solvents. The trained version of the model for the solubility of drugs in aqueous binary mixture of ethanol is:[16]

$$\begin{gathered}\log X_{\mathrm{m},T} = w_1 \log X_{1,T} + w_2 \log X_{2,T} + \\ + \left(\frac{w_1 w_2}{T}\right)(558.45 + 358.60E + 22.01S - 352.97A + \\ +130.48B - 297.10V) + \left(\frac{w_1 w_2 (w_1 - w_2)}{T}\right)(45.67 - 165.77E - \\ -321.55S + 479.48A - 409.51B + 827.63V) + \left(\frac{w_1 w_2 (w_1 - w_2)^2}{T}\right)(-493.81 - \\ -341.32E + 866.22S - 36.17A + 173.41B - 555.48V)\end{gathered} \tag{5}$$

This extended version provided another prediction tool for computing the solubility of drugs in aqueous binary mixtures of ethanol. The first two terms of Eq. (5) represent the ideal mixing behaviors of saturated solutions of the analyte in the mono-solvents, and the other model constants and variables present the effects of solvent composition and temperature on the non-ideal mixing behavior of the saturated solution and the interactions between solvent 1–solvent 2 and the solute in the mixed solvent system. These model constants for a single analyte were explained in more detail in earlier reports.[17,18] Concerning the modeling of the solubility of different solutes in ethanol + water mixtures at various temperatures, the Abraham solute parameters for representing the effects of different chemical structures of drugs on their solubilities were included. Although it might be possible find some theoretical justifications for this numerical treatment, we consider it preferable to consider Eq. (5) as a semi-empirical one, since there are 18 model constants and it is very hard to explain this number of curve-fitting parameters as theoretical parameters.

Therefore, the objectives of this work are:

– To report the experimental solubility of atenolol in binary mixtures of ethanol and water at 298.2, 303.2, 308.2 and 313.2 K.

– To predict the solubility of atenolol in ethanol + water mixtures at different temperatures by means of the Jouyban–Acree model.

– To predict the solubility of atenolol in ethanol + water at different temperatures using a combination of the Jouyban–Acree model and the van't Hoff equation.

To predict the solubility of atenolol at different temperatures using the Jouyban–Acree model combined with the Abraham solute parameters.

To predicting the solubility of atenolol using a minimum number of experimental data points.

EXPERIMENTAL

Materials

Atenolol (*MW* = 266.3 g·mol^{-1}) was purchased from the Daru Pakhsh Company (Tehran, Iran) and used without further purification. The claimed value for the purity of the solute in its certificate was 0.993 (in mass fraction). Its purity was also verified by determination of its melting point (425–427 K). Distilled water was used throughout this work. Ethanol (mass fraction purity of 0.995 in mass fraction) was obtained from the Scharlau Chemie Company (Sentmenat, Barcelona, Spain).

Solubility determination procedure

Various solubility determination methods used in the literature were reviewed in a recent work.[19] The solubility of atenolol was determined using the saturation shake-flask method of Higuchi and Connors.[20] Briefly, ethanol + water binary mixtures were prepared by mixing appropriate masses of solvents (0.00 to 1.00 in mass fractions) varying by 0.10, in order to study 9 mixtures and two mono-solvents. The solvent masses were measured using an electronic balance (Sartorius, Germany) with an uncertainty of 0.01 g. Excess amount of drug was added to each flask and the flasks were placed in an incubator-shaker (Heidolph Unimax 1010, Germany) with a temperature controlling system having an uncertainty of 0.1 K. All the experiments were performed at temperatures ranging from 298.2 to 313.2 K. The solutions were shaken until the solubility equilibrium was reached and the saturation is verified by the presence of undissolved drug. The saturated mixtures (after 3 days) were centrifuged (Ependorph Centrifuge 5810R, Germany) and the solid phase was removed. In order to determine the concentrations, aliquots of the solutions were diluted with distilled water. Both the centrifuging and dilution steps were performed under the same temperature. The absorbance of the diluted solutions was recorded at 275 nm using a UV–Vis spectrophotometer (Cecil CE 7250, UK) and the molar concentrations were determined using UV absorbance calibration curve. Each experimental solubility datum indicates an average of at least three repeated measurements.

Computational method

The J_i constants of Eq. (1) for the solubility of atenolol in ethanol + water mixtures at various temperatures were obtained using a no intercept least square analysis (method I). The same procedure was used to compute the model constants of Eq. (3) (method II). The computed constants were used to back-calculate the solubility using Eqs. (1) and (3). The previously trained version of Jouyban–Acree model employing the Abraham solvation parameters (*i.e.*, Eq. (5)) was used to predict the solubility of atenolol in ethanol + water mixtures (method III). The experimental solubility data at 298.2 K was used to train Eq. (1), and the solubilities at other temperatures were predicted using the model (method IV). The experimental solubility data at the lowest and highest temperatures were fitted to Eq. (3) and the model constants, *i.e.*, A, B and J_i values were correlated using a no intercept least square analysis. Then the solubilities at the other temperatures were predicted using an interpolation technique (method V).

The mean percentage deviations (*MPD*s) were calculated as an accuracy criterion of the computations using:

$$MPD = \frac{100}{N}\sum\left(\frac{\left|C_{\mathrm{m},T}^{\mathrm{Calculated}} - C_{\mathrm{m},T}^{\mathrm{Exprimental}}\right|}{C_{\mathrm{m},T}^{\mathrm{Exprimental}}}\right) \tag{6}$$

where N is the number of data points in each set.

RESULTS AND DISCUSSION

The mass fractions of the binary solvent mixtures, the experimental and back-calculated solubilites using numerical methods I and II at four investigated temperatures 298.2, 303.2, 308.2 and 313.2 K are listed in Table I. The solubilites of atenolol increased with increasing temperature, as was expected and the solubilites at a given temperature first increased with the addition of ethanol, reached a maximum value and then decreased with further addition of ethanol, which is the usual pattern for the solubility of drugs in ethanol + water mixtures. The measured aqueous solubility of atenolol was 0.072 mol·L^{-1} at 298.2 K, which is in agreement with literatures data (*i.e.*, 0.077[21] and 0.075 mol·L^{-1}(22)). Equation (1) was used to fit the experimental data points and the obtained model

TABLE I. Experimental (Exp.) and calculated molar solubility of atenolol in ethanol (1) + water (2) mixtures at different temperatures using methods I to V

w_2	T / K	Exp.	Method				
			I	II	III	IV	V
1.00	298.2	0.07264	0.07264	0.06265	–	–	–
0.90	298.2	0.10000	0.12101	0.10526	0.07396	–	–
0.80	298.2	0.13998	0.19556	0.17211	0.09663	–	–
0.70	298.2	0.26726	0.30275	0.26981	0.14321	–	–
0.60	298.2	0.44943	0.44074	0.39750	0.21728	–	–
0.50	298.2	0.59798	0.58859	0.53659	0.31098	–	–
0.40	298.2	0.64000	0.69921	0.64370	0.39490	–	–
0.30	298.2	0.68378	0.71209	0.66204	0.42729	–	–
0.20	298.2	0.56489	0.59552	0.56027	0.38620	–	–
0.10	298.2	0.38094	0.38938	0.37245	0.29182	–	–
0.00	298.2	0.18835	0.20743	0.18471	–	–	–
1.00	303.2	0.07518	0.07518	0.07442	–	–	0.07777
0.90	303.2	0.13184	0.12516	0.12392	0.07713	0.10187	0.12298
0.80	303.2	0.19105	0.20224	0.20088	0.10111	0.16098	0.19836
0.70	303.2	0.32027	0.31328	0.31246	0.15004	0.26696	0.31399
0.60	303.2	0.45912	0.45678	0.45721	0.22785	0.42553	0.46970
0.50	303.2	0.61284	0.61186	0.61388	0.32671	0.60782	0.64010
0.40	303.2	0.68041	0.73046	0.73389	0.41648	0.73833	0.76684
0.30	303.2	0.78176	0.74950	0.75412	0.45356	0.73671	0.78010
0.20	303.2	0.57905	0.63358	0.63967	0.41383	0.59371	0.65158
0.10	303.2	0.44662	0.42043	0.42793	0.31660	0.38674	0.43250
0.00	303.2	0.20743	0.20743	0.21460	–	–	0.22103
1.00	308.2	0.07804	0.07804	0.08791	–	–	0.09250
0.90	308.2	0.14844	0.13009	0.14510	0.08080	0.10623	0.14502
0.80	308.2	0.22378	0.21057	0.23329	0.10646	0.16823	0.23185
0.70	308.2	0.35277	0.32698	0.36013	0.15848	0.27936	0.36386
0.60	308.2	0.51132	0.47840	0.52349	0.24134	0.44618	0.54014
0.50	308.2	0.68138	0.64390	0.69923	0.34733	0.63972	0.73158
0.40	308.2	0.75199	0.77385	0.83315	0.44525	0.78205	0.87289
0.30	308.2	0.82259	0.80130	0.85539	0.48887	0.78785	0.88673
0.20	308.2	0.68138	0.68572	0.72720	0.45099	0.64325	0.74197
0.10	308.2	0.51898	0.46246	0.48946	0.34985	0.42598	0.49522
0.00	308.2	0.23301	0.23301	0.24811	–	–	0.25557
1.00	313.2	0.09814	0.09814	0.10329	–	–	–
0.90	313.2	0.18000	0.16226	0.16906	0.10154	0.13293	–
0.80	313.2	0.29492	0.26061	0.26964	0.13320	0.20895	–
0.70	313.2	0.45767	0.40181	0.41319	0.19702	0.34415	–
0.60	313.2	0.57386	0.58427	0.59681	0.29799	0.54553	–
0.50	313.2	0.80000	0.78262	0.79315	0.42634	0.77762	–
0.40	313.2	0.95110	0.93774	0.94202	0.54433	0.94751	–
0.30	313.2	1.01324	0.97038	0.96635	0.59672	0.95435	–
0.20	313.2	0.82259	0.83242	0.82332	0.55115	0.78166	–
0.10	313.2	0.60098	0.56490	0.55743	0.42925	0.52101	–
0.00	313.2	0.28773	0.28773	0.28553	–	–	–

for representing the solubility of atenolol in ethanol + water mixtures at various temperatures was:

$$\log C_{\mathrm{m},T}^{\mathrm{sat}} = w_1 \log C_{1,T}^{\mathrm{sat}} + w_2 \log C_{2,T}^{\mathrm{sat}} + 837.039\left(\frac{w_1 w_2}{T}\right) + \\ +365.522\left(\frac{w_1 w_2 (w_1 - w_2)}{T}\right) + 82.325\left(\frac{w_1 w_2 (w_1 - w_2)^2}{T}\right) \tag{7}$$

Equation (7) is a significant correlation with an *F* value of 2540 and a *p* value of <0.0005 and the *MPD* of the back-calculated solubilities was 5.6±7.1 %. The main limitation of Eq. (7) for predicting the solubility of atenolol in ethanol + water mixtures at other temperatures is that it requires two experimental data points for each temperature of interest, *i.e.*, $C_{1,T}^{\mathrm{sat}}$ and $C_{2,T}^{\mathrm{sat}}$. To cover this limitation, Eq. (3) could be used. When Eq. (3) was trained using the generated data, the obtained model was:

$$\log C_{\mathrm{m},T}^{\mathrm{sat}} = w_1 (3.216 - \frac{1177.800}{T}) + w_2 (3.330 - \frac{1351.781}{T}) + \\ +832.494\left(\frac{w_1 w_2}{T}\right) + 358.568\left(\frac{w_1 w_2 (w_1 - w_2)}{T}\right) + 70.961\left(\frac{w_1 w_2 (w_1 - w_2)2}{T}\right) \tag{8}$$

which is a significant correlation with *F* and *p* values of 1900 and <0.0005, respectively, and with an *MPD* of 5.1±4.6 %.

In practical applications of the solubility data of drugs in mixed solvents at various temperatures, it would be preferred to predict the data using *in silico* models without using any experimentally measured data points. However, to the best of our knowledge, there are no such models in the literature. As an alternative, a number of attempts were made to predict the solubility of drugs using a minimum number of experimental data points, including the discussed numerical methods III–V. The predicted solubilities of atenolol in ethanol + water mixtures at various temperatures along with the corresponding experimental values are reported in Table I. In method III, two experimental solubility data points at each temperature are required as input experimental data and the rest of data points could be predicted using a globally trained version of the model, *i.e.*, Eq. (5). The *MPD* for the predicted data points was 34.1±28.0 % (*N* = 36). When Eq. (1) was trained using the solubility data of atenolol in ethanol + water mixtures at 298.2 K, and the solubilities at the other temperatures were predicted, (*i.e.*, the numerical method IV), the obtained *MPD* was 10.0±9.6 % (*N* = 30). The corresponding *MPD* for the numerical method V was 6.6±4.8 % (*N* = 22). The main advantage of trained version of Eq. (3) is that it does not require any further experimental data as input values. The *MPD* values of the different numerical methods are listed in Table II. As is evident, the more data point used as input values, the more accurate were the predictions made. In practice, one must decide on a balance between the demanded accuracy of the solubility data and the time and cost that has to be spent on the project. The experimental and simulated solubility data of atenolol in various mass fractions of ethanol using the numerical methods I to V are illustrated in Fig. 2. As shown in this figure, the most accurate simulations were made when more experimental data were employed in the simulation process, *i.e.*, numerical methods I and II, but with the cost of requiring more experimental data points.

TABLE II. Mean percent deviations ± standard deviations (*MPD*±*SD*) for the solubility of atenolol in ethanol + water mixtures at different temperatures for correlative (methods I and II) and predictive (methods III–V) along with the number of correlated and/or predicted data points

Method	*MPD*±*SD*	*N*
I	5.6±7.1	44
II	5.1±4.6	44
III	34.1±28.0	6
IV	10.0±9.6	11
V	6.6±4.8	22

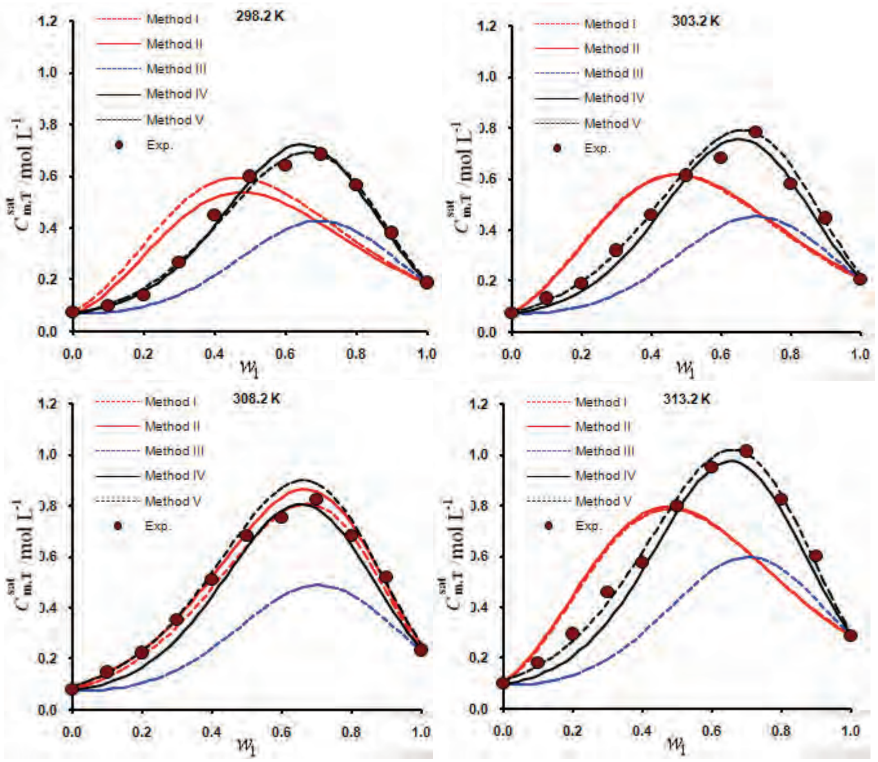

Fig. 2. Experimental and simulated molar solubility data of atenolol ($C^{sat}_{m,T}$) in various mass fractions of ethanol (w_1) at four investigated temperatures using numerical methods I–V.

CONCLUSIONS

The experimental solubilities of atenolol in aqueous mixture of ethanol at four temperatures were reported. The generated data was mathematically represented using numerical methods I and II. These sorts of numerical analyses could be used for screening the measured solubility data for detecting possible outliers. In addition, they provide the most accurate predictions using the interpolation technique. The expected *MPD*s for these analyses are < 6 %. Some data points are predicted employing numerical methods III, IV and V and reasonably accurate predictions are provided. These predictive methods could be employed in the early stages of drug development investigations, when solubilization of a drug candidate is required and only a small quantity of the drug powder is available. The expected *MPD*s for these analyses are between 6 to 35 % depend on the number of experimental input data in the prediction procedure.

ИЗВОД

РАСТВОРЉИВОСТ АТЕНОЛОЛА У РАСТВОРУ ЕТАНОЛ + ВОДА НА РАЗЛИЧИТИМ ТЕМПЕРАТУРАМА

SAMIN HAMIDI[1] и ABOLGHASEM JOUYBAN[2,3]

[1]*Liver and Gastrointestinal Diseases Research Center, Tabriz University of Medical Sciences, Tabriz, Iran,* [2]*Drug Applied Research Center and Faculty of Pharmacy, Tabriz University of Medical Sciences, Tabriz 51664, Iran и* [3]*Pharmaceutical Engineering Laboratory, School of Chemical Engineering, College of Engineering, University of Tehran, P. O. Box 11155/4563, Tehran, Iran*

Добијене су експерименталне растворљивости атенолола у смеши етанол + вода на различитим температурама (298,2, 303,2, 308,2 и 313,2 K). Растворљивости су израчунате коришћењем пет метода, тј. Jouyban–Acree моделом (метод I), његовом комбинација са van't Hoff једначином (метод II), проширеном верзијом Jouyban–Acree модела са Abraham параметрима (метод III), коришћењем је минималаног број експерименталних тачака (*N*) за Jouyban–Acree модел (*N* = 11), као и његова комбинација са van't Hoff једначином (*N* = 22), а затим су добијени параметри модела коришћене за израчунавање растворљивости на другим температурама (методи IV и V). Тачност израчунатих растворљивости су оцењене израчунавањем средњег процентуалног одступања (*MPD*). Добијене *MPD* вредности (± стандардна девијација) за методе I–V су: 5,6±7,1; 5,1±4,6; 34,1±28,0; 10,0±9,6 и 6,6±4,8 %, редом.

(Примљено 17. јуна, ревидирано 17. септембра, прихваћено 18. септембра 2014)

REFERENCES

1. A. Li, S. H. Yalkowsky, *J. Pharm. Sci.* **83** (1994) 1735
2. S. H. Yalkowsky, *Solubility and solubilization in aqueous media*, American Chemical Society, Washington DC, 1999
3. C. Leuner, J. Dressman, *Eur. J. Pharm. Biopharm.* **50** (2000) 47
4. H. Viernstein, P. Weiss-Greiler, P. Wolschann, *Int. J. Pharm.* **256** (2003) 85
5. A. Jouyban-Gharamaleki, L. Valaee, M. Barzegar-Jalali, B. Clark, W. E. Acree Jr., *Int. J. Pharm.* **177** (1999) 93
6. T. Loftsson, M. E. Brewster, *J. Pharm. Sci.* **85** (1996) 1017
7. B. Carlberg, O. Samuelsson, L. H. Lindholm, *Lancet* **364** (2004) 1684

8. J. A. Jiménez, F. Martínez, *J. Solution Chem*. **35** (2006) 335
9. A. Jouyban-Gharamaleki, P. York, M. Hanna, B. J. Clark, *Int. J. Pharm*. **216** (2001) 33
10. A. Jouyban, *J. Pharm. Pharm. Sci.* **11** (2008) 32
11. D. J. W. Grant, M. Mehdizadeh, A. H. L. Chow, J. E. Fairbrother, *Int. J. Pharm*. **18** (1984) 25
12. V. Panahi-Azar, A. Shayanfar, F. Martínez, W. E. Acree Jr., A. Jouyban, *Fluid Phase Equilib*. **308** (2011) 72
13. W. E. Acree Jr., M. H. Abraham, *Fluid Phase Equilib*. **201** (2002) 245
14. D. M. Stovall, W. E. Acree Jr., M. H. Abraham, *Fluid Phase Equilib*. **232** (2005) 113
15. Pharma-Algorithms, ADME Boxes, Version 4.0, PharmaAlgorithms Inc., Toronto, Canada, 2008
16. A. Jouyban, S. Soltanpour, S. Soltani, E. Tamizi, M. Fakhree, W. E. Acree Jr., *J. Mol. Liq*. **146** (2009) 82
17. W. E. Acree Jr., *Thermochim. Acta* **198** (1992) 71
18. A. Jouyban-Gharamaleki, W. E. Acree Jr., *Int. J. Pharm.* **167** (1998) 177
19. A. Jouyban, M. A. A. Fakhree, *Experimental and computational methods pertaining to drug solubility. Toxicity and drug testing*, Intech Co., New York, 2012
20. T. Higuchi, K. A. Connors, *Adv. Anal. Chem. Instrum*. **4** (1965) 117
21. A. M. Ramezani, A. Shayanfar, J. L. Manzoori, A. Jouyban, *Latin Am. J. Pharm.* **31** (2012) 1176
22. G. L. Perlovich, T. V. Volkova, A. Bauer-Brandl, *Mol. Pharm*. **4** (2007) 929.

Journal of the Serbian Chemical Society
JSCS-info@shd.org.rs • www.shd.org.rs/JSCS

J. Serb. Chem. Soc. 80 (5) 705–715 (2015)
JSCS–4750

UDC 546.821–31+546.57:678.746:678.026.2:
544.032.6.004.4:615.281–188
Original scientific paper

Antibacterial and UV protective properties of polyamide fabric impregnated with TiO_2/Ag nanoparticles

MILICA MILOŠEVIĆ[1], ANA KRKOBABIĆ[2], MARIJA RADOIČIĆ[1], ZORAN ŠAPONJIĆ[2], VESNA LAZIĆ[3], MILOVAN STOILJKOVIĆ[1#] and MAJA RADETIĆ[2*#]

[1]"Vinča" Institute of Nuclear Sciences, University of Belgrade, P. O. Box 522, 11001 Belgrade, Serbia, [2]Faculty of Technology and Metallurgy, University of Belgrade, Karnegijeva 4, 11120 Belgrade, Serbia and [3]Innovation Center of the Faculty of Technology and Metallurgy, University of Belgrade, Karnegijeva 4, 11120 Belgrade, Serbia

(Received 4 November, revised 15 December, accepted 19 December 2014)

Abstract: The possibility of *in situ* photoreduction of Ag^+ using colloidal TiO_2 nanoparticles deposited on the surface of polyamide fabric in the presence of the amino acid alanine and methanol is discussed. The presence of TiO_2/Ag nanoparticles on the polyamide fabric was confirmed by FESEM and ICP analyses. The antibacterial activity of the fabric was tested against the Gram-negative bacterium *Escherichia coli* and the Gram-positive bacterium *Staphylococcus aureus*. The TiO_2/Ag nanoparticles fabricated on the surface of the polyamide fabric provided maximum bacterial reduction and thus, excellent antibacterial activity. In spite of silver leaching from the fabric during washing, the impregnated polyamide fabric preserved the maximum reduction of *E. coli* colonies. The antibacterial activity against *S. aureus* was slightly decreased after ten washing cycles, but still the antibacterial activity could be considered as satisfactory. In addition, the presence of TiO_2/Ag nanoparticles ensured better UV protection efficiency, which belonged to the UV protection category very good.

Keywords: TiO_2/Ag nanoparticles; polyamide; photoreduction; antibacterial activity; UV protection.

INTRODUCTION

Growing interest for the exploitation of silver nanoparticles (Ag NPs) in the production of medical and healthcare textiles due to their extraordinary antimicrobial activity has initiated broad research in this field.[1–4] Many efforts have been made to develop simple routes for the manufacture of stable and durable antimicrobial nanocomposite textile materials with Ag NPs.[4] Hitherto, major

---

[*] Corresponding author. E-mail: maja@tmf.bg.ac.rs

[#] Serbian Chemical Society member.

doi: 10.2298/JSC141104125M

research was focused on the application of Ag NPs to cotton and polyester fibers.[4–16] Polyamide (PA) fibers were less investigated despite their share in the production of healthcare and non-implantable medical textiles.[10,17–24] In addition, good biocompatibility with different human cells and tissues make PA a very attractive material for implants.[24] Dip-coating techniques were the most commonly employed methods for the impregnation of PA materials with Ag NPs.[10,19–23] Dubas *et al*. proposed an interesting approach based on layer-by-layer deposition whereby a thin film with antibacterial properties was formed on PA fibers by the sequential dipping of the fibers into solutions of poly(diallyldimethylammonium chloride) (PDADMAC) and Ag NPs caped with poly(methacrylic acid) (PMA).[18] Sonochemical coating of Ag NPs onto PA fabrics was also reported as an alternative method for the impregnation of PA fabrics with Ag NPs.[13] However, to the best of our knowledge, *in situ* fabrication of Ag NPs on the PA fabrics has not been reported.

The use of various reducing agents and organic compounds that control the formation, size, shape and stability of Ag NPs seems to be great disadvantage of conventional procedures for the fabrication of colloidal Ag NPs. These organic compounds can diminish or even inhibit the antimicrobial action of Ag NPs and they often have a negative environmental impact. The problematic use of strong reducing agents and stabilizers could be overcome by a previously proposed procedure.[25,26].

Recent research indicated that *in situ* photoreduction of Ag^+ using TiO_2 NPs deposited on the surface of polyethylene terephthalate (PET), cotton and cotton/PET fabrics in the presence of the amino acid alanine and methanol could be a viable alternative to conventional routes for the fabrication of Ag NPs.[25,26] The proposed treatment is acceptable from the environmental point of view as it does not involve any aggressive chemicals or reducing agents. On the other hand, it provides large amounts of evenly distributed Ag NPs on the fiber surface and thus, excellent antimicrobial efficiency. The approach relies on the fact that surface modification of TiO_2 NPs smaller than 20 nm with alanine results in the replacement of hydroxyl groups on the surface of TiO_2.[27,28] This further facilitates the coordination of surface Ti atoms with a carboxyl group and the simultaneous binding of Ag^+.[27,28] When TiO_2 is exposed to UV light with an energy that matches or exceeds its band gap, the formation of electron/hole pairs occurs. These charges can participate in different oxidation and reduction processes on the TiO_2 NPs surface, but their fast recombination appears as a serious limitation. In addition to improved adsorption of Ag^+ before UV illumination, surface modification of TiO_2 NPs with amino acids results in enhanced charge separation and thus, elevated photocatalytic activity of photogenerated electrons.[27,28] Photogenerated electrons are utilized for the photoreduction of adsorbed Ag^+ and hence fabrication of TiO_2/Ag NPs.

Methanol has been exploited as an efficient hole-scavenger ($E^\ominus$($CH_3OH/^\bullet CH_2OH$) = 1.2 V), which ultimately provides an increase in the yield of trapped electrons.[29] Electrochemical oxidation of methanol results in the formation of the electron-donating methanol radical ($E^\ominus$($^\bullet CH_2$–OH/CH_2O) = = –0.95 V), meaning that from one photon of absorbed light, two electrons are generated.[30] This phenomenon, known as a current-doubling effect, brings about an enhanced photoreduction rate of Ag^+.[31] The methanol radical is also able to reduce Ag^+ ($^\bullet CH_2OH$, –0.95 V).

The current study was aimed at highlighting whether the proposed method could be efficient in the impregnation of PA fabric with TiO_2/Ag NPs. The PA fabric impregnated in this manner was characterized by field emission scanning electron microscopy (FESEM) and ICP atomic emission spectroscopy analyses. The antibacterial activity of the deposited TiO_2/Ag NPs was tested against the Gram-negative bacterium *Escherichia coli* and the Gram-positive bacterium *Staphylococcus aureus*. In order to explore the stability of the fabricated nanocomposite system, washing fastness and perspiration fastness in artificial sweat under acidic and alkaline conditions were examined. The release of silver during washing and 24-h long incubation in artificial sweat was also monitored. The presence of TiO_2 NPs on the PA fabric surface was the essential motive to evaluate the UV protection efficiency of the impregnated PA fabric.

EXPERIMENTAL

Materials and methods

Desized and bleached polyamide (PA 6.6, 150 g m^{-2}) fabric was cleaned in a bath containing 0.5 % the nonionic washing agent Felosan RG-N (Bezema) at a liquor-to-fabric ratio of 50:1. After 15 min of washing at 50 °C, the fabric was rinsed once with warm water (50 °C) for 3 min and three times (3 min) with cold water. The fabric was then dried at room temperature.

The colloid consisting of TiO_2 NPs was synthesized by acidic hydrolysis of $TiCl_4$ in a manner already described in detail in the literature.[28] Most of the synthesized TiO_2 NPs were single crystalline and irregularly shaped with average dimensions of 6 nm.[32] The electron diffraction pattern and Raman spectroscopy measurements indicated the formation of the anatase crystal structure.[32]

Impregnation of PA fabric with TiO_2 NPs (PA+TiO_2) was performed by immersion of the sample in 0.1 M TiO_2 colloid at a liquor-to-fabric ratio of 30:1 for 30 min. After squeezing at a pressure of 2 kg cm^{-2}, the sample was dried at room temperature. Subsequently, the sample was cured at 100 °C for 30 min, double rinsed with deionized water and dried at room temperature.

Alanine (0.1333 g) was dissolved in 40 mL of Milli-Q deionized water. PA fabric impregnated with TiO_2 NPs was immersed in this solution for 10 min. $AgNO_3$ solution (1.5 mL, c = 0.015 mol L^{-1}) and methanol (0.4 mL) were added into 58 mL of HNO_3 solution (1×10^{-3} M, pH 3). This solution was added to the alanine solution and mixed. After purging with argon for 30 min, the system was illuminated with an Ultra-Vitalux lamp (300 W, Osram) for 30 min under exclusion of air. The applied lamp simulated sun-like irradiation with a spectral radiation power distribution at wavelengths between 300–1700 nm. The PA fabric was removed from the solution, dried at room temperature, rinsed in Milli-Q deionized water for 15 min and dried at room temperature. The fabricated textile nanocomposite was denoted as PA+TiO_2/Ag.

The morphology of the PA fibers was analyzed by a Mira3 Tescan field emission scanning electron microscope (FESEM). The samples were coated with a thin layer of Au/Pd (85/15) prior to analysis.

The total content of Ag and Ti in the impregnated PA fabrics was determined using an ICP Emission Spectrometer: ICAP 6000 series (Thermo Electron Corporation). 40 mg of sample immersed in 60 mL of concentrated sulfuric acid was moderately heated for 5–10 min. Subsequently, 2 mL of nitric acid (1:1) was added and after short heating, a clear solution was obtained.

The reflectance spectra of the PA fabrics were recorded using a Datacolor SF300 spectrophotometer. The color coordinates of untreated PA fabric, PA+TiO_2 and PA+TiO_2/Ag fabric (*CIE L*, a*, b**) were determined under illuminant D_{65} using a 10° standard observer. Based on the measured *CIE* color coordinates, the color difference (ΔE^*) was calculated as:

$$\Delta E^* = \sqrt{\left(\Delta a^*\right)^2 + (\Delta b^*)^2 + (\Delta L^*)^2} \qquad (1)$$

where: ΔL^* is the color lightness difference between the PA+TiO_2/Ag fabric and the control PA fabric; Δa^* is the red/green difference between the PA+TiO_2/Ag fabric and the control PA fabric and Δb^* is the yellow/blue difference between the PA+TiO_2/Ag fabric and the control PA fabric.

Transmission spectra of the samples were measured using a Cary 100 Scan UV–Vis spectrophotometer (Varian). The UV protection factor (*UPF*) values were automatically calculated based on the recorded data in accordance with the Australia/New Zealand standard AS/NZS 4399:1996 using a Startek UV fabric protection application software version 3.0 (Startek Technology).

The antibacterial activity of impregnated PA fabrics was assessed against Gram-negative bacterium *E. coli* ATCC 25922 and Gram-positive bacterium *S. aureus* in accordance with the standard test method ASTM E 2149-01.[33] The percentage bacterial reduction (R / %) was calculated using the following equation:

$$R = 100\frac{C_0 - C}{C_0} \qquad (2)$$

where C_0 (CFU – colony forming units) is the number of bacterial colonies on the control PA fabric (untreated PA fabric without TiO_2/Ag NPs) and C (CFU) is the number of bacterial colonies on the PA fabric loaded with TiO_2/Ag NPs.

Washing fastness of impregnated PA fabrics was tested after five and ten washing cycles in Polycolor (Werner Mathis AG) laboratory beaker dyer at 45 rpm. The samples were washed in the bath containing 5 g L^{-1} Society of Dyers & Colourists (SDC) standard detergent and 2 g L^{-1} Na_2CO_3 at a liquor-to-fabric ratio of 80:1. After 30 min of washing at 40 °C, the fabrics were soaked twice in cold distilled water. The samples were afterwards held under the tap water for 10 min, squeezed and dried at 70 °C. The percentage of bacterial reduction after five and ten washing cycles was calculated according to Eq. (2). The concentration of silver released from the PA fabrics into washing bath after each washing cycle was measured using a Spectra AA 55 B (Varian) atomic absorption spectrometer (AAS).

The perspiration fastness of the impregnated PA fabrics was analyzed in artificial sweat. The artificial sweat at pH 5.5 and 8.0 were prepared according to ISO 105-E04:1989E.[34] The acidic artificial sweat (pH 5.5) contained: 0.5 g L^{-1} of L-histidine monohydrochloride monohydrate, 5 g L^{-1} of sodium chloride and 2.2 g L^{-1} of sodium dihydrogen orthophosphate dihydrate. The alkaline artificial sweat (pH 8.0) contained: 0.5 g L^{-1} of L-histidine monohydrochloride monohydrate, 5 g L^{-1} of sodium chloride and 5 g L^{-1} of disodium hydrogen orthophosphate dodecahydrate. The solutions were brought to pH 5.5 and 8.0 with a 0.1 M solution of sodium hydroxide. PA fabric (0.300 g) was rinsed in artificial sweat at a liquor-to-fabric ratio of 50:1. The samples were incubated in a water bath at 37 °C for 24 h. The artificial sweat was collected and the concentration of released silver was determined by AAS.

RESULTS AND DISCUSSION

The presence of Ag and Ti on the PA+TiO_2/Ag fabric was confirmed by ICP measurements. It was found that one gram of impregnated PA fabric contained 0.49±0.01 mg of Ag and 3.40±0.04 mg of Ti. These results clearly indicate that three times larger amount of Ag was detected on PA fabric than on PET fabric impregnated in the same manner.[25] EDX analysis of a single TiO_2/Ag nanoparticle deposited on the cotton and cotton/PET fibers in a previous study implied that metallic silver was formed exactly on the deposited TiO_2 NPs.[26] This was also confirmed by XPS mapping.[26] A thorough analysis of he FTIR spectra of pure alanine, alanine after binding to Ag^+, after adsorption on the surface of TiO_2 NPs, and after adsorption on TiO_2 NPs and binding to Ag^+ suggested that an interaction between TiO_2, alanine and silver was established, *i.e.*, the carboxyl group of alanine bridges the surface Ti and Ag^+.[26] Therefore, this is the argument to denote the PA fabric impregnated in described manner as a PA+TiO_2/Ag fabric in the further text.

The morphology of PA fibers was analyzed by FESEM. A characteristic smooth surface of untreated PA fibers could be observed in Fig. 1a. On the other hand, Fig. 1b reveals that after the photoreduction process, the surface of the PA fibers became impregnated with TiO_2/Ag NPs. It is evident that agglomerates ranging from approximately 80 to 230 nm were randomly grouped over the surface of PA fibers (inset in Fig. 1b).

Antibacterial efficiency of PA+TiO_2/Ag fabrics was tested against *E. coli* and *S. aureus* bacteria. The results presented in Table I demonstrate that maximum bacterial reduction (R = 99.9 %) was obtained for both bacteria. It is well established that TiO_2 NPs exhibit antibacterial properties but only when they are exposed to UV light.[32,35,36] Taking into account that these tests were conducted in the dark, the excellent antibacterial activity of the impregnated PA fabric are attributable only to the generated Ag NPs on the surface of the deposited TiO_2 NPs. Maximum reduction of bacteria *E. coli* was preserved after 10 washing cycles, indicating good washing fastness. In contrast, although the maximum reduction of *S. aureus* colonies remained after five washing cycles, after 10 washing cycles, bacterial reduction slightly decreased (R = 99.5 %). Still, the obtained antibacterial activity could be considered as satisfactory.

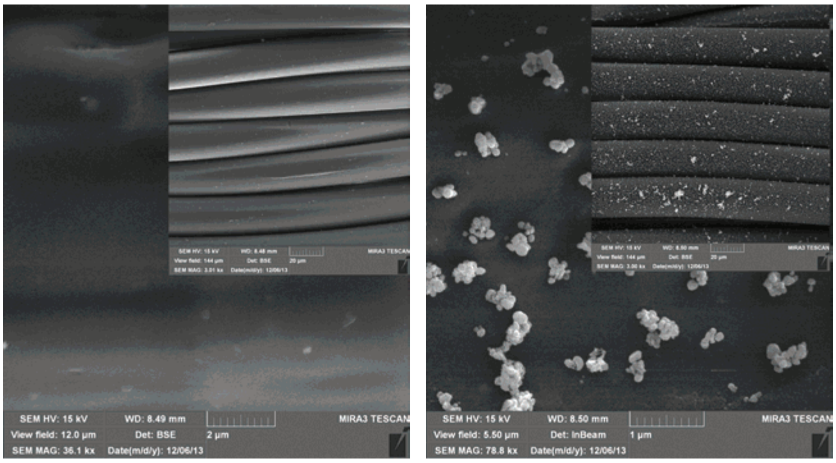

(a) (b)

Fig. 1. FESEM images of: a) untreated PA and b) PA+ TiO_2/Ag fabrics.

TABLE I. Antibacterial activity of the PA+TiO_2/Ag fabric before and after washing

Sample	Bacterium	Number of bacterial colonies, CFU	R / %
		Before washing	
Control PA	*E. coli*	1.6×10^5	
PA+TiO_2/Ag		<10	99.9
Control PA	*S. aureus*	2.1×10^5	
PA+TiO_2/Ag		<10	99.9
		After 5 washing cycles	
Control PA	*E. coli*	2.5×10^5	
PA+TiO_2/Ag		<10	99.9
Control PA	*S. aureus*	8.0×10^3	
PA+TiO_2/Ag		10	99.9
		After 10 washing cycles	
Control PA	*E. coli*	1.9×10^5	
PA+TiO_2/Ag		140	99.9
Control PA	*S. aureus*	2.1×10^5	
PA+TiO_2/Ag		1.0×10^3	99.5

The growth of bacterial colonies on the PA+TiO_2/Ag fabric after 10 washing cycles is suggested to be due to a decrease in Ag content after washing. AAS measurements of the Ag content in the washing bath after each washing cycle indicated that, particularly in the first four washing cycles, large amounts of silver had been released from the PA+TiO_2/Ag fabric. The results from Table II demonstrated that in each subsequent washing cycle, leaching of silver was less pronounced. After the first washing cycle, the amount of silver was halved. However, in the last three washing cycles, the content of silver in washing bath was below the detection limit. Bearing in mind that initial silver content was around 490 μg g^{-1} as well as that approximately 413 μg g^{-1} of silver was released during washing, obviously sufficient amount of silver remained on the PA fabric surface to provide the desired level of antibacterial efficiency.

TABLE II. Silver release from the PA+TiO$_2$/Ag fabric during washing

Number of washing cycles	Silver release, μg g^{-1}
1	254.4±22.6
2	100.8±6.8
3	33.6±3.4
4	10±1.7
5	4.4±1.7
6	6.8±2.8
7	2.8±0.6
8	Below the detection limit
9	Below the detection limit
10	Below the detection limit

The photoreduction of Ag$^+$ was followed by the color change of PA fabric, which turned from white to yellowish/gray. However, the color was paler after washing due to silver leaching. The reflectance measurements in the visible region of the spectra revealed that there was no significant difference in the reflectance intensity between untreated PA fabric and PA fabric impregnated with TiO$_2$ NPs (Fig. 2). However, after generation of TiO$_2$/Ag NPs, the reflectance

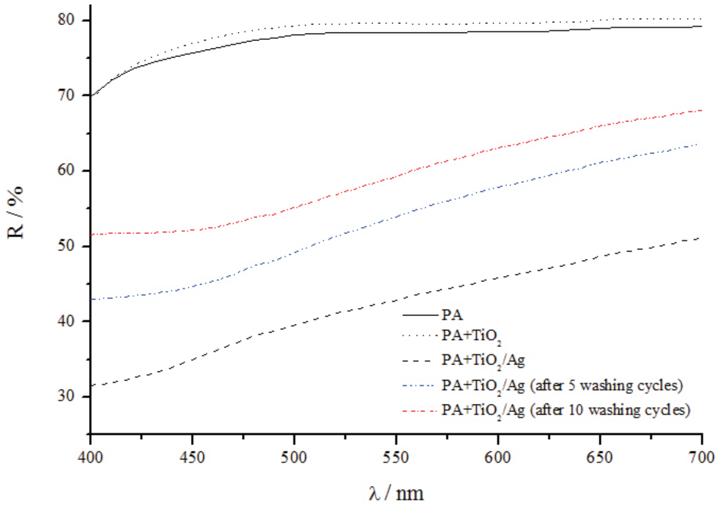

Fig. 2. Reflectance curves of the PA fabric, PA+TiO$_2$ fabric and PA+TiO$_2$/Ag fabrics before and after washing.

curve changed its shape, which was preserved after five and ten washing cycles, but the reflectance intensities decreased due to silver release. The color differences between PA fabrics impregnated with TiO_2/Ag NPs and control fabric (untreated PA fabric), expressed *via* ΔE^*, ΔL^*, Δa^* and Δb^* values, are presented in Table III. In general, the color differences (ΔE^*) greater than one can be visually detected. It is evident that after impregnation of PA with TiO_2/Ag NPs, ΔE^* drastically increased indicating a large color change, which declined after five and particularly after ten washing cycles.

TABLE III. Color change of the PA+TiO_2/Ag fabric after washing

Sample	L^*	a^*	b^*	ΔL^*	Δa^*	Δb^*	ΔE^*	Description
PA	90.91	–0.66	2.02	–	–	–	–	–
PA+TiO_2/Ag	71.40	1.35	9.41	–19.51	2.01	7.39	20.98	Darker, less green, yellow
PA+TiO_2/Ag (after 5 washing cycles)	78.34	2.27	9.23	–12.57	2.93	7.21	14.79	Darker, less green, yellow
PA+TiO_2/Ag (after 10 washing cycles)	81.47	2.43	6.65	–9.44	3.09	4.63	10.98	Darker, less green, yellow

The perspiration fastness of the PA+TiO_2 fabric in acidic and alkaline artificial sweat was also evaluated. The results showed that silver release occurred at both pH. Namely, 9.25 and 20.2 μg g^{-1} of silver leached from the PA+TiO_2/Ag fabric at pH 5.5 and 8.0, respectively. Several reports revealed that silver is released to a larger extent under alkaline conditions.[25,26,37,38]

Bearing in mind the ever-increasing warning on ozone layer depletion and potential health risks, much more attention has recently been paid on UV protective finishing of textile goods. Although many organic finishing agents have been conventionally used for UV protection of textiles, lately TiO_2 NPs appeared as a very attractive alternative since a small amount of TiO_2 NPs efficiently imparts the desired levels of UV protection.[32,35,36,39,40] The present study also confirmed that TiO_2/Ag NPs could significantly enhance the UV protective properties of PA fabric. The UPF values and UPF ratings of untreated and impregnated PA fabric before and after washing are given in Table IV. As expected, the PA fabric exhibited poor UV protection with a UPF rating of only 10. The deposition of TiO_2 NPs on the PA fabric led to an increase in the UPF value from 12.76 to 28.13. Consequently, the UPF rating of the PA+TiO_2 fabric rose to 25, indicating very good UV protection. The presence of silver on the surface of TiO_2 NPs and corresponding color change of the PA fabric into yellowish brought about a further elevation of the UPF rating to 30. However, after washing, UPF rating decreased to 25, very likely due to silver release. There was no significant difference between UPF values of the PA+TiO_2/Ag fabric after five and ten washing cycles. The UPF values measured after washing were almost equivalent to the one corresponding to the PA+TiO_2 fabric. These results are in a good correlation with a fact that approximately 85 % of silver had been released after ten washing cycles.

TABLE IV. UV protection properties of the PA fabric, PA+TiO_2 fabric and PA+TiO_2/Ag fabrics before and after washing

Sample	UPF	UPF rating
PA	12.76	10
PA+TiO_2	28.13	25
PA+TiO_2/Ag	38.24	30
PA+TiO_2/Ag (after 5 washing cycles)	28.22	25
PA+TiO_2/Ag (after 10 washing cycles)	27.59	25

CONCLUSIONS

The results of this study indicated that colloidal TiO_2 nanoparticles deposited on PA fabric could be efficiently exploited for the photoreduction of Ag^+ ions in the presence of the amino acid alanine and methanol. The fabricated TiO_2/Ag nanoparticles could be utilized for imparting antibacterial and UV protective properties to PA fabric. PA fabric impregnated with TiO_2/Ag nanoparticles provided the maximum reduction of *E. coli* and *S. aureus* bacterial colonies. Maximum bacterial reduction was preserved after ten washing cycles in the case of *E. coli*, whereas the antibacterial activity of the fabric slightly decreased against *S. aureus*. This was suggested to be due to leaching of silver during washing and thus, a smaller amount of retained silver on the surface of the fabric. The leaching of silver occurred to a much smaller extent in artificial sweat, particularly under alkaline conditions. In addition, the impregnated PA fabric had a UPF rating of 30, which could be classified as very good UV protection.

Excellent antibacterial activity and good washing fastness of PA impregnated with TiO_2/Ag nanoparticles could be utilized in the production of medical and protective textiles, which show an ever-increasing demand.

Acknowledgements. The financial support for this work was provided by the Ministry of Education, Science and Technological Development of Republic of Serbia (Projects Nos. 45020 and 172056). The work is realized under the umbrella of COST Action MP1106. We gratefully acknowledge Dr B. Jokić (University of Belgrade, Serbia) for providing the FESEM measurements.

ИЗВОД

АНТИБАКТЕРИЈСКА И UV-ЗАШТИТНА СВОЈСТВА ПОЛИАМИДНЕ ТКАНИНЕ ИМПРЕГНИРАНЕ НАНОЧЕСТИЦАМА TiO_2/Ag

МИЛИЦА МИЛОШЕВИЋ[1], АНА КРКОБАБИЋ[2], МАРИЈА РАДОИЧИЋ[1], ЗОРАН ШАПОЊИЋ[2], ВЕСНА ЛАЗИЋ[3],
МИЛОВАН СТОИЉКОВИЋ[1] и МАЈА РАДЕТИЋ[2]

[1]Универзитет у Београду, Институт за нуклеарне науке“Винча”, п. пр. 522,11001 Београд,
[2]Универзитет у Београду, Технолошко–металуршки факултет, Карнегијева 4, 11120 Београд и
[3]Универзитет у Београду, Иновациони центар Технолошко–металуршког факултета,
Карнегијева 4, 11120 Београд

У овом раду је дискутована могућност *in situ* фоторедукције Ag^+ помоћу колоидних наночестица TiO_2 депонованих на површину полиамидне тканине у присуству амино киселине аланина и метил-алкохола. Присуство наночестица TiO_2/Ag на полиамидној тканини потврђено је FESEM и ICP анализама. Антибактеријска активност тканине је тестирана према грам-негативној бактерији *Escherichia coli* и грам-позитивној бактерији *Staphylococcus aureus*. Генерисане наночестице TiO_2/Ag на површини полиамидне тканине обезбеђују максималну бактеријску редукцију и тиме одличну антибактеријску активност. Упркос ослобађању сребра са тканине током прања, импрегнирана полиамидна тканина је очувала максималну редукцију колонија *E. coli*. Антибактеријска активност према бактерији *S. aureus* је смањена након десет циклуса прања, али се још увек може сматрати задовољавајућом. Присуство наночестица TiO_2/Ag такође обезбеђује бољу ефикасност UV заштите која се може класификовати као врло добра.

(Примљено 4. новембра, ревидирано 15. децембра, прихваћено 19. децембра 2014)

REFERENCES

1. Y. Gao, R. Cranston, *Text. Res. J.* **78** (2008) 60
2. M. Rai, A. Yadav, A. Gade, *Biotechnol. Adv.* **27** (2009) 76
3. R. Dastjerdi, M. Montazer, *Colloids Surfaces, B* **79** (2010) 5
4. A. M. Grancarić, E. Rybicki, A. Tarbuk, G. Pavlović, L. Botteri, *Tekstil* **60** (2011) 629 (in Croatian)
5. M. Radetić, *J. Mater. Sci.* **48** (2013) 95
6. H. J. Lee, S. Y. Yeo, S. H. Jeong, *J. Mater. Sci.* **38** (2003) 2199
7. H. J. Lee, S. H. Jeong, *Text. Res. J.* **75** (2005) 551
8. M. Gorenšek, P. Recelj, *Text. Res. J.* **77** (2005) 138
9. N. Vigneshwaran, A. A. Kathe, P. V. Varadarajan, R. P. Nachane, *J. Nanosci. Nanotechnol.* **7** (2007) 1893
10. D. Pohle, C. Damm, J. Neuhof, A. Rösch, H. Münstedt, *Polym. Polym. Compos.* **15** (2007) 357
11. T. Yuranova, A. G. Rincon, A. Bozzi, S. Parra, C. Pulgarin, P. Albers, J. Kiwi, *J. Photochem. Photobiol. A* **161** (2003) 27
12. V. Ilić, Z. Šaponjić, V. Vodnik, S. Lazović, S. Dimitrijević, P. Jovančić, J. M. Nedeljković, M. Radetić, *Ind. Eng. Chem. Res.* **49** (2010) 7287
13. I. Perelshtein, G. Applerot, N. Perkas, G. Guibert, S. Mikhailov, A. Gedanken, *Nanotechnology* **19** (2008) 245705
14. M. Gorjanc, F. Kovač, M. Gorenšek, *Text. Res. J.* **82** (2012) 62
15. M. Gorjanc, V. Bukošek, M. Gorenšek, A. Vesel, *Text. Res. J.* **80** (2010) 557
16. M. Gorjanc, V. Bukošek, M. Gorenšek, M. Mozetič, *Text. Res. J.* **80** (2010) 2204
17. R. Czajka, *Fibres Text. East. Eur.* **13** (2005) 13

18. S. T. Dubas, P. Kumlangdudsana, P. Potiyaraj, *Colloids Surfaces, A* **289** (2006) 105
19. M. Radetić, V. Ilić, V. Vodnik, S. Dimitrijević, P. Jovančić, Z. Šaponjić, J. Nedeljković, *Polym. Adv. Technol.* **19** (2008)1816
20. V. Ilić, Z. Šaponjić, V. Vodnik, D. Mihailović, P. Jovančić, J. Nedeljković, M. Radetić, *J. Serb. Chem. Soc.* **74** (2009)349
21. V. Ilić, Z. Šaponjić, V. Vodnik, R. Molina, S. Dimitrijević, P. Jovančić, J. Nedeljković, M. Radetić, *J. Mat. Sci.* **44** (2009) 3983
22. V. Ilić, Z. Šaponjić, V. Vodnik, D. Mihailović, P. Jovančić, J. Nedeljković, M. Radetić, *Fiber. Polym.* **10** (2009) 650
23. N. K. Vu, A. Zille, F. R. Oliveira, N. Carneiro, A. P. Souto, *Plasma Proc. Polym.* **10** (2013) 285
24. A. D. Erem, G. Ozcan, M. Skrifvars, M. Cakmak, *Fiber. Polym.* **14** (2013) 1415
25. M. Milošević, M. Radoičić, Z. Šaponjić, T. Nunney, D. Marković, J. Nedeljković, M. Radetić, *J. Mat. Sci.* **48** (2013) 5447
26. M. Milošević, M. Radoičić, Z. Šaponjić, T. Nunney, C. Deeks, V. Lazić, M. Mitrić, T. Radetić, M. Radetić, *Cellulose* **21** (2014) 3781
27. T. Rajh, A. Ostafin, O. I. Mićić, D. M. Tiede, M. C. Thurnauer, *J. Phys. Chem.* **100** (1996) 4538
28. T. Rajh, J. Nedeljković, L. X. Chen, D. M. Tiede, M. C. Thurnauer, *J. Adv. Oxid. Technol.* **3** (1998) 292
29. V. K. Stockhausen, A. Henglein, *Ber. Bunsenges, Phys. Chem.* **75** (1971) 833
30. M. Breitenkamp, A. Henglein, J. Lilie, *Ber. Bunsenges, Phys. Chem.* **80** (1976) 973
31. G. Nogami, J. H. Kennedy, *J. Electrochem. Soc.* **136** (1989) 2583
32. D. Mihailović, Z. Šaponjić, M. Radoičić, T. Radetić, P. Jovančić, J. Nedeljković, M. Radetić, *Carbohyd. Polym.* **79** (2010) 526
33. ASTM E2149-13a, *Standard Test Method for Determining the Antimicrobial Activity of Antimicrobial Activity of Antimicrobial Agents Under Dynamic Contact Conditions*, ASTM International, West Conshohocken, PA, 2001, www.astm.org
34. ISO 105-E04, 1989, *Colour fastness to perspiration*, International Organization for Standardization, Geneva
35. D. Mihailović, Z. Šaponjić, R. Molina, M. Radoičić, J. Esquena, P. Jovančić, J. Nedeljković, M. Radetić, *Polym. Composites* **32** (2011) 390
36. D. Mihailović, Z. Šaponjić, R. Molina, N. Puač, P. Jovančić, J. Nedeljković, M. Radetić, *ACS Appl. Mater. Inter.* **2** (2010) 1700
37. V. Lazić, Z. Šaponjić, V. Vodnik, P. Jovančić, J. Nedeljković, M. Radetić, *Industria Textila* **64** (2013) 89
38. K. Kulthong, S. Srisung, K. Boonpavanitchakul, W. Kangwansupamonkon, R. Maniratanachote, *Part. Fibre Toxicol.* **7** (2010) 1
39. W. A. Daoud, J. H. Xin, *J. Am. Ceram. Soc.* **87** (2004) 953
40. W. A. Daoud, J. H. Xin, Y. H. Zhang, *Surf. Sci.* **599** (2005) 69.

Journal of the Serbian Chemical Society
JSCS-info@shd.org.rs • www.shd.org.rs/JSCS

J. Serb. Chem. Soc. 80 (5) 717–729 (2015)
JSCS–4751

UDC 547.992+544.478+546.3–31:549.67:
547.56:665.61–57+66.092–977
Original scientific paper

Modification of natural clinoptilolite and ZSM-5 with different oxides and a study of the obtained products in lignin pyrolysis

JELENA A. MILOVANOVIĆ[1]*, RUTH ELISABETH STENSRØD[2], ELISABETH M. MYHRVOLD[2], ROMAN TSCHENTSCHER[2], MICHAEL STÖCKER[2], SLAVICA S. LAZAREVIĆ[3] and NEVENKA Z. RAJIĆ[3]

[1]Innovation Centre of the Faculty of Technology and Metallurgy, University of Belgrade, Karnegijeva 4, 11000 Belgrade, Serbia, [2]SINTEF, Forskningsveien 1, 0314 Oslo, Norway and [3]Faculty of Technology and Metallurgy, University of Belgrade, Karnegijeva 4, 11000 Belgrade, Serbia

(Received 31 July, revised 17 October, accepted 6 November 2014)

Abstract: In this work, different metal oxides (MO) supported on two types of zeolites: 1) natural clinoptilolite (NZ) and 2) synthetic zeolite, ZSM-5 were prepared and tested as catalysts in the fast pyrolysis of hardwood lignin. NZ was modified with the CaO and MgO by a simple two steps procedure consisting of an ion exchange reaction and subsequent calcination at 773 K. The synthetic ZSM-5 was modified with several MO species (Ni, Cu, Ca, Mg) by wet impregnation and calcination at 873 K. The prepared catalysts were characterized by X-ray diffraction analysis (XRD), scanning electron microscopy and energy dispersive X-ray analysis (SEM/EDS), and measurement of their specific surface area (BET method). Acid sites were characterized and quantified by pyridine (py) absorption using Fourier transform infrared spectroscopy (FTIR). The catalysts exhibit catalytic activity depending on modification, reaction temperature and of the MO contents. The highest yield of useful phenol in bio-oil was obtained with NiO/ZSM-5 (34.8 wt. %) which exhibits the highest specific surface area and the highest concentration of Brönsted and Lewis acid sites. The studied catalysts did not increase significantly the content of polycyclic aromatic hydrocarbons (PAHs) and ʻheavy' compounds (phenols with M_r > 164 g mol^{-1}) compared to non-catalytic experiment.

Keywords: lignin; catalysts; natural zeolite; ZSM-5; bio-oil; phenol.

INTRODUCTION

Lignocellulose is the cheapest and most abundant source of biomass that is considered as a green and renewable energy source for potential replacement of fossil fuels. Lignin is the second most important component of lignocellusosic

---

* Corresponding author. E-mail: jmilovanovic@tmf.bg.ac.rs

doi: 10.2298/JSC310714109M

biomass, exceeded only by cellulose, representing about 4–35 wt. % of most biomass, 16–25 wt. % of hardwoods and 23–35 wt. % of softwoods.[1] Lignin is an amorphous, aromatic biopolymer that is a byproduct of the pulp and paper industries and is conventionally regarded as a waste material having low economic usage. However, its structural feature being comprised of variously linked phenylpropane units indicates that lignin could be considered as a potential source of some value-added chemicals, such as phenolic compounds.

In the last decade, fast pyrolysis is considered as the method of choice for biomass conversion to bio-oils.[2–7] Pyrolysis is the thermal decomposition of biomass in the absence of oxygen performed at moderate temperatures (723–873 K) and at high heating rates. Since lignin is the most heat-resistant component in lignocellulosic biomass, its pyrolysis is regarded as a challenge because of the high amount of residual char. Accordingly, the aim of this study was to examine the direct conversion of hardwood lignin into useful chemicals by catalytic fast pyrolysis. For this purpose, two catalytic systems based on zeolites were explored.

Zeolites are open-framework aluminosilicates that are widely used in various applications. Their high concentration of active sites, high thermal/hydrothermal stability and enhanced shape selectivity make them perspective candidates for the design of catalysts for lignin pyrolysis. In a previous investigation, it was found that pyrolysis of hardwood lignin in the presence of natural clinoptilolite modified with nano-oxide particles (NiO and Cu_2O) yielded a pyrolysis oil with a high amount of phenols.[8] This results suggest that natural clinoptilolite, as an important mineral resource in Serbia, could be used as a cheap, available and environmentally friendly precursor for the design of a catalytic system for lignin pyrolysis.

In the present study two types of zeolites were investigated for catalyst design: natural clinoptilolite (NZ) and synthetic ZSM-5. The natural clinoptilolite was modified with CaO and MgO (CaO–NZ and MgO–NZ, respectively) whereas ZSM-5 was modified with CaO, MgO, Cu_2O and NiO (CaO/ZSM-5, MgO/ZSM-5, Cu_2O/ZSM-5 and NiO/ZSM-5, respectively).

EXPERIMENTAL

Materials and methods

Natural clinoptilolite modified with oxide particles. Zeolitic tuff (from the Zlatokop deposit in Serbia) containing about 72 % of clinoptilolite, 13 % of quartz and 15 % of feldspars was previously investigated in detail.[9] Samples with a grain size of 65–100 μm were modified into MgO- and CaO-containing catalysts by a procedure slightly altered from that described in the literature.[10] Suspensions containing MCl_2 (M = Mg or Ca), NaOH and NZ were evaporated to dryness during approximately 5 h at 423 K on a sand bath. The obtained products were further calcined at 773 K for 3 h, cooled to room temperature and washed several times with distilled water until the filtrate was Cl-free.

ZSM-5 modified with oxide particles. ZSM-5 was synthesized using a procedure reported in the literature.[11] Aluminum sulfate octadecahydrate (Acros Organics), sodium hydroxide (Lach-Ner), and tetrapropylammonium bromide (TPABr, 98 %, Aldrich) were of analytical grade, whereas the colloidal SiO_2 solution (30 wt. %, Ludox AS, Aldrich) was of technical grade. From a reaction mixture containing reagents in the following molar oxide ratio: $7Na_2O$–$0.25Al_2O_3$–$100SiO_2$–3TPABr–$3500H_2O$, a white highly crystalline product crystallized the XRD analysis of which confirmed it to be pure ZSM-5.

In order to prepare MgO/ZSM-5 and CaO/ZSM-5, a suspension containing MCl_2 (M = Mg or Ca), NaOH and ZSM-5 was heated to dryness on a sand bath. Cu_2O/ZSM-5 and NiO/ZSM-5 were prepared in a manner similar to that described in the literature[12] using $CuSO_4\cdot 5H_2O$ (Aldrich) or $NiSO_4\cdot 6H_2O$ (Aldrich), NaOH, NH_4OH (25 %) and ZSM-5. All the obtained products were calcined at 873 K for 2 h. All the used chemicals were of analytical grade.

Prior to catalytic test, the prepared catalysts were characterized by the XRD, SEM/EDS, FTIR and BET methods.

Pyrolysis test

The lignin pyrolysis experiments were carried out in a bench-scale, fixed-bed reactor under nitrogen atmosphere at different temperatures (723, 773 and 823 K) for about 15 min.

The body of the reactor, made of a beryllium–copper alloy, was filled in the following order with: 0.06 g of quartz wool (in order to hold the reactants), 0.70 g of the catalyst and 1.50 g of hardwood lignin (obtained from Innventia, Sweden)

The liquid products were collected in a liquid bath (256 K) and quantitatively measured in a pre-weighed glass receiver. The bio-oil consisted of two phases, *i.e.*, liquid-organic and aqueous phase. The organic fraction was separated by extraction with dichloromethane and the samples were stored immediately in a refrigerator. The gaseous products were collected and measured by water displacement, while the amount of the solid residue was measured by direct weighing.

The pyrolysis products were analyzed by GC, GC–MS and TG–MS.

Instrumentation

Elemental analyses of the parent and modified zeolitic samples were performed using an SEM/EDS microscope JEOL JSM-6610LV. Samples based on natural zeolite were prepared by embedding grains in an epoxy film, polishing the crystallites, cutting with a fine-grid diamond cut and coating with gold. The samples based on ZSM-5 were coated with gold. An average elemental composition of the samples was obtained by a data collection at 10 different mm^2-sized windows on the pellet surface.

The XRD patterns of the samples were recorded using an Ital Structure APD2000 diffractometer operating with CuK_α radiation in the 2θ range 5–65°. The Rietveld method[13] was used for quantitative analysis of CaO–NZ and MgO–NZ. The estimated errors for the phase composition were under 5 % for clinoptilolite and feldspars, and under 2 % for the other phases.[8]

The BET specific surface areas (S_{BET}) of all samples were measured by a Micrometics ASAP 2020. The samples were previously out-gassed under vacuum for 10 h at 423 K. The specific surface area was determined from the desorption isotherm at a relative pressure of 0.998.

The acid sites were characterized and quantified by pyridine (py) absorption using FTIR spectroscopy. The FTIR spectra were recorded with a resolution of 4 cm^{-1} on a Nicolet spectrometer equipped with a MCT detector. The samples were pulverized and pressed into self-supported disks (20 mg; area of 2 cm^2) and placed in a quartz IR cell with KBr windows. Thermal treatment for 2 h at 673 K (277 K min^{-1}) was performed under vacuum in order to remove physisorbed water. After cooling to room temperature, an IR spectrum was recorded as the reference sample. Adsorption of py was then realized, dosing 0.133 kPa at equilibrium for 15 min followed by a thermal treatment at 373 K for 15 min to promote py diffusion. A second spectrum was recorded after removal of physisorbed py by out-gassing at 423 K for 15 min. The characterization of acid sites was effectuated on the difference spectrum obtained by subtraction of the background from the spectrum recorded after py adsorption.

Interaction of py with the Brönsted and Lewis acid sites in the samples gives rise to bands in the 1575–1525 cm^{-1} and 1470–1435 cm^{-1} range, respectively. Concentrations of the sites were calculated using the integrated absorbance of the bands and the molar extinction coefficients as measured by Emeis *et al.*, *i.e.*, 2.22 cm mol^{-1} for Lewis sites and 1.67 cm mol^{-1} for Brönsted sites. The weight and surface area of the disk was also considered.

The gaseous products of the pyrolysis test were analyzed using an Agilent 7890A instrument equipped with an FID and two TCD detectors, and an HP-PONA silica capillary column from Agilent, 50 m × 0.20 mm. The liquid products were analyzed by Agilent 5975C Inert MSD with a Triple-Axis detector. A combination of two silica capillary columns was used for the separation: a slightly polar DB-17 from J & W Scientific, 30 m×0.32 mm, and a nonpolar HP-5 from Agilent, 30 m×0.25 mm. Helium at a flow rate of 2.5 cm^3 min^{-1} was used as the gas carrier. Thermogravimetric analyses (TGA) were performed on the solid products in order to verify the inorganic carbon content. The outlet gas from the TGA was analyzed using a HPR-20 quadrupole mass spectrometer (Hiden Analytical) with regard to CO_2.

RESULTS AND DISCUSSION

Characterization of the obtained catalysts

Representative SEM micrographs of NZ and ZSM-5 are shown in Fig. 1. ZSM-5 consisted of prismatic, twinned crystals, typical for the MFI phase. Some of the crystals were sprinkled with small flower-shaped crystals (marked with “a” in Fig. 1a), which were reported to belong to ZSM-5 with a different Si/Al mole ratio than that of the bulk sample.[15] The shape and color contrast in the SEM image of NZ indicates the presence of different mineral phases. The phase in which the Si/Al molar ratio was higher than 4 corresponds to the zeolite – clinoptilolite, which was examined in detail by EDS (Fig. 1b).

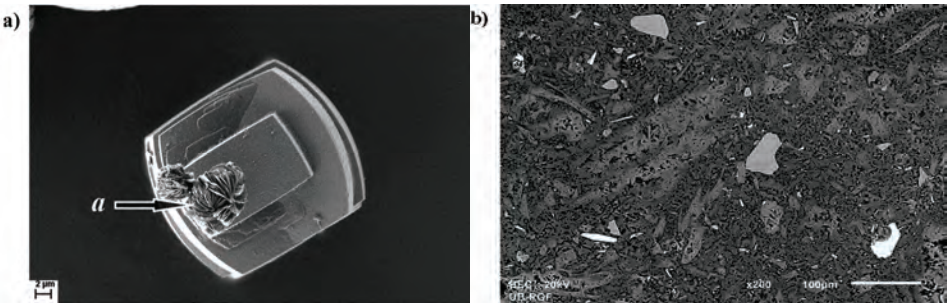

Fig. 1. SEM images of a) ZSM-5 and b) NZ.

The results of EDS analysis of the parent and the MO-loaded samples are given in Table I. The increase in the Ca and Mg content in CaO–NZ and MgO–NZ, respectively, in comparison to the parent sample (NZ) confirmed that the clinoptilolite was enriched with Ca, *i.e.*, Mg.

TABLE I. Average chemical composition of the parent (NZ and ZSM-5) and the MO-loaded zeolites obtained by EDS (wt. %)

Oxide	ZSM-5	CaO/ ZSM-5	MgO/ ZSM-5	NIO/ ZSM-5	Cu_2O/ ZSM-5	NZ	CaO–NZ	MgO–NZ
SiO_2	97.8	85	54.6	96.8	95.8	72.2	61.2	66.0
Al_2O_3	1.2	0.6	0.7	1.2	0.8	12.2	10.7	11.1
Na_2O	1	0.2	0.8	0.1	0.7	0.5	0.5	0.6
CaO		14.2				5.0	13.9	4.8
MgO			44			1.0	1.1	9.0
NiO				1.8				
Cu_2O					2.7			
Cl_2O						0.0	5.4	1.8
K_2O						2.5	1.6	2.1
TiO_2						0.9	0.9	1.3
Fe_2O_3						5.7	4.7	3.3

Decreases in the SiO_2, Al_2O_3 and Na_2O contents in favor of the metal oxide content, in comparison to the parent sample (ZSM-5), was observed for all modified samples.

XRD data were used for qualitative and quantitative analysis of CaO–NZ and MgO–NZ samples. Qualitative analysis showed the presence of anorthide, biotite, quartz, clinoptilolite, MgO in MgO–NZ, and CaO in CaO–NZ. The first three mineral phases are usually present in zeolitic tuffs.[16] Quantitative analysis by the Rietveld method revealed 0.42 wt. % of CaO (JCPDS 37-1497) in CaO–NZ and 3.66 wt.% of MgO (JCPDS 89-7746) in MgO–NZ (Fig. 2).

On comparing the results of Rietveld and SEM/EDS analyses, it is evident that the Rietveld analysis gave lower values for the CaO and MgO contents in the MO-modified NZ samples than that obtained by elemental analysis (SEM/EDS). This could be explained by the facts that not only crystalline but also amorphous oxides form during the modification and/or by the incomplete transformation of Ca/Mg into the corresponding oxides. It seems likely that not all the crystallographic sites in the clinoptilolite lattice are available for the transformation of hydrous cations into oxide species.

Moreover, the XRD patterns of ZSM-5 samples (given in Fig. S-1 of the Supplementary material to this paper) showed that the modification affected the ZSM-5 crystal structure in different manner depending on the oxide type. Thus, the crystal structure of ZSM-5 collapsed during modification with CaO and MgO. The XRD patterns of CaO/ZSM-5 and MgO/ZSM-5 (not shown) display only diffraction lines corresponding to CaO/MgO. The modification with NiO did not influence the crystallinity of ZSM-5, whereas the modification with Cu_2O led to a transformation of ZSM-5 into to a novel unknown crystal phase.

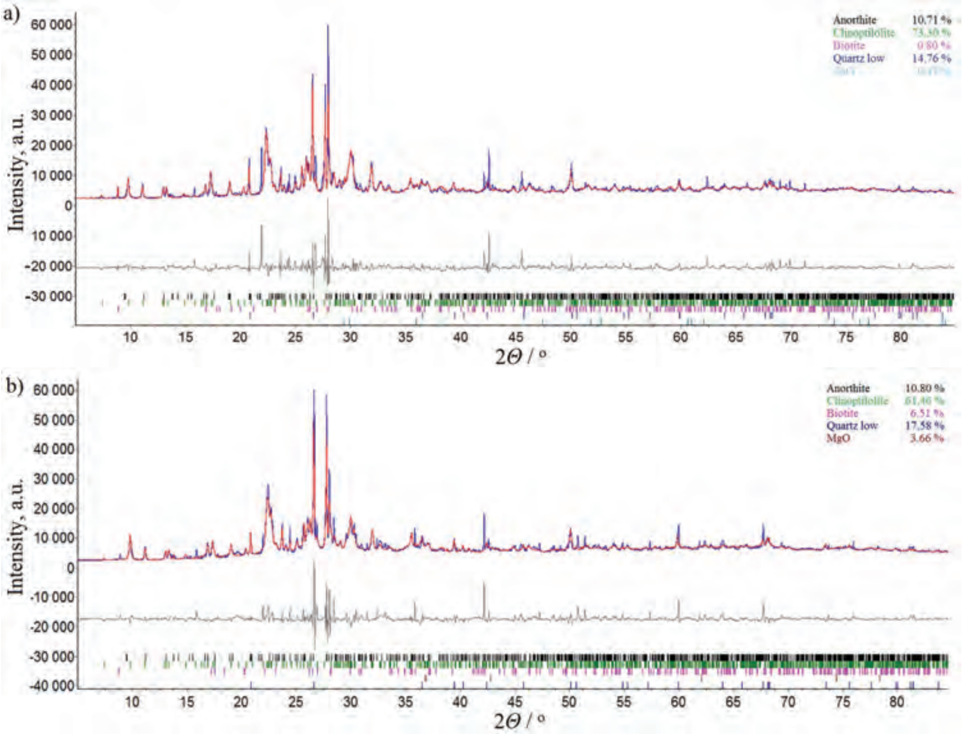

Fig. 2. Final Rietveld plot of: a) CaO–NZ and b) MgO–NZ. Observed – blue line; calculated – red crosses; difference – black line; calculated reflection positions for each phase are represented with different colored tick marks.

The results of specific surface area measurements are summarized in Table II. The results showed that the modification of NZ with CaO decreased the specific surface area of NZ, which could be attributed to the size of CaO particles that blocked the pore openings of the clinoptilolite lattice. On the other hand, the specific surface area of MgO–NZ was larger than that of NZ, indicating that MgO particles could be smaller than the CaO particles. Furthermore, the specific surface areas of CaO/ZSM-5 and MgO/ZSM-5 were significantly smaller than that of ZSM-5, confirming that the crystal structure of ZSM-5 had collapsed. The modification of ZSM-5 with NiO increased the specific surface area, indicating that the size of the NiO particles could be nano-metric.[8] Finally, the specific surface area of Cu_2O/ZSM-5 was smaller than that of ZSM-5, which could be explained by structural transformation of ZSM-5 and the formation of a novel crystalline product.

TABLE II. BET specific surface area of the zeolite materials

Sample	S_{BET} / m^2 g^{-1}
NZ	30.9
CaO–NZ	17.5
MgO–NZ	45.4
ZSM-5	229.8
CaO/ZSM-5	99.8
MgO/ZSM-5	53.4
NiO/ZSM-5	311.4
Cu_2O/ZSM-5	135.8

The acid sites of the zeolite samples were characterized and quantified by py absorption using FTIR spectroscopy. Interaction of py with the Brönsted and Lewis acid sites of the samples gave rise to bands in the 1575–1525 cm^{-1} and 1470–1435 cm^{-1} range, respectively. For CaO– and MgO–NZ, the concentration of Brönsted sites was practically negligible (1 μmol g^{-1}). Both the samples showed the presence of the Lewis acid sites with concentrations that were higher on MgO–NZ than on both CaO–NZ and NZ. Two IR vibration bands at 1449 and 1456 cm^{-1}, marked in Fig. S-2a of the Supplementary material, can be clearly observed and assigned to the interaction of lattice Al^{3+} and py.

The concentrations of the acid sites on the catalysts are summarized in Table III. It is evident that the unmodified NZ contained both Brönsted and Lewis sites, which were ascribed to the presence of extra-framework cations (Lewis sites) or to silanol groups (Si–OH) (Brönsted sites) formed on the surface of the zeolites.[17] The presence of MgO (MgO–NZ) significantly increased the concentration of Lewis acid sites on clinoptilolite, whereas the presence of CaO generally decreased the acidity (CaO–NZ).

TABLE III. Quantitative evaluation (μmol g^{-1}) of the Lewis and Brönsted acid sites on the zeolite samples; n.d. – no data

Sample	Brönsted sites	Lewis sites (1456–1448 cm^{-1})
ZSM-5	n.d.	65
CaO/ZSM-5	n.d.	51
NiO/ZSM-5	17	53
Cu_2O/ZSM-5	n.d.	33
NZ[8]	7.9	14.2
MgO–NZ	1.6	38
CaO–NZ	1.4	11

It can be noticed that the modification of ZSM-5 with the metal oxides changed the acidity (Fig. S-2b of the Supplementary material). The presence of

NiO introduced Brönsted acid sites on ZSM-5. These sites were referred to as the bridging hydroxyl groups consisting of protons bonded to the zeolite lattice in the micropores (Si–O(H)–Al).[17] The modification of ZSM-5 with the other oxides decreased the acidity of ZSM-5.

Results of the catalytic test

The prepared catalysts were tested in the fast pyrolysis of hardwood lignin using the pyrolysis unit schematically shown in Fig. S-3 of the Supplementary material.

The pyrolysis products consist of a liquid product (*i.e.*, bio-oil), a gas mixture and a solid residue. Since the bio-oil has the highest industrial impact, this product was analyzed in detail in the present work.

The compounds identified in the bio-oil were classified into eight groups: hydrocarbons, phenols, acids/esters, alcohols/ethers, carbonyls/aldehydes, polycyclic aromatic hydrocarbons (PAHs), phenylpropanoid and heavy compounds (phenols with $M_r > 164$). These groups were then classified into desirable and undesirable,[18] according to their impact on the effective and the environmentally friendly use of the bio-oil. For example, phenols and hydrocarbons are desirable fractions as they have a high commercial value as industrial chemicals. Acids are undesirable since acidic bio-oils are corrosive for engines. Furthermore, carbonyls and heavy compounds are undesirable since they reduce the chemical stability of the bio-oil. PAHs are hazardous for the environment due to their mutagenic and carcinogenic properties.

The effects of the type of catalysts, the reaction temperature and the metal-oxide content on the yield and composition of the bio-oil were investigated.

The types of the catalysts had different influences on the yield of bio-oil as can be seen from Table IV. In the table, the results from the pyrolysis experiments (under similar conditions) using an inert solid material (silica) and system without catalysts are also given. In this manner, the results of the catalytic pyrolysis process with the prepared catalysts could be compared with those from a conventional (non-catalytic) pyrolysis process.

TABLE IV. Product yields (wt. %) from the pyrolysis of hardwood lignin

Sample	Solid phase	Liquid phase	Gas phase
Without catalyst	62.2	27.2	10.6
Inert	70.5	21.4	8.2
MgO–NZ	59.3	27.7	12.9
CaO–NZ	59.2	26.7	14.1
MgO/ZSM-5	61.4	23.8	14.9
CaO/ZSM-5	60.8	25.5	13.6
Cu_2O/ZSM-5	57.4	25.0	17.6
NiO/ZSM-5	55.1	34.8	10.1

The highest yield was obtained in the presence of NiO/ZSM-5 (34.8 wt. %) whereas other catalysts gave lower liquid yield then that obtained for the non-catalytic pyrolysis (27.2 wt. %). On the other hand, all catalysts except NiO/ /ZSM-5 led to an increase in the gas production, which reached 17.6 wt. % for Cu_2O/ZSM-5. The results are given in Table V and shown in Fig. 3.

TABLE V. Composition of the organic phase (wt. % of the organic fraction) in bio-oil; $M > 164$ g mol^{-1} phenols were not found

Catalyst	Phenol	HC	Acids/ esters	Alcohols/ ethers	Carbonyls/ aldehydes	PAHs	Phenyl-propanoid
Without catalyst	66.6	11.5	0.0	12.9	1.3	0.0	0.0
Inert	66.8	2.4	0.0	21.6	0.0	0.0	0.0
MgO–NZ	77.6	14.5	0.0	6.2	0.0	0.0	0.0
CaO–NZ	77.8	14.8	0.5	5.7	1.2	0.0	0.0
MgO/ZSM-5	79.7	0.5	1.8	15.4	0.0	0.6	0.0
CaO/ZSM-5	84.1	4.2	4.9	1.9	0.0	1.2	0.5
Cu_2O/ZSM-5	77.2	15.0	0.0	7.2	0.0	0.0	0.0
NiO/ZSM-5	68.7	12.2	7.4	3.5	2.3	0.0	0.0

The results in Table V and Fig. 3 clearly indicate that the presence of the catalysts led to an increase in the yield of phenol and the increase was most noticeable in the presence of CaO/ZSM-5 (84.1 wt. %). Moreover, the catalysts did not increase significantly the content of PAHs and heavy compounds compared to the non-catalytic experiment. The catalysts exhibited small changes in the acids/esters and carbonyls/aldehydes production with the exception of CaO/ and NiO/ZSM-5, which produced a significant amount of acids/esters (4.9 and 7.4 wt. %, respectively).

The influence of the reaction temperature on the liquid yield was examined for catalysts that gave the highest liquid yield (NiO/ZSM-5) and the highest amount of phenols (CaO/ZSM-5). The results are summarized in Table S-I of the Supplementary material.

An increase in the temperature also affected the yield of bio-oil. Both catalysts gave the highest amount of bio-oil at 773 K. In addition, an increase in temperature affected the composition of the bio-oil. The results are summarized in Table S-II of the Supplementary material.

It is evident that the influence depends on the catalyst type. The presence of CaO/ZSM-5 led to an increase of the desirable and a decrease of the undesirable fractions at higher temperatures, whereas the trend was opposite in the presence of NiO/ZSM-5.

The influences of the MO content on the liquid yields are summarized in Table S-III of the Supplementary material.

It is evident that an increase in the CaO amount on ZSM-5 slightly decreased the yield of bio-oil. On the other hand, an increase in the NiO amount on ZSM-5

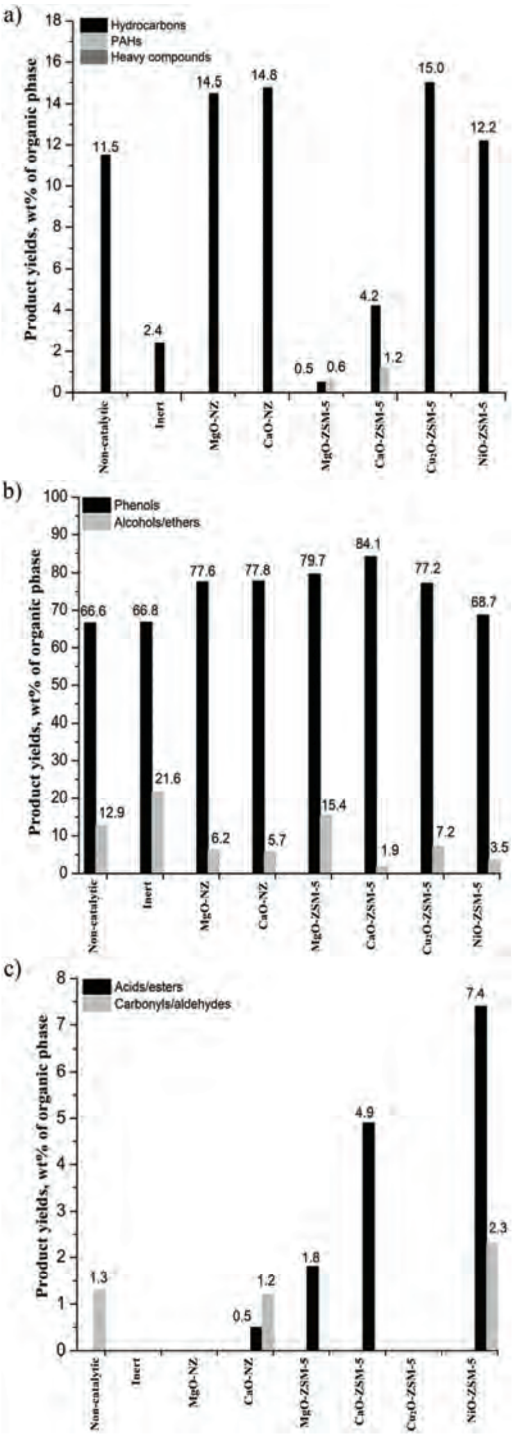

Fig. 3. Product yields (wt. % of the organic phase): a) hydrocarbons, PAHs and heavy compounds; b) phenols and alcohols/ethers and c) acids/esters and carbonyls/aldehydes.

increased the yield of the bio-oil. At this moment, an explanation for the opposite trend could not be offered since the structure of ZSM-5 collapsed during the modification with CaO. However, it seems likely that the type of metal oxide affects the mechanism of pyrolysis and it could not be excluded that the oxide carrier (*i.e.*, ZSM-5) also influenced the pyrolysis process.

Table S-IV of the Supplementary material shows that not only the yield, but also composition of the bio-oil was influenced by the MO amount. An increase of the MO content increases the amounts of phenols and undesirable acids/esters, and decreases the amounts of both hydrocarbons (HCs) and alcohols/ethers.

Preliminary analysis of solid residues analyzed by GC–MS showed that the residues are C-rich and that amount of liberated CO_2 depended on the catalyst (31.7 wt. % $CO_2$was obtained with CaO/ZSM-5 and 52.3 wt. % with NiO/ZSM-5).

Finally, the GC analysis of the gas products indicated that there was no significant difference between catalytic and non-catalytic experiments.

CONCLUSIONS

Natural clinoptilolite and synthetic ZSM-5 were studied as carriers for several metal oxides in order to test their catalytic activity in fast pyrolysis of hardwood lignin. The studied catalysts affected the pyrolysis mechanism in different manners depending on the zeolite type and type and amount of metal oxide. The highest bio-oil yield was obtained in the presence of NiO/ZSM-5 (34.8 wt. %), while the highest content of phenols in bio-oil was obtained in the presence of CaO/ZSM-5 (84.1 wt. %). For CaO/ZSM-5, it was found that the crystal structure of ZSM-5 collapsed during the modification with CaO.

Increasing the amount of NiO on ZSM-5 increased the yield of the bio-oil while increasing the CaO amount decreased it. This was explained by acidity and specific surface area, considering that the presence of NiO on ZSM-5 changed the concentration and type of the acid sites on the ZSM-5, and increased its specific surface area. The reaction temperature also influenced the pyrolysis mechanism, showing the highest bio-oil and phenol yields at 773 K.

All the obtained results indicated that NiO/ZSM-5 could be considered as a perspective catalyst for further optimization and use in fast pyrolysis of hardwood lignin. Since the crystallinity of the catalyst did not change during the catalytic test, one of the important objectives of future investigation would be performing long-term stability tests.

SUPPLEMENTARY MATERIAL

XRD patterns, FTIR spectra, the scheme of experimental pyrolysis unit, the influence of temperature and the MO content on bio-oil yield and composition of the organic phases are available electronically from http://www.shd.org.rs/JSCS/, or from the corresponding author on request.

Acknowledgments. The authors gratefully acknowledge BRISK- Biofuels Research Infrastructure for sharing knowledge, Innventia AB, SINTEF and the Ministry of Education, Science and Technological Development of the Republic of Serbia (Project No. 172018).

ИЗВОД

ПИРОЛИЗА ЛИГНИНА У ПРИСУСТВУ КАТАЛИЗАТОРА НА БАЗИ ПРИРОДНОГ ЗЕОЛИТА И ZSM-5

ЈЕЛЕНА А. МИЛОВАНОВИЋ[1], RUTH ELISABETH STENSRØD[2], ELISABETH M. MYHRVOLD[2],
ROMAN TSCHENTSCHER[2], MICHAEL STÖCKER[2], СЛАВИЦА С. ЛАЗАРЕВИЋ[3] и НЕВЕНКА З. РАЈИЋ[3]

[1]*Иновациони центар Технолошко–металуршког факултета,Универзитет у Београду, Карнегијева 4, 11000 Београд,* [2]*SINTEF, Forskningsveien 1, 0314 Oslo, Norway и* [3]*Технолошко–металуршки факултет, Универзитет у Београду, Карнегијева 4, 11000 Београд*

Припремљени су и тестирани различити оксиди метала везани за две врсте зеолита: 1) природни клиноптилолит (NZ) и 2) синтетички зеолит, ZSM-5, као катализатори у брзој пиролизи тврдог лигнина. NZ је једноставним двостепеним поступком који се састојао од јонске измене и накнадне калцинације на 773 K модификован оксидима калцијума и магнезијума. Претходно синтетисан ZSM-5 је такође модификован са неколико врста оксида (Ni, Cu, Ca и Mg) коришћењем влажне импрегнације и калцинације на 873 K. Припремљени катализатори су окарактерисани рендгенском дифракционом анализом, скенирајућом електронском микроскопијом спрегнутом са симултаном енерго-дисперзивним спектрометријом (SEM/EDS) и мерењем специфичне површине (BET метода). Кисела места на катализаторима окарактерисана су и квантификована адсорпцијом пиридина уз инфрацрвену спектроскопију са Фуријевом трансформацијом (FTIR). Припремљени катализатори испољавају каталитичку активност у зависности од начина модификације зеолита, реакционе температуре и садржаја оксида на зеолиту. Највећи принос корисног фенола у био-уљу добијен је са NiO/ZSM-5 (34,8 мас. %) који има највећу специфичну површину и највећу концентрацију Бренштедових и Луисових киселих места. Присуство испитиваних катализатора током пиролизе не доприноси значајно повећању садржаја полицикличних ароматичних угљоводоника нити једињења са великом моларном масом у односу на не-катализован процес.

(Примљено 31. јула, ревидирано 17. октобра, прихваћено 6. новембра 2014)

REFERENCES

1. A. V. Bridgwater, *Therm. Sci.* **8** (2004) 21
2. Sh. Li, Sh. Xu, Sh. Liu, Ch. Yang, Q. Lu, *Fuel Process. Technol.* **85** (2004) 1201
3. B. S. Kang, K. H. Lee, H. J. Park, Y. K. Park, J. S. Kim, *J. Anal. Appl. Pyrolysis* **76** (2006) 32
4. J. Lédé, F. Broust, F. T. Ndiaye, M. Ferrer, *Fuel* **86** (2007) 1800
5. J. Du, P. Liu, Z. Liu, D. Sun, Ch. Tao, *J. Fuel Chem. Technol.* **38** (2010) 554
6. A. Pattiya, *Bioresource Technol.* **102** (2011) 1959
7. D. Mourant, C. Lievens, R. Gunawan, Y. Wang, X. Hu, L. Wu, S. Sh. A. Syed-Hassan, Ch. Z. Li, *Fuel* **108** (2013) 400
8. N. Rajić, N. Zabukovec Logar, A. Rečnik, M. El-Roz, F. Thibault-Starzyk, P. Sprenger, L. Hannevold, A. Andersen, M. Stöcker, *Micropor. Mesopor. Mater.* **176** (2013) 162
9. Dj. Stojakovic, J. Milenkovic, N. Daneu, N. Rajic, *Clay Clay Miner.* **59** (2011) 277
10. L. M. Camacho, R. R. Parra, S. Deng, *J. Hazard. Mater.* **189** (2011) 286
11. W. J. Kim, M. Ch. Lee, D. T. Hayhurst, *Micropor. Mesopor. Mat.* **26** (1998) 133

12. A. Masalska, *Catal. Today* **65** (2001) 271
13. A. X. S. Bruker, TOPAS V2.1, *General profile and structure analysis software for powder diffraction data* – User's Manual, Bruker AXS, Karlsruhe, 2003
14. C. A. Emeis, *J. Catal.* **141** (1993) 347
15. S. Sang, F. Chang, Z. Liu, Ch. He, Y. He, L. Xu, *Catal. Today* **93–95** (2004) 729
16. Š. Cerjan Stefanović, N. Zabukovec Logar, K. Margaret, N. Novak Tušar, I. Arčon, K. Maver, J. Kovač, V. Kaučič, *Micropor. Mesopor. Mater.* **105** (2007) 251
17. A. Godelitsas, D. Charistos, A. Tsipis, C. Tsipis, A. Filippidis, C. Triantafyllidis, G. Manos, D. Siapkas, *Chem. Eur. J.* **7** (2001) 3705
18. K. S. Triantafyllidis, E. F. Iliopoulou, E. V. Antonakou, A. A. Lappas, H. Wang, Th. J. Pinnavaia, *Micropor. Mesopor. Mat.* **99** (2007) 132.

Journal of the Serbian Chemical Society
JSCS@tmf.bg.ac.rs • www.shd.org.rs/JSCS
J. Serb. Chem. Soc. 80 (5) S186–S188 (2015) *Supplementary material*

SUPPLEMENTARY MATERIAL TO

Modification of natural clinoptilolite and ZSM-5 with different oxides and a study of the obtained products in lignin pyrolysis

JELENA A. MILOVANOVIĆ[1]*, RUTH ELISABETH STENSRØD[2], ELISABETH M. MYHRVOLD[2], ROMAN TSCHENTSCHER[2], MICHAEL STÖCKER[2], SLAVICA S. LAZAREVIĆ[3] and NEVENKA Z. RAJIĆ[3]

[1]*Innovation Centre of the Faculty of Technology and Metallurgy, University of Belgrade, Karnegijeva 4, 11000 Belgrade, Serbia,* [2]*SINTEF, Forskningsveien 1, 0314 Oslo, Norway and* [3]*Faculty of Technology and Metallurgy, University of Belgrade, Karnegijeva 4, 11000 Belgrade, Serbia*

J. Serb. Chem. Soc. 80 (5) (2015) 717–729

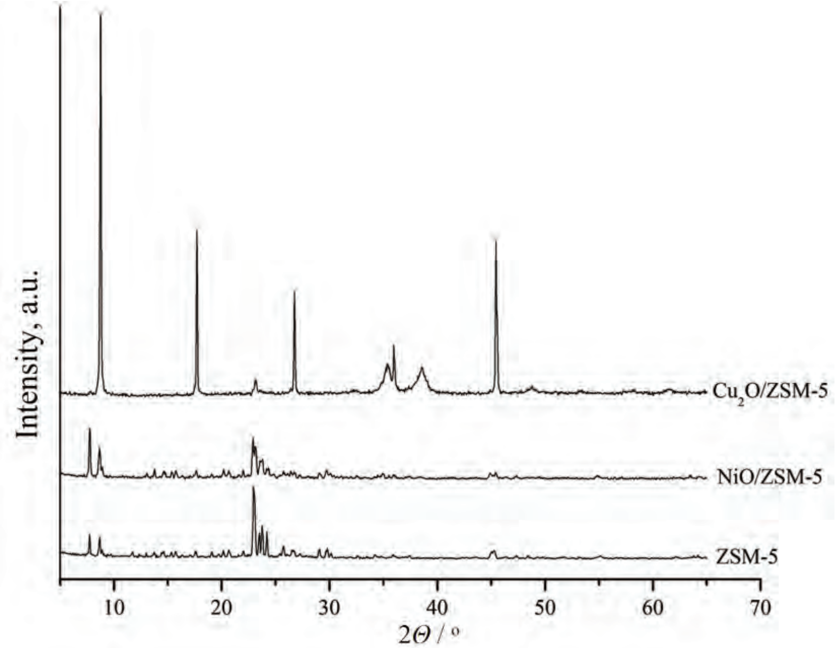

Fig. S-1. XRD patterns of ZSM-5, NiO/ZSM-5 and Cu_2O/ZSM-5.

---

* Corresponding author. E-mail: jmilovanovic@tmf.bg.ac.rs

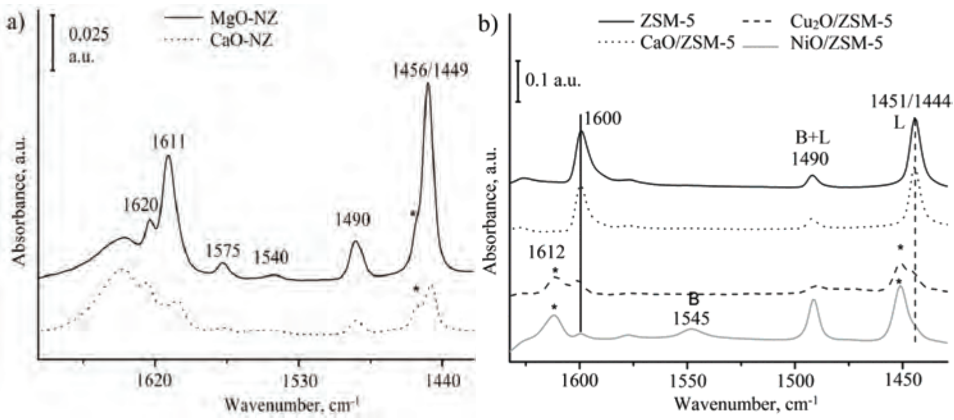

Fig. S-2. FTIR spectra of: a) NZ and b) ZSM-5 samples after pyridine adsorption. B – pyridine adsorbed on Brönsted sites, L – pyridine adsorbed on Lewis sites, B+L – common bands. * – distinct Lewis sites.

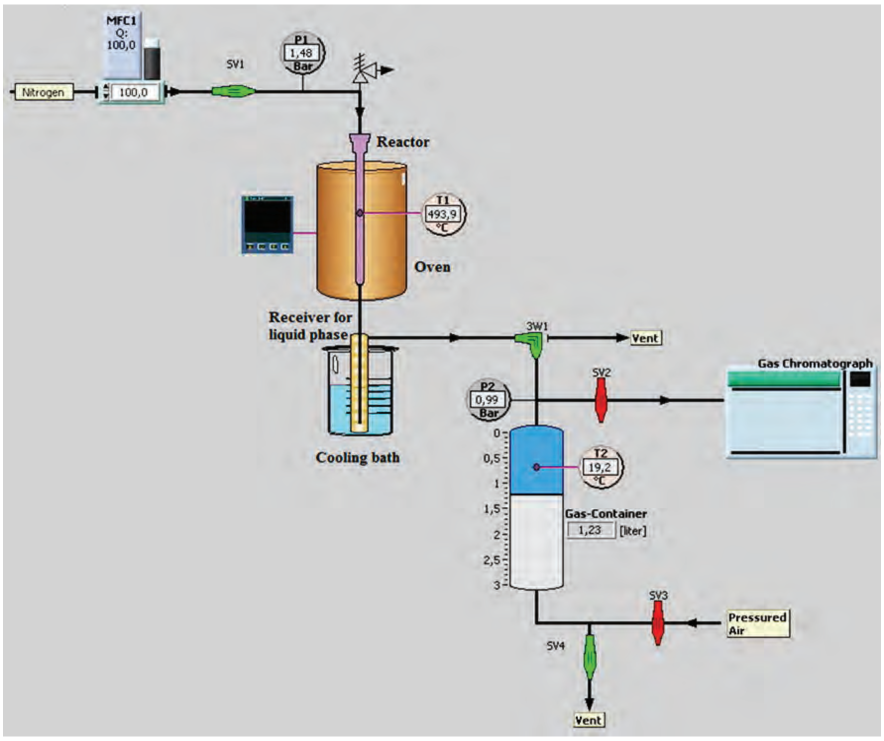

Fig. S-3. Experimental pyrolysis unit.

TABLE S-I. The influence of temperature on bio-oil yield

Temperature, K	Solid phase	Liquid phase	Gas phase
	CaO/ZSM-5		
723	66.1	22.8	11.1
773	60.8	25.5	13.6
823	59.5	20.8	19.7
	NiO/ZSM-5		
723	69.7	24.8	5.5
773	55.1	34.8	10.1
823	53.3	33.4	13.3

TABLE S-II. Composition of the organic phases (wt. % of the organic fraction) in bio-oil; $M > 164$ g mol^{-1} phenols were not found

Temp., K	Phenols	HCs	Acids/ esters	Alcohols/ ethers	Carbonyls/ aldehydes	PAHs	Phenyl propanoid
				CaO/ZSM-5			
723	71.5	3.2	14.5	0.0	0.6	0.0	0.0
773	84.1	4.2	4.9	1.9	0.0	1.2	0.5
823	85.6	3.5	2.6	0.8	0.0	0.0	0.0
				NiO/ZSM-5			
723	65.6	21.8	0.8	8.0	2.1	0.0	0.0
773	68.7	12.2	7.4	3.5	2.3	0.0	0.0
823	71.2	9.3	15.9	0.0	2.6	0.0	0.0

TABLE S-III. The influence of the MO content on bio-oil yield

Metal-oxide content, wt. %	Solid phase	Liquid phase	Gas phase
	CaO/ZSM-5		
1	51.7	33.3	15.0
3	56.0	29.4	14.6
	NiO/ZSM-5		
1	56.3	25.6	18.1
3	51.2	27.0	21.8

TABLE S-IV. Composition of the organic phase (wt. % of the organic fraction) in bio-oil; $M > 164$ g mol^{-1} phenols and PAHs were not found

Metal-oxide content, wt. %	Phenols	HCs	Acids/ esters	Alcohols/ ethers	Carbonyls/ aldehydes	Phenyl propanoid
			CaO/ZSM-5			
1	60.5	30.9	0.0	5.8	1.8	0.0
3	69.5	6.7	14.4	3.0	1.7	0.4
			NiO/ZSM-5			
1	56.8	21.7	6.7	8.7	1.0	0.0
3	61.4	16.3	7.4	6.2	1.2	0.0